Imperial College London

Gold-Silica Quantum Rattles for Cancer Therapy and Diagnosis

Mathew Thomas Hembury

A thesis submitted to Imperial College London for the award of a PhD and the Diploma of Imperial College

Department of Materials
Imperial College London

September 2012

Abstract

The Holy Grail of cancer research is to find effective treatments that can be easily delivered to diseased cells with minimal collateral damage to healthy tissue. In this context, recent developments in nanoparticle technology have aroused considerable interest with the promise of multifunctional vectors for both diagnostic and treatment of cancer.

Recently, new emphasis has been placed on hybrid nanoparticle (NP) systems, where combinations of different types of nanostructured materials are used to create multimodal systems that exhibit the combined beneficial properties of the component modules. In particular, nanorattles, which are NPs with a core-shell structure containing a distinctive void separating the core material from the shell, constitute promising launch platforms for many biomedical applications.

Current hybrid NP systems tend to concentrate on adding extra properties by increasing the number of modules and therefore, system complexity. However, added complexity in itself does not guarantee higher effectiveness. Therefore, in this thesis, a more holistic approach is proposed whereby simplicity, efficiency and usefulness of the design are not overlooked.

The work presented here describes a gold-silica rattle-type particle, the Quantum Rattle (QR), made of a hollow mesoporous silica shell (HS) hosting two classes of hydrophobic gold nanostructures: gold quantum dots (AuQDs) and gold nanoparticles (AuNPs). The HS stabilises the gold nanostructures, making them dispersible in water and thereby enables biomedical applications. It also allows passive targeting for the QR via the enhanced permeability and retention (EPR) effect. The AuQDs absorb and

emit light in the near-infrared (NIR) biological window where blood and soft tissue are relatively transparent (650 nm - 900 nm). With their NIR photonics, the AuQDs mediate both photothermal therapy (PPT) and live infrared imaging. Finally, the hydrophobic AuNPs optimise the system's drug carrying performance by increasing the payload's loading efficiency as well as controlling its release profile. This thesis exhibits the first evidence of the intrinsic and efficient therapeutic and diagnostic potential of this new class of hybrid NP system and discusses how these results could have a significant impact on the growing field of nanosystems used for cancer treatment.

Preface

Author's Declaration

This thesis is a record of the work carried out by me in the Department of Materials and the Department of Bioengineering at Imperial College London (London, UK) and the Laboratoire de Chimie de la Matière Condensée de Paris at the Collège de France (Paris, France). The work described herein is my own, unless otherwise stated.

Article in Preparation

Hembury M, Chiappini C, Bertazzo S, Drisko G, Hedegaard M, Gormley A, Katla S, Kumar C, Ghandehari H, Porter A, Sanchez C, Boissière C, Stevens M. (2012) Gold-Silica Quantum Rattles for Cancer Therapy and Diagnosis. *In preparation for submission to Nature Nanotechnology.*

Acknowledgments

After four years, the time has finally come to submit my thesis. In doing so I would like to express my sincere gratitude to all the people who helped me complete this project. Without the continuous help and support of my colleagues and friends, my research and resulting thesis would not have come to fruition.

First, I would like to thank my two supervisors, Prof. Molly Stevens and Dr. Alexandra Porter, for their support and guidance throughout all the high spots as well as the trials and tribulations that marked the route to the completion of my thesis. In particular, I would like to thank Molly for believing in me and giving me the opportunity to realise the potential of this project which has become such an important part of my life during the last four years. Likewise my sincere thanks to Alex for her unremitting advice and patience coupled with her contagious motivation.

I would also like to thank Prof. Clément Sanchez who generously offered me the opportunity of being a guest researcher at his laboratory at the Collège de France in Paris. His advice and unsurpassed knowledge of hybrid materials proved invaluable for the development of the Quantum Rattle system. Likewise, my thanks to Dr. Cédric Boissière and Dr. Glenna Drisko, at the Collège de France, for introducing me to the world of mesoporous silica and for providing me with the competence and advice necessary to make silica particles an essential ingredient in the Quantum Rattle system.

In addition, I would like to express my gratitude to Prof. Francesco Stellacci for offering me the opportunity of visiting his research laboratory at MIT in Boston, USA. The scientific discussions and the experience gained in his group have been invaluable on both an academic and a personal level.

During the course of this research project, I also had the privilege to work, and become friends with Dr. Ciro Chiappini and Dr. Sergio Bertazzo, without whom this project would simply not have been realised in its existing form. Their enormous passion and creativity stimulated our many discussions and elevated my work to a higher level than would otherwise have been attained.

I am very grateful to all the great and interesting colleagues I worked with in the Stevens group over the years. A special thank you goes to Stu, Dave, Seth, John, James, Yann, Thomas, Heiko, Tommy, Nicolas, Hélène, Jess, Amanda, Maria, Farina, Elsie, Lesley and Silvia for making my time in London so enjoyable and memorable. Furthermore, I would like to thank my friends back in Paris for their continuous support and interest in my Quantum Rattle research. Of course, having received so much help and support from so many people, it is inevitable that there will be some important omissions in these acknowledgements. Nevertheless, you know who you are and I am sure you will understand this lapse on my part.

Lastly, this thesis would not have been possible without the support and encouragement of my family, especially my parents. In particular, a thank you to my father for helping me break communications barriers and to my mother for helping fix them afterwards. Thank you for always being there for me. Finally, to Lise, a very special thank you for putting up with me and being so supportive. You kept me on the straight and narrow especially with regard to my logic. I do not believe I would have been able to finish this PhD without your help and unrelenting optimism.

Contents

Abstract **3**

Preface **5**

Acknowledgments **7**

Table of Contents **12**

List of Figures **28**

List of Movies **30**

List of Tables **31**

1 Introduction **33**

1.1 Introduction 33

1.1.1 Scope of the Thesis 34

1.2 Nanotechnology 35

1.2.1 Gold Nanoparticles 37

1.2.2 Gold Quantum Dots 42

1.2.3 Multifunctional Hybrid Systems 46

1.3 Nanoparticles for Cancer Treatment 48

1.3.1 Diagnosis for Cancer Treatment 50

1.3.2 Photothermal Therapy 56

1.3.3 Chemotherapy 59

2 Experimental Techniques **63**

2.1 Microscopy 63

2.1.1 Transmission Electron Microscopy 63
2.1.2 Laser Confocal Scanning Microscopy 68
2.2 Spectrophotometry 70
2.2.1 UV-Visible Spectroscopy 70
2.2.2 Steady-State Photoluminescence Spectroscopy 72

3 The Quantum Rattle System: Synthesis and Characterisation 75
3.1 Introduction 75
3.2 Materials and Methods 78
3.2.1 Hollow Mesoporous Silica Particles 78
3.2.2 Gold Synthesis 79
3.2.3 Quantum Rattle Syntheses 80
3.2.4 Particle Morphology and Composition 82
3.2.5 Photonic Characterisation 85
3.3 Results and Discussion 86
3.3.1 Hollow Mesoporous Silica Particles 86
3.3.2 Quantum Rattle 91
3.3.3 Quantum Rattle Photonic Properties 101
3.4 Conclusions 107

4 Quantum Rattle Interactions with Cells 109
4.1 Introduction 109
4.2 Materials and Methods 111
4.2.1 Quantum Rattles Cytotoxicity 112
4.2.2 Quantum Rattle Silica Shells Functionalisation 115
4.2.3 Microscopy 115
4.3 Results and Discussion 118
4.3.1 Quantum Rattles Cytotoxicity 118
4.3.2 Quantum Rattles Internalisation 122
4.4 Conclusions 130

5 Quantum Rattles Mediate Hyperthermia *In Vitro* 133
5.1 Introduction 133

5.2 Materials and Methods 138
5.2.1 Photothermal Properties of the Quantum Rattles . . 138
5.2.2 *In Vitro* Assessment of the Quantum Rattles Photothermal Properties 139
5.2.3 *Ex Vivo* Assessment of the Quantum Rattles Photothermal Properties 144
5.3 Results and Discussion 144
5.3.1 Photothermal Properties of the Quantum Rattles . . 144
5.3.2 *In Vitro* Assessment of the Quantum Rattles Photothermal Properties 150
5.3.3 *Ex Vivo* Assessment of the Quantum Rattles Photothermal Properties 157
5.4 Conclusions 159

6 Quantum Rattles for Drug Delivery 161
6.1 Introduction 161
6.2 Materials and Methods 164
6.2.1 Drug Loading 164
6.2.2 Drug Release 165
6.3 Results and Discussion 166
6.3.1 Drug Loading 166
6.3.2 Drug Release 169
6.4 Conclusions 171

7 Conclusions and Future Work 173

A Appendices 177
A.1 Photonic Properties of 'Thick' Quantum Rattles 178
A.2 NIR Imaging Potential of the Quantum Rattles 179
A.3 Magnetic Properties of the Quantum Rattles 180
A.4 Statistical Analyses 180
A.4.1 *In Vitro* Cytotoxicity 181
A.4.2 LIVE/DEAD Quantification Study 187

A.4.3 *Ex Vivo* Assessment of the Quantum Rattles Photothermal Properties Study 191
A.4.4 Drug Delivery Study 193
A.5 Thermal Camera Movies - Real-Time Temperature Acquisition 196
A.6 LIVE/DEAD Assay Quantification - Killing Efficiency . . . 198

Bibliography **207**

List of Figures

1.1 Scale comparing the dimensions of organic molecules and biological entities with examples of nanomaterials. 36
1.2 Schematics representing the syntheses of thiol-protected AuNPs using (a) the Brust-Schiffrin reaction and (b) the Stucky reaction. 39
1.3 Schematic of plasmon oscillations of a metal nanosphere in response to an incident electric field. Adapted from [1]. . . . 41
1.4 Crystal structure of a $Au_{25}(SR)_{18}$ gold quantum dot. $Au_{25}(SR)_{18}$ is based on a core-shell striker with (a) a centred icosahedral Au_{13} core surrounded by (b) a Au_{12} exterior shell protected by (c) 18 thiolate ligands arranged in six 'staple' motifs -S-Au-S-Au-S-. Adapted from [2]. 44
1.5 (a) Kohn-Sham orbital level diagram and (b) peak assignment for the UV-Vis absorption spectrum of $Au_{25}(SR)_{18}$ gold quantum dots. Adapted from [2]. 45
1.6 Schematic illustrations of rattle-type particles with different morphologies. Rattle-type particles with (a) a single core, (b) multiple cores and (c) multiple shells. Adapted from [3]. 47

1.7 Schematic illustrations for preparing gold-silica rattle-type particles employing (a) etching strategies and (b) soft templating methods. (c-d) Transmission electron microscopy (TEM) images of Au@SiO_2 nanorattles obtained through etching with KCN at different concentrations, resulting in varying gold core diameters. Scale bars: 200 nm. (e-f) TEM images of Au@SiO_2 nanorattles obtained through soft templating method using different concentrations of the initial gold salt solution to vary the final gold loading. Scale bars: 20 nm. Adapted from [3–5]. 48

1.8 Enhanced permeability and retention (EPR) effect. (a) Vasculature in normal tissues is tight, preventing targeting nanoparticles from penetrating and extravasating. (b) Vascular walls in tumour tissue have multiple narrow slits and are leaky and thus hyperpermeable to nanoparticles (60 nm to 400 nm), which preferentially accumulate in the tumour. Adapted from [6] 51

1.9 Advantages and limitations associated with different imaging techniques. Adapted from [7]. 52

1.10 Wavelength range of the near-infrared (NIR) tissue transmission window. Photothermal therapy and optical diagnostic imaging are most efficient in the 650 nm to 900 nm spectral range due to minimal light absorption by haemoglobin (< 650 nm) and water (> 900 nm). Adapted from [8]. 54

1.11 Various types of nanoparticle-based systems used in biomedical research and drug delivery.[9] 60

2.1 Comparison between optical microscopy, transmission electron microscopy and scanning electron microscopy. Basic set-ups of (a) an optical microscope, (b) a transmission electron microscope (TEM) and (c) a scanning electron microscope (SEM). 64

2.2 Basic set-up of a confocal microscope. Light from the laser (blue line) is scanned across the specimen by the scanning mirrors. Optical sectioning occurs as the fluoresced light (green line) passes through a pinhole before reaching the detector. 69
2.3 UV-Vis spectrophotometer basic set-up. 71
2.4 Mechanism of photoluminescence. The horizontal lines indicate quantum energy levels of the photoluminescent object. When a photoluminescent object absorbs a photon, an electron will be excited into a higher energy state. When it returns to its ground state, a photon is emitted. 73

3.1 The Quantum Rattle design specifications. The Quantum Rattles are thin shells of mesoporous silica hosting gold nanoparticles within their core and gold quantum dots within their mesopores. The biocompatible silica shell stabilises the gold nanostructures inside it and has a diameter (< 400 nm) which sets well within the range to exploit the enhanced permeability and retention (EPR) effect. The gold quantum dots are photonically active in the near-infrared biological window allowing both photothermal therapy and live fluorescent imaging. The gold nanoparticles enhance the mesoporous silica shell as a drug vector by improving loading efficiency and prolonging sustained release. 77
3.2 Schematic of Quantum Rattle synthesis. (a) Chloro(triphenylphosphine) gold (I) salt and 1-octanethiol are infused into hollow mesoporous silica shells. (b) Nucleation and formation of gold quantum dots inside the silica shell's pores and gold nanoparticles inside and outside the hollow shell after the addition of the borane tert-butylamine complex reducing agent. (c) Purification step separating Quantum Rattles (QRs) from gold nanoparticles formed outside the hollow silica shells. 81

3.3 Morphology and size distribution of polystyrene particles used in the hollow mesoporous silica synthesis as template for the cavity. (a-c) Scanning electron microscopy images of the polystyrene particle template showing a monodisperse and spherical population at different magnifications. Scale bars: 500 nm. 88

3.4 Morphology of hollow mesoporous silica particles. Bright field transmission electron microscopy images of the (a-b) thick and (c-d) thin hollow mesoporous silica particles (HSs). Both type of HSs are monodisperse and spherical. The mesopores of both silica shells possess an ordered and radial organisation, starting from the core. Scale bars: 100 nm. . . . 90

3.5 Effect of the Quantum Rattle synthetic process on the mesoporous silica shell. (a) Nitrogen adsorption and desorption isotherm of thin (grey) and thick (black) and (b) small angle x-ray scattering (SAXS) spectra of thin (grey) and thick (black) Quantum Rattles (QRs, plain line) and hollow mesoporous silica particles (HSs, dashed line) showing that the QR synthetic pathway does not affect the integrity and pore structure of the mesoporous silica shells. 91

3.6 Attempted Quantum Rattle synthesis using gold (III) salt as metallic precursor. (a) Bright field transmission electron microscopy image showing hollow mesoporous silica particles without any gold nanostructures inside the cavity. White cross indicates where energy dispersive X-ray spectroscopy (EDS) analysis was performed. Scale bar: 100 nm. (b) Corresponding EDS spectra showing no elemental trace of gold. 93

3.7 Morphology of Quantum Rattles. Bright field transmission electron micrographs of (a-b) thick and (c-d) thin Quantum Rattles (QRs) showing gold nanostructures (yellow arrows) inside hollow mesoporous silica particles (blue arrows). (a,c) Ultrathin sections of resin-embedded QRs, obtained through microtomy showing suprastructures formed of 5 nm to 10 nm gold nanoparticles; (b,d) Higher magnification of QRs deposited on carbon coated TEM copper grid. Scale bars: 100 nm. 96

3.8 Quantum Rattle elemental analysis. (a) Bright field transmission electron micrographs of thin Quantum Rattles (QR) showing gold nanostructures (yellow arrows) inside hollow mesoporous silica particles (blue arrows). White cross indicates where energy dispersive X-ray spectroscopy (EDS) analysis was performed. Scale bar: 100 nm. (b) Corresponding EDS spectra of QR indicating the presence of silica and gold. 97

3.9 The Quantum Rattle system. Bright field high resolution transmission electron micrographs (HRTEM) of thin Quantum Rattles (QRs). HRTEM images of (a) a QR showing AuQDs (red arrow) within the mesoporous silica shell (blue arrow) of the QR and AuNPs (yellow arrow) within the cavity and (b) close-up on a QR silica shell. Scale bars: 20 nm. (c) Zoom in on the AuNPs inside the QR cavity showing the different crystal faces of the larger AuNPs. Scale bar: 5 nm. 98

3.10 The Quantum Rattle system. High angle annular dark field scanning transmission electron micrographs (HAADF-STEM) of thin Quantum Rattles (QRs). (a) HAADF-STEM images of a QR highlighting the gold nanostructures of the QR: AuQDs within the QR mesoporous silica shell and AuNPs within the cavity. Scale bar: 50 nm. (b) Close-up on the QRs mesoporous silica shell. Scale bar: 10 nm. 99

3.11 Monolayer protected gold nanoparticles. (a-b) Bright field transmission electron micrographs of 1-octanethiol protected gold nanoparticles (OT AuNPs) synthesised using QR process in the absence of hollow mesoporous silica shells at different magnifications. The OT AuNPs are highly monodisperse 8 nm particles with a hexagonal packing on the TEM copper grid. No AuQDs are visible. Scale bars: 20 nm. . . . 100

3.12 Extinction spectra of thin Quantum Rattles (QR, red) compared to hollow mesoporous silica shells without gold (HS, blue) and spherical gold nanoparticles synthesised using the same method as the QR but in the absence of hollow silica shells (AuNPs, black). Inset: zoomed in on the near infrared region of interest, showing an extinction peak centred around 672 nm. 102

3.13 Photoluminescence spectra of thin Quantum Rattles showing an excitation peak centred at 672 nm and an emission peak centred at 827 nm. Emission spectrum (λ_{ex} = 672 nm, red) and excitation spectrum (λ_{em} = 827 nm, grey). 103

3.14 Photoluminescence spectra of (a) hollow mesoporous silica particles (HS) and (b) spherical gold nanoparticles synthesised using the same method as the QR but in the absence of hollow silica shells (Free AuNPs). Both controls do not exhibit the characteristic photoluminescent peaks of the Quantum Rattles. Emission spectra (λ_{ex} = 672 nm) and excitation spectra (λ_{em} = 827 nm). 104

3.15 Morphology of non-hollow Quantum Rattles. (a) Bright field transmission electron micrograph of a non-hollow Quantum Rattle (NQR) and (b) zoom in showing gold quantum dots (AuQDs, red arrows) within the mesoporous silica shell of the NQR. Scale bars: 50 nm. 105

3.16 Photonic properties of non-hollow Quantum Rattle: (a) Extinction spectra of non-hollow Quantum Rattles (NQRs, orange) showing the same characteristic features as the Quantum Rattles (QRs) extinction spectra. Inset: zoomed onto the near infrared region of interest showing an extinction peak centred around 673 nm. (b) Photoluminescence spectra of NQRs showing an excitation peak centred at 673 nm and an emission peak centred at 826 nm. Both emission spectrum (λ_{ex} = 673 nm, orange) and excitation spectrum (λ_{em} = 826 nm, grey) are similar to the QRs photoluminescent spectra. 106

4.1 Functionalised Quantum Rattles cytocompatibility evaluated by MTT assay. The different concentrations were obtained by 10-fold dilutions of either 10^{11} particle.mL^{-1} dispersions of fluorescently labelled particles or of media pre-soaked in 5 cm^2.mL^{-1} of control material (from 100% to 0.1%). HeLa cells after 1 day incubation in media containing different concentrations (10^8 particle.mL^{-1} to 10^{11} particle.mL^{-1}) of fluorescein functionalised Quantum Rattles (fQR) or fluorescein functionalised hollow mesoporous silica particles (fHS), do not show alterations of metabolic activity compared to medical grade PVC (Negative Control). Organo-tin PVC (Positive Control) shows expected cytotoxic effect on the cell metabolic activity, proportional to the dilution factor of the original organo-tin PVC solution. Results are normalised to blank control (cells culture media without nanoparticles). Error bars represent the standard deviations of triplicate experiments. 120

4.2 Quantum Rattles cytocompatibility evaluated by MTT assay. HeLa cells after 1 day and 3 days incubation in media containing either 10^{11} particle.mL^{-1} Quantum Rattles (QR, red) or hollow mesoporous silica particles (HS, blue) do not show alterations of metabolic activity compared to medical grade PVC (Negative Control, white), whereas no metabolic activity is measured with organo-tin PVC (Positive Control, black). Results are normalised to blank control (cells culture media without nanoparticles). Error bars represent the standard deviations of triplicate experiments. 121

4.3 Quantum Rattles cytocompatibility evaluated by total DNA assay. HeLa cells after 1 day and 3 days incubation in media containing either 10^{11} particle.mL^{-1} Quantum Rattles (QR, red) or hollow mesoporous silica particles (HS, blue) do not show alterations of cell proliferation compared to medical grade PVC (Negative Control, white). Cell proliferation and viability are significantly affected by organo-tin PVC (Positive Control, black). Error bars represent the standard deviations of triplicate experiments. 123

4.4 Quantum Rattle internalisation and near-infrared fluorescence. (a,b) Laser confocal scanning microscopy images of HeLa cells incubated for 1 day with Quantum Rattles (QR), which are imaged through their native fluorescence (red). Cells are stained for F-actin (phalloidin AF488, green) and nucleus (DAPI, blue). QRs are localised by their own photoluminescence within the cells, accumulating in the perinuclear region. (a) Cell overview and (b) close-up of on one HeLa cell showing a QR aggregate in the perinuclear region. Scale bars: 10 μm. 125

4.5 Quantum Rattle silica shell functionalisation. Laser confocal scanning microscopy images of HeLa cells incubated for 1 day with (a) fluorescein functionalised hollow mesoporous silica particles (fHSs) or (b) fluorescein functionalised Quantum Rattles (fQR). Cells are stained for F-actin (phalloidin AF569, red) and nucleus (DAPI, blue). Both particles are localised by the fluorophore (fluorescein, green) functionalised on their silica shells demonstrating the silane functionalisation potential of the QRs. Scale bars: 10 µm. . . 127

4.6 Quantum Rattle internalisation. Transmission electron micrographs of ultrathin sections of HeLa cells incubated with Quantum Rattles (QRs) for 1 day, showing the co-internalisation and trafficking of the entire QR structure. (a-b) Cell overview. Red arrows points at internalised QRs. Scale bar: 2 µm. (c-d) Close-ups of the QR cluster. Scale bar: 500 nm. 128

4.7 Quantum Rattle internalisation (a-c) Transmission electron micrographs of ultrathin sections of HeLa cells incubated with Quantum Rattles (QR) for 1 day showing the co-internalisation and trafficking of the entire QR structure. (a) Cell overview. Red arrow points at internalised QRs being trafficked within a membranous vesicle. Scale bar: 2 µm. (b) Close-up of the QR cluster inside the vesicle. Inset: Zoom in on one QR. Scale bar: 100 nm. (c) Zoom in on several QRs, where energy dispersive x-ray spectroscopy analysis was performed. Scale bar: 100 nm. (d) EDS spectrum of the QR region indicating the presence of silica and gold. 129

4.8 Mapping Raman spectroscopy of Quantum Rattles (QR) internalised by HeLa cells. Each pixel represents a Raman spectrum, which were categorised in 4 groups: nuclei (blue), cytoplasm (green), gold (red) and gold with lipids (yellow). Peaks originating from lipid molecules are clearly visible for spectra around the QRs. Scale bar: 8 µm. 130

5.1 LIVE/DEAD assays quantification - irradiated cell population (a-b) Representative merged fluorescent microscopy image series of LIVE/DEAD assays performed on HeLa cells (live cells in green, dead cells in red) incubated with Quantum Rattles for 1 day and irradiated for 8 min with 671 nm laser light (38 W.cm^{-2}). The dashed surface represents the mask applied to obtain the cropped image of the LIVE and DEAD channels of (a) the irradiated cell population and (b) the cells adjacent to the laser spot. Scale bars: 200 µm 141

5.2 LIVE/DEAD assays quantification - image segmentation. Representative fluorescent microscopy image series of LIVE/DEAD assays performed on HeLa cells (live cells in green, dead cells in red) incubated with either cell media only, hollow silica shells (HS) or Quantum Rattles (QRs) for 1 day and irradiated for either 0, 2, 5, 8, 10 or 15 min with 671 nm laser light (38 W.cm^{-2}) showing their corresponding binary image series obtained after applying a segmentation algorithm. The percentage cell death is calculated by calculating the sum of the binary image matrices and normalising the DEAD channel value over the total of both LIVE and DEAD channel values. 143

5.3 Schematic of the experimental set-up used for the *ex vivo* study of Quantum Rattles (QRs) NIR light absorption potential. QRs were subcutaneously injected in chicken thighs, which were subsequently treated with NIR light at 671 nm (38 W.cm^{-2}). Temperature profiles were monitored using a thermocouple probe inserted under the skin of the chicken thigh and recorded with a RTD thermometer. 145

5.4 Photothermal properties of Quantum Rattles. Temperature profiles monitored with a thermal camera of hollow mesoporous silica shells (HS, blue) and Quantum Rattles (QR, red) dried on a glass slide showing a temperature increase in the QR samples upon irradiation with a 671 nm laser (38 $W.cm^{-2}$) compared to the HS control. 146

5.5 Photothermal properties of Quantum Rattles. Temperature profiles monitored through a thermal camera of (a) hollow mesoporous silica shells (HS, blue) and (b) Quantum Rattles (QR, red) dried on a glass slide showing a temperature increase in the QR samples upon irradiation with a 671 nm laser (7 $W.cm^{-2}$) compared to the HS control. The temperature increase is lower than when the QR are irradiated at a power density of 38 $W.cm^{-2}$(Figure 5.4), demonstrating the photothermal conversion is dependent on the incident laser irradiation power. 147

5.6 Photothermal properties of Quantum Rattles. Temperature profiles monitored through a thermocouple probe of (a) hollow mesoporous silica shells (HS, blue) and (b) Quantum Rattles (QR, red) in solution showing a bulk increase in the solvent temperature upon irradiation with a 671 nm laser (38 $W.cm^{-2}$) for the QRs compared to the HS control. 149

5.7 Effect of irradiation on the Quantum Rattles. Bright Field high resolution transmission electron microscopy (HRTEM) images of (a) overview and (b) close-up of a Quantum Rattle after irradiation by a 671 nm laser (38 $W.cm^{-2}$) for 15 min. Scale bars: 50 nm. 150

5.8 Quantum Rattles mediate hyperthermia *in vitro*. LIVE/ DEAD assays on HeLa cells (live cells in green, dead cells in red) treated with 671 nm laser light (38 W.cm^{-2}, spot size ~ 1mm). Representative fluorescent microscopy images of (a-f) cells incubated for 1 day with Quantum Rattles (QRs) and irradiated for 0, 2, 5, 8, 10 and 15 min; (g) cells irradiated for 15 min; (h) cells incubated with hollow mesoporous silica shells (HS) for 1 day and irradiated for 15 min. Scale bars: 500 µm. 152

5.9 Quantum Rattles mediate hyperthermia *in vitro*. LIVE/ DEAD assay quantification. Percentage of cell death inside the laser spot saturates after 10 min of laser irradiation. The hyperthermia and cell death caused by the QRs/laser light combination is dose dependent (*i.e.* dependent on the energy provided by the laser irradiation). Error bars represent the standard deviations of quadruplicate experiments. 154

5.10 Quantum Rattles mediate hyperthermia *in vitro*. LIVE/ DEAD assay quantification. Percentage of cell death outside the laser spot showing a linear trend ($R^2 = 0.97$) between cell death and irradiation time in the close proximity of the laser spot. Error bars represent the standard deviations of quadruplicate experiments. 155

5.11 The photothermal potential of Quantum Rattles *ex vivo*. Temperature profiles monitored through a thermocouple probe inserted under the skin of a chicken thigh after (a) no injection (Negative Control, grey), (b) phosphate buffer injection (PBS, grey) and (c) Quantum Rattles in PBS injection (QR, red). (d) Maximum temperature increase recorded for QRs in PBS injections (QR, red) compared to no injections (Negative Control, grey) and PBS alone injections (PBS, grey). A higher temperature increase is observed upon irradiation with a 671 nm laser (38 $W.cm^{-2}$) for the QR injection compared to the two controls, which show identical temperature profiles. Error bars represent the standard deviations of triplicate experiments. 158

6.1 Quantum Rattles loading efficiency of doxorubicin (DOX). DOX loading efficiency of Quantum Rattles (QR, red) compared to hollow mesoporous silica shells without gold (HS, blue) and non-hollow Quantum Rattles (NQR, orange) showing up to 9 and 5 fold increased loading efficiency for the QRs compared to the HSs and NQRs, respectively. The higher surface area and hydrophobic environment provided by the gold nanoparticles inside the cavity of the silica shell drastically enhance the DOX loading efficiency of the system, starting from concentrations as low of 31.3 $\mu g.mL^{-1}$. Error bars represent the standard deviation of triplicate experiments. Inset: Transmission electron micrographs of QR, NQRs and HS. Scale bars: 50 nm. 167

6.2 Release of doxorubicin (DOX) from Quantum Rattles. Drug release profile of Quantum Rattles (QR, red) compared to hollow mesoporous silica shells without gold (HS, blue) and non-hollow Quantum Rattles (NQR, orange) showing a 10 and 4 fold increase in the total DOX released compared to the HSs and NQRs, respectively. The QRs appear to modulate the release kinetics providing prolonged release for up to 12 h compared to HSs where the DOX release plateaus after 4 h. Error bars represent the standard deviation of triplicate experiments. Inset: Transmission electron micrographs of QR, NQRs and HS. Scale bars: 50 nm. 170

A.1 Photonic properties of thick Quantum Rattles (silica shell thickness of $\sim$ 50 nm for a total diameter of $\sim$ 200 nm). (a) Extinction spectra of thick Quantum Rattles (thick QR, red) showing the same characteristic features as the thin QRs extinction spectra. Inset: zoomed in on the near infrared region of interest showing an extinction peak centred around 672 nm. (b) Photoluminescence spectra of thick QR showing an excitation peak centred at 672 nm and an emission peak centred at 827 nm. Both emission spectrum (λ_{ex} = 672 nm, red) and excitation spectrum (λ_{em} = 827 nm, grey) are identical to the thin QRs photoluminescent spectra. 178

A.2 NIR imaging of Quantum Rattles. DU145 bilateral prostate tumours in NU/NU mice were injected with 500 µL of (a) Quantum Rattles (QR, 20 mg.mL^{-1} in PBS) or (b) saline solution. The mice were sacrificed 1 day after the intratumoural injections and the excised tumours were fixed in 4% paraformaldehyde (PFA). QRs are localised by their own photoluminescence within the tumours, accumulating in intense epifluorescent spots, which are not observed in tumorous tissue injected with saline solution. These results show the great potential of the strong NIR absorption of the QRs for selective photothermal tumour ablation. NIR imaging set-up: λ_{ex} = 675 nm and λ_{em} = 840 nm. 179
A.3 Magnetic properties of the Quantum Rattle. Magnetisation curve of Quantum Rattles (QR, red dotted line) at 2 K showing paramagnetic properties. These intrinsic QR paramagnetic characteristics could enable efficient MRI imaging, thereby providing another imaging modality to the QR system. 180
A.4 Multicomparison test for the MTT assay of cells cultured in the presence of fluorescein-functionalised Quantum Rattles. . 182
A.5 Multicomparison test for the MTT assay of cells cultured in the presence of Quantum Rattles. 184
A.6 Multicomparison test for the tDNA assay of cells cultured in the presence of Quantum Rattles. 186
A.7 Multicomparison test for the LIVE/DEAD study of the cell population inside the laser spot, which has been incubated with Quantum Rattles and treated with NIR light. 188
A.8 Multicomparison test for the LIVE/DEAD study of the cell population adjacent to the laser spot, which has been incubated with Quantum Rattles and treated with NIR light. . . . 190
A.9 Multicomparison test for the *ex vivo* assessment of the Quantum Rattles photothermal properties study. 192
A.10 Multicomparison test for the Quantum Rattles doxorubicin loading efficiency study. 194

A.11 Multicomparison test for the Quantum Rattles doxorubicin release study. 195

List of Movies

4.1 Quantum Rattle internalisation and near-infrared fluorescence. Three-dimensional reconstruction of laser confocal scanning microscopy images of HeLa cells incubated for 1 day with Quantum Rattles (QR), which are imaged through their native photoluminescence (red). Cells are stained for F-actin (phalloidin AF488, green) and nucleus (DAPI, blue). QRs are localised by their own fluorescence within the cells, accumulating in the perinuclear region. *(Click to play. Requires Adobe Reader 8.× or higher)* 124

5.1 Confocal time-lapse series of HeLa cells incubated with Quantum Rattles for 1 day. (a-b) LIVE channel during laser irradiation showing calcein (LIVE stain, green) disappearing due to the loss of intracellular esterase activity with cell death. (b) Zoomed-in view with bright field (inset) showing cells bursting during death with cytoplasm leaking and, organelles and nuclei appearing. (c-d) LIVE and DEAD channels after laser irradiation of 2 and 5 min, showing DNA-bound ethidium bromide homodimer-1 (DEAD stain, red) appearing indicating the loss of plasma membrane integrity (d) Zoomed-out view after laser irradiation showing laser spot. *(Click to play. Requires Adobe Reader 8.× or higher)* . 156

A.1 Hollow mesoporous silica particles photothermal properties. Movie showing the real-time acquisition by a thermal camera of the temperature profile of a coverslip with hollow mesoporous silica particles (HSs) drop-deposited on its surface. No heat increase is observed when a 671 nm laser is irradiated on the HS. *(Click to play. Requires Adobe Reader 8.× or higher)* 196

A.2 Quantum Rattles photothermal properties. Movie showing the real-time acquisition by a thermal camera of the temperature profile of a coverslip with Quantum Rattles (QRs) drop-deposited on its surface. A temperature increase of $\sim$ 1.5 °C is observed upon irradiation by a 671 nm laser of the QR sample. *(Click to play. Requires Adobe Reader 8.× or higher)* 197

List of Tables

1.1 Detailed overview of gold-based platforms for cancer treatment and diagnosis summarising the advantages and disadvantages of each system. 58

5.1 Detailed overview of gold-based platforms for cancer treatment and diagnosis, summarising the advantages and disadvantages of each system compared to the Quantum Rattles. . 137

Chapter 1

Introduction

1.1 Introduction

Nanotechnology, in biology, focusses on the development of novel strategies for diagnosis and therapy of disease as well as on exploring fundamental biological processes by exploiting the unique phenomena associated with materials of nanoscale dimensions. In order to tackle such biological problems, nanotechnology-based approaches are often by necessity cross-disciplinary, incorporating elements of chemistry, molecular biology, materials science, physics and optics.

When material dimensions are reduced to the nanometer scale, new and unique properties can emerge from the nanomaterial. For example, nanomaterials can exhibit advanced electronic, optical, magnetic, and mechanical properties compared to their bulk counterparts.[10–13] Nanotechnology, in its broadest sense, tries to combine and employ these unique nanoscale properties for functional devices. The properties of the nanostructured materials can resemble those of biomolecules and biomolecular assemblies, such as proteins and nucleic acids.[14] Therefore, systems incorporating nanomaterials provide unique opportunities to investigate biological interactions and processes at the nanoscale. For example, the high extinction and plasmonic optical properties exhibited by noble metal or semiconductor NPs allows them to serve as powerful biological detection

reagents.[15–20]

The unique properties of nanomaterials also show great potential for new applications originating in the field of medical technology. Especially oncology research has attracted a great deal of interest in nanotechnology.[21] Despite allocations of huge research funds and resources towards cancer diagnosis and therapy, cancer still remains one of the leading cause of death worldwide.[22].

In the past decade, nanotechnology has already played a crucial role in the development of more advanced cancer therapeutics.[23–28] By combining nanomaterial-specific properties with environment-responsive and specific bio-recognition motifs, new materials for use in oncology have been developed, including *in vitro* and *in vivo* imaging, drug delivery, diagnostics and advanced therapeutic strategies.[29] An example that shows the potential arising from the inherent interdisciplinary of nanotechnology approaches are biomolecule-nanoparticle formulations, which are capable of simultaneously imaging and treating tumours in live mice.[30, 31] In consideration of the numerous potential benefits of using nanotechnology in cancer treatment, this thesis aims to develop an improved, simple and multifunctional system to achieve simultaneous diagnosis and therapy of cancer.

1.1.1 Scope of the Thesis

This thesis explores the use of gold and silica nanostructures to devise advanced approaches towards cancer diagnostics and therapy. To this end a new straightforward synthesis has been developed to produce a novel, synergistic gold-silica rattle-type system, the Quantum Rattle (QR). The QR system is composed of a hollow mesoporous silica shell functionalised with two distinct populations of gold nanostructures - gold quantum dots (AuQDs) and gold nanoparticles (AuNPs). The overall aim of this project is to develop a multifunctional system capable of both live imaging and targeted, efficient therapy. Chapter 1 provides an overview of the emergent

properties of AuNPs and AuQDs, and explores the use of nanotechnology in cancer treatment, giving representative examples of nanomaterial uses in cancer diagnosis and therapy. The chapter concludes on the use of multifunctional composite nanosystems for use in oncology and, in particular, systems combining silica and gold in one treatment agent. Chapter 2 describes the main experimental techniques used to accomplish the work presented in this thesis. Chapter 3 focuses on the synthesis and emergent properties of the QR platform. After demonstrating the QR synthesis process, the characterisation of the morphology and composition of the QR and the promising properties of the QR with regards to cancer imaging and/or therapy are described. Following from these results, chapter 4 focusses on demonstrating the QR suitability for bioapplications and, in particular, for NIR imaging. In parallel, chapter 5 explores the photothermal properties of the QRs and their potential use as photothermal anticancer agents. Finally, chapter 6, investigates the QR potential use as drug delivery vector for hydrophobic cancer drugs. The outlook of this thesis is towards a very promising candidate for highly efficient targeted cancer treatment, which natively incorporates multimodal tools for both cancer imaging and therapy.

1.2 Nanotechnology

Nanotechnology is a rapidly expanding field, encompassing the development of man-made materials in the 5 nm to 200 nm size range. These dimensions vastly exceeds that of standard organic molecules, but its lower range approaches that of many proteins and biological macromolecules (Figure 1.1).[9] When working with materials of nanoscale dimensions, often the properties of the nanomaterial are different to those of the bulk material, whose characteristic length scale is bigger. As the size of the materials tends towards the nanoscale, the percentage of atoms at the surface increases and, consequently, the surface-to-volume ratio increases.[11] Because the surface atoms are not subjected to the same environmental

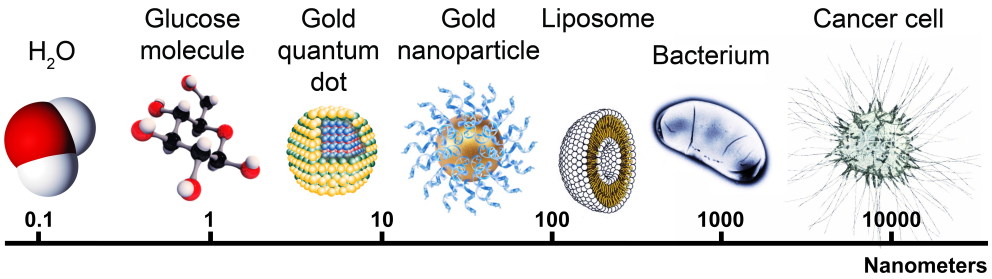


Figure 1.1: Scale comparing the dimensions of organic molecules and biological entities with examples of nanomaterials.

stress as those in the core, the nanoparticle (NP) surface atoms tend to express different physical properties. Where the composition of the core determines many intrinsic material properties, such as plasticity, hardness and conductivity, the atoms on the surface of nanomaterials have boundary properties that are determined by the characteristics of the particle in isolation plus properties arising from its interaction with other materials.[11] Furthermore, the boundary properties may be amplified in any interaction involving NPs, as the ratio of atoms on the surface to atoms in the bulk becomes greater. This interesting physical behaviour can be ascribed to quantum-mechanical rules, such as quantum confinement, superparamagnetism and surface plasmon resonance.[10, 11]

In biology, the ability to exploit the phenomena associated with NPs requires the functionalisation of the particles surfaces by either direct chemical modification or by the association of molecular ligands.[9] For example, biomolecule-metal or biomolecule-semiconductor NP hybrid systems combine the recognition and catalytic properties of biomolecules with the distinctive electronic and optical properties of NPs.[14] Furthermore, biomolecule-coupled NPs (metal or semi-conductor) are employed as nano connectors that activate redox enzymes as well as optical or electrical labels for biorecognition processes.[14] Next to that, peptide/protein-conjugated AuNPs can be used to specifically target the cell nucleus using peptide sequences from various animal virus proteins.[32] Combining unique properties enables new possibilities for developing advanced electronic and optical

biological targeted systems.

1.2.1 Gold Nanoparticles

With the emergence of nanoscience and nanotechnology, gold is increasingly becoming a key material for use in NP systems due to a variety of highly attractive properties.[11, 23, 33] AuNPs or gold colloids are the most stable metal NPs and present fascinating properties, which offer researchers great possibilities in the bottom-up approach for biology. For instance, AuNPs exhibit useful optical properties and are used in sensors for detecting numerous disease-related enzymes and proteins.[15, 18, 34] Furthermore, gold is a reasonably inert material.[11, 35] It does not oxidise at temperatures below its melting point and is not reactive with most chemicals or atmospheric dioxygen.[35] These favourable properties facilitate easy handling and manipulation of samples under atmospheric conditions, such as microfabrication and biology.[35] Besides, gold binds thiols with high affinity, which is of practical convenience for the formation of self-assembled monolayers (SAMs).[35, 36] The simplicity of AuNPs synthesis[37–39] and the ease with which their properties can be tailored, makes AuNPs highly attractive in nanotechnology-based applications.[40]

Monolayer protected AuNPs are now routinely prepared by a wide variety of colloidal methods, which provide the ability to readily functionalise the gold with both hydrophobic and hydrophilic surface ligands. The preparation of AuNPs commonly involves the chemical reduction of gold salts in aqueous, organic, or mixed solvent systems. However, as the gold surface is extremely reactive under these conditions, aggregation occurs.[9] To circumvent this problem, AuNPs are regularly reduced in the presence of a stabiliser, which binds to the surface and prevents aggregation *via* favourable cross-linking and charge properties.[9, 11, 41] Several capping ligands exist for passivation of the AuNP surface, including thiols, amines, phosphines and a range of polymers or dendrimers.[11] Historically, AuNPs were discovered by Faraday in the 19th century.[42] However, the simplest

method of synthesising AuNPs, which involved the citrate reduction of gold salt in water, was developed by Turkevich in 1951,[43] and updated by Frens in 1973.[44] These AuNP synthesis methods provide approximately spherical AuNPs with a size range of 10 nm to 100 nm and reasonably low polydispersity.

An important advance in the fabrication of stable AuNPs was introduced by Brust *et al.* in 1994,[38] who first synthesised stable alkanethiol-protected AuNPs using a two-phase reaction process, which was later extended to a single-phase system (Figure 1.2a).[45] By modifying this method, AuNPs have been successfully synthesised using numerous biomolecular coatings.[37, 46, 47] More recently, Zheng *et al.*[48] introduced a one-phase synthesis method for fabricating AuNPs using amine-borane complexes as reducing agents (Figure 1.2b). Amine-borane complexes are weaker reductants compared to conventional reducing agents, such as sodium borohydride ($NaBH_4$). By slowing down the reduction of gold cations, amine-borane complexes enable greater control over the growth of the AuNP. Using this method, Zheng *et al.* were able to synthesise different AuNPs with a size range of 2 nm to 10 nm and narrow size distributions.[48] The strength of all these gold synthesis techniques are:

- The synthetic processes are easily scalable;
- The mild synthetic conditions allow for a wide range of ligand functionalities;
- Gold core dimensions can be tailored by varying the ratio between the gold salt and the ligand ratios, reaction time and/or temperature.

One of the most commonly used properties of nanoscale gold is its intense and environment-sensitive optical absorption, which allows AuNPs to provide the basis for a wide range of applications. Well-dispersed AuNPs, or other metal NPs (*e.g.* silver, copper), exhibit intense optical extinction spectra due to localised surface plasmon resonance (LSPR). LSPR arises due to coherent, collective dipolar oscillations of conduction band electrons on the NP surface, induced by an irradiating electromagnetic wave, and results in an intense absorption band called the surface plasmon absorption

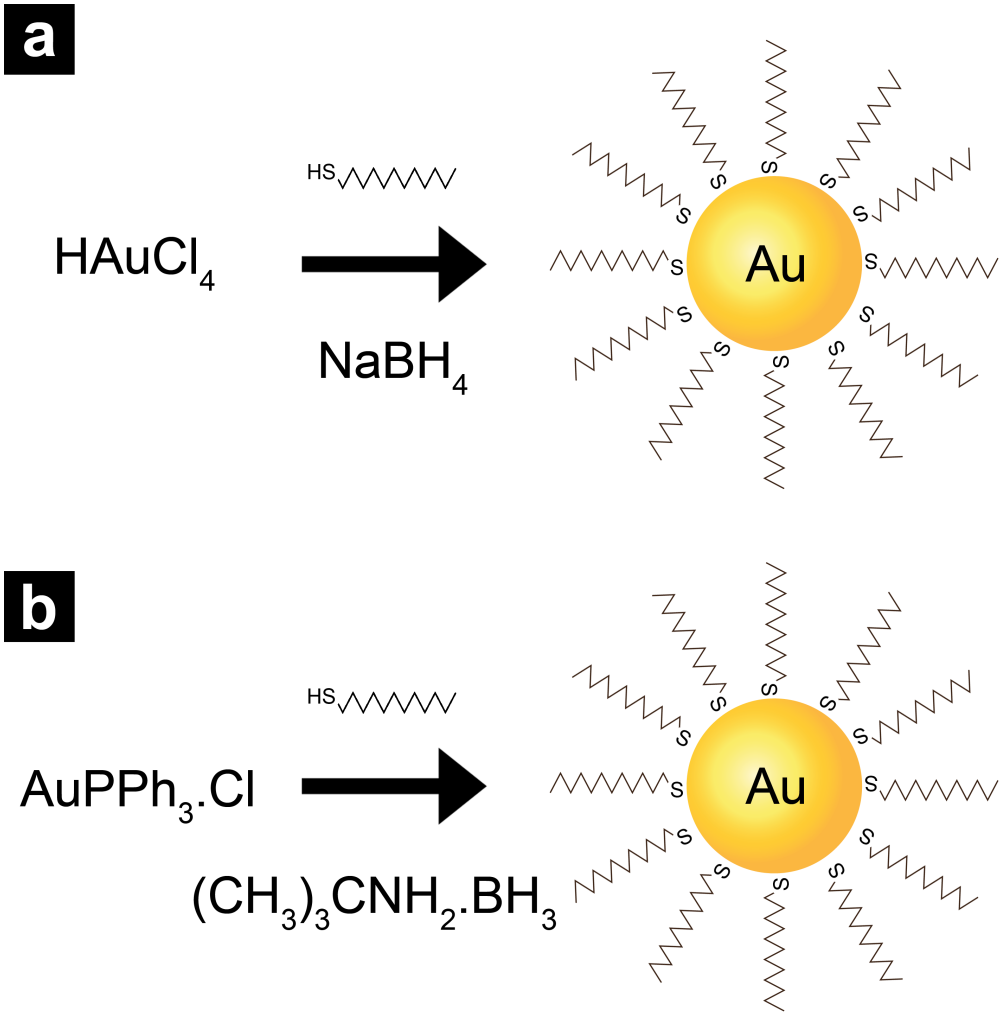


Figure 1.2: Schematics representing the syntheses of thiol-protected AuNPs using (a) the Brust-Schiffrin reaction and (b) the Stucky reaction.

band (Figure 1.3). This phenomenon is the consequence of the quantum size effect where the de Broglie wavelength of the valence electrons is of the same order as the size of the particle itself.[11, 49, 50]

The basis of the surface plasmon resonance band was first rationalised by Mie in 1908.[51] Mie's theory solves Maxwell's equations for small spherical particles assuming that the particles's diameter, d, is significantly lower than the wavelength of the incident light, λ (quasistatic approximation).[1, 41] It should be noted that Mie's theory only explains the optical behaviour of small particles with simple morphologies (*e.g.* spherical, rod-like) of characteristic dimensions above 10 nm.[49, 52] For smaller particles other effects, such as quantum confinement effects, need to be taken in account.[49, 52] However, for these small objects, Mie's solution provides a relationship between the extinction cross-section, $\sigma = \sigma_a + \sigma_s$, ($\sigma_a$ and σ_s are the absorption and scattering cross-sections, respectively) as a summation over all electric and magnetic oscillations.[1, 41]

$$\begin{cases} \sigma_a = \frac{3\pi^2}{\lambda}\varepsilon_m^{3/2}\frac{\varepsilon_2}{|\varepsilon+2\varepsilon_m|^2}d^3 \\ \sigma_s = \frac{2\pi^5}{\lambda^4}\varepsilon_m^2\left|\frac{\varepsilon-\varepsilon_m}{\varepsilon+2\varepsilon_m}\right|^2 d^6 \end{cases} \tag{1.1}$$

$$\Rightarrow \frac{\sigma_s}{\sigma_a} \propto \left(\frac{d}{\lambda}\right)^3$$

With the quasistatic approximation, absorption dominates:

$$d \ll \lambda \Rightarrow \sigma_a \ll \sigma_s$$

and therefore,

$$\Rightarrow \sigma \simeq \frac{3\pi^2}{\lambda}\varepsilon_m^{2/3}\frac{\varepsilon_2}{|\varepsilon+2\varepsilon_m|^2}d^3 \tag{1.2}$$

where ε_m and $\varepsilon = \varepsilon_1 + i\varepsilon_2$ are the permittivity of the surrounding medium and metal particle, respectively. Therefore, according to the quasistatic approximation of Mie theory for small particles, the LSPR peak occurs

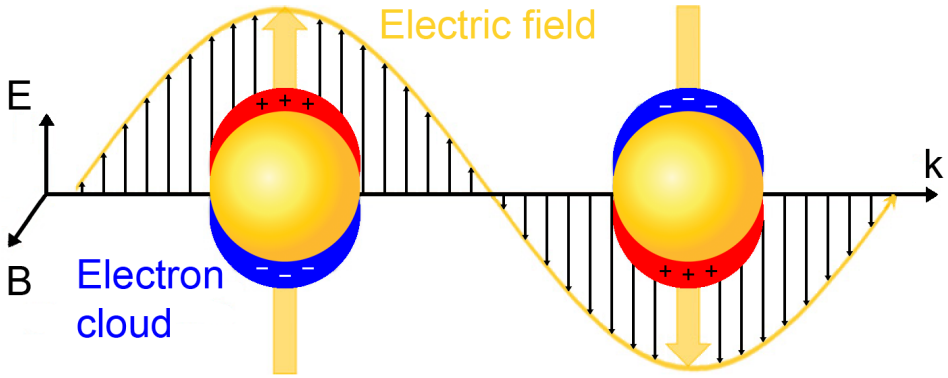


Figure 1.3: Schematic of plasmon oscillations of a metal nanosphere in response to an incident electric field. Adapted from [1].

when the NPs extinction cross-section is maximised. This condition is satisfied when $|\varepsilon + 2\varepsilon_m|$ is minimised. The bulk plasmon resonance occurs when the real component of the metal permittivity crosses zero. Thus, the spectral properties of plasmonic NPs depend, very sensitively, on their dielectric function.

All metals possess these optical characteristics but gold, silver and copper have their LSPR absorption predominantly in the visible region of the electromagnetic spectrum.[53] The intensity and wavelength of the absorption maximum is not only size dependent, but also depends on the size distribution, the environment and the particle shape.[53–56] As the surface plasmon is sensitive to its direct environment, it is also sensitive to the SAM molecules capping the AuNP surface and, in particular, their dielectric constant (as demonstrated in the previous paragraph). For instance, electron-donating ligands, such as alkanethiols, induce a bathochromic shift of the plasmon band, whereas electron-accepting ligands, such as phosphines, induce a hypsochromic shift.[12, 57] Therefore, absorbance measurements of the surface plasmon resonance can be used to detect aggregation or even size changes due to the conjugation of biomolecules to the metal surface.[15, 18, 34, 58]

Nevertheless, before being able to use the properties of inorganic AuNPs in

any biological system, it is necessary to modify the gold surfaces with molecules that can act as a bridge between the inorganic and organic systems. One way to functionalise AuNPs is by using so-called place-exchange reactions, as gold shows a strong affinity towards thiols, disulphides, amines and phosphines.[11] Using derivatives of these ligands, a monolayer of conjugated functional ligands can be deposited onto a gold surface.[37, 46, 47] The exact composition of the immobilised layers can be controlled by using the natural equilibrium established between the ligands initially present on the NP surface and those present in the surrounding medium.[37, 59]

1.2.2 Gold Quantum Dots

While Mie's theory explains the optical behaviour of metal NPs for particles exceeding 10 nm in diameter, the photonic properties of NPs below that size (metal QDs) are poorly understood.

In noble metal NPs ($>$ 10 nm in diameter), the LSPR can largely be described using a classical picture of electrons whereas in quantum dots (QDs) the optical extinction and photoluminescence characteristics are governed by quantum confinement effects.[49,52] Experimental studies of metal QDs are extremely challenging as optical detection is made difficult by the AuQDs diminishing absorption and scattering intensities, which are proportional to the third and sixth power of the particle's radius, respectively (*c.f.* equation 1.1).[1, 41] As a result, conflicting observations are reported on metal QDs, showing either a decrease (blueshift) or an increase (redshift) in the LSPR for reduced metal QD dimensions. While Genzel *et al.* reported a blueshift of approximately 15 nm for glass-embedded AgQDs with diameters ranging from 10 nm to 2 nm,[60] Peng *et al.* reported a redshift of approximately 43 nm for oleylamine-stabilised AgQDs with diameters ranging from 18 nm to 2 nm.[61]

Due to the difficulties in experimentally exploring the photonic properties of metal QDs, theoretical models were developed. Although computer-assisted models, such as density functional theory (DFT), have been used

to predict metal QDs properties,[2,62] these theoretical approaches are limited to particles smaller than 2 nm due to high computational demands.[49] AuQDs of less than 2 nm exhibit discrete electronic structure and molecule-like properties,[63] such as a HOMO-LUMO transition of one electron, which is in contrast with the collective-electron plasmon excitation in larger NPs. The free electron theory can be used to estimate at what size AuNPs will exhibit distinct quantum effects. The average spacing, δ, between electronic energy levels roughly follows the following relation:[64]

$$\delta = \frac{E_f}{N}$$

where E_f is the Fermi energy and N is the number of gold atoms.

Therefore, assuming that the electronic energy quantisation becomes distinct for:

$$\delta \geq k_B T$$

$$N \geq \frac{E_f}{k_B T} \tag{1.3}$$

At room temperature ($\sim$ 298 K) and inputing the E_f of gold (5.5 eV), this equates to a critical number of gold atoms N_{max} of 300 atoms, which is equivalent to roughly 2 nm in diameter.[52] This rationale demonstrates that for AuNPs of less than 2 nm, the collective plasmon mode will not be supported, as the electronic energy quantisation is not sufficiently important.

Whetten *et al.* were the first to isolate and characterise distinct populations of AuQDs ranging from 1 nm to 3.5 nm.[65,66] They observed critical sizes with discrete core masses from 5 kDa to 93 kDa. The obtention of truly monodisperse AuQDs (denoted Au_nR_m, where n is the number of gold atoms and m is the number of ligands) as well as the reliable determination of the number of gold atoms composing the AuQD remains a

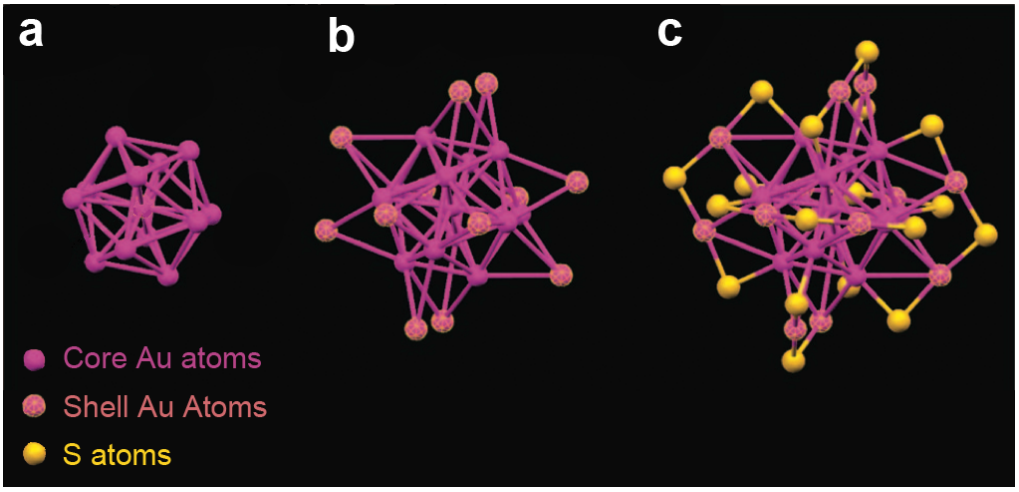


Figure 1.4: Crystal structure of a $Au_{25}(SR)_{18}$ gold quantum dot. $Au_{25}(SR)_{18}$ is based on a core-shell striker with (a) a centred icosahedral Au_{13} core surrounded by (b) a Au_{12} exterior shell protected by (c) 18 thiolate ligands arranged in six 'staple' motifs -S-Au-S-Au-S-. Adapted from [2].

challenge.[2] For instance, Link *et al.* erroneously assigned $Au_{25}(SG)_{18}$to $Au_{28}(SG)_{16}$ due to insufficient mass spectrometry resolution at the time of the study.[67] Jin *et al.* were the first to report a kinetically controlled method to obtain high purity $Au_{25}(SR)_{18}$ using a size-focusing method, which proved to be be applicable to other AuQDs.[68–70] However, to date, the most studied AuQDs remain $Au_{25}(SR)_{18}$. Zhu *et al.* used a combination of x-ray crystallography and DFT analysis to determine the crystal structure of $Au_{25}(SR)_{18}$ (Figure 1.4). They showed that, compared to the face-centred cubic (fcc) structure of bulk gold,[52] $Au_{25}(SR)_{18}$ is based on a core-shell structure with a centred icosahedral Au_{13} core (Figure 1.4a), which is capped by an Au_{12} exterior shell composed of six 'staple' motifs of -S-Au-S-Au-S- (Figure 1.4b), while the whole cluster is encapsulated by eighteen thiolate ligands (Figure 1.4c).[2]

The resolving of the crystal structure of $Au_{25}(SR)_{18}$ permitted the in-depth investigation of the electronic structure and optical properties of the AuQD by computational methods. Using DFT, the electronic structure of $Au_{25}(SR)_{18}$ was calculated (Figure 1.5a) and a theoretical absorp-

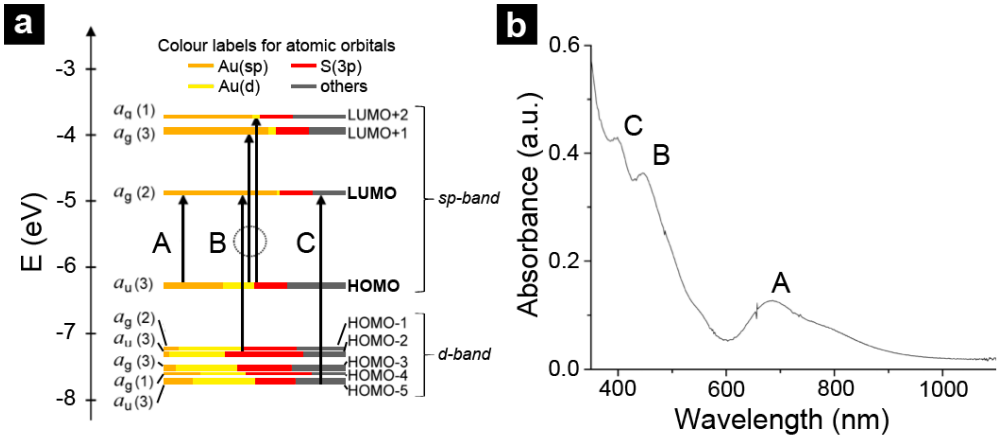


Figure 1.5: (a) Kohn-Sham orbital level diagram and (b) peak assignment for the UV-Vis absorption spectrum of $Au_{25}(SR)_{18}$ gold quantum dots. Adapted from [2].

tion spectrum was predicted (Figure 1.5b), which correlated well with experimental observations.[69–73] The multiple absorption bands are due to single-electron transitions between quantised electronic energy levels, which is different in nature to the collective oscillation observed with the LSPR of larger AuNPs.[49, 52, 74]

In addition to the absorption bands of AuQDs, their photoluminescent properties have attracted a lot of attention, especially for application in biology and sensing.[75] However, the origin of their luminescent nature is still not clearly understood.[73, 76–78] Luminescence in AuQDs has been shown to originate both from the gold core and the interactions between the gold core and surface ligands.[77–79] Even less clearly understood is the magnetic nature of some AuQDs, as many contradicting studies were reported in the literature.[12] Compared to diamagnetic bulk gold, AuQDs of different sizes and surface functionalisation can exhibit magnetic polarisation.[12] Most AuQDs characterisation has been undertaken using superconducting quantum interference device (SQUID) magnetometers.[12, 80] These studies observed that the magnetic moment of AuQDs displays very weak or no temperature dependence between 2 K and 400 K and the magnetisation curve shows either paramagnetic- or soft ferromagnetic-like be-

haviours.[12] All these properties, if better understood and characterised, could offer unprecedented opportunities for applications in biology, catalysis and quantum optics.[49]

1.2.3 Multifunctional Hybrid Systems

Recently, new emphasis has been placed on composite NPs, where combinations of different types of nanostructured materials are used to create multimodal systems that exhibit the beneficial properties of the component modules.[81, 82] In particular, rattle-type NPs, which are NPs with a core-shell structure containing a distinctive void that separates the core material from the shell (Figure 1.6), have already been extensively investigated for a variety of applications ranging from catalysis, lithium-ion batteries, solar cells, drug delivery, biosensing and surface-enhanced Raman scattering (SERS).[83–88] Compared to core-shell particles, rattle-type NPs have not only the advantage of a useable hollow cavity, but they also allow added tailorability and functionality through the free floating core. More recently, in the biomedical field, multifunctional NP systems have gained increasing interest for targeting, imaging and drug delivery purposes.[33, 86, 89–92]

In 2003, Xia *et al.* were the first to demonstrate the synthesis of gold-polymer rattle-type NPs[93] and, since then, the development of other rattle-type systems has grown enormously, offering a wide variety of core and shell compositions as well as a wide range of sizes, shapes and structures.[94, 95] Different materials, including metal oxides, metals, silica, carbon and polymers, have been used both as core and shell material in rattle-type systems.[84,86,93] Furthermore, rattle-type systems with multilayered shells or multiple cores were developed (Figure 1.6b-c).[96,97] By synergistically combining nanostructured materials, the resulting system not only exhibits the linear combination of the components properties but also emergent properties of its own.

Rattle-type systems can be prepared through a variety of different techniques, including selective etching or dissolution, bottom-up approaches by

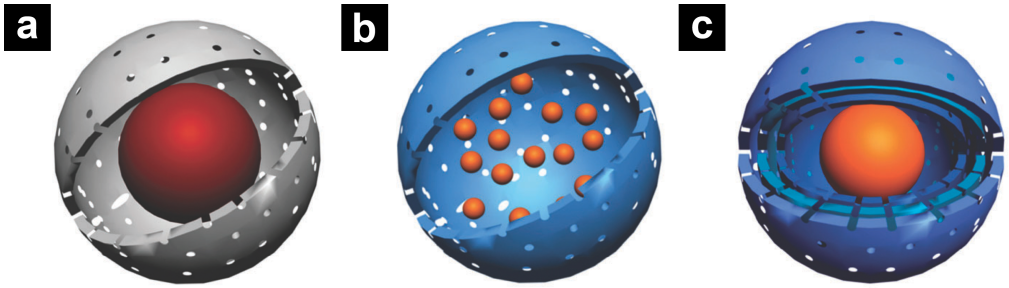


Figure 1.6: Schematic illustrations of rattle-type particles with different morphologies. Rattle-type particles with (a) a single core, (b) multiple cores and (c) multiple shells. Adapted from [3].

soft templating assembly, ship-in-bottle methods, Ostwald ripening methods, galvanic replacement processes and Kirkendall effect based methods.[3] The most commonly used methods are etching procedures[91, 98, 99] and soft template approaches.[5,97] The selective etching process relies on coating pre-synthesised core materials with one or two layers of different materials before either removal of the sacrificial connecting layer or etching of the core by either dissolution or calcination (Figure 1.7a). This method was used to create gold-silica rattle-type particles with spherical (Figure 1.7c-d) and rod-like morphology for catalysis and cancer therapy, respectively.[4, 91] However, these selective etching based methods usually involve multiple complex steps, making the scaling-up of such processes difficult. Furthermore, for biomedical applications, the thorough removal of all traces of etchant can be challenging, but nevertheless critical considering the cytotoxicity of rattle-type systems produced through selective etching processes.

The soft template methods can be easily scaled up and have been reported for the preparation of gold-silica rattle-type particles used in catalysis (Figure 1.7e-f).[5] These methods rely on micelles, vesicles or microemulsions as soft-templates for the assembly of inorganic nanomaterials and are useful for the preparation of rattle-type particles composed of porous shells.[100,101] However, as for the etchant in the selective etching method, all traces of the toxic surfactant need to be removed before any possible

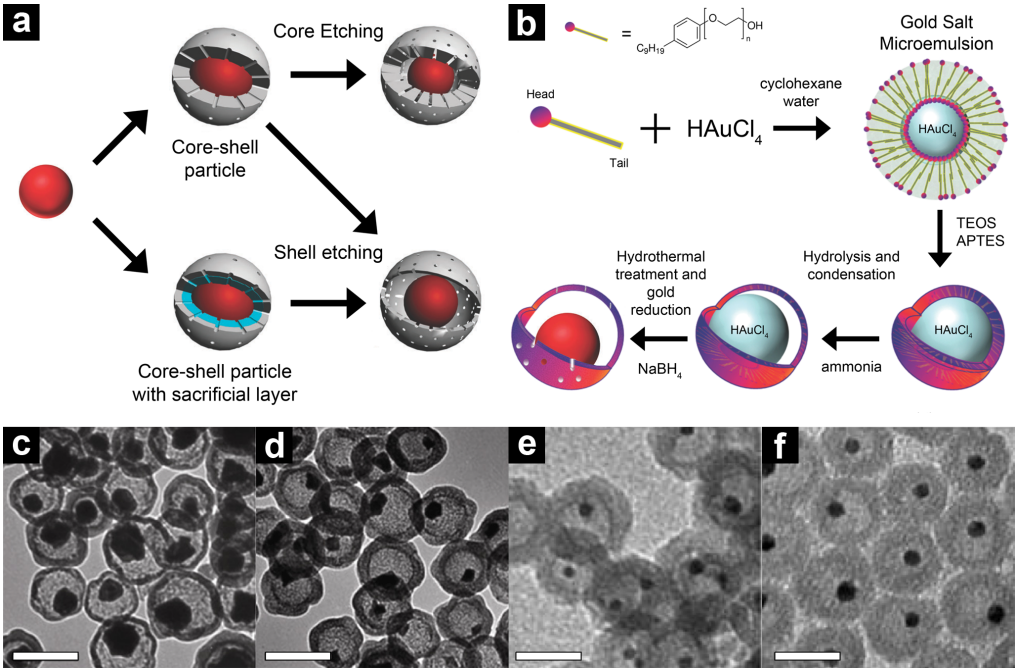


Figure 1.7: Schematic illustrations for preparing gold-silica rattle-type particles employing (a) etching strategies and (b) soft templating methods. (c-d) Transmission electron microscopy (TEM) images of $Au@SiO_2$ nanorattles obtained through etching with KCN at different concentrations, resulting in varying gold core diameters. Scale bars: 200 nm. (e-f) TEM images of $Au@SiO_2$ nanorattles obtained through soft templating method using different concentrations of the initial gold salt solution to vary the final gold loading. Scale bars: 20 nm. Adapted from [3–5].

use of the produced system in biomedical applications.

1.3 Nanoparticles for Cancer Treatment

Although large amounts of funding is injected into cancer research, cancer remains one of the leading causes of death worldwide.[22] Much promising cancer research has been developed over recent years, however, translation of this laboratory knowledge to functional clinical technology remains slow.[24] This translational clogging effect is mainly due to inadequacies

in the ability to administer therapeutic agents so that they will selectively reach the diseased tissue without causing negative side effects.[24, 102, 103] To minimise the collateral damage induced by systemic therapeutics, drugs can be administered in a specific and targeted manner.[104, 105] In order to improve the targeting potential and efficacy per dose of imaging or therapeutic agent, two main synergistic goals should be striven for:

- Increase the agent targeting selectivity;[106]
- Overcome the biological barriers of the body that prevent the agent from reaching its target.[107]

The ideal therapeutic agent allows for efficient and specific targeting of cells at an early stage of cancer development.[6, 7] To this end, nanotechnology offers many advantages that can contribute to improved targeting as well as the development of tools to overcome the biological barriers preventing efficient drug delivery.[6, 108] In particular, NP-based systems have been widely investigated for both active and passive targeting approaches of cancer cells.[25, 28, 109–111] Active targeting depends on the integration within the therapeutic system of recognition moieties, which have been shown to target cancer-specific biomarkers.[25] Ligands that have been functionalised to nanosystems for active tumour-targeting applications, include epidermal growth factor (EGF) receptors (EGFR), hypoxia-inducible factor 1 alpha (HIF-1α) and $\alpha_v\beta_3$ and $\alpha_v\beta_5$ integrins.[25] However, these surface modifications increase the overall complexity of the NP system.[112] Passive targeting, on the other hand, relies on the agents physicochemical properties to reach the tumours. By employing the enhanced permeability end retention (EPR) effect, size-dependent accumulation of NPs can be achieved in cancer cells (Figure 1.8).[110, 111, 113] The EPR effect happens because malignant cells replicate at a higher rate than healthy cells[6, 25]. As the accelerated growth of the tumour leads to an increase in nutrient demand, tumours develop their own vasculature (angiogenesis) through which increasing amount of blood can be supplied.[6, 25] However, this accelerated angiogenesis is carried out in a highly disordered manner, resulting in gaps in the endothelium that allow the preferential pen-

etration and accumulation of nanosized objects with diameters between 60 nm and 400 nm.[25, 113, 114] Additionally, the diminished lymphatic drainage is responsible for the retention of the nanosized objects in the tumour.[6, 25] Both active and passive targeting approaches have been shown to successfully accumulate AuNPs in tumours, reaching NP concentrations up to 13% and 5% by weight, respectively, after systemic injections *in vivo*.[109–111] Since NPs have proven to be eligible for selective targeting, a wide variety of NP systems have been explored for cancer diagnosis and therapy.[7, 23, 28, 115]

1.3.1 Diagnosis for Cancer Treatment

Early identification and localisation of cancerous tumours is critical to improve the success of cancer therapy and patient survival rates.[115, 116] Various imaging techniques have been developed to visualise tumours, including nuclear imaging (positron emission tomography, PET), x-ray computed tomography (CT), ultrasound imaging (US), magnetic resonance imaging (MRI) and optical imaging.[117] Those five imaging techniques can be separated into two categories: morphological imaging techniques, characterised by high spatial resolution (CT, US and MRI); and molecular imaging, characterised by sensitive detection of molecular or cellular changes (PET and optical imaging).[117, 118] These techniques have their own inherent advantages and limitations (Figure 1.9), but all contribute importantly to cancer diagnosis in the clinic. Nevertheless, in the past few years, optical imaging has emerged as a promising non-invasive and real-time modality for cancer detection.[115, 119, 120] Compared to other imaging technologies, such as MRI, CT, PET and US,[121–124] optical imaging is based on the detection of the luminescence of either specific *in vivo* reactions or targeting probes. Due to its high sensitivity, multiplex detection abilities and low equipment cost, optical imaging is highly suitable for cancer diagnosis (Figure 1.9).[75, 120]

To be more specific, optical imaging is an imaging technique that makes

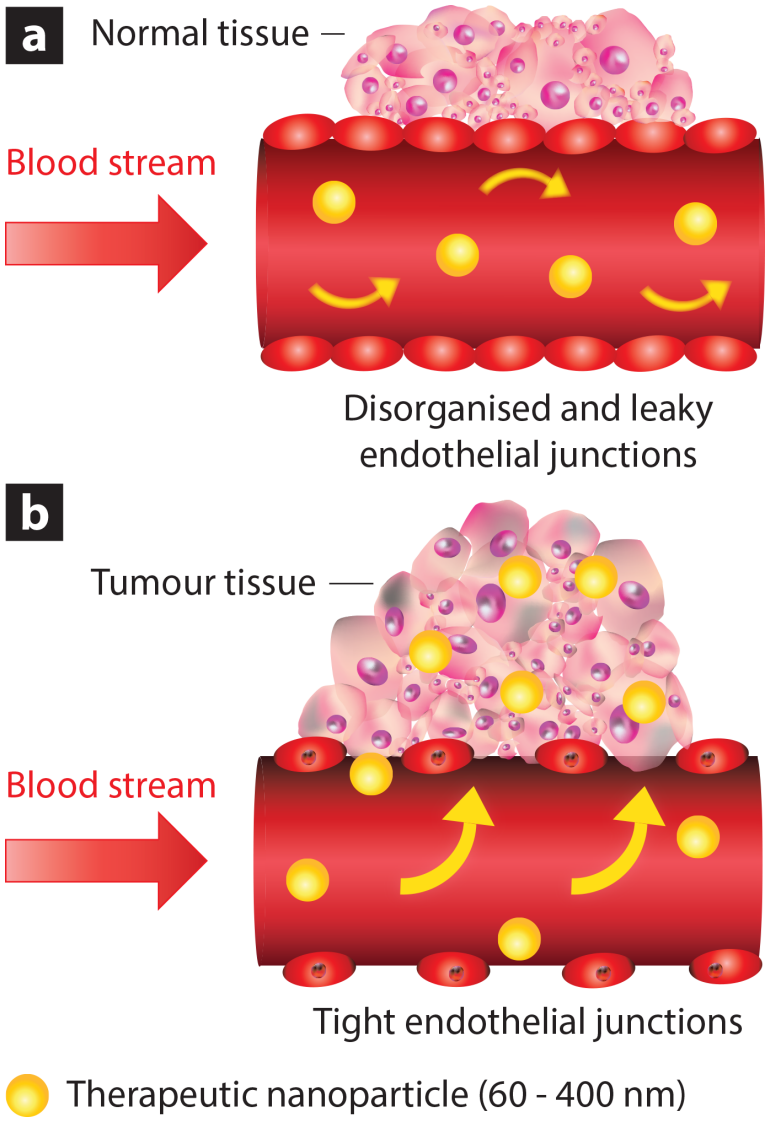


Figure 1.8: Enhanced permeability and retention (EPR) effect. (a) Vasculature in normal tissues is tight, preventing targeting nanoparticles from penetrating and extravasating. (b) Vascular walls in tumour tissue have multiple narrow slits and are leaky and thus hyperpermeable to nanoparticles (60 nm to 400 nm), which preferentially accumulate in the tumour. Adapted from [6]

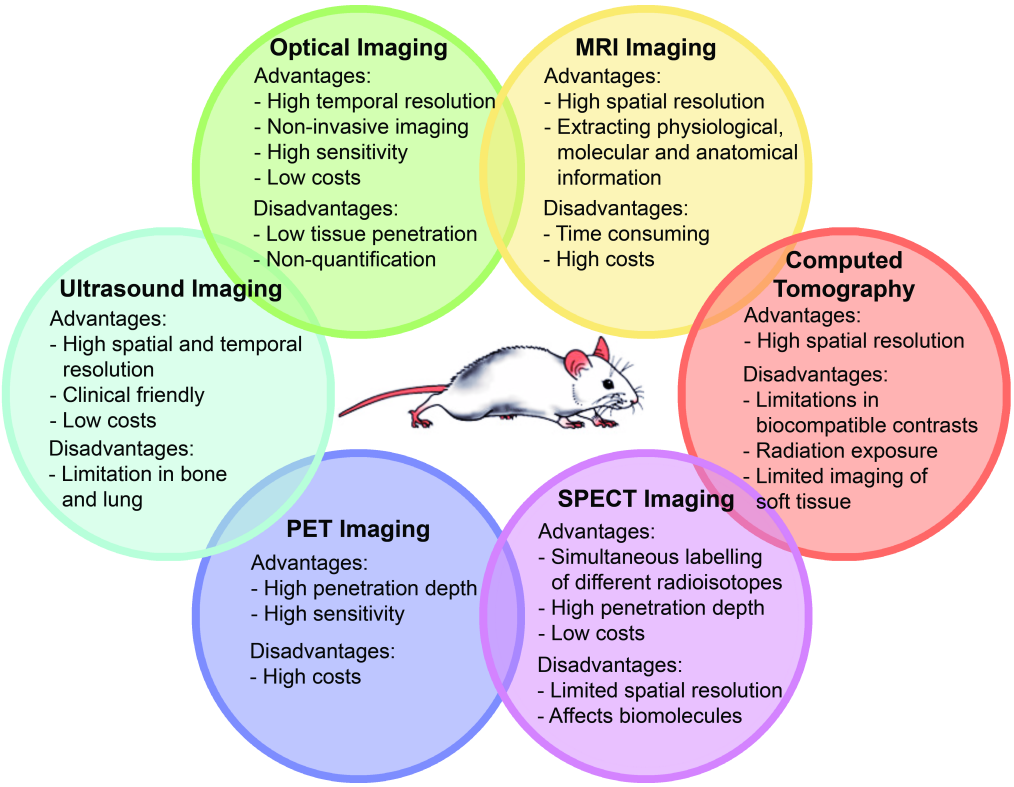


Figure 1.9: Advantages and limitations associated with different imaging techniques. Adapted from [7].

use of electromagnetic light waves (visible, ultraviolet or infrared) to visualise specific entities and can be categorised into bioluminescence imaging and fluorescence imaging.[7] Bioluminescence imaging employs the light emission generated by specific chemiluminescent enzyme reactions and has been mainly applied to monitor events, such as transgene expression, transplantation, toxicology, viral infections, and gene therapy.[125] Bioluminescence imaging allows real-time, rapid and easy simultaneous localisation and quantification of biological processes *in vivo*.[126] Unlike bioluminescence imaging, fluorescence imaging relies on the detection of photon emissions that are generated by fluorescent probes, which emit light at one wavelength in response to excitation by light at a different wavelength. This technique has been widely applied in the early detection of disease by using fluorescent proteins possessing inherent multiplexing abilities, which can be differentiated by colorimetry (*i.e.* different emission wavelength of the proteins).[115, 119, 120, 127, 128]

The limitation of fluorescence imaging is the use of visible light as the visualisation signal, which has especially low penetration depth due to the high absorption of living tissues in the visible light range (Figure 1.10). To circumvent this problem, more and more studies focus on the use of near-infrared (NIR) imaging systems. Near-infrared (NIR) light and, in particular, NIR light in the so-called 'bio-window' (650 nm - 900 nm) is minimally absorbed by biological tissues and physiological fluids (*e.g.* skin and blood) (Figure 1.10).[6, 7, 23, 28, 115, 129] This lack of absorption in the NIR bio-window enables NIR light to penetrate deeper into living tissues compared to visible light.[6, 130] Lasers of microwatt power densities have been reported to penetrate almost 7 cm through muscle tissues and 10 cm through breast tissue.[6, 130] Over the years, many different types of fluorescent probes have been developed for the visualisation of tumours.[131, 132] Conventionally, organic fluorophores are used as NIR probes for fluorescent imaging.[116, 119, 133] However, these organic fluorescent probes have many drawbacks, such as low water solubility and low chemical- and photostability, which makes them unsuitable for long-term

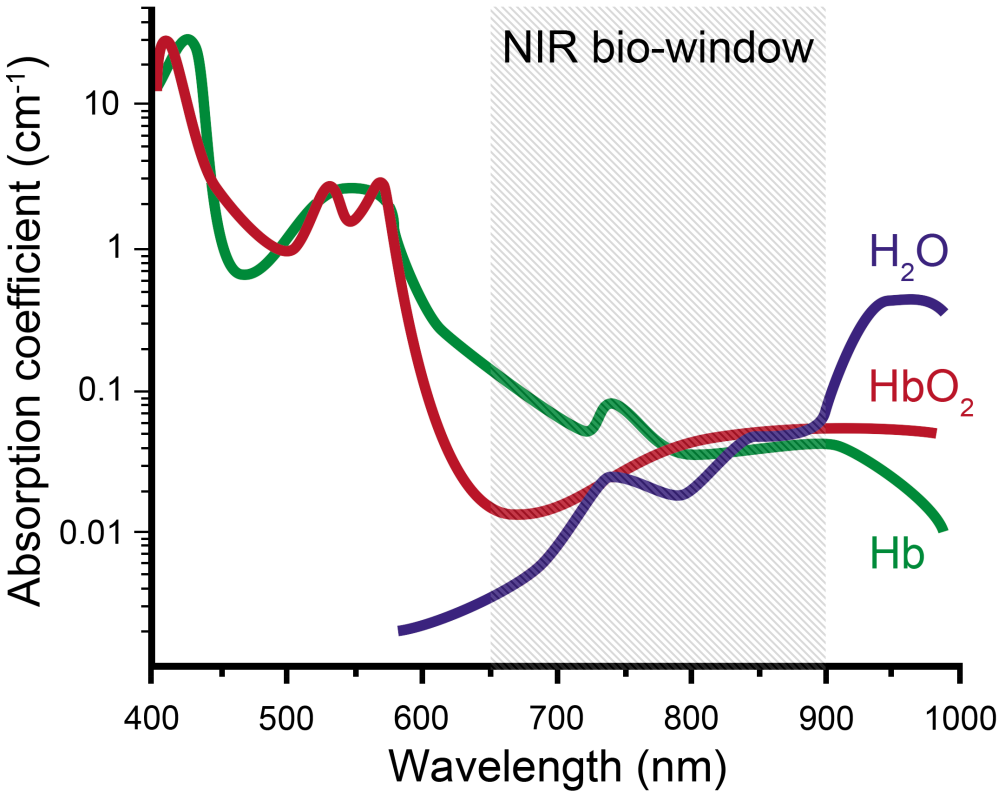


Figure 1.10: Wavelength range of the near-infrared (NIR) tissue transmission window. Photothermal therapy and optical diagnostic imaging are most efficient in the 650 nm to 900 nm spectral range due to minimal light absorption by haemoglobin ($<$ 650 nm) and water ($>$ 900 nm). Adapted from [8].

molecular imaging.[115, 133, 134] Moreover, the fluorophore detection sensitivity is relatively low, and the cytotoxic effects of many fluorophores are still unknown.[75]

Recently, a lot of emphasis has been placed on nanotechnology-based approaches to improve the detections limits and clinical efficiency of NIR imaging.[7, 24] Moreover, the significant progress made in nanotechnology, makes NP-based NIR probes promising agents for early diagnosis, therapy and prevention of diseases.[7] NP probes are of particular interest for cancer diagnosis, as the NPs can accumulate in the tumours by exploiting the enhanced permeability and retention (EPR) effect (passive targeting) or the

specific binding between the tumour cell receptors and biofunctionalised NPs (active targeting).[115] Many different kinds of nanostructures, such as quantum dots (QDs) and gold-based NPs, have been designed and tuned to enable NIR live imaging as well as targeting.[135, 136] Semiconductor QDs have been extensively researched and are currently the fastest growing imaging agent due to their highly attractive optical and structural properties.[75] In particular, semiconductor QDs possess high quantum yields and photostability.[75] Multifunctional NPs, based on encapsulated semiconductor QDs inside triblock copolymers, have been developed for live imaging and targeted (active) drug delivery applications.[135,137] However, the inherent toxicity of semiconductor QDs still needs to be overcome before successful translation into clinical use.[138] By comparison, gold-based nanostructures, such as nanorods and nanoshells, are attractive for optical imaging due to their good biocompatibility, unique optical/electronic properties and tuneable surface plasmon resonance in the NIR.[136, 139] However, these gold-based probes depend on the functionalisation or association to a fluorophore in order to enable fluorescence imaging. Noble metal quantum dots (*e.g.* AuQDs, AgQDs), on the other hand, exhibit a native photoluminescent emission in the NIR, which makes them a highly attractive candidate for NIR fluorescent imaging.[75,140–142] Then again, AuQDs are inherently unstable in biological environments and, therefore, require stabilisers or carriers.[75, 142] The few studies that have explored the use of AuQDs for cancer imaging applications, employ protein carriers to modulate the interaction of the AuQDs *in vitro* and *in vivo*, which can impair their biocompatibility.[75, 142] Finally, AuQDs can also possess paramagnetic properties, which, in combination with their NIR photoluminescence, make them ideal systems for multimodal imaging applications.

Multimodal imaging offers the advantage of combining the advantages of two or more imaging techniques, while diminishing each others limitations. To tackle an issue as complex as the diagnosis of cancer, there is no single technique available that provides all the answers. Therefore, merging together different imaging modalities might be a powerful strategy to improve

imaging quality and efficiency as well as offering possibilities for early and reliable cancer diagnosis. For example, the combination of magnetic and optical imaging provides multimodal systems that possess the advantages of both imaging modalities, such as high spatial and temporal resolution (MRI) and high sensitivity (NIR fluorescence imaging).[136, 143] To date, many nanocomposite systems combine gold and iron to create multimodal imaging probes.[144] However, due to their different surface crystal structures these elements are not compatible with each other. Therefore, many approaches employ a dielectric material as an intermediate (*e.g.* silica).[7] Although multimodal MRI-optical imaging has been demonstrated to be feasible,[136, 145–147] it is still challenging to engineer simple, robust and reliable synthesis pathways that achieve high performance imaging systems.

1.3.2 Photothermal Therapy

Photothermal therapy (PTT) is a cancer treatment that relies on selective targeting or increasing the sensitivity of cancer cells to cytotoxic damage using heat.[6] PTT has become increasingly popular mainly due to the fact that localised photoenergy is delivered directly to the tumour, resulting in a less invasive alternative to conventional cancer therapies, such as surgery and non-targeted chemotherapy.[92] PTT causes an increase in the temperature of *in vivo* tissues, which can be used to selectively destroy tumours because of their reduced heat tolerance compared to healthy tissue.[6,148,149] By heating tissues to temperatures between 42 °C and 46 °C (so-called hyperthermia),[150] the healthy tissue remains intact, whereas the cancerous tissue is killed.[6, 148, 149]

Gold nanoparticles have generated significant interest for their use as photothermal agents due to their high photostability and strong plasmonic properties .[23, 54, 92] The AuNPs either absorb or scatter incoming light, which can be harnessed to destroy tissue by local heating.[129] The surface plasmon resonance of AuNPs exhibits a more sensitive response to environ-

mental changes than traditional photothermal agents, like light-absorbing dyes.[129, 148, 151] Such enhanced sensitivities make AuNPs particularly useful as optical probes for PTT.

As mentioned before (*c.f.* section 1.3.1), only NIR light penetrates sufficiently through blood and soft tissues.[6, 23, 28, 115, 129] AuNPs, however, mainly absorb light in the visible region of the electromagnetic spectrum.[28] In order to shift the AuNP plasmon resonance towards the NIR bio-window, many NP systems have been developed, including gold nanoshells, gold nanocages and gold nanorods.[109,139,152–157] Table 1.1 summarises the advantages and limitations of these gold-based platforms for cancer treatment.[109, 139, 153, 156–160] By tailoring the composition, size or shape of these NPs, absorbance in the NIR can be obtained.[152,153,161–163] In particular, the elongated shape of gold nanorods offers very strong absorption cross-sections and heats faster than gold (-silica) nanoshells or nanocages.[10, 164–167] The recent advance to clinical trials of some gold-based systems (Nanospectra Bioscience and CytImmune) shows the progress made in the exploitation of the plasmon resonance of AuNPs in photothermal therapeutic medicine and the great potential for gold NPs to improve cancer treatment.[29, 50]

Table 1.1: Detailed overview of gold-based platforms for cancer treatment and diagnosis summarising the advantages and disadvantages of each system.

	Spherical Gold Nanoparticles	Gold Nanoshells (SiO_2 core)	Gold Nanorods	Gold Nanocages
Hyperthermia	✓ Absorb light by SPR, works *in vitro* x Does not work *in vivo*, not in NIR	✓ Light absorption by SPR in the NIR ✓ Tuneable absorption peak	✓ Light absorption by LSPR in the NIR ✓ Tuneable absorption peak x Unstable LSPR peak position & Intensity	✓ Light absorption by SPR in the NIR ✓ Tuneable absorption peak
Imaging	x No native imaging x Quenching of fluorophores	x No native imaging x Quenching of fluorophores ✓ Incorporation of iron oxide Particles	x No native imaging x Quenching of fluorophores	x No native imaging x Quenching of fluorophores ✓ Incorporation of iron oxide Particles
Drug Delivery	x Limited to surface functionalisation x No sustained release	x Limited to surface functionalisation x No sustained release	x Limited to surface functionalisation x No sustained release	✓ Yes but relatively low payloads
Targeting	✓ Passive by EPR if in the right size range ✓ Active by functionalisation of targeting ligand to gold surface	✓ Passive by EPR ✓ Active by functionalisation of targeting ligand to gold surface	✓ Passive by EPR if in the right size range ✓ Active by functionalisation of targeting ligand to gold surface	✓ Passive by EPR ✓ Active by functionalisation of targeting ligand to gold surface
Biocompatibility	x Au ligand directly exposed to bioenvironment x Non-biodegradable	x Au ligand directly exposed to bioenvironment x Non-biodegradable x Size does not allow renal clearance	x Au ligand directly exposed to bioenvironment x Non-biodegradable x Size does not allow renal clearance	x Au ligand directly exposed to bioenvironment x Non-biodegradable x Size does not allow renal clearance
Synthesis	✓ Most documented ✓ Simple ✓ Scalable	✓ Simple ✓ Scalable	✓ Scalable x Complex synthesis x Difficult purification x Harsh chemistry (retains cytotoxic molecules)	✓ Scalable x Complex Synthesis x Low reproducibility
Other	✓ In clinical trials for drug/gene delivery (Aurimmune)	✓ In clinical trials for PTT (AuroLase)	+/- Anisotropic shape	
Main references	El-Sayed *et al.* Cancer Lett. (2006) Li *et al. Cancer Lett. (*2009)	Hirsch *et al.* PNAS. (2003) Loo *et al.* Nano Lett. (2005)	Huang *et al.* JACS. (2006) and Adv Mater. (2009*)*	Melancon *et al.* Mol Cancer Ther. (2008) Chen *et al.* Nano Lett. (2007)

1.3.3 Chemotherapy

The treatment of cancer with drugs, chemotherapy, is one of the most well-established cancer treatments available today, and is currently used alongside radiotherapy and surgical ablations to treat most types of cancer.[7, 144, 168, 169] However, all these treatments have inherent limitations and are associated with negative side-effects, which significantly reduces the quality of life of the patients.[25, 170] For example, most chemotherapy drugs are injected systemically in the blood stream, which induces collateral damage to healthy tissue.[23, 25, 170] Currently, at best 0.01% of intravenously administered monoclonal antibodies reach their targets *in vivo*.[171] The inherent lack of specificity of systemic chemotherapy not only diminishes the efficacy of the treatment but also drastically reduces the cost-effectiveness of the treatment.

The emergence of nanotechnology has played a crucial role in the development of new cancer therapeutics.[7, 23–28] Nanotechnology has enabled passive or active targeting to be employed for selectively delivering various drugs to tumours (*c.f.* section 1.3), thereby confining the treatment to the tumour site.[25, 28, 109–111] Furthermore, the drug circulation time can be increased by encapsulating the drug in a delivery vector (*e.g.* mesoporous silica) or by coating the delivery vector (*e.g.* PEGylation on AuNPs).[172]

A wide range of nanoparticles has been explored for drug delivery applications, including ceramics, liposomes, micelles and various types of inorganic NPs (Figure 1.11). Polymeric NPs are one of the most established nanomaterial drug delivery vectors due to the fact that they are biodegradable, can be tailored through surface modifications, provide good pharmacokinetic control and can easily trap and delivery a wide range of anticancer drugs.[9, 21] Furthermore, polylactic acid- (PLA) and poly(lactic-*co*-glycolic acid)- (PLGA) based NPs have been approved by the US Food and Drug Administration (FDA) for use in humans. [9, 21]. Liposomes and micelles are composed of amphiphilic molecules, which self-assemble into spherical structures. Liposomes are formed of concentric lipid bilayers that

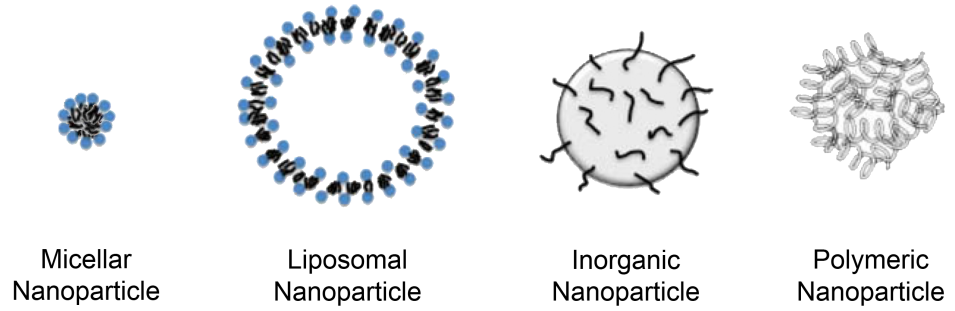


Figure 1.11: Various types of nanoparticle-based systems used in biomedical research and drug delivery.[9]

can incorporate hydrophilic therapeutic agents in their internal spaces or hydrophobic drugs within the bilayers.[173, 174] Micelles are smaller (5 nm - 10 nm) compared to liposomes (50 nm - 150 nm), but can incorporate relatively larger amounts of poorly soluble hydrophobic anticancer drugs, because their inner volume is composed of the hydrophobic tail of the surfactant constituent.[21] Drugs incorporated in liposomes or micelles have the advantage that they can be slowly released in tumours, generating high local dosages and, therefore, minimising side-effects.[173, 174] The lipids of the liposomes or micelles can then be readily dissociated and, subsequently, harmlessly cleared by the body.[21, 173, 174] At the same time, the latter advantage of these organic molecule drug delivery systems can also become a drawback, as the liposome or micelle carrier might already be degraded *in vivo* before reaching the tumour site.[9]

Mesoporous silica nanomaterials are showing great promise as potential anticancer drug carriers due to their high surface area and tuneable size and porosity, which offer a unique advantage for loading and releasing large quantities of biomedical agents.[175–179] Furthermore, in contrast to organic drug vehicles, these NPs are not subjected to early enzymatic degradation.[9] The synthesis of mesoporous silica is based on sol-gel processes, forming liquid-crystalline mesophases of amphiphilic molecules that serve as templates for the condensation of orthosilic acid.[180] The synthesis can

be performed in either acidic or basic conditions using different sources of silica, such as sodium silicate or tetraethyl orthosilicate (TEOS).[180] Mobile™ was the first to produce mesoporous silica particles with hexagonally ordered mesopores (MCM-41) in 1992.[181] Since then, mesoporous silica nanospheres (MSNs) have been highly attractive for drug delivery applications due to their low cytotoxicity and ease of surface modification for improved internalisation.[182–184] In 2001, Vallet-Regi *et al.* showed that MSNs could be used to deliver relatively large doses of drug in a controlled manner.[185] More recently, Torney *et al.* developed responsive MSN-based drug delivery vectors by using NPs caps or 'gatekeepers' (*e.g.* AuNPs, Fe_3O_4 NPs oxide, semiconductor QDs) to trap drugs inside the silica pores. Depending on the NP 'gatekeepers' used, the drug delivery system can be tailored, and drug release can be triggered by changing the temperature, pH or magnetic field.[186–188] Liu *et al.* reported on the use of multifunctional, gold-coated, silica nanorattles for the combination of photothermal therapy and chemotherapy.[189] This multimodal cancer treatment exhibited enhanced overall therapeutic efficacy and reduced systemic toxicity.[189] Such multifunctional nanostructured materials, which are able to combine targeted diagnosis and therapy into one, integral system, can simultaneously image early tumour sites, deliver polyvalent payloads and kill cancer cells in a controlled and verifiable manner.[30, 91, 190]

The nanoparticles used as examples in this introductory chapter, provide just a glimpse of the huge potential hidden in the variable chemistry and architecture of nanotechnology. This thesis goes on to develop and demonstrate the flexibility and performance of a simple NP-based cancer treatment approach that enables simultaneous imaging and multilayered therapy. Yet, the details provided here only scratch the surface of what promises to be the beginning of a new era in the development of novel strategies for combatting not only cancer, but many other diseases that afflict mankind.

Chapter 2

Experimental Techniques

2.1 Microscopy

2.1.1 Transmission Electron Microscopy

Transmission Electron Microscopy (TEM) uses energetic electrons to provide morphologic, compositional and crystallographic information of samples at the nanoscale. A TEM functions under the same basic principles as an optical microscope, however, in a TEM set-up, electrons replace photons, electromagnetic lenses replace glass lenses and images are viewed on a screen rather than through an eyepiece (Figure 2.1).

The relatively large wavelength (400 nm to 700 nm) of light used to illuminate a sample in an optical microscope limits the ability to resolve detail in that object. Theoretically, the maximum resolution, d, obtained through a lens is proportional to the wavelength of the incident beam, λ, defined by,

$$d = \frac{\lambda}{2n \sin \alpha}$$

where n is the index of refraction of the medium and α is the half-angle of the maximum cone of light that can enter or exit the lens.

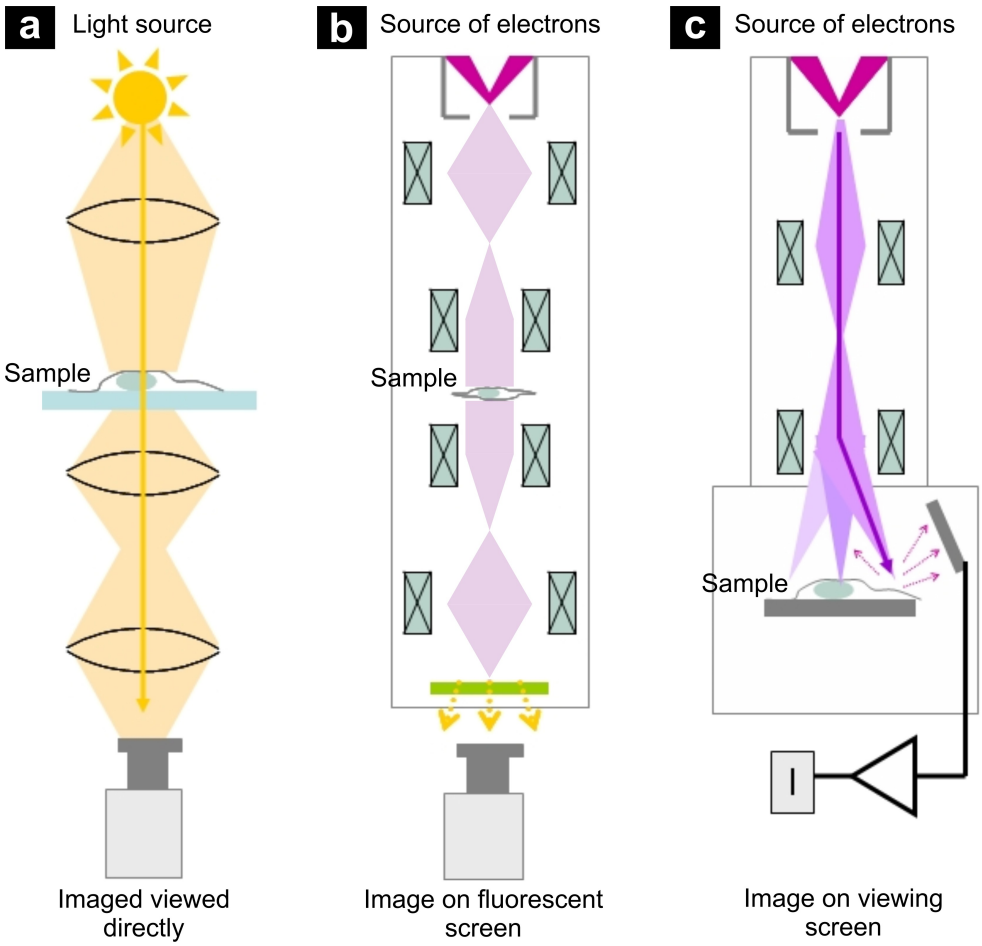


Figure 2.1: Comparison between optical microscopy, transmission electron microscopy and scanning electron microscopy. Basic set-ups of (a) an optical microscope, (b) a transmission electron microscope (TEM) and (c) a scanning electron microscope (SEM).

The idea of using electrons to magnify objects was realised after de Broglie introduced particle-wave duality, showing that the wavelength of electrons was many orders of magnitude smaller than that of light. De Broglie showed that the wavelength of a particle and its momentum are inversely proportional,

$$\lambda = \frac{h}{p}$$

where p is the particle's momentum and h is the Planck's constant.

Furthermore, the momentum is by definition related to the kinetic energy by,

$$p = \sqrt{2m_0E}$$

where m_0 is the rest mass of an electron and E the kinetic energy of the accelerated electrons ($E = eV$, where e is the elementary charge and V is the potential through which the electrons are accelerated)

Therefore, the wavelength of electrons in a TEM is related to the electrons energy or the acceleration potential used to accelerate the electrons by,

$$\lambda = \frac{h}{\sqrt{2m_0eV}}$$

For particles travelling at speeds close of the speed of light in vacuum, c, relativistic effects have to be accounted for. Then, the wavelength of the electrons can be described by,[191]

$$\lambda = \frac{h}{\sqrt{2m_0eV(1 + \frac{eV}{2m_0c^2})}} \tag{2.1}$$

In the TEM, electrons accelerated over a potential of 300 kV are travelling at high velocities and, therefore, the relativistic wavelength becomes $\sim$ 0.002 nm. During transmission, the velocity of electrons directly correlates

to their wavelength. In other words, the faster electrons move, the shorter the wavelength and the greater the resolution of the image. In TEM, electrons typically have wavelengths over the range of 10^{-3} nm to 10^{-2} nm (equation 2.1), which explains the much higher resolution obtained through TEM compared to light microscopy.

Electrons are generated from either thermal sources or field emission sources. Emitted electrons are accelerated through an electric field, typically between 80 kV and 300 kV. The higher the voltage, the better the theoretical resolution. The electron beam is initially focussed through a series of two or three condenser lenses onto the sample. Subsequently, the forward scattered electrons are focused by the objective lens onto the sample into a diffraction pattern on the back focal plane of the TEM. After the back focal plane, the first intermediate image is formed and the intermediate lens can be used to form either an image or a diffraction pattern, depending on which mode the TEM is set-up to operate, imaging mode or diffraction mode. Finally, projection lenses are used to vary the magnification of the image or diffraction pattern. The entire TEM column is kept under vacuum in order to minimise interactions between the electrons and the gas molecules in the column as well as to protect the electron source.

Contrast in the TEM image emerges from inhomogenous scattering of the electrons by the sample and should not be confused with resolution. While image resolution defines the ability to resolve adjacent features in an image, the image contrast is defined by the difference in intensities between these features. Different contrast mechanisms can contribute to the overall contrast in an image, as scattering of the electrons can occur *via* different processes. These processes are dependent on the atomic number, Z, the density and the thickness of the sample. Consequently, three basic mechanisms contribute to contrast formation: mass-thickness contrast, phase contrast and diffraction contrast. Out of the three, mass-thickness contrast is the most important when imaging biological samples. Mass-thickness contrast appears when electrons are scattered off-axis by elastic scattering events and reflects variations in the mass and the thickness of the sample.

Areas of the samples that have a low mass-thickness scatter less strongly and appear brighter in bright field TEM images.

In the case of scanning transmission electron microscopy (STEM) the incident electron beam is focused into a spot, which is scanned over the sample. Post-specimen detectors collect different scattered or unscattered beams. The scattered or unscattered electrons are collected serially and the image is displayed pixel by pixel. High angle annular dark field scanning transmission electron microscopy (HAADF-STEM) only collects electrons that are scattered to relatively high angles (*e.g.* 30 mrad) by Rutherford scattering. At these angles the screening effect of the electron cloud can be ignored.[191] The intensity in HAADF-STEM images is therefore dependent on the square root of the atomic number of the sample, Z^2. This Z-contrast imaging is highly attractive for detecting gold nanoparticles and heavy metal-stained organelles inside cells.

Additionally, in a TEM, the chemical composition of a sample can be determined through energy dispersive X-ray spectroscopy (EDS). The principle underlying the operation of EDS is the detection of X-rays that are produced when the electron beam is accelerated onto the sample. The electron beam excites the atoms in the sample that subsequently produce X-rays with discrete energies that are different for every element and, therefore form a chemical fingerprint of the sample. The number and energy of the X-rays emitted from the specimen are then measured by a detector recording an energy spectrum of intensity versus energy. The characteristic energy distribution in the spectrum provides information about the composition of the sample being studied, and the intensity of the peaks provides information about the amount of each element present in the sample.

TEM and STEM images are used extensively in nanomedicine research as they can provide visual evidence of the distribution and morphology of assembled nanostructures inside biological entities. In this thesis, three TEM microscopes were used to investigate the morphology and composition of the Quantum Rattles (QRs) as well as their internalisation in cells, namely, a JEOL 2000 TEM, a JEOL 2010 TEM and a FEI TITAN 80/300

Cs aberration corrected TEM/STEM.

2.1.2 Laser Confocal Scanning Microscopy

A confocal laser scanning microscope (CLSM) creates sharp, detailed 2D images by incorporating two principal ideas: point-by-point illumination of the sample and filtering of out-of-focus light.[192] In the set-up of the confocal microscope (Figure 2.2), laser light is directed by a dichroic mirror towards an assembly of horizontally and vertically scanning mirrors. The motor-driven mirrors scan the laser through the microscope objective across the sample, where the light excites the fluorescent sample. The fluoresced light is de-scanned by the same mirrors used to scan the sample, passes through the dichroic mirror and, finally, through a pinhole placed in the conjugate focal plane of the sample. This pinhole filters all out-of-focus light arriving from the sample, after which a detector, such as a photomultiplier tube (PMT), collects the remaining focused light emerging from the pinhole. By excluding the light that is not in the focal plane, sharper and better-resolved images are obtained compared to conventional fluorescence microscopy. As only one point of the sample is observed at any particular instant, a computer is connected to the detector to reconstruct a 2D image one pixel at a time. The resulting confocal 2D images represent thin cross-sections through the sample. By assembling a series of these slices at different depths, a 3D reconstruction of the sample can be built.

CLSM represented a revolution in numerous biological science disciplines, from cell biology and genetics to microbiology and developmental biology.[193, 194] The combination of confocal microscopy and fluorescent molecules allows visualisation of alive and fixed cells, thereby investigating, for example, protein trafficking, cellular organisation, organelle dynamics, apoptosis, membrane fluidity, and enzymatic activity. A great variety of fluorescent probes are currently available, ranging from molecular dyes to gold nanoparticles.[75, 116] In this thesis, confocal microscopy was used for the 2D and 3D mapping of the QR internalisation and dynamics in cells

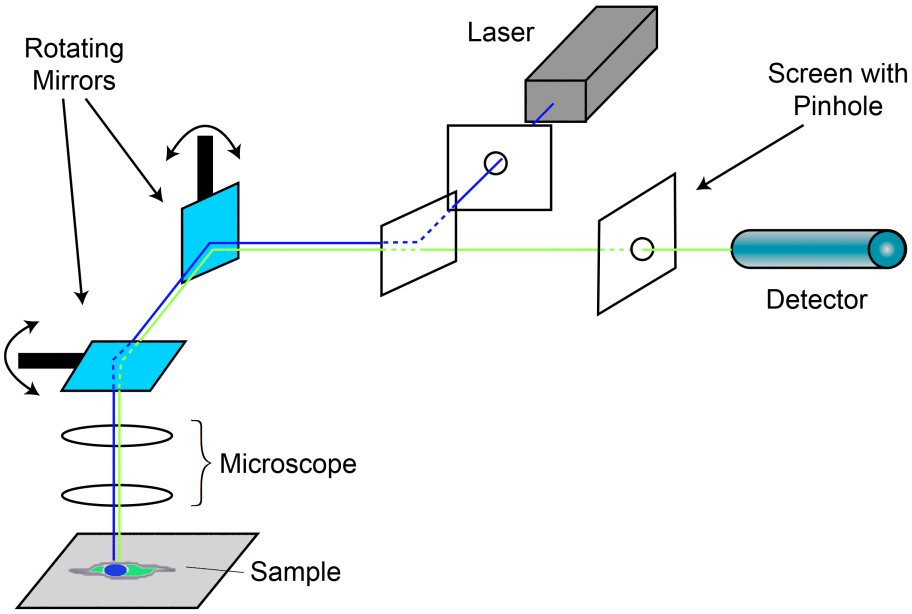


Figure 2.2: Basic set-up of a confocal microscope. Light from the laser (blue line) is scanned across the specimen by the scanning mirrors. Optical sectioning occurs as the fluoresced light (green line) passes through a pinhole before reaching the detector.

using a Leica SP5 MP/Flim inverted confocal microscope.

2.2 Spectrophotometry

2.2.1 UV-Visible Spectroscopy

UV-Visible spectroscopy measures the attenuation in intensity of incident light, in the ultraviolet (UV) and visible ranges of the electromagnetic spectrum, upon passing through a sample analyte relative to a reference. This attenuation is due to the extinction of light by the sample arising from electronic transitions to an excited state and scattering phenomena. The UV-Vis spectrometer uses a light source to irradiate a solution of interest, such as an incandescent bulb for the visible range and a deuterium arc lamp for the UV region, and monitors the transmittance of the sample depending on the incident wavelength, λ. The spectrometer uses a diffraction grating or monochromater to separate the different wavelengths and directs them at a photodiode or charge-coupled device (CCD) that detects the intensity over the spectral range (Figure 2.3).

The transmittance, $T(\lambda)$, is defined by,

$$T(\lambda) = \frac{I(\lambda)}{I_0(\lambda)}$$

where $I(\lambda)$ is the intensity of the light transmitted through a sample as a function of λ and $I_0(\lambda)$ is the intensity of light transmitted through a reference as a function of λ.

For analytes, where scattering is negligible compared to absorption, the absorption, $A(\lambda)$, is defined by Beer-Lambert's law,

$$A(\lambda) = log\left(\frac{1}{T(\lambda)}\right) = \varepsilon(\lambda)cl$$

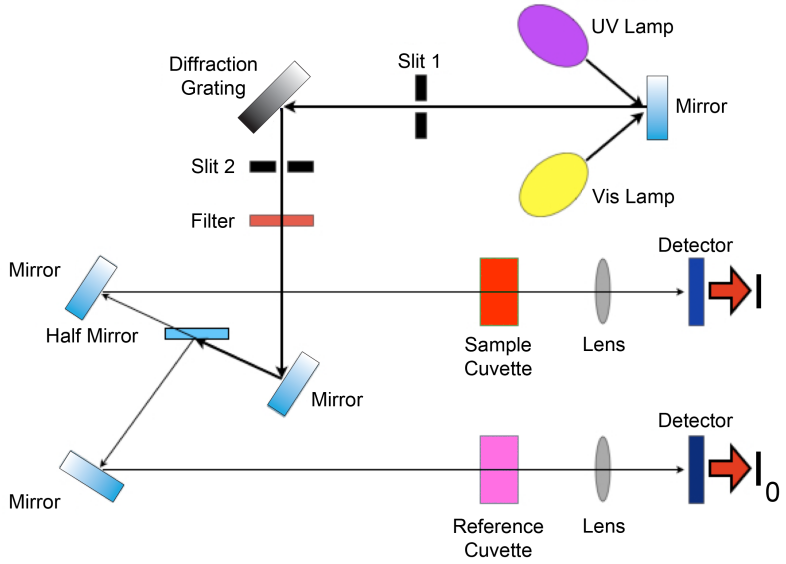


Figure 2.3: UV-Vis spectrophotometer basic set-up.

where $\varepsilon(\lambda)$ is the molar extinction coefficient as a function of λ ($M^{-1}.cm^{-1}$), c the molar concentration of the absorbing species (M), and l is the absorption pathlength (cm).

Therefore, UV-Vis spectroscopy enables the acquisition of the absorption spectrum of analyte by monitoring the intensity of light transmitted through a sample and a reference.

$$A(\lambda) = log\left(\frac{I_0(\lambda)}{I(\lambda)}\right) \tag{2.2}$$

For analytes with known molar extinction coefficients, the concentration of a sample can also be determined by UV-Vis spectroscopy from Beer-Lambert's law. It should be noted that for species where the scattering is not negligible compared to absorption, such as metal or silica NPs, the UV-Vis spectrometer monitors the extinction spectrum (sum of the absorption and scattering spectra) of the NPs and not the absorption alone. In this thesis, UV-Vis spectroscopy was used to investigate the extinction spectra of the QR system using a PerkinElmer Lambda 25 UV-Vis spectrophotometer.

2.2.2 Steady-State Photoluminescence Spectroscopy

Photoluminescence spectroscopy measures the intensity of photoluminescence (PL) of a sample analyte upon excitation with high-energy photons. When photoluminescent species absorb a photon, electrons are excited into a higher energy state. When the electrons return to their ground state, they release energy in the form of a photon (Figure 2.4). A spectrofluorimeter is capable of detecting and measuring the wavelength of that photon.

Light from an excitation source, such as a lasers, photodiodes or lamps (*e.g.* xenon arcs and mercury-vapour lamp), are sent through a diffraction grating monochromator that isolates a single wavelength to irradiate the sample. The incident light strikes the sample solution contained in a quartz cuvette. The electrons of the sample absorb the incident light and are excited. They release the energy in the form of emitted photons as the excited electrons drop down to a lower energy state (Figure 2.4). Those emitted photons pass through a second monochromator and into a photo detector that can detect the emission spectrum. The photo detector is usually placed at a right angle to the incident light to minimise any erroneous detection due to reflection or transmission of the incident light.

Quantum dots (QDs) absorb and emit photons in a very similar manner to fluorescent molecules, as depicted in Figure 2.4. When QDs or fluorescent molecules absorb a photon, an electron-hole pair is created. When the electron-hole pair recombines again, a photon is released at a discrete energy equal to the band-gap energy that gives the fluorescent entity its characteristic colour (if the emission wavelength is in the visible part of the electromagnetic spectra).

The quantum yield, QY, of any photoluminescent object is defined as the ratio of the number of photons emitted per photon absorbed.

$$QY = \frac{photons\,emitted}{photons\,absorbed}$$

In this thesis, steady-state photoluminescence spectroscopy was employed

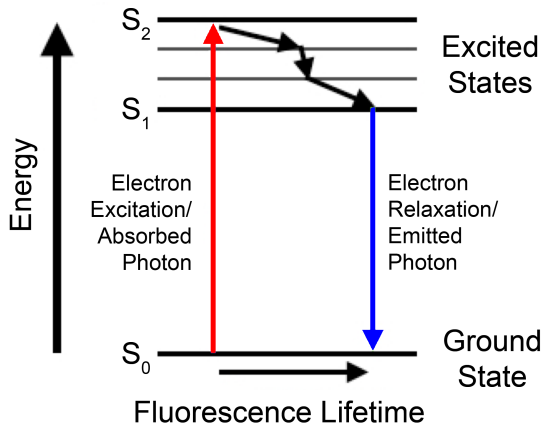


Figure 2.4: Mechanism of photoluminescence. The horizontal lines indicate quantum energy levels of the photoluminescent object. When a photoluminescent object absorbs a photon, an electron will be excited into a higher energy state. When it returns to its ground state, a photon is emitted.

to investigate the photoluminescent properties of the QR system in the near-infrared (NIR) region and to measure its quantum yield, using a Horiba Scientific Fluorolog-3 (FL3-21) spectrophotometer.

Chapter 3

The Quantum Rattle System: Synthesis and Characterisation

3.1 Introduction

Recently, new emphasis has been placed on hybrid particle systems where multiple nanostructured materials are combined to create multimodal systems possessing the properties of the component modules.[3, 82, 86, 90–92] Such multifunctional systems have been extensively investigated for a variety of catalytic applications.[3, 83, 99, 185, 195–197] Likewise, in the biomedical field, multifunctional systems have been developed for targeting, imaging and drug delivery purposes by adding together properties from different materials and bioconjugates.[33, 86, 89–92] In particular, rattle-type particles, which are particles with a core-shell structure containing a distinctive void that separates the core material from the shell, are promising platforms for many biomedical applications.[3, 23, 82, 198]

Compromises are often made in order to synthesise multifunctional hybrid particles, as functionalities can be intrinsically difficult to combine. For example, improving absorption for efficient photothermal conversion in gold nanoparticles for photothermal therapy (PTT) can be detrimental to generating intense emission from attached fluorescent dyes for live imaging. Achieving the optimal efficiency for each functionality (*i.e.* efficiency of the

best equivalent monofunctional systems) is very challenging, and currently many studies concentrate on getting an optimal trade-off. Multiple step processes are usually employed to accumulate different functionalities into a hybrid system thereby adding complexity. In this thesis, a holistic approach is taken, whereby a simple multifunctional design induces emergent properties and contributes to improved efficiency and versatility.

The overall aim of the project is to create a simple synthetic pathway, which produces tailorable and multipurpose hybrid particles and, in particular, particles that combine multimodal therapy and diagnosis for cancer treatment. The ideal system design for cancer treatment should have the following emergent properties:

- Near-infrared (NIR) absorbance and photoluminescence for PTT and live imaging;
- Biocompatibility and stability;
- Smart drug release;
- Targeting.

This chapter presents the synthesis and characterisation of a novel gold-silica, rattle-type particle, the Quantum Rattle (QR), made of a hollow mesoporous silica shell (HS) hosting two classes of hydrophobic gold nanostructures: gold quantum dots (AuQDs) and gold nanoparticles (AuNPs) (Figure 3.1). Each component of the QR synergistically combines to endow the QR with emergent properties ideally suited for cancer treatment. In addition to stabilising the gold nanostructures, making them dispersible in water and thereby enabling biomedical applications, the HS can leverage passive targeting for the QR *via* the enhanced permeability and retention (EPR) effect.[25, 113, 114] The AuQDs absorb and emit light in the near-infrared region (NIR) bio-window where blood and soft tissue are relatively transparent (650 – 900 nm).[28,115,129] With their NIR photonics, the AuQDs should allow the QR to mediate photothermal therapy (*c.f.* Chapter 5) as well as live infrared imaging *in vitro* (*c.f.* Chapter 4). Finally, the hydrophobic AuNPs can optimise the drug carrying performance of the

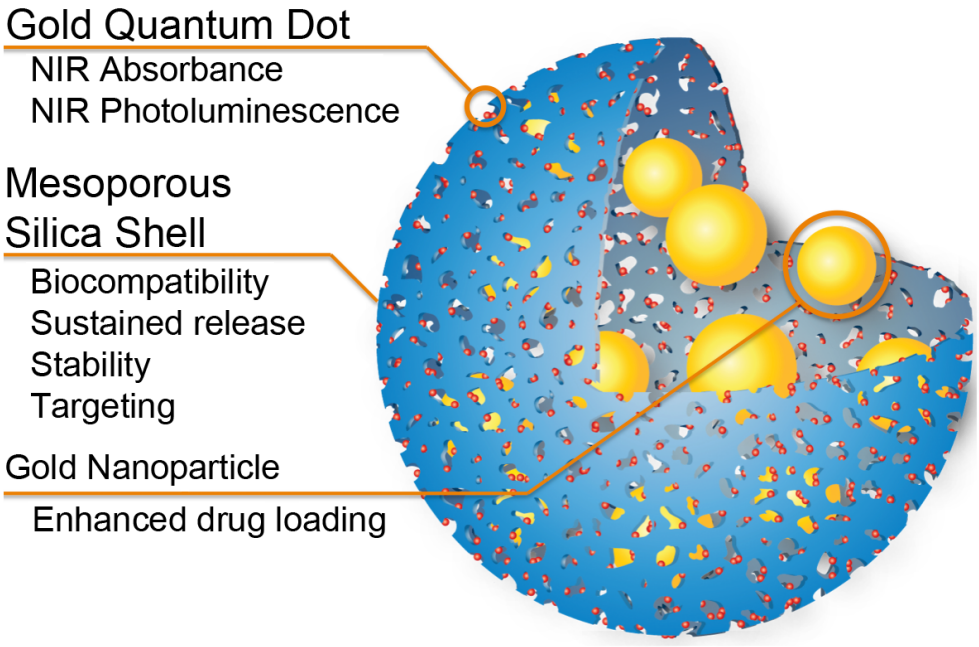


Figure 3.1: The Quantum Rattle design specifications. The Quantum Rattles are thin shells of mesoporous silica hosting gold nanoparticles within their core and gold quantum dots within their mesopores. The biocompatible silica shell stabilises the gold nanostructures inside it and has a diameter (< 400 nm) which sets well within the range to exploit the enhanced permeability and retention (EPR) effect. The gold quantum dots are photonically active in the near-infrared biological window allowing both photothermal therapy and live fluorescent imaging. The gold nanoparticles enhance the mesoporous silica shell as a drug vector by improving loading efficiency and prolonging sustained release.

system by increasing the payload's loading efficiency inside the particle as well as controlling its release profile (*c.f.* Chapter 6).

Rattle-type systems can be prepared through a variety of different techniques, including: selective etching or dissolution;[91,98,99] bottom-up approaches by soft templating assembly;[5,97] and ship-in-bottle methods.[3] In this study, a ship-in-bottle approach was used to synthesis the QRs using hollow containments. First, hollow mesoporous silica particles (HS) were synthesised using a previously published co-templating method.[199] Secondly, the QRs were obtained by infusing and nucleating gold precurs-

ors inside the pores and cavity of the silica shells. This chapter describes the synthesis and morphological and physicochemical characterisation of this novel QR design.

3.2 Materials and Methods

The hollow mesoporous silica shells syntheses were performed both at Imperial College London and at the Collège de France in Professor Clément Sanchez's group with the help of Dr. Glenna Drisko. The characterisation of the hollow mesoporous silica shells with small angle x-ray scattering and nitrogen physisorption as well as the synthesis of the non-hollow mesoporous Stöber silica particles were performed at the Collège de France by Dr. Glenna Drisko in Professor Clément Sanchez's group. The ultramicrotomy images were acquired with the help of Dr. Ciro Chiappini. The transmission and scanning electron microscopy images were acquired with the help of Dr. Sergio Bertazzo.

Materials: Chloro(triphenylphosphine) gold (I) salt, 1-octanethiol (OT), borane tert-butylamine complex, gold (III) chloride ($HAuCl_4$), sodium borohydride ($NaBH_4$), sodium citrate, styrene, dihexylsulfosuccinate sodium salt, sodium bicarbonate, potassium persulfate (KPS), hexadecyltrimethylammonium bromide (CTAB), tetraethyl orthosilicate (TEOS), potassium hydroxide (KOH) and ammonia solution (28%) were purchased from Sigma-Aldrich, UK. Solvents and acids, such as chloroform, absolute ethanol, diethyl ether or nitric acid, were purchased from VWR, UK. Carbon coated copper TEM grids (300 mesh) were purchased from Agar Scientific, UK.

3.2.1 Hollow Mesoporous Silica Particles

Polystyrene Particle Synthesis: Polystyrene particles were prepared using an emulsion polymerisation with an anionic initiator, potassium persulfate (KPS). Dihexylsulfosuccinate sodium salt (2.6 g), MilliQ H_2O (206 mL), sodium bicarbonate (0.43 g) and styrene (30.2 g) were mixed in a round

bottom flask. The solution was degassed over 30 min by bubbling with argon. The solution was then added to a pre-heated 90 °C oil bath. As styrene can autoinitiate at this temperature, the initiator, KPS (0.43 g) in MilliQ H_2O (14.9 mL) was promptly added to the hot solution *via* syringe. The reaction was performed under a slight positive pressure of argon. After 6 h the reaction was complete. The particles were dialysed over one week producing an 8.9 wt% polystyrene dispersion.

Hollow Mesoporous Silica Shell Synthesis: Mesoporous silica was grown on the polystyrene particles to produce a core cavity. The surfactant (CTAB, 3.2 g) was dissolved in MilliQ H_2O (100 mL) at 35 °C. The polystyrene particles (17.5 g or 5 g for thin and thick shell particles respectively) were diluted with 500 mL MilliQ H_2O, 200 mL of ethanol and basified with 7.5 g of ammonia. The CTAB/H_2O was added to the polystyrene dispersion and allowed to equilibrate for 45 min. TEOS (5.4 g) was added drop-wise to the solution, which was subsequently allowed to react for 1 day. To collect the particles, the solution was centrifuged at 8000 rpm.min^{-1} for 1 h. The resulting material was calcined using the following program: 25 to 250 °C at a rate of 5 °C min^{-1}, held at 250 °C for 2 h, 250 to 550 °C at a rate of 2 °C min^{-1}, held at 550 °C for 5 h.

3.2.2 Gold Synthesis

All glassware were pre-washed in aqua regia (1:3 HNO_3:HCl) and left in saturated ethanolic KOH overnight before any synthesis.

Monolayer Protected Gold Nanoparticle Synthesis: Gold NPs were synthesised following a slightly modified one-step, one-phase Stucky method[48] using gold (I) salt as metallic precursor, thiol ligand as capping agent and a borane complex as reducing agent in a ratio of 1:2:10. Chloro(triphenylphosphine) gold (I) salt (222.6 mg) and 1-octanethiol (156.2 µL) were dissolved in chloroform (30 mL) and left to mix for 20 min. A solution of borane tert-butylamine complex (391.4 mg) was then prepared in chloroform (10 mL) and added to the gold-thiol solution while mixing in a round

bottom flask. The reaction vessel was equipped with a condensation column and transferred to a pre-heated 55 °C oil bath. The solution was left to react for 1 h. After cooling the solution to room temperature, ethanol (250 mL) was added and the particles were left to settle overnight at 4 °C. The supernatant was removed and the particles were washed and centrifuged 3 times at 4000 rpm.min^{-1} for 8 min in ethanol before leaving to dry at room temperature.

3.2.3 Quantum Rattle Syntheses

The QRs were obtained by infusing hollow mesoporous silica shells (HSs, *c.f.* section 3.2.1) with gold precursors and generating nucleation anchors both inside the pores and cavity of the HS using a one-step, one-phase method (Figure 3.2).

Chloro(triphenylphosphine) gold (I) salt (222.6 mg) and HSs (100 mg) were suspended in chloroform (25 mL) and left to mix overnight ($>$ 12 h) at room temperature. The next day, 1-octanethiol (156.2 µL) was added to the gold-silica suspension and left to mix for 20 min. A solution of borane tert-butylamine complex (391.4 mg) was then prepared in chloroform (15 mL) and added to the gold-silica-thiol solution while mixing in a round bottom flask. The reaction vessel was then equipped with a condensation column and transferred to a pre-heated 55 °C oil bath. The solution was left to react for 1h. After cooling the solution to room temperature, diethyl ether (250 mL) was added and the particles were left to settle overnight at 4 °C. The supernatant was removed and the particles were washed and centrifuged 3 times at 1500 rpm.min^{-1} for 8 min in diethyl ether and 2 times at 6500 rpm.min^{-1} for 20 min in 0.5 mL EtOH and 10 mL chloroform before leaving to dry at room temperature.

Non-hollow Quantum Rattles (NQRs) were synthesised to deconvolve the role of the AuQDs from the AuNPs in the photonic properties of the QRs. The same protocol used for the QRs was used for the NQRs with the exceptions that non-hollow Stöber mesoporous silica particles with the same

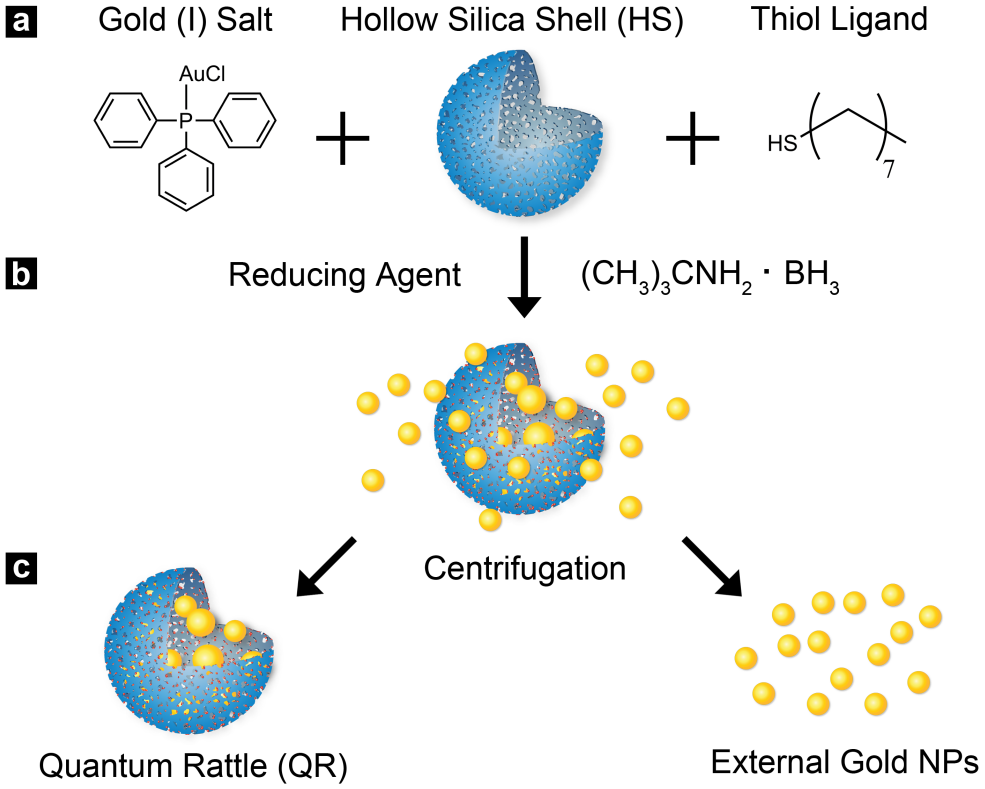


Figure 3.2: Schematic of Quantum Rattle synthesis. (a) Chloro(triphenylphosphine) gold (I) salt and 1-octanethiol are infused into hollow mesoporous silica shells. (b) Nucleation and formation of gold quantum dots inside the silica shell's pores and gold nanoparticles inside and outside the hollow shell after the addition of the borane tert-butylamine complex reducing agent. (c) Purification step separating Quantum Rattles (QRs) from gold nanoparticles formed outside the hollow silica shells.

pore size as the HS were used instead of HSs.

Citrate protected gold NP synthesis was also tried in the presence of HS. Gold (III) chloride (1.7 mg) and HSs (100 mg) were suspended in MilliQ H_2O (20 mL) and left to mix overnight at room temperature. The next day, sodium citrate (7.35 mg) was dissolved in MilliQ H_2O (1mL) and 10 μL was added to the gold-silica suspension which was left to mix for 20 min. A solution of sodium borohydride (3.78 mg) was then prepared in MilliQ H_2O (1 mL) and 600 μL was added drop-wise to the gold-silica-citrate solution while mixing in a round bottom flask at room temperature. The solution was left to react until it turned a ruby red colour and the particles were then left to settle overnight at 4 °C. The supernatant was removed and the particles were washed and centrifuged 3 times at 1500 rpm.min^{-1} for 8 min in MilliQ H_2O.

3.2.4 Particle Morphology and Composition

Small angle x-ray scattering (SAXS) was collected on a Rigaku S-Max 3000 equipped with a microfocus source of 20 μm x 20 μm. The radiation wavelength (Kα) used was 0.154 nm. A 2D Gabriel type detector was placed 1469 mm from the sample. Diffraction patterns were analysed using SAXGUI V2.04.05 software. Bragg's law was used to calculate the d-spacing, d, from the SAXS data:

$$\begin{cases} n\lambda = 2d\sin\theta \\ q = \frac{4\Pi\sin\theta}{\lambda} \end{cases}$$

$$\Rightarrow d = \frac{2\Pi n}{q} \tag{3.1}$$

where n is an integer describing the order, λ is the wavelength, θ is the scattering angle and q is the magnitude of the scattering vector.

The nitrogen physisorption method was used to determine the effect of the QR synthesis on the integrity of the silica shell of the QR. The nitrogen

adsorption and desorption curves were obtained on a BELSORP-max (BEL Japan) instrument. The samples were degassed at 80 °C at a pressure of 10^{-2} kPa for 1 day prior to analysis using a BELPREP-vacII (BEL Japan) pretreatment instrument.

Electron Microscopy

Scanning electron microscopy was used to assess the morphology and size distribution of the polystyrene particles used as templates for the core of the HS. SEM images were acquired using a Leo 1525 Gemini scanning electron microscope (SEM) operated at an accelerating voltage of 5 kV.

Transmission electron microscopy (TEM) was used to determine the morphology and size distribution of the QRs. TEM images of the particles were acquired using a JEOL 2010 TEM equipped with an energy dispersive x-ray spectroscopy (EDS) detector (Carl Zeiss SMT Ltd.) operated at an accelerating voltage of 200 kV. Samples were dissolved in EtOH (1 $mg.ml^{-1}$) and drop-deposited on TEM grids prior to analysis.

EDS analysis was used to quantify the chemical composition of the QRs. X-ray counts were recorded over five separate areas per specimen (in triplicate) during a 1 minute period at 10 kV and analysed using INCA Energy 3000 software (Oxford Instruments).

The contribution of each component of the QR (SiO2 shell, AuQD and AuNP) to the total mass of one QR was calculated using the EDS data and the following set of equations.

From geometrical considerations, the mass of the silica shell of the QR, m_{SiO_2} , and the mass of the AuNPs inside the cavity of the QR, m_{AuNP}, were calculated using:

$$m_{SiO_2} = \tfrac{4}{3}\pi(r^3_{SiO_2outer} - r^3_{SiO_2inner}) \cdot d_{SiO_2}$$
$$m_{AuNP} = \tfrac{4}{3}\pi r^3_{AuNP} \cdot d_{Au}$$

where d_{SiO_2} and d_{Au} are the densities of mesoporous silica (1.8 $g.cm^{-3}$) and gold (19.3 $g.cm^{-3}$), respectively. r_{SiO_2outer} and r_{SiO_2inner} are the outer and

inner radius of the silica shell (75 nm and 50 nm, respectively, as determined from TEM analysis). r_{AuNP} is the radius of the entire aggregate of AuNPs inside the cavity, assuming they aggregate in a spherical structure (15 nm, as determined from TEM analysis).

From the mass percentage of silica composing a QR obtained from the EDS data, $x_{EDS}(SiO_2)$, the total mass of AuQDs per QR, m_{AuQD}, was evaluated using:

$$\begin{cases} m_{QR} = m_{SiO_2} + m_{AuNP} + m_{AuQD} \\ \frac{m_{SiO_2}}{m_{QR}} = \frac{x_{EDS}(SiO_2)}{100} \end{cases} \tag{3.2}$$

$$\Rightarrow m_{AuQD} = (\frac{100}{x_{EDS}(SiO_2)} - 1) \cdot m_{SiO_2} - m_{AuNP} \tag{3.3}$$

By re-inputing m_{AuQD} into the first equation of 3.2, the mass of one QR, m_{QR}, was obtained. The mass percentage of AuQDs and AuNPs was then calculated using:

$$\begin{cases} x_{calculated}(AuQD) = \frac{m_{AuQD}}{m_{QR}} \\ x_{calculated}(AuNP) = \frac{m_{AuNP}}{m_{QR}} \end{cases} \tag{3.4}$$

The number of AuQDs per QR, n_{AuQD} was then induced from the mass of AuQDs per QR, m_{AuQD}, using:

$$\begin{cases} m_{Au_nQD} = n \cdot \frac{M_{Au}}{N_a} \\ n_{AuQD} = \frac{m_{AuQD}}{m_{Au_nQD}} \end{cases}$$

$$\Rightarrow n_{AuQD} = \frac{m_{AuQD} \cdot N_a}{n \cdot M_{Au}} \tag{3.5}$$

where m_{Au_nQD} is the mass of one AuQD composed of n gold atoms. N_a and M_{Au} are Avogadro's number (6.02×10^{23} mol^{-1}) and the molar mass of gold (196.96 g.mol^{-1}), respectively.

Ultramicrotomy was used to assess the inner structure of the QRs. The QRs (1 mg) were embedded through a graded Epon812/Araldite resin:acetone series (1:2, 2:1, 1:0 v/v), transferred to fresh pure Epon812/Araldite and polymerised at 60 °C for 1 day. Ultrathin sections of approximately 100 nm were cut on a Power Tome XL ultramicrotome (RMC Products, USA) using a 35° diamond knife and transferred to a TEM copper grid. TEM images were acquired using a JEOL 2000 TEM operated at 120 kV.

High resolution transmission electron microscopy (HRTEM) and high angle annular dark field scanning transmission electron microscopy (HAADF-STEM) was used to resolve and image gold inside of the QRs pores. HRTEM and HAADF-STEM images of the particles were acquired using FEI TITAN 80/300 STEM/TEM operated at an accelerating voltage of 200 kV. Samples were dissolved in EtOH (1 $mg.ml^{-1}$) and drop-deposited on TEM grids prior to analysis.

3.2.5 Photonic Characterisation

The photonic properties of the QRs and in particular the extinction and photoluminescent properties were assessed by UV-Vis and Fluorescent spectroscopy. UV-Vis measurements were collected using a 1 cm path-length quartz cuvette using a PerkinElmer Lambda 25 UV-Vis spectrophotometer at a scanning rate of 480 $nm.min^{-1}$ from 400 nm to 1000 nm with 0.2 nm resolution. Spectra were normalised to the peak maximum intensity at 672 nm. Samples were dispersed in EtOH (1 $mg.ml^{-1}$) and sonicated for 5 min prior to analysis.

Steady-state photoluminescence measurements were collected using a 1 cm path-length quartz cuvette using a Horiba Scientific Fluorolog-3 (FL3-21) spectrophotometer with an integration time of 1 s and 12 nm slits for the QRs and 5 nm for the controls. Emission spectra were collected from 700 nm to 900 nm with an excitation at 672 nm and 673 nm for the QRs and NQRs, respectively. Excitation spectra were collected from 550 nm to 800 nm by acquiring the emission intensity at 827 nm and 826 nm for the QRs

and NQRs, respectively. The acquired spectra were corrected for variations in lamp and detector efficiency and normalised to either the peak maximum for the QRs and NQRs or the maximum in the range scanned for the controls. Each emission peak observed was confirmed to be a photoluminescent peak or a Raman peak by acquiring a new emission measurement at an excitation wavelength 20 nm lower than the original. If the wavelength of the emission peak maximum was independent from the excitation wavelength (*i.e.* the peak did not shift between the two measurements) then the peak was confirmed to be a photoluminescent peak. QR samples were dispersed in EtOH (1 mg.ml^{-1}) and sonicated for 5 min prior to analysis.

The quantum yield (QY) of the QRs was calculated relative to adsorption-matched dilutions of Qdot 705 ITK (Molecular Probes, UK) organic quantum dots (QY = 0.63) in hexane. The extinction E of both the reference Qdot 705 and the QRs was adjusted to be below 0.2 optical density at the excitation wavelength (672 nm) for the QRs and at the adsorption maximum of the Qdot (450 nm) for the reference Qdot in order to minimise luminescence quenching due to internal reabsorption. The final QY of the QRs was calculated according to:

$$QY = QY_{ref} \frac{I}{I_{ref}} \frac{n^2}{n_{ref}^2} \frac{(1 - 10^{-E_{ref}})}{(1 - 10^{-E})} \tag{3.6}$$

where I is the integrated luminescence intensity and ref denotes the reference sample (the Qdot in this study).

3.3 Results and Discussion

3.3.1 Hollow Mesoporous Silica Particles

The QR synthetic pathway uses a ship-in-bottle method to combine hollow mesoporous silica particles (HSs) with gold nanostructures. The HSs were obtained by means of a a dual-template approach.[199] Briefly, polystyrene particles with anionic surface charges acted as core template, while CTAB

served as a co-template to structure the mesopores formation during TEOS hydrolysis/condensation. This dual templating approach using a soft core and surfactant as co-template has been shown to provide a better control on the ordering of the mesopores inside the silica shell.[199] The surfactant acts as a structuring agent for the pore formation during the sol-gel condensation of the silica precursor (TEOS).[200–202] However, soft-templating approaches tend to lack in particle dispersity, control of particle dimensions, independent tuning of hollow cavity diameter and shell thickness or mesopores ordering and orientation. To circumvent such problems, hard core templates, and in particular polymer dispersions, combined with a surfactant co-template seem to be a preferable choice for more reliable dual-templating syntheses of hierarchically structured silica particles.[203, 204] However, the use of a polymer dispersion template and a surfactant co-template to assist in the silica formation can lead to various morphologies depending on the reaction parameters. The dual-template protocol used here produced monodisperse spherical hollow particles with ordered mesoporous silica shells.

Polystyrene Particle Synthesis - Core Template for Hollow Mesoporous Silica Particle Synthesis

The first step in obtaining the HSs, is the synthesis of polystyrene beads which serve as templates for the growth of mesoporous silica and create the cavity after removal by calcination. Being the template on which the silica shell of the HS is grown, the morphology and size distribution of the polystyrene beads is crucial to the final dimension of the HSs. The polystyrene bead size should be large enough to create a cavity in the HS (after calcination) that can accommodate several AuNPs in the range of 5 to 10 nm in diameter. Furthermore, the polystyrene particles should allow the growth of an intact mesoporous silica shell (*i.e.* thicker than 5 nm[199]) to enable controlled gold salt diffusion. Finally, the total dimensions of the resulting HS particle (cavity + silica shell) should not exceed 400 nm in diameter in order to accumulate inside the tumorous tissue by means of

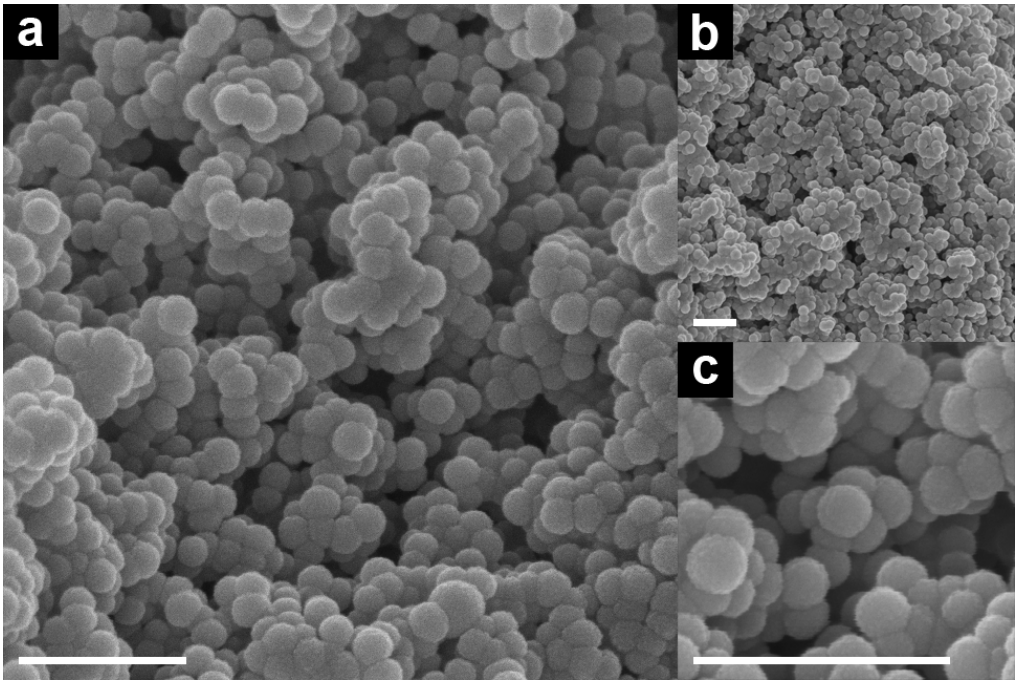


Figure 3.3: Morphology and size distribution of polystyrene particles used in the hollow mesoporous silica synthesis as template for the cavity. (a-c) Scanning electron microscopy images of the polystyrene particle template showing a monodisperse and spherical population at different magnifications. Scale bars: 500 nm.

the EPR effect (*c.f.* Chapter 1).[25, 113, 114]

Using an anionic precursor (KPS), highly monodisperse and spherical polystyrene beads, with diameters varying between 110 nm and 120 nm (n = 10) were formed (Figure 3.3). These beads have an optimal size specifications for hosting small AuNPs and growing a robust silica shell, whilst staying within the size range for the EPR (60 nm - 400 nm).

Hollow Mesoporous Silica Shell Synthesis

The next step in the QR synthesis process is the formation of mesoporous silica on the polystyrene particle surface. The hydrolysis-condensation of TEOS in the presence of CTAB micelles was performed using two different amounts of polystyrene beads. A decrease in the ratio of silica precursor

to polystyrene bead resulted in the formation of thicker silica shells. After calcination of the polystyrene filling, the two type of HSs were characterised by TEM (Figure 3.4). Both thin and thick HSs are monodisperse in size (around 150 nm and 200 nm, respectively) and perfectly spherical. The silica shells of both thin and thick HSs are uniform in thickness (around 25 nm and 50 nm, respectively) and exhibit highly ordered mesopores perpendicularly oriented to the core of the HS particle. The HSs mesostructure was further investigated by SAXS (Figure 3.5b). The sharp SAXS peaks confirm the mesopore ordering in the shell of both HSs. Furthermore, the d-spacing, calculated by inputing the q values corresponding to the diffraction peaks of both HSs into equation 3.1, decreases with increasing shell thickness (6.0 nm and 4.6 nm for the thin and thick HS, respectively). The d-spacing is in good agreement with those of common mesoporous silica powders prepared in basic media.[205]

As can be seen on the TEM images, the average diameter of both thin and thick HSs hollow core (around 100 nm) is slightly lower than the polystyrene beads diameter. This might be due to a constriction phenomenon occurring during the calcination step.[199] However, the calcination process does not affect the particle stability as the silica shell remains intact with a perfectly spherical hollow core.

The highly ordered and radial organisation of the mesopores and the integrity of the silica shells are the predominant characteristics to consider before attempting the synthesis of QRs. The mesopore organisation is important in order to get the most controlled and consistent diffusion process of molecules inside the HS particles, in particular of gold salts for the synthesis of QRs. The integrity of the silica shells is critical in order to obtain hollow mesoporous particles with cavities sealed off from the external environment that are only reachable through the mesopores. Creating an independent space sealed off from the external environment is crucial in the application of the QRs, where a hydrophobic environment contained inside the shells is beneficial to drug loading and release kinetics (*c.f.* Chapters 6).

To conclude, compared to synthetic pathways described in the literature,

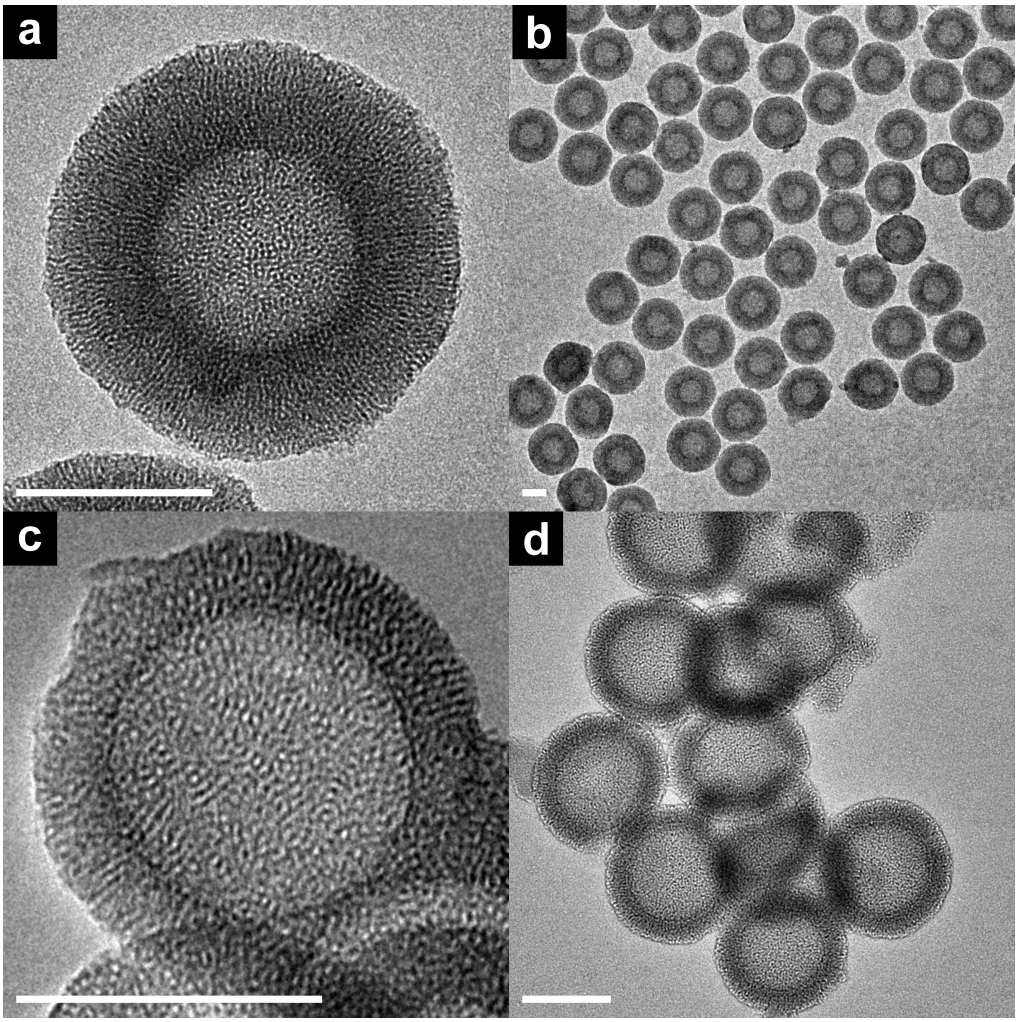


Figure 3.4: Morphology of hollow mesoporous silica particles. Bright field transmission electron microscopy images of the (a-b) thick and (c-d) thin hollow mesoporous silica particles (HSs). Both type of HSs are monodisperse and spherical. The mesopores of both silica shells possess an ordered and radial organisation, starting from the core. Scale bars: 100 nm.

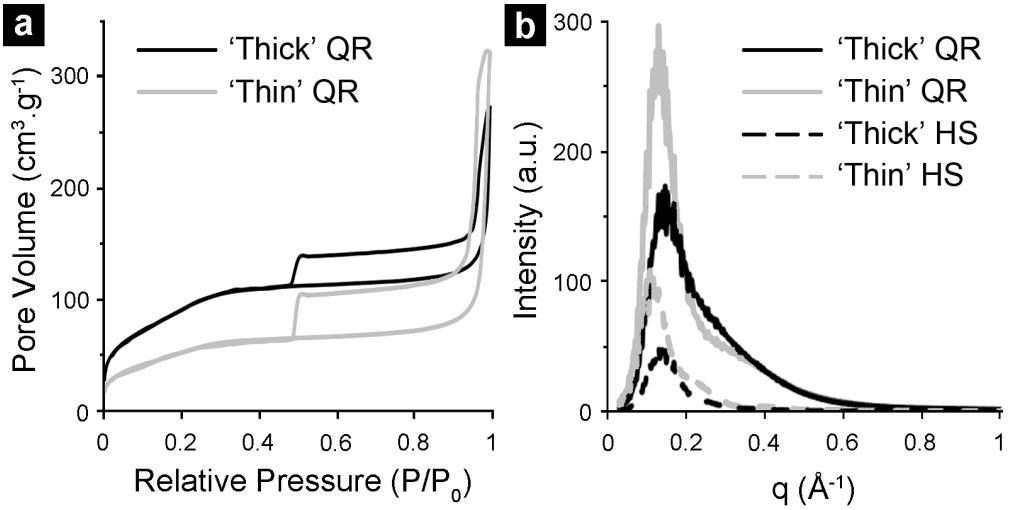


Figure 3.5: Effect of the Quantum Rattle synthetic process on the mesoporous silica shell. (a) Nitrogen adsorption and desorption isotherm of thin (grey) and thick (black) and (b) small angle x-ray scattering (SAXS) spectra of thin (grey) and thick (black) Quantum Rattles (QRs, plain line) and hollow mesoporous silica particles (HSs, dashed line) showing that the QR synthetic pathway does not affect the integrity and pore structure of the mesoporous silica shells.

where the inhomogenous morphology of both particles and pores could be an issue for the QR synthesis,[195, 206, 207] the method used here to synthesise HSs produces highly monodisperse hollow particles with silica shells of controlled thickness containing radially oriented mesopores.

3.3.2 Quantum Rattle

Quantum Rattle Synthesis

Once monodisperse, spherical hollow mesoporous silica shells with radially oriented mesopores were obtained, Au@Si rattle-type particles (Quantum Rattles, QRs) could be synthesised. Two types of monodisperse QRs were synthesised by nucleating gold into thin and thick HSs by means of a one-step, one-phase synthesis (*c.f.* section 3.2.3).

Briefly, chloro(triphenylphosphine) gold (I) was left to infuse into the HSs

pores and cavity overnight ($>$ 12 h). The next day, a thiol ligand (1-octanethiol) was added before the gold nucleation was triggered using borane tert-butylamine complex as reducing agent. Compared to the more commonly used gold (III) salt[38, 43], the QR synthesis uses a gold (I) salt as the gold precursor. The nature of the gold salt is crucial to the QR synthesis as adaptations of methods using gold (III) chloride ($HAuCl_4$) as metallic precursor to the QR process do not induce gold nucleation inside the QRs silica shells (Figure 3.6). TEM images do not show any denser particles inside the cavity of the QRs silica shell (Figure 3.6a) and EDS analysis show no trace of gold in the samples (Figure 3.6b) confirming that gold does not nucleate inside the HSs while using gold (III) precursor in the QR synthesis.

Chloro(triphenylphosphine) gold (I) has been used in many studies as a metallic precursor to synthesise of $<$ 2 nm AuQDs.[72, 208–210] The more commonly used gold (III) precursor, $HAuCl_4$, however, first forms an intermediate Au(I):SR complex (where R can be alkyl- or arythiols) before full gold reduction.[68–70, 73, 211] Previous studies have shown that this intermediate Au(I):SR forms structures larger than 100 nm. This can explain the failure of QR synthesis using gold (III) precursors, as such complexes will not be able to diffuse in HSs to create gold particles inside the cavity. Another factor that could influence the formation of gold nanostructures within the HS is the reducing ability of the reductant. Borane complexes have a weaker reducing ability than more commonly used reducing agents, such as sodium or lithium borohydride, which can slow the reducing rate of gold cations and, therefore, allow for a better diffusion of the reducing agent inside the HSs. Upon the addition of strong reductants, gold cations are reduced rapidly, resulting in an immediate colour change of the reaction mixture from colourless or yellow to dark red.[38, 48] With the use of a weaker reductants, such as borane complexes, a much slower but continuous colour change from colourless to yellow to brown, and finally to deep red/purple is observed, which indicates a relatively slow reducing rate of gold (I). In the QR synthesis, where the diffusion kinetics of the reducing

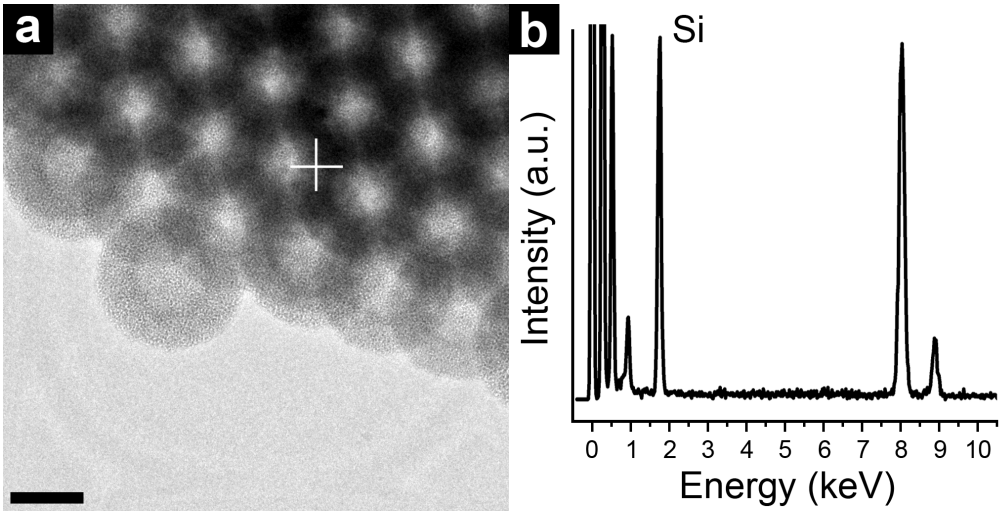


Figure 3.6: Attempted Quantum Rattle synthesis using gold (III) salt as metallic precursor. (a) Bright field transmission electron microscopy image showing hollow mesoporous silica particles without any gold nanostructures inside the cavity. White cross indicates where energy dispersive X-ray spectroscopy (EDS) analysis was performed. Scale bar: 100 nm. (b) Corresponding EDS spectra showing no elemental trace of gold.

agent inside the silica shells is crucial, a rapid reducing rate could prevent nucleation of gold inside the HSs.

Moreover, the borane complex reducing agent allows the integrity of the silica shell to be preserved without evident signs of erosion or perforations (Figures 3.5 and 3.7). The nitrogen adsorption and desorption isotherms of both thick and thin QRs are type IV isotherms characteristic of mesoporous materials.[199, 212] The large box-like hysteresis observed in the isotherms shows that the QR synthetic pathway does not affect the integrity of the silica shells (Figure 3.5a).

The pore structure and organisation within the silica shells of the QRs is confirmed by small angle x-ray scattering (SAXS, Figure 3.5b). The d-spacing, calculated by inputing the q values corresponding to the diffraction peaks of both QRs into equation 3.1, is 4.9 nm and 4.3 nm for the thin and thick QRs, respectively and is slightly lower than the d-spacing observed

for the HS (6.0 nm and 4.6 nm for thin and thick, respectively). The QR synthesis alters the pore distribution slightly, which is to be expected by the addition of AuQDs inside the pore structure of the QR silica shells. Furthermore, the intensity of the diffraction peak of the QRs is higher compared to the signal observed for the HS, indicating the addition of a denser material than silica, such as gold, into the HS system.

The hydrophobic ligand in the QR synthesis was chosen to simplify the purification process of the QRs from the external AuNPs (Figure 3.2c) by precipitation of the hydrophilic silica shells from the free hydrophobic AuNPs. In addition, the ligand was also chosen as it can contribute to the emergent QR properties in two ways:

- The hydrophobic surface of the thiol-protected AuNPs create an hydrophobic environment inside the QR cavity, favourable for the loading of cancer drugs[91, 213] (*c.f.* Chapter 6);
- The thiol ligand plays a critical role in the AuQDs photonic properties and therefore the QRs photonic properties.[52, 71, 77, 214]

By changing the functional group of the thiol-ligand capping the AuQDs, the photonic properties of the AuQDs can be adapted[77, 79] and, in the future, different type of thiol-ligands could be used to tailor the photonic properties of the QRs (*c.f.* Chapter 7).

Quantum Rattle Morphology and Composition

Transmission electron microscopy (TEM) was used to investigate the morphology and composition of both type of QRs. Ultrathin sections (100 nm) of resin-embedded QRs obtained through ultramicrotomy in combination with drop-deposited QRs on carbon coated TEM grids show that the QRs are well-defined monodisperse particles (approximately 150 nm and 200 nm total diameter for the thin and thick QRs, respectively) composed of mesoporous silica shells (approximately 25 nm and 50 nm thickness for the thin and thick QRs, respectively) with AuNPs of 5 nm to 10 nm diameter inside the cavity of the QRs (Figure 3.7). The composition of the QR was

confirmed by EDS analysis, where both silica and gold peaks are present (Figure 3.8). The other peaks can be attributed to the carbon and copper of the TEM grids used.

The images obtained through ultramicrotomy (Figure 3.7a and c) show that the AuNPs are present in the cavity of nearly all QRs (thin and thick) and, in dry conditions, tend to assemble into suprastructures of around 30 nm for both thin and thick QRs. The quantity of AuNPs is not only similar for all the QRs in the thin or thick groups, but also similar when the two groups are compared to each other. This difference in AuNP amount is not expected, as the diffusion of the borane complex reducing agent, which is the key step in the QR synthesis, should be slower for the thick silica shell compared to the thin one. A slower diffusion was thought to lead to less AuNPs overall, but larger and more polydisperse in size. However, the similarity in AuNP formation for both thin and thick QRs may be due to the difference in thickness being too little to influence the AuNPs synthesis. The higher magnification TEM images of the drop-deposited QR on TEM grids show radially oriented mesopore channels visible in both type of QRs (Figure 3.7b and d), confirming in addition to the SAXS data (Figure 3.5b) that the mesostructure of the silica shell is not affected by the process of QR synthesis.

The proposed QR system composed of only AuNPs of more than 5 nm diameter inside a silica shell does not explain the photonic properties observed for the QRs (*c.f.* next section 3.3.3), which indicates that smaller gold structures must be present in the system.[52,67–74,79] High-resolution transmission electron microscopy (HRTEM) was used to characterise the thin QRs morphology and composition in more detail (Figure 3.9), while high angle annular dark field scanning transmission electron microscopy (HAADF-STEM) was used to complement the HRTEM study, highlighting all gold nanostructures present in the QRs (Figure 3.10). The thin QRs are well-defined monodisperse particles (around 150 nm diameter) with a mesoporous silica shell (around 25 nm thickness) hosting both AuQDs ($<$ 2 nm diameter) and AuNPs (5 - 10 nm diameter) (Figure 3.9a-b). The crys-

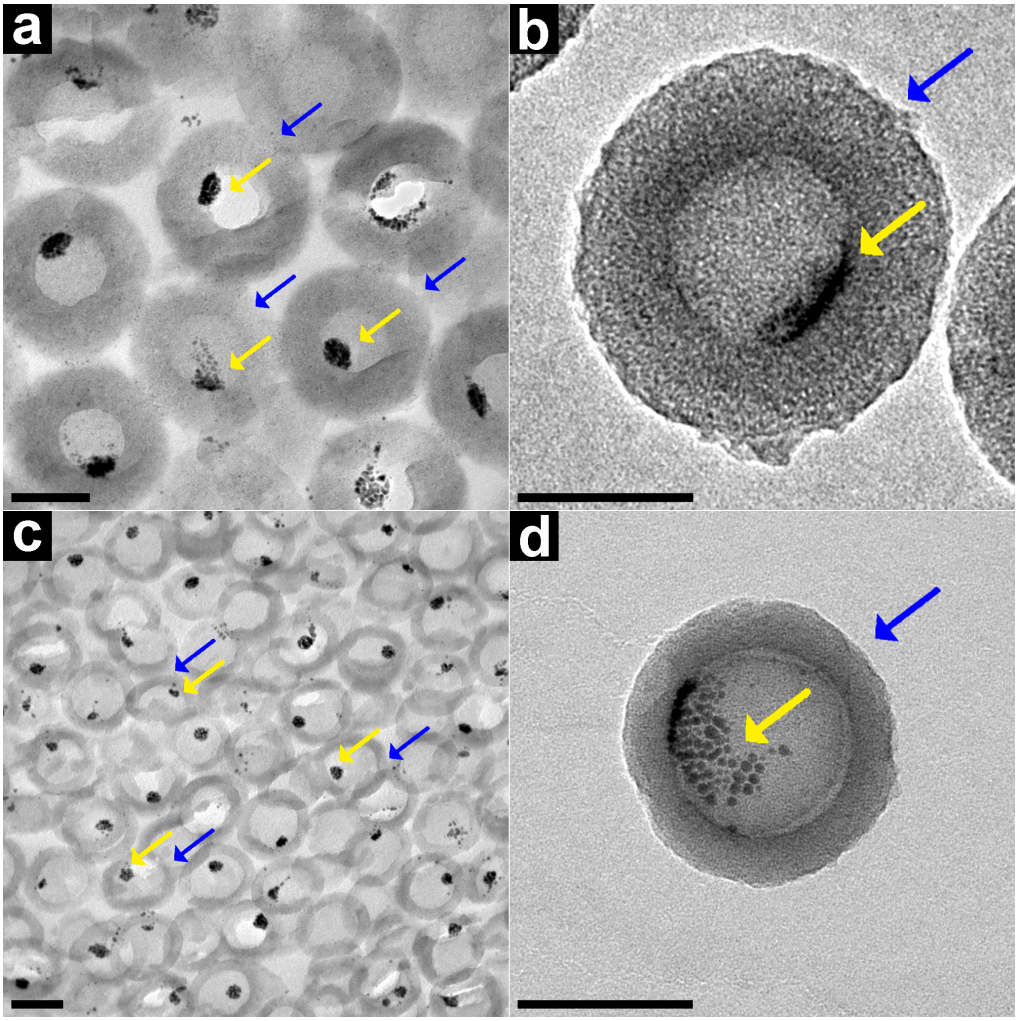


Figure 3.7: Morphology of Quantum Rattles. Bright field transmission electron micrographs of (a-b) thick and (c-d) thin Quantum Rattles (QRs) showing gold nanostructures (yellow arrows) inside hollow mesoporous silica particles (blue arrows). (a,c) Ultrathin sections of resin-embedded QRs, obtained through microtomy showing suprastructures formed of 5 nm to 10 nm gold nanoparticles; (b,d) Higher magnification of QRs deposited on carbon coated TEM copper grid. Scale bars: 100 nm.

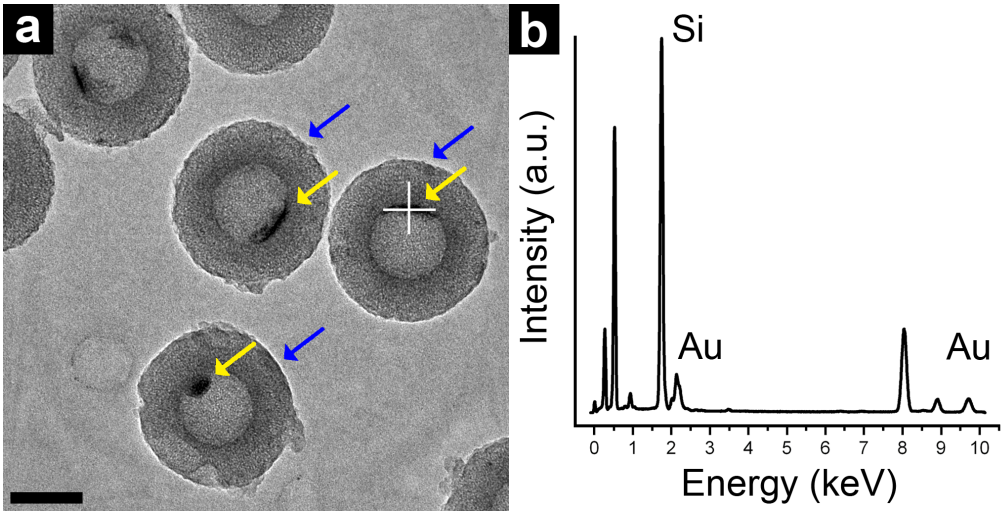


Figure 3.8: Quantum Rattle elemental analysis. (a) Bright field transmission electron micrographs of thin Quantum Rattles (QR) showing gold nanostructures (yellow arrows) inside hollow mesoporous silica particles (blue arrows). White cross indicates where energy dispersive X-ray spectroscopy (EDS) analysis was performed. Scale bar: 100 nm. (b) Corresponding EDS spectra of QR indicating the presence of silica and gold.

tal faces of the larger AuNPs can be clearly identified through the silica shell on high magnification HRTEM images (Figure 3.9d). The HAADF-STEM images of the QRs highlight the complete loading of the silica shell with AuQDs (Figure 3.10). The AuQDs are confined within the pores of the silica shells and give the QRs their photonic properties.[52,79] EDS analysis demonstrated that the silica shell and the gold nanostructures of the QR accounted for 73% and 27% of the total mass of the QR, respectively. The mass percentages attributable to AuQDs and AuNPs were calculated using equation 3.4 and were found to be 18% and 9% of the total mass of the QR for AuQDs and AuNPs, respectively. Finally, by inputing the mass of AuQDs per QR calculated using equation 3.3 into equation 3.5 and assuming that the AuQDs are composed by 25 gold atoms, the number of AuQDs per QR was calculated to be approximately 7.10^4.

In parallel to the QR synthesis, OT protected AuNPs were synthesised using the QR process in the absence of HSs (Figure 3.11). The synthesised

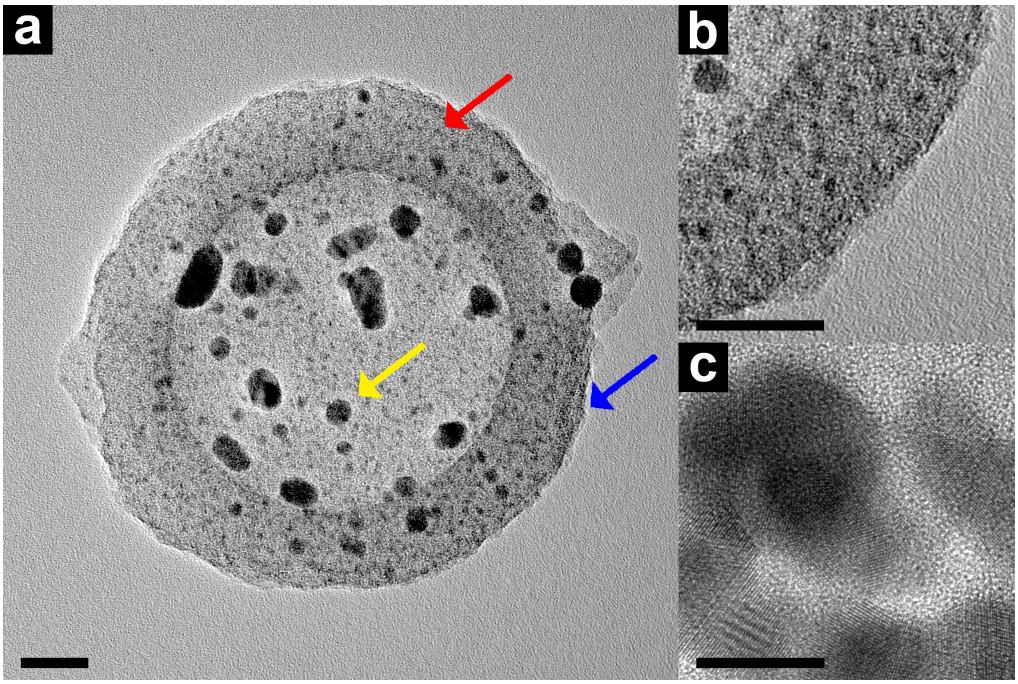


Figure 3.9: The Quantum Rattle system. Bright field high resolution transmission electron micrographs (HRTEM) of thin Quantum Rattles (QRs). HRTEM images of (a) a QR showing AuQDs (red arrow) within the mesoporous silica shell (blue arrow) of the QR and AuNPs (yellow arrow) within the cavity and (b) close-up on a QR silica shell. Scale bars: 20 nm. (c) Zoom in on the AuNPs inside the QR cavity showing the different crystal faces of the larger AuNPs. Scale bar: 5 nm.

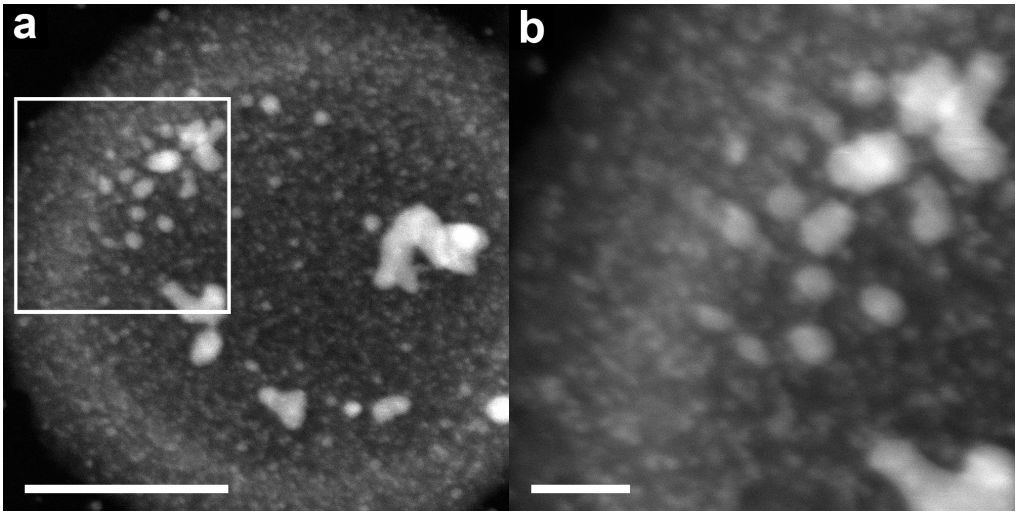


Figure 3.10: The Quantum Rattle system. High angle annular dark field scanning transmission electron micrographs (HAADF-STEM) of thin Quantum Rattles (QRs). (a) HAADF-STEM images of a QR highlighting the gold nanostructures of the QR: AuQDs within the QR mesoporous silica shell and AuNPs within the cavity. Scale bar: 50 nm. (b) Close-up on the QRs mesoporous silica shell. Scale bar: 10 nm.

AuNPs were then employed as a control to assess both the importance of the silica as a template for AuQD formation and the influence of hollow silica shells on the polydispersity of the AuNPs inside the cavity. The pores of the silica shells appear to be crucial in the formation of the AuQDs, anchoring the gold salt to promote nucleation sites and, at the same time, spatially restraining the growth of the gold structures by their inherent size. Finally, the particles synthesised within the QRs cavities (Figure 3.9) are clearly less spherical and more polydisperse than the OT protected AuNPs formed in the absence of HSs (Figure 3.11). This can be explained by the diffusion barrier imposed by the silica shells on the reducing agent. Furthermore, it was found that the silica shell does not allow homogeneous stirring inside the cavity. Therefore, the nucleation inside the cavity is expected to be less homogeneous resulting in polydisperse and less spherical gold particles than the particles obtained in the absence of HS.

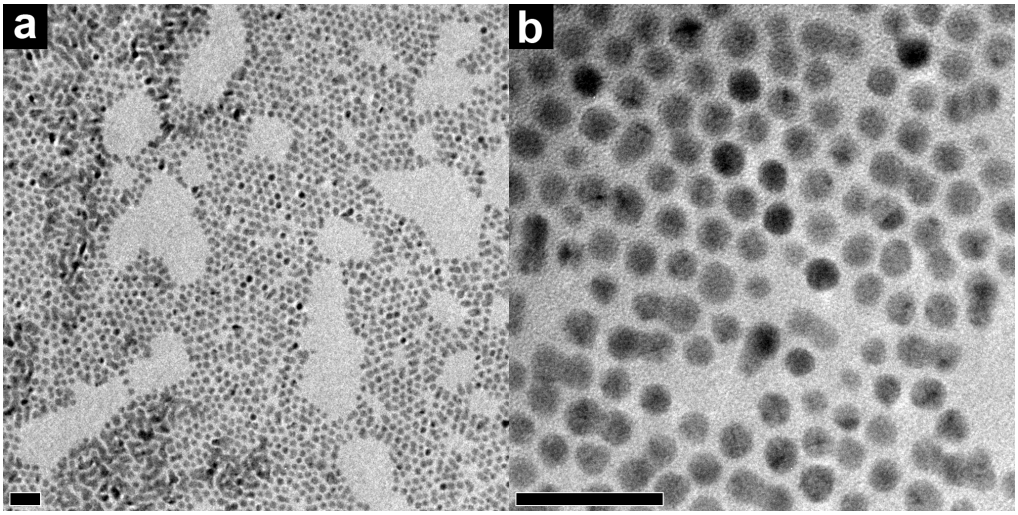


Figure 3.11: Monolayer protected gold nanoparticles. (a-b) Bright field transmission electron micrographs of 1-octanethiol protected gold nanoparticles (OT AuNPs) synthesised using QR process in the absence of hollow mesoporous silica shells at different magnifications. The OT AuNPs are highly monodisperse 8 nm particles with a hexagonal packing on the TEM copper grid. No AuQDs are visible. Scale bars: 20 nm.

3.3.3 Quantum Rattle Photonic Properties

The QRs were designed to be photonically active in the NIR to exploit the biological window (*c.f.* Chapter 1 section 1.3.1) and mediate light-induced therapeutic processes. The QRs show distinct extinction peaks at 411 nm and 672 nm, which can be attributed to the stable AuQDs trapped within the silica shell's mesopores. Such peaks are absent from the HS or the AuNPs synthesised using the same protocol in the absence of HS (free AuNPs) (Figure 3.12). Compared to free AuNPs, where the plasmon peak hardly goes above 600 nm for gold particles > 100 nm[54], the AuQDs place the quantum plasmon peak of the QRs[1] in the NIR (672 nm), thereby enabling their effective use for PTT. Other research groups have studied the optical absorption spectrum of AuQDs by performing density functional theory (DFT) calculations.[2, 215] The calculated spectrum of stable AuQDs consisting of 25 atoms ($Au_{25}(SR)_{18}$) show similar extinction spectra to that of the QRs while larger AuQDs do not.[2, 52, 215] Zhu *et al.*[2] stated that the 670 nm peak corresponds to the LUMO $\leftarrow$ HOMO transition, which is essentially an intraband (sp $\leftarrow$ sp) transition. The 411 nm peak is harder to assign as the DFT calculations report peaks at 400 nm and 450 nm. Although there is a shoulder around 450 nm in the extinction spectrum of the QRs, the only distinct peak appears at 411 nm. The lack of peaks could be the result of the interference from the plasmon resonance of the larger AuNPs inside the QRs silica shells which probably red shifts the 400 nm and attenuates the 450 nm peaks. On the other hand, another study on 11 atoms AuQDs ($Au_{11}C_{12}$)[79] shows identical extinction spectra which seems to imply that the QRs could also be populated by 11 atoms AuQDs.

The extinction peak at 672 nm excites a photoluminescent emission peak at 827 nm, which also sits in the bio-window (650 nm - 900 nm) and is suitable for live imaging applications (Figure 3.13). The photoluminescent

[1]The results presented in this section are obtained using thin QR samples. The thick QR samples present identical photonic properties and the results are presented in the Appendices (Figure A.1).

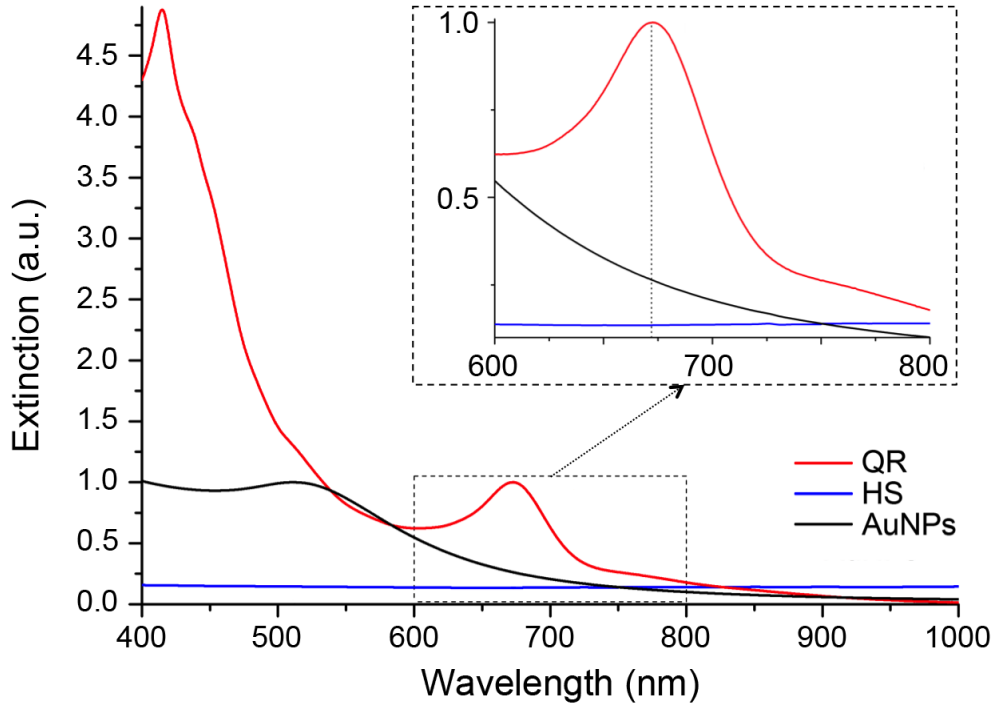


Figure 3.12: Extinction spectra of thin Quantum Rattles (QR, red) compared to hollow mesoporous silica shells without gold (HS, blue) and spherical gold nanoparticles synthesised using the same method as the QR but in the absence of hollow silica shells (AuNPs, black). Inset: zoomed in on the near infrared region of interest, showing an extinction peak centred around 672 nm.

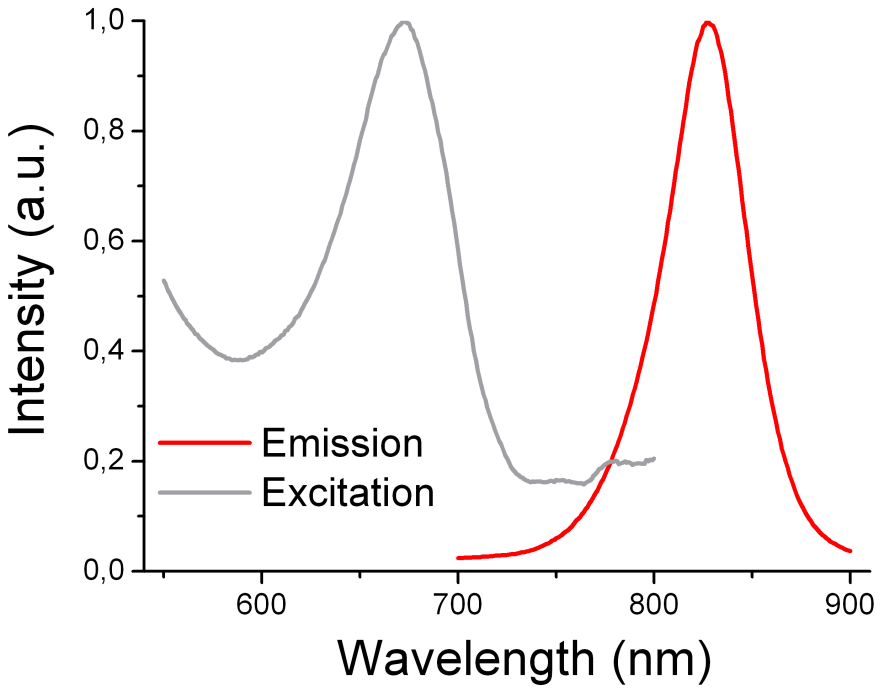


Figure 3.13: Photoluminescence spectra of thin Quantum Rattles showing an excitation peak centred at 672 nm and an emission peak centred at 827 nm. Emission spectrum (λ_{ex} = 672 nm, red) and excitation spectrum (λ_{em} = 827 nm, grey).

spectra of HS and AuNPs when synthesised using the same protocol and in the absence of HS (free AuNPs), were also acquired in the same NIR region of interest. Neither of the controls exhibited any peaks at 411 nm or 672 nm, demonstrating that the QR emergent photoluminescent properties arise from the QR synthetic process, supporting AuQD formation in the mesopores of the silica shell. (Figure 3.14).

The QRs have a quantum yield of 2.10^{-4} (calculated using equation 3.6), which is comparable to the quantum yield of other free gold QDs reported in the literature.[71] The attainment of a similar quantum efficiency to that of the best performing AuQDs reported in contemporary studies,[71] can be attributed to the high density of AuQDs per QR ($> 6.10^4$)

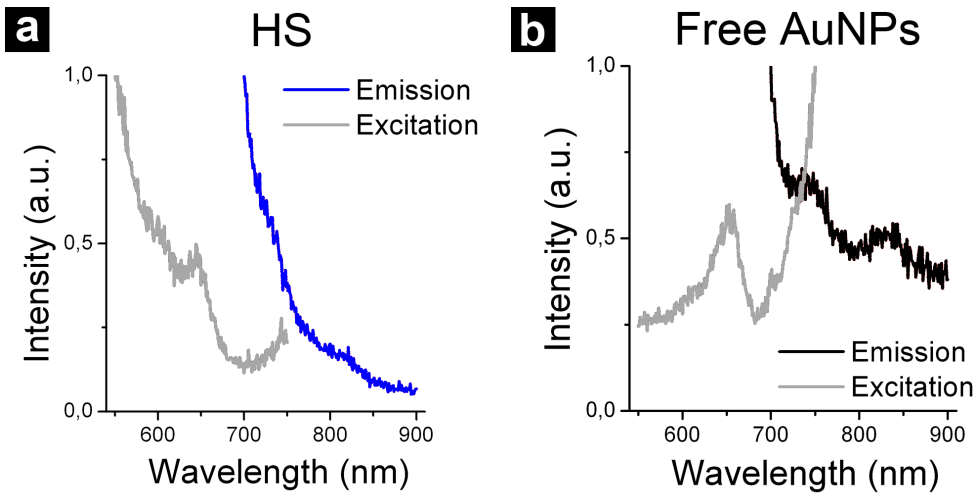


Figure 3.14: Photoluminescence spectra of (a) hollow mesoporous silica particles (HS) and (b) spherical gold nanoparticles synthesised using the same method as the QR but in the absence of hollow silica shells (Free AuNPs). Both controls do not exhibit the characteristic photoluminescent peaks of the Quantum Rattles. Emission spectra (λ_{ex} = 672 nm) and excitation spectra (λ_{em} = 827 nm).

and the highly controlled organisation inside the mesopores of the QRs silica shells. Importantly, other reported AuQDs systems with comparable performance,[67, 71, 216] are not natively water soluble, which makes the water soluble QRs a highly attractive NIR dye for bio-applications. In addition to the high photostability of AuQDs,[75] the large stokes shift of the QRs also provides a lower background signal with more flexible excitation options, resulting in an improved signal-to-noise ratio over standard NIR fluorophores.[133]

To further clarify the photonic role of the AuQDs trapped within the mesopores, non-hollow QRs (NQRs) were synthesised in order to obtain particles with only AuQDs (*i.e.* without AuNPs), which allowed the roles of the AuQDs and AuNPs to be deconvolved. The NQRs were synthesised using the same strategy as the one used for QRs, except that the HSs were replaced by non-hollow mesoporous silica particles with the same pore size and dimensions as the HSs. HRTEM confirmed the presence of AuQDs

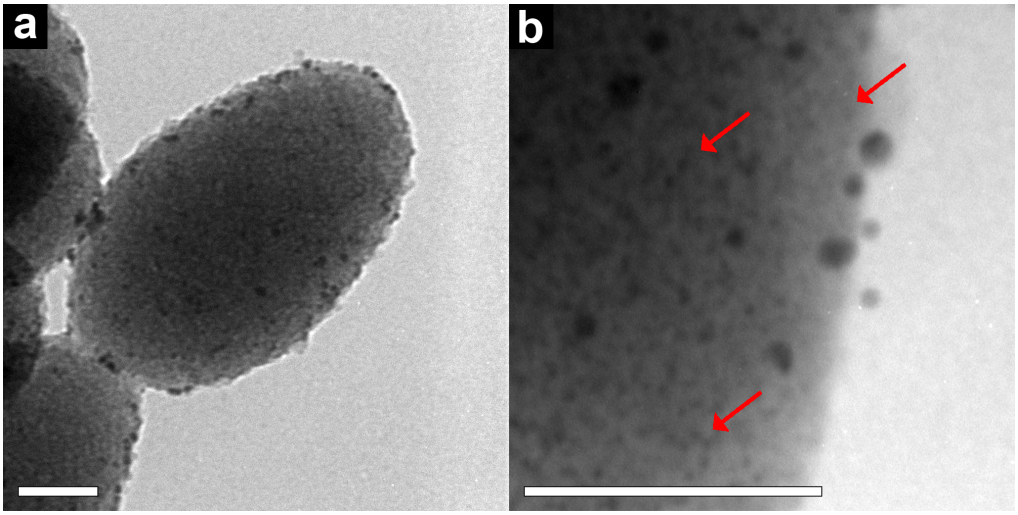


Figure 3.15: Morphology of non-hollow Quantum Rattles. (a) Bright field transmission electron micrograph of a non-hollow Quantum Rattle (NQR) and (b) zoom in showing gold quantum dots (AuQDs, red arrows) within the mesoporous silica shell of the NQR. Scale bars: 50 nm.

within the mesopores of NQRs (Figure 3.15). Furthermore, the NQRs present the same extinction peaks at 411 nm and 673 nm and fluorescent emission at 826 nm as the QRs (Figure 3.16). This supports the attribution of the photonic properties of the QRs to AuQDs trapped within their silica shell. This data is confirmed by several other studies where AuQDs of less than 25 atoms, capped with alkanethiol ligands, possess similar photonics to the QRs.[52,67,71,79] From the photonic properties and HRTEM we can infer that the QRs host a population of AuQDs of less than 25 atoms.

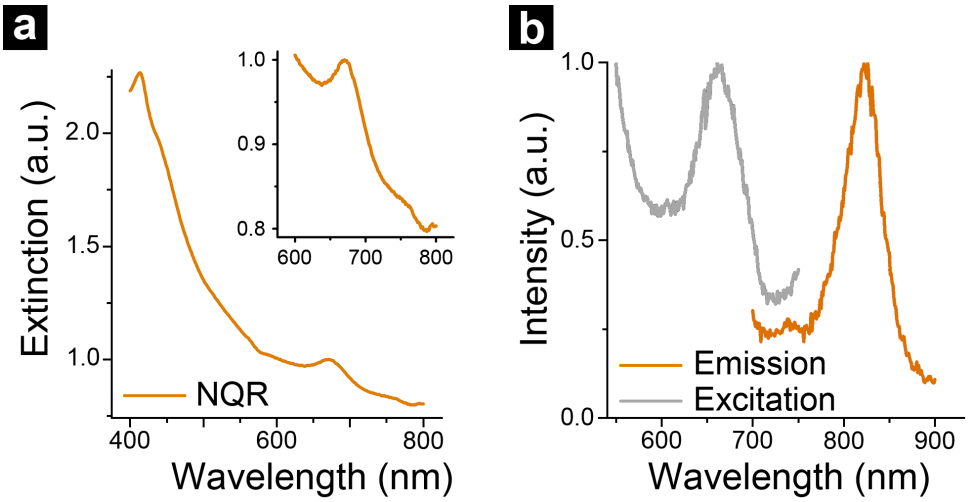


Figure 3.16: Photonic properties of non-hollow Quantum Rattle: (a) Extinction spectra of non-hollow Quantum Rattles (NQRs, orange) showing the same characteristic features as the Quantum Rattles (QRs) extinction spectra. Inset: zoomed onto the near infrared region of interest showing an extinction peak centred around 673 nm. (b) Photoluminescence spectra of NQRs showing an excitation peak centred at 673 nm and an emission peak centred at 826 nm. Both emission spectrum (λ_{ex} = 673 nm, orange) and excitation spectrum (λ_{em} = 826 nm, grey) are similar to the QRs photoluminescent spectra.

3.4 Conclusions

To conclude, two types of Quantum Rattles (QRs) were successfully synthesised using a ship-in-bottle approach. Starting from a hollow mesoporous silica particle (HSs), gold (I) salt was infiltrated inside the HSs cavities before the gold reduction was initiated. The nucleation of gold was achieved both in the cavity and in the mesopores of the silica shell, which, by imposing a spatial constraint on the gold formation, resulted in the formation of two distinct populations: 5 nm - 10 nm diameter AuNPs inside the cavity and $<$ 2 nm AuQDs inside the mesopores of the QRs silica shell.

Each component of the QR system works synergistically to create emergent properties ideally suited for cancer treatment:

- The AuQDs absorb and emit light in the NIR bio-window where blood and soft tissue are relatively transparent (650 – 900 nm).[6, 23, 28, 115, 129] With their NIR photonics, the AuQDs mediate PTT (*c.f.* Chapter 5) as well as live infrared imaging *in vitro* (*c.f.* Chapter 4);
- The hydrophobic AuNPs can optimise the drug carrying performance of the system by increasing the loading efficiency of the payload within the QR particle as well as controlling its release profile (*c.f.* Chapter 6);
- The hydrophilic mesoporous silica shell of the QR not only stabilises the gold nanostructures, making them dispersible in aqueous solutions, but also acts as a protecting barrier between the system's payload and the external environment. Furthermore, the QRs silica shell dimensions are in the range suitable to exploit the EPR effect (60 - 400 nm) allowing passive targeting through the tumour-associated leaky vasculature.[25, 113, 114] Finally, the HS structure is fully biodegradable into harmless intermediates and end products[217], which are highly abundant in the body, while the AuQDs small size allows for rapid renal clearance.[218]

Compared to other methods used to obtain rattle-type particles [3, 5, 21, 23, 82, 91, 97–99], the QRs synthesis is simple and natively 'bio-friendly'. Fur-

thermore, the morphology and composition of the QRs is more controlled than other rattle-type particles where monodispersity, shell integrity, mesostructure and gold core functionalisation are subject to design compromises. Finally, the QR is the first system to include AuQDs in a mesoporous shell structure.

Chapter 4

Quantum Rattle Interactions with Cells

4.1 Introduction

Early identification and localisation of cancerous tumours is critical to improve the success of cancer therapy and patient survival rates.[115, 116] In the past few years, fluorescence imaging approaches have emerged as promising non-invasive, real-time modalities for cancer detection.[115, 119, 120] Compared to other imaging technologies, such as magnetic resonance imaging, x-ray, positron emission tomography (PET), and ultrasound,[121–124] fluorescence imaging is highly suitable for cancer diagnosis due to its high sensitivity, multiplex detection abilities and low equipment cost.[75, 120]

In vivo fluorescence imaging is based on the detection of photon emissions from within living tissues, generated by fluorescent probes which emit light at a predetermined wavelength in response to excitation by light of a different wavelength. Most of the *in vivo* fluorescence imaging systems were first developed for imaging in the visible region of the spectrum.[119] Although, most *in vivo* fluorescence imaging systems were first developed for imaging in the visible region of the spectrum,[119] more and more studies now concentrate on the use of near-infrared (NIR) imaging systems. The advantage of NIR imaging is that biological tissues show very

low absorption and autofluorescence in the NIR bio-window (650 nm - 900 nm).[6, 23, 28, 115, 129] The most conventional NIR probes for fluorescent imaging are organic fluorophores, the most common being polymethines (*e.g.* indocyanine green).[116, 119, 133] However, these organic fluorescent compounds suffer from several limitations, including low water solubility and low chemical- and photostability.[115] Furthermore, the detection sensitivity is relatively low because only a limited number of fluorophores can be conjugated per tumour targeting ligand.[115, 133] Additionally, conventional fluorophores undergo rapid photobleaching, which is not a feature suitable for long-term molecular imaging.[115, 133, 134] Finally, the cytotoxicity of many fluorophores is still currently unknown.[75]

Recently, the emergence of nanomedicine has led to the development of nanoparticle (NP) probes for *in vivo* cancer imaging. By exploiting the enhanced permeability and retention (EPR) effect (passive targeting) or the specific binding between the tumour cell receptors and biofunctionalised NP (active targeting), these probes can be made to accumulate at tumour sites. Both passive and active targeting of tumours by NP-based probes offer the promise of detecting cancers at an earlier stage of development compared to more conventional organic fluorophores dyes.[115] NIR semiconductor quantum dots (QDs) have gained increasing interest for *in vivo* imaging and are, currently, the fastest growing imaging agents due to their high quantum yield and photostability.[75] Although QDs have been used in small animal models of human cancer,[219,220] their inherent toxicity is still a main issue, which will have to be efficiently tackled before any successful translation into clinical use.[138]

On the other hand, noble metal quantum dots (*e.g.* AuQDs, AgQDs) are highly attractive for biomedical purposes due to their low toxicity as well as their photonic and magnetic properties.[12, 140, 141] Noble metal QDs of less than 10 nm exhibit emerging properties derived from the quantum nature of their valence electrons,[49] such as NIR photoluminescence[75, 142] and paramagnetism,[12, 52, 80] yet they are rarely used in cancer imaging applications. Such lack of interest is often due to the

AuQDs unfavourable biointeraction (*e.g.* poor dispersibility), with the result that protein carriers are usually necessary to modulate their interaction in biological systems.[75, 142] The Quantum Rattle (QR) system in this thesis, however, is designed to have the AuQDs trapped within a silica shell, allowing the AuQDs to maintain their photonic properties in aqueous environment without any protein carrier.

The aim of this chapter is to demonstrate the QR suitability for bioapplications and, in particular, for fluorescence live imaging. The QRs are designed for photothermal therapy (PTT) and, therefore, to selectively kill cancer cells when subjected to NIR irradiation. However, until the QRs are triggered to kill cancerous cells, the particles should be biocompatible and accumulate at tumour sites for *in vivo* cancer imaging detection. The first part of the chapter focuses on investigating the *in vitro* cytotoxicity of the QRs. Cervical cancer cells (HeLa) were incubated with cell culture media containing QRs, either with or without a fluorescent dye conjugated to the silica shells, to evaluate the effect of QRs and their functionalisation on cell viability and proliferation. The second part of the chapter investigates the internalisation process of the QRs into cells, thereby, evaluating the fate of QRs *in vitro* and demonstrating the potential of the QRs for NIR live imaging of tumour sites *in vivo*. To this end, the QR cellular internalisation was characterised using multiple techniques, including mapping Raman spectroscopy, transmission electron microscopy (TEM) and laser confocal scanning microscopy.

4.2 Materials and Methods

The ultrathin sectioning was performed by Dr. Ciro Chiappini. The transmission electron microscopy images and the confocal images were acquired with the help of Dr. Ciro Chiappini. The Raman spectra acquisition and analysis were performed by Dr. Martin Hedegaard.

Materials: Paraformaldehyde (PFA), glutaraldehyde, cacodylate buffer, 3-[4,5-dimethylthiazol-2-yl]-2,5-diphenyltetrazolium bromide (MTT), ethyle-

nediaminetetraacetic acid (EDTA), cystein-HCl, papain from papaya latex (P3125) , osmium tetroxide, NHS-fluorescein, (3-Aminopropyl)triethoxysilane (APTES), potassium ferrocyanide, Epon 812 and Araldite were purchased from Sigma-Aldrich, UK. Solvents such as absolute ethanol, acetone and dimethyl sulfoxide (DMSO) were purchased from VWR, UK. Quant-iT PicoGreen dsDNA assay kit (tDNA assay), Dulbecco's modified eagle medium (DMEM), foetal bovine serum (FBS), Antibiotic-Antimycotic (A/A), AlexaFluor 568 (AF568) phalloidin, AlexaFluor 488 (AF488) phalloidin, 4',6-diamidino-2- phenylindole (DAPI), trypsin-EDTA, phosphate buffer (PBS, pH 7.4), were purchased from Invitrogen, UK. Magnesium fluoride (MgF_2) coverslips were purchased from Global Optics, UK. Carbon coated copper TEM grids (300 mesh) were purchased from Agar Scientific, UK.

4.2.1 Quantum Rattles Cytotoxicity

Cell Culture

The human cervical cancer HeLa cells used in this study were obtained from European Collection of Cell Cultures (ECACC, UK). This immortal cell line is the oldest and most commonly used cancer cell line.[221] The cells were maintained in an incubator at a temperature of 37 °C, regulated with 5% CO2, 95% air, and a saturated humidity. DMEM medium supplemented with 10% (v/v) FBS and 1% (v/v) A/A was used as the cell culture medium. Cell media was changed every 2-4 days and the cells were passed using trypsin-EDTA upon reaching 80% confluency.

Particle Sterilisation

Prior to cell seeding, all the particles were sterilised by ethanol washing steps. Samples were dispersed in 70% ethanol and left for 2 h before being washed twice in ethanol, twice in PBS and twice in medium at 14000 $rpm.min^{-1}$ for 5 min. The samples were then diluted to the appropriate

concentration for the different assays. The samples were all used the same day because, once in saline solution, the silica shells start degrading.[217]

MTT Assay

The influence of QRs and HSs on cell metabolic activity was assayed against cervical HeLa cells using a MTT assay. This colorimetric assay measures the enzymatic reduction of the yellow tetrazolium salt MTT by mitochondria in living cells. Within active mitochondria, dehydrogenases split tetrazolium rings into blue-violet, alcohol-soluble formazans. HeLa cells were cultured as previously described (*c.f.* section 4.2.1) before being seeded in a 48-well plates at a density of 2.10^4 cells.cm^{-2} and incubated in 5% CO_2 at 37 °C for 1 day. Cell culture media was replaced with media containing particles at concentrations ranging from 10^8 particle.mL^{-1} to 10^{11} particle.mL^{-1}. The cells were then incubated in the same conditions for another 1 day or 3 days. At the end of the incubation, the media containing the particles was removed, and 300 µL of MTT salt solution (diluted in a culture media without red-phenol and with a final concentration of 0.5 mg.mL^{-1}) was added and incubated for another 2 h. The media was replaced with 300 µL of DMSO per well, and the absorbance was monitored using a microplate reader (SpectraMax M5) at the wavelength of 570 nm with a reference wavelength at 650 nm. Formazan solution absorbs light at 550 nm to 570 nm, and the amount of absorbance is directly proportional to the number of viable cells and their metabolic activity.[222] The cytotoxicity was expressed as the percentage of cell viability compared to each time points respective untreated cell controls. The experiment was run in triplicate and the results are presented as percentage averages ± standard deviation. Statistical significance is determined using MatLab (Appendix A.4.1) and is assessed for each time point assayed.

The negative and positive controls were medical grade PVC and organo-tin PVC respectively, which were used in ISO 10993-5 cytotoxicity tests.[223] Both plastic materials were left in 70% ethanol for 2 h and thoroughly washed in PBS and media. Media (0.2 mL.cm^{-2}of plastic control material)

was added to dry samples of both control materials and left in the incubator for 1 day. The media obtained was then used in the same way as the particle containing sample media.

Total DNA Assay

The influence of QRs and HSs on cell proliferation was assayed against cervical HeLa cells using a tDNA assay. This quantitative fluorescent assay is based on an ultrasensitive fluorescent nucleic acid stain which binds to double-stranded DNA. HeLa cells were cultured as previously described (*c.f.* section 4.2.1) before being seeded in a 48-well plates at a density of 2.10^4 cells.cm^{-2} and incubated in 5% CO_2 at 37 °C for 1 day. Cell culture media was replaced with media containing particles at a concentration of 10^{11} particle.mL^{-1}. The cells were then incubated in the same conditions for another 1 day or 3 days. At the end of the incubation, DNA was extracted from the cells lysed by incubating them in papain digest (5 mM Cystein-HCl, 5 mM EDTA, 1 - 2 units.mL^{-1} of papain in PBS) for 2 h in 5% CO_2 at 60 °C. A 20 fold dilution of the TE buffer (10 nM Tris-HCl, 1 mM EDTA) from the tDNA assay kit was prepared to make the working solution of PicoGreen reagent (200 fold dilution in TE). The working reagent was added to the lysate and allowed to react for 5 min in the dark. The fluorescence emission was monitored at 535 nm with an excitation wavelength set at 480 nm using a microplate reader (SpectraMax M5). The cytotoxicity was expressed as concentration of double stranded DNA which was calculated subtracting the values obtained for DNA cell-free controls against a DNA standard curve constructed from known DNA concentrations. The DNA samples for the standard curve were obtained by diluting the DNA solution provided in the tDNA kit (100 µg.mL^{-1}bacteriophage lambda DNA) to concentrations varying from 1 µg.mL^{-1}to 1 ng.mL^{-1}, in 1 order of magnitude steps. The negative and positive controls are identical to the controls prepared for the MTT assay (*c.f.* section 4.2.1). The experiment was run in triplicate and the results are presented as percentage averages ± standard deviation. Statistical significance is determined using MatLab (Appendix

A.4.1) and is assessed for each time point assayed.

Statistical Analysis

The statistical analysis was performed using MatLab R2012a (MathWorks). To statistically assess differences in cytotoxicity between the QRs, HSs and controls, a one-way ANOVA and Tukey's honestly significant difference criterion was used in the multiple comparison tests. These differences were then deemed significant if the probability of the results occurring by random chance was less than 5% ($p < 0.05$). The MatLab scripts and the results from the multiple comparison tests are presented in Appendix A.4.1.

4.2.2 Quantum Rattle Silica Shells Functionalisation

The functionalisation potential of the QR silica shells was investigated by functionalising the QR or HS silica shells with a fluorophore. QRs or HSs (1 mg.mL^{-1}) were left to incubate for 2 h in a 2% (v/v) APTES solution in ethanol. The samples were then washed 3 times in MilliQ H_2O by centrifugation at 14000 rpm.min^{-1} for 2 min. Next the particles were left to react with NHS-fluorescein in DMSO (1 mg.mL^{-1}) for 15 min while stirring, before being washed 3 more times in MilliQ H_2O by centrifugation at 14000 rpm.min^{-1}. The particles were then sterilised in the same way as QRs and HSs (*c.f.* section 4.2.1) and always used the same day.

4.2.3 Microscopy

Laser Confocal Scanning Microscopy

*Confocal Microscopy for Particle Internalisation Stud*y: HeLa cells were cultured as previously described (*c.f.* section 4.2.1) in 8-well glass chamber slides (Lab-Tek®). Briefly, the cells were seeded at a density of 2.10^4 cells.cm^{-2} and cultured for 1 day before they were incubated with particles at a concentration of 10^{11} particle.mL^{-1}. After the medium was removed,

the cells were washed 3 times with PBS and fixed with 4% (v/v) paraformaldehyde (PFA) in PBS. The cells F-actin and nuclei were stained respectively with phalloidin, AF488 phalloidin and DAPI using established methods. The cells were first permeabilised using 0.1% (v/v) Triton X in PBS for 5 min. The cell samples were then blocked with 1% (w/v) BSA in PBS for 30 min. The phalloidin and DAPI solutions were added under dark conditions for 30 min and 5 min, respectively. In between each step the samples were washed twice with PBS. The QRs were observed using a multiphoton NIR laser set at 710 nm[1]. The glass slides were visualised under a confocal microscope (Leica SP5 MP/Flim inverted) and the images were analysed with Volocity 6.0 (PerkinElmer) and Amira 3D visualisation software (Mercury Computer Systems). Finally, the 3D confocal internalisation movie was edited using iMovie (Apple).

Confocal Microscopy for QRs Silica Shell Functionalisation Study: HeLa cells were cultured and stained as previously described (*c.f.* section 4.2.3) in 8-well glass chamber slides (Lab-Tek®), with the exceptions that AF568 phalloidin was used to replace AF488 phalloidin to prevent the fluorescein emission (518 nm) from overlapping with the phalloidin and that the fluorescein conjugated QRs and HSs were used (*c.f.* section 4.2.2). The glass slides were visualised under a confocal microscope (Leica SP5 MP/Flim inverted) and the images were analysed with Volocity 6.0 (PerkinElmer).

Transmission Electron Microscopy

Transmission Electron Microscopy for Particle Internalisation Study: HeLa cells were cultured as previously described (*c.f.* section 4.2.1) in 24-well plates. Briefly, the cells were seeded at a density of 2.10^4 cells.cm^{-2} and cultured for 1 day before they were incubated with particles at a concentration of 10^{11} particle.mL^{-1}. After the medium was removed, the cells were

[1]Although the NIR multiphoton laser range is from 690 nm to 1020 nm, 710 nm was chosen because the power attenuation below it was too strong. At 710 nm the effective power of the multiphoton laser was 500 mW compared to $<$ 200 mW at 690 nm.

detached by incubation with 0.25% (v/v) trypsin-EDTA for 5 min. The cell suspension was centrifuged at 1200 rpm.min^{-1} for 5 min. The supernatant was removed and the cells were fixed on ice by 2.5% (v/v) glutaraldehyde, 0.1 M cacodylate buffer in MilliQ water for 30 min. Further fixation with 2% (w/v) osmium tetroxide, 2% (w/v) potassium ferrocyanide in 0.1 M cacodylade buffer also provided heavy metal contrast staining for electron microscopy visualisation of cells. The cells were dehydrated through a graded ethanol series and then washed twice in 100% acetone. The embedding was performed through a graded Epon812/Araldite resin:acetone series (1:2, 2:1, 1:0 v/v), transferred to fresh pure Epon812/Araldite and polymerised at 60 °C for 1 day. Ultrathin sections of approximately 100 nm were cut on a Power Tome XL ultramicrotome (RMC Products, USA) using a 35° diamond knife and transferred to a TEM copper grid. Transmission electron microscopy (TEM) images of more than 30 different cells were acquired using a JEOL 2000 TEM equipped with EDS detector, operated at 120 kV.

Mapping Raman Spectroscopy

Mapping Raman Spectroscopy for Particle Internalisation Study: HeLa cells were cultured as previously described (*c.f.* section 4.2.1) on 1 mm x 1 mm MgF_2 slides. The MgF_2 slides were sterilised by incubating them in 70% ethanol for 2 h before thoroughly washing them with PBS and media. The cells were seeded at a density of 2.10^4 cells.cm^{-2} and cultured for 1 day before they were incubated with particles at a concentration of 10^{11} particle.mL^{-1}. After the medium was removed, the cells were washed 3 times with PBS and fixed with 4% (v/v) paraformaldehyde (PFA) in PBS. The QRs were observed using a Renishaw RM2000 Raman spectrometer connected to a Leica microscope and equipped with a 600l grating. Raman images were collected with 0.8 µm resolution using 60X, NA = 1.0, Nikon objective. Acquisition time for individual spectra were 1 second and collected in the region of 400 cm^{-1} to 3100 cm^{-1}. MatLab R2012a (MathWorks) was used to process the Raman images by implementing in-house written

scripts employing the N-FINDR algorithm with 4 endmembers.[224] Briefly, the N-FINDR algorithm works by finding the most dissimilar spectra from the entire data set of images and defining as endmembers. Each pixel of the mapped sample is then described as a linear combination of the resulting endmember spectra.

4.3 Results and Discussion

4.3.1 Quantum Rattles Cytotoxicity

Although a good indication of the favourable toxicology of QRs can be inferred by the nature of their components, which are either biodegradable (HS), clearable (AuQDs) or highly biocompatible (AuNPs), it is still important to show that their assembly does not impart cytotoxic properties. Therefore, assessing the cytocompatibility of the QRs is key in evaluating the QR suitability for cancer treatment.

Cell Metabolic Activity

The QRs cell metabolic activity *in vitro* was evaluated using a MTT assay over a period of 3 days. This time frame is longer than the time period of a typical photothermal therapeutic intervention *in vivo* using the EPR effect to accumulate the photothermal agent at the tumour site.[113, 146, 225] Based on previous studies demonstrating the use of NPs as photothermal agents in both *in vitro* and *in vivo* environments,[29, 113] HeLa cells were incubated for 1 day with QR and HS concentrations varying from 10^8 particle.mL^{-1} to 10^{11} particle.mL^{-1}. Functionalised particles are more likely to exhibit cytotoxic effects compared to non-functionalised particles because they require additional chemical treatments. Therefore, the metabolic activity of fluorescein-functionalised QRs (fQRs) and HSs (fHSs) was first evaluated for the above mentioned various concentrations. The MTT assays (Figure 4.1) show similar cellular responses to all concentrations of

fQRs, fHSs and the dilution series of the negative, medical grade PVC control, with no statistical differences observed in the dilution series of each group (Appendix Figure A.4). The dilution effect of the positive, organo-tin PVC control on cell metabolic activity is also clearly visible, demonstrating that the HeLa cells response to toxic materials is normal.

After observing that fluorescein-functionalised QRs did not affect cell metabolic activity, the cytotoxic behaviour over time of the as synthesised QRs was examined. HeLa cells were incubated for up to 3 days with either QRs or HSs at a concentration of 10^{11} particle.mL^{-1}. The MTT assays (Figure 4.2) show similar cellular responses to QRs, HSs and the negative, medical grade PVC control, with no significant statistical differences between the groups (Appendix Figure A.5). These assays demonstrate that both QRs and HSs do not interfere with cell metabolism or the cell cycle. Only the positive, organo-tin PVC control shows significant statistical differences from all the other groups, demonstrating that the HeLa cells response to toxic materials is normal. These cell studies demonstrate the suitability of the QRs, employed at a high concentration[146], for PTT treatment as the QRs do not affect cell metabolic activity over the time period of a typical therapeutic intervention *in vivo*.[113, 146, 225]

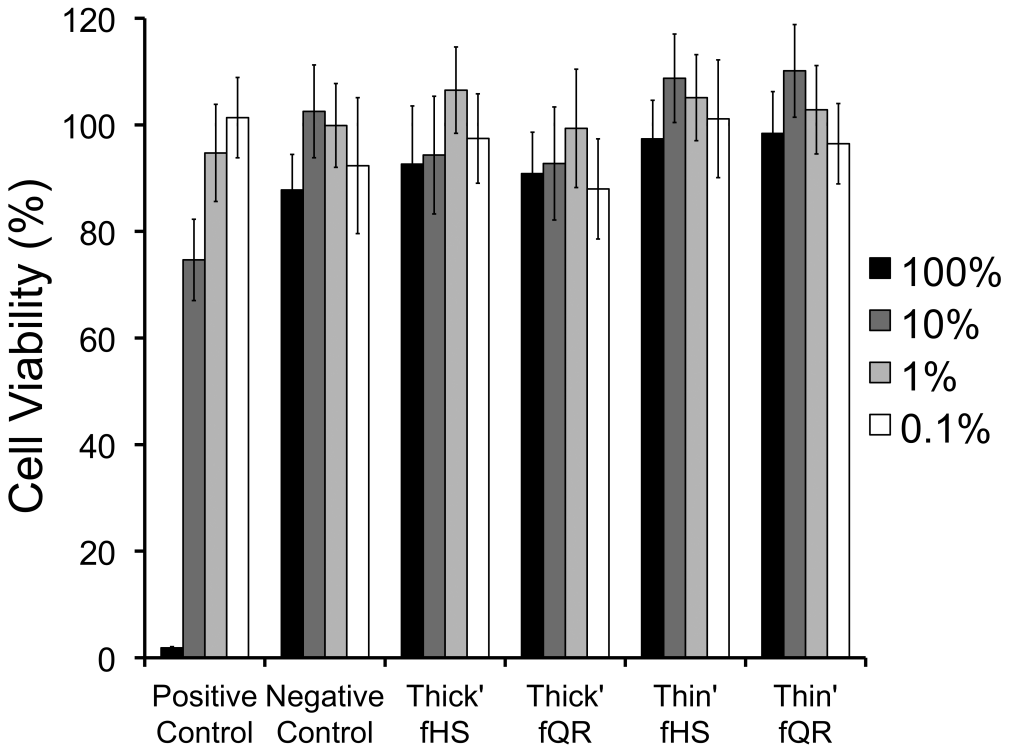


Figure 4.1: Functionalised Quantum Rattles cytocompatibility evaluated by MTT assay. The different concentrations were obtained by 10-fold dilutions of either 10^{11} particle.mL^{-1} dispersions of fluorescently labelled particles or of media pre-soaked in 5 cm^2.mL^{-1} of control material (from 100% to 0.1%). HeLa cells after 1 day incubation in media containing different concentrations (10^8 particle.mL^{-1} to 10^{11} particle.mL^{-1}) of fluorescein functionalised Quantum Rattles (fQR) or fluorescein functionalised hollow mesoporous silica particles (fHS), do not show alterations of metabolic activity compared to medical grade PVC (Negative Control). Organo-tin PVC (Positive Control) shows expected cytotoxic effect on the cell metabolic activity, proportional to the dilution factor of the original organo-tin PVC solution. Results are normalised to blank control (cells culture media without nanoparticles). Error bars represent the standard deviations of triplicate experiments.

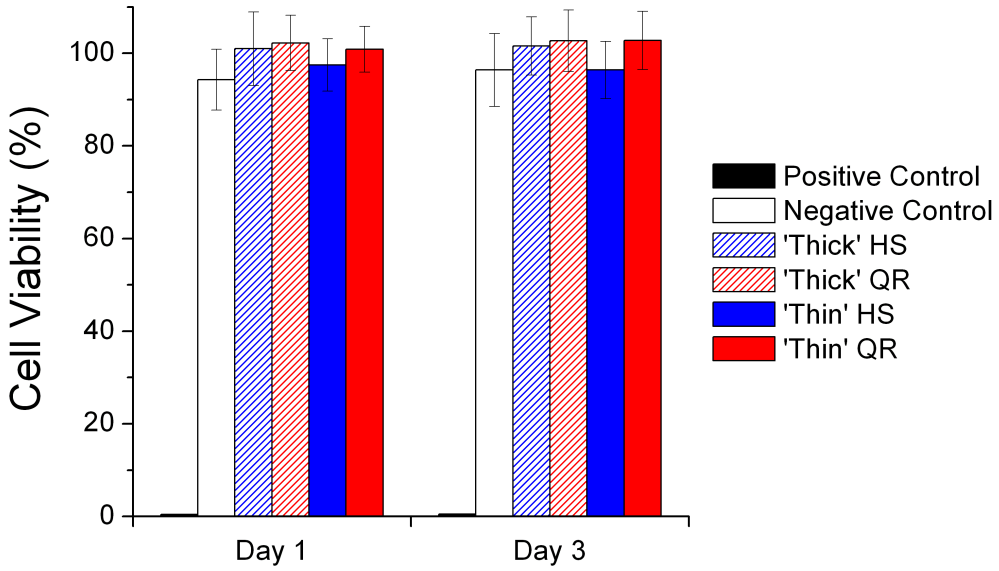


Figure 4.2: Quantum Rattles cytocompatibility evaluated by MTT assay. HeLa cells after 1 day and 3 days incubation in media containing either 10^{11} particle.mL^{-1} Quantum Rattles (QR, red) or hollow mesoporous silica particles (HS, blue) do not show alterations of metabolic activity compared to medical grade PVC (Negative Control, white), whereas no metabolic activity is measured with organo-tin PVC (Positive Control, black). Results are normalised to blank control (cells culture media without nanoparticles). Error bars represent the standard deviations of triplicate experiments.

Cell Proliferation

PicoGreen total DNA assays were performed on QR-incubated HeLa cells, to further evaluate the QRs cell viability and proliferation *in vitro* (Figure 4.3). The same incubation times and particle concentration used in the MTT assays (up to 3 days at 10^{11} particle.mL^{-1}) were employed in the tDNA assay. As with the MTT assay, the tDNA assay shows similar cell responses to QR, HS and the negative, medical grade PVC control. The results show a general increase in double-stranded DNA content, which correlates to the amount of viable cells. Cell proliferation is neither up-regulated nor down-regulated by the presence of QR particles as there is no significant statistical difference observed between cells cultured with QR or with the negative, medical grade PVC control. (Appendix Figure A.6). As expected, cell proliferation is impeded by the positive, organo-tin control, which shows significant statistical differences with all other groups. These cell proliferation results confirm the MTT cell viability results, and prove again the potential of the QR system for PTT.

4.3.2 Quantum Rattles Internalisation

The processes and mechanisms of internalisation, alongside the QRs localisation, are critical to establish the QRs performance for PTT, chemotherapy and imaging. Cell internalisation of the QRs into isolated compartments is necessary for accurate live imaging as it ensures that the QR components are trafficked together for the course of a typical PTT treatment.[113, 146, 225] The QRs cellular internalisation process was investigated by laser confocal scanning microscopy, TEM of ultrathin sections and mapping Raman spectroscopy.

For the confocal microscopy study, HeLa cells were incubated with QRs for 1 day and stained for fluorescence microscopy. The QRs native NIR photoluminescence enabled facile luminescent imaging by means of a multiphoton NIR laser, thereby demonstrating the QRs potential for live imaging (Figure 4.4 and Movie 4.1). The luminescent images and reconstructed 3D

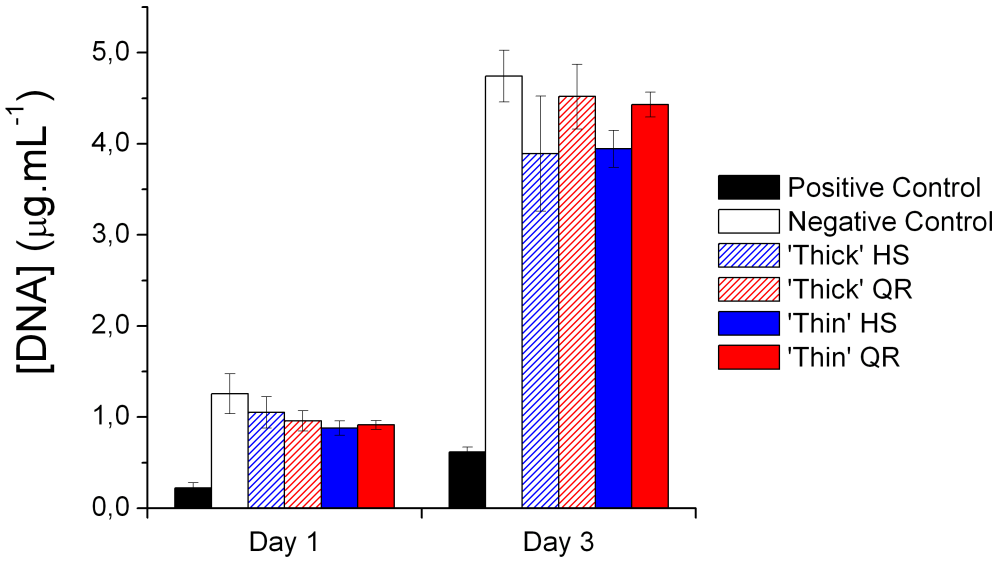
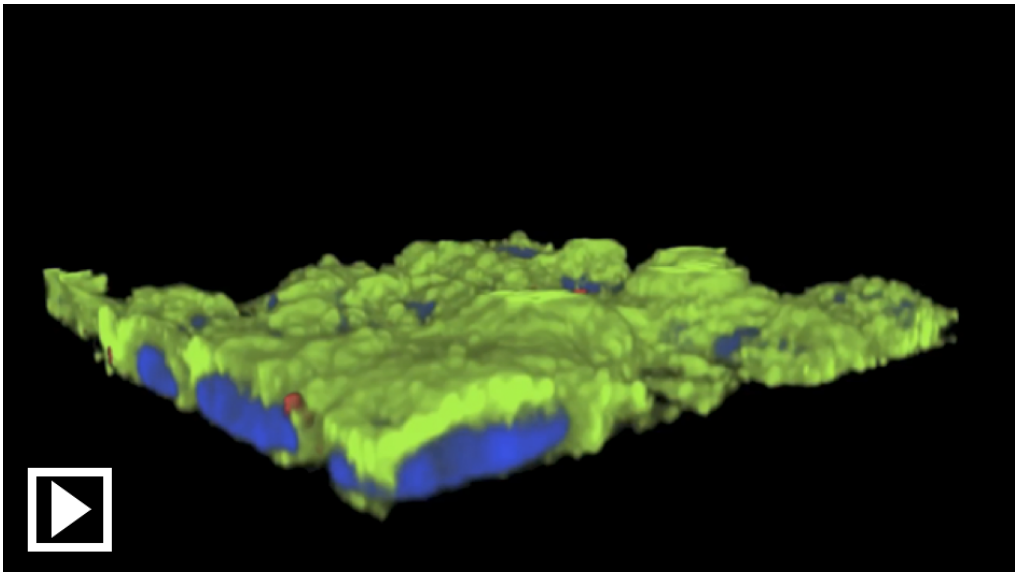


Figure 4.3: Quantum Rattles cytocompatibility evaluated by total DNA assay. HeLa cells after 1 day and 3 days incubation in media containing either 10^{11} particle.mL^{-1} Quantum Rattles (QR, red) or hollow mesoporous silica particles (HS, blue) do not show alterations of cell proliferation compared to medical grade PVC (Negative Control, white). Cell proliferation and viability are significantly affected by organo-tin PVC (Positive Control, black). Error bars represent the standard deviations of triplicate experiments.



Movie 4.1: Quantum Rattle internalisation and near-infrared fluorescence. Three-dimensional reconstruction of laser confocal scanning microscopy images of HeLa cells incubated for 1 day with Quantum Rattles (QR), which are imaged through their native photoluminescence (red). Cells are stained for F-actin (phalloidin AF488, green) and nucleus (DAPI, blue). QRs are localised by their own fluorescence within the cells, accumulating in the perinuclear region. *(Click to play. Requires Adobe Reader 8.× or higher)*

movie show QRs localised within the cells cytoplasm and accumulating in the perinuclear region. This is compatible with endocytotic processes that internalise particles, traffic them through the endolysosomal system to finally accumulate in the perinuclear area. The QRs PTT performance could take advantage of this perinuclear localisation, which sensitises cells to heat shock. Other QRs are localised within actin-rich cups at the cell membrane, a further indication in support of cell-mediated endocytosis processes for internalisation.

Another approach, based on conjugating fluorescent dyes to the QRs and HSs, was used in this study to follow the internalisation process of the QRs. In this way, the potential of QR silane functionalisation could also be investigated. A fluorophore (fluorescein) was conjugated to the silica shells of HSs (fHSs) and QRs (fQRs), and internalised particles were now

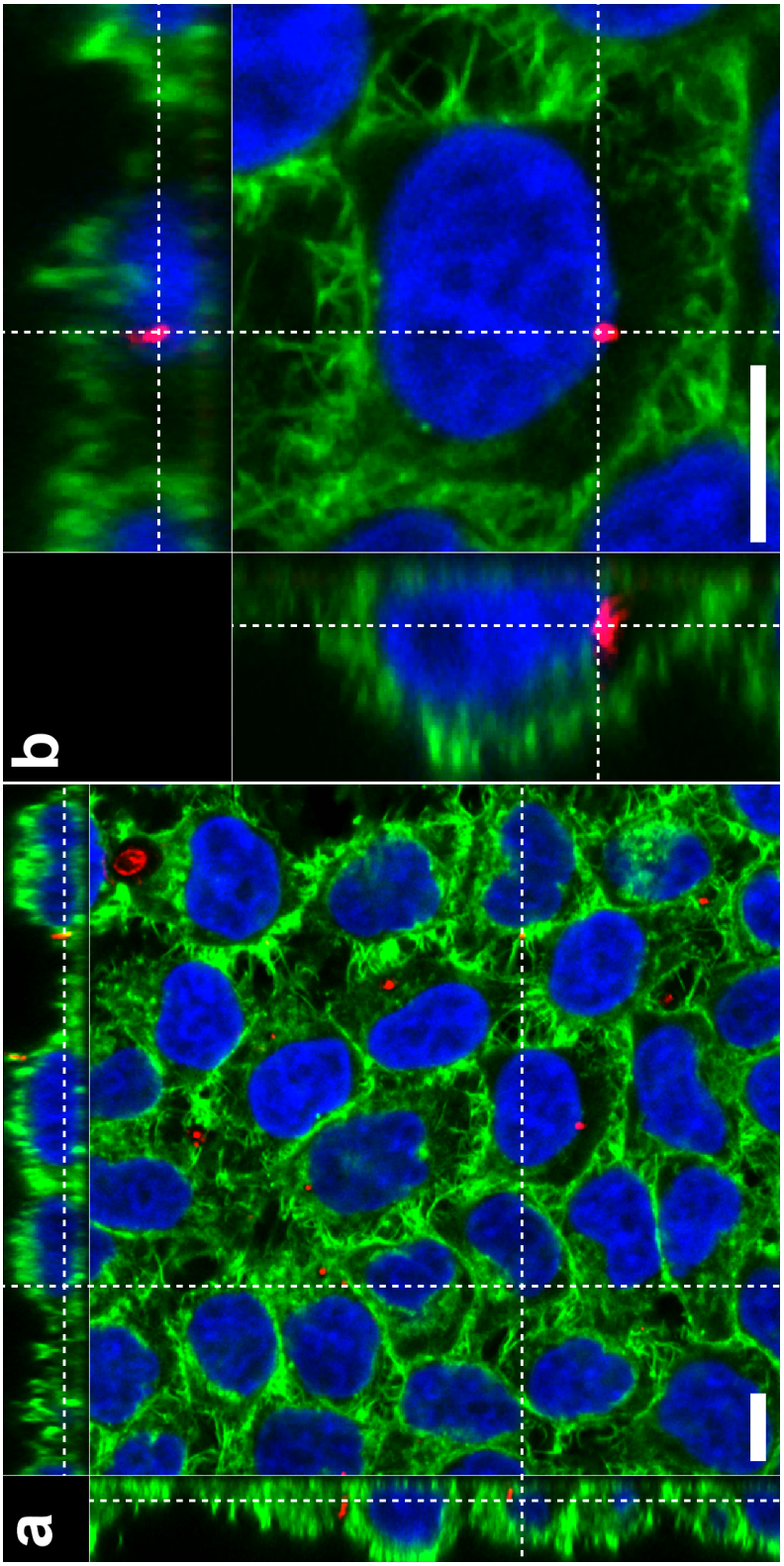


Figure 4.4: Quantum Rattle internalisation and near-infrared fluorescence. (a,b) Laser confocal scanning microscopy images of HeLa cells incubated for 1 day with Quantum Rattles (QR), which are imaged through their native fluorescence (red). Cells are stained for F-actin (phalloidin AF488, green) and nucleus (DAPI, blue). QRs are localised by their own photoluminescence within the cells, accumulating in the perinuclear region. (a) Cell overview and (b) close-up of on one HeLa cell showing a QR aggregate in the perinuclear region. Scale bars: 10 µm.

imaged using the fluorescence of the functionalised dye instead of the native QR photoluminescence. HeLa cells were incubated with dye-conjugated particles for 1 day and stained for fluorescence microscopy. Both fHSs and fQRs are clearly visible using the fluorescence of the fluorophore. This simple, yet effective functionalisation process opens the door to a more advanced QR system, including active targeting ability, improved stability, triggered drug delivery, *etc.*

In addition to the fluorescent confocal microscopy results, TEM of ultrathin sections provided further insight into the localisation and trafficking of the QRs (Figures 4.6 and 4.7). The TEM images show that the QRs are internalised by HeLa cells without affecting the cell structure or cell morphology (Figure 4.6). In some cells, the QRs are localised in large groups within membranous vesicles inside the cytoplasm (Figure 4.7). Furthermore, the QR clusters inside the vesicle clearly show AuNPs surrounded by silica shells (Figure 4.7c). The smaller, darker spots most probably represent the AuQDs. EDS analysis confirmed the presence of both gold and silica inside the vesicles (Figure 4.7d), supporting cellular internalisation of the QRs.

Finally, HeLa cells, incubated with QRs for 1 day at a concentration of 10^{11} particle.mL^{-1}, were also examined using Raman mapping spectroscopy. The Raman results detected the presence of amino acids and DNA molecules of the nuclei, proteins of the cytoplasm, gold and lipids. In particular, the Raman mapping showed that lipids tend to surround gold (as seen in the gold with lipid spectra between 2800 cm^{-1} and 3000 cm^{-1}) within the cell cytoplasm. The intracellular membranes encapsulating the QRs, as observed with TEM, can be attributed to these lipid vesicles.

It has been reported in many studies that the particle size is a key factor in the process of particle internalisation.[226–228] Other research groups showed internalisation of nanoparticles smaller than 200 nm mainly involved clathrin-mediated endocytosis (CME).[229] By means of this CME pathway, NPs are directed in clathrin-coated vesicles of around 120 nm towards lysosomes.[229] The QR-surrounding vesicles observed in the TEM images, however, appeared to have sizes varying from 300 nm to 1 µm, con-

Figure 4.5: Quantum Rattle silica shell functionalisation. Laser confocal scanning microscopy images of HeLa cells incubated for 1 day with (a) fluorescein functionalised hollow mesoporous silica particles (fHSs) or (b) fluorescein functionalised Quantum Rattles (fQR). Cells are stained for F-actin (phalloidin AF569, red) and nucleus (DAPI, blue). Both particles are localised by the fluorophore (fluorescein, green) functionalised on their silica shells demonstrating the silane functionalisation potential of the QRs. Scale bars: 10 µm.

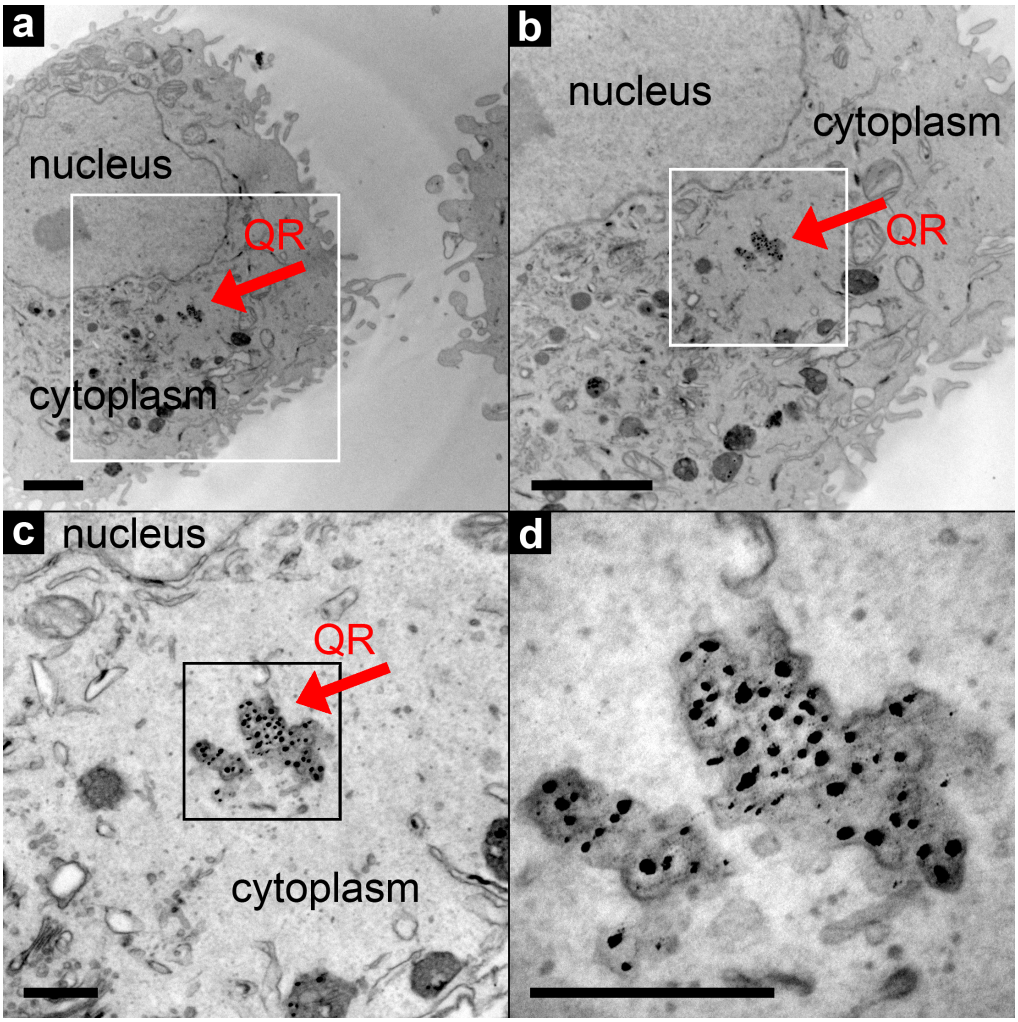


Figure 4.6: Quantum Rattle internalisation. Transmission electron micrographs of ultrathin sections of HeLa cells incubated with Quantum Rattles (QRs) for 1 day, showing the co-internalisation and trafficking of the entire QR structure. (a-b) Cell overview. Red arrows points at internalised QRs. Scale bar: 2 µm. (c-d) Close-ups of the QR cluster. Scale bar: 500 nm.

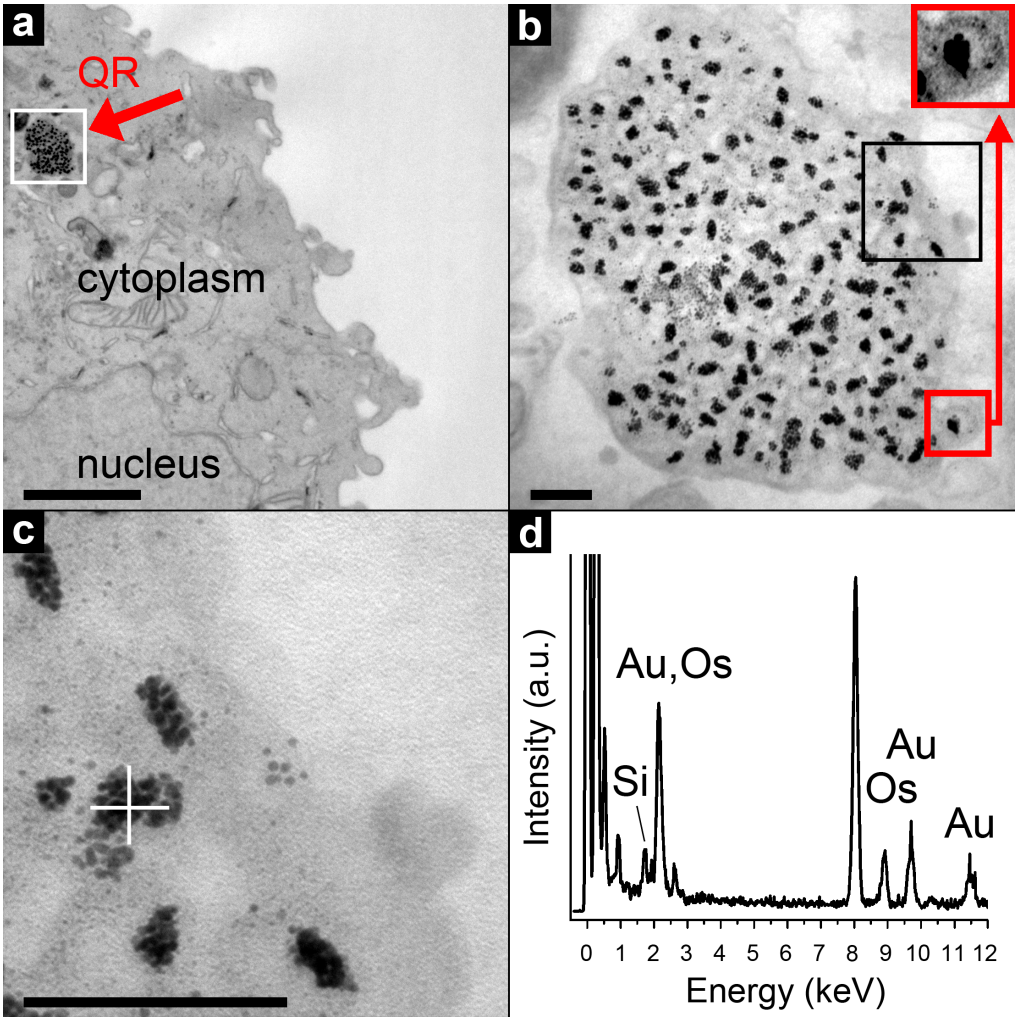


Figure 4.7: Quantum Rattle internalisation (a-c) Transmission electron micrographs of ultrathin sections of HeLa cells incubated with Quantum Rattles (QR) for 1 day showing the co-internalisation and trafficking of the entire QR structure. (a) Cell overview. Red arrow points at internalised QRs being trafficked within a membranous vesicle. Scale bar: 2 µm. (b) Close-up of the QR cluster inside the vesicle. Inset: Zoom in on one QR. Scale bar: 100 nm. (c) Zoom in on several QRs, where energy dispersive x-ray spectroscopy analysis was performed. Scale bar: 100 nm. (d) EDS spectrum of the QR region indicating the presence of silica and gold.

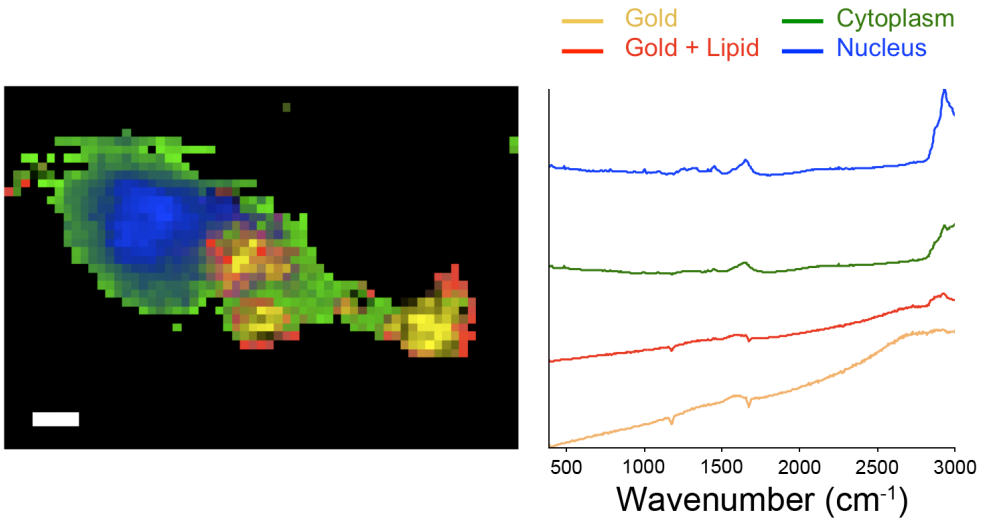


Figure 4.8: Mapping Raman spectroscopy of Quantum Rattles (QR) internalised by HeLa cells. Each pixel represents a Raman spectrum, which were categorised in 4 groups: nuclei (blue), cytoplasm (green), gold (red) and gold with lipids (yellow). Peaks originating from lipid molecules are clearly visible for spectra around the QRs. Scale bar: 8 µm.

taining mostly clusters of QRs. This suggests the QRs are taken up by the cells through a clathrin-independent macropinocytosis mechanism. During macropinocytosis cell-surface protrusions collapse onto the foreign material, in this case the QRs, and fuse with the plasma membrane to generate large endocytotic vesicles (0.5 µm - 10 µm).[227] When the QRs are internalised *via* this non-specific pathway, the vesicles deliver the QRs into other, non-lysosomal compartments.[230] The bypass of the acidic and harmful milieu *via* the macropinocytotic pathway might be a major advantage of the QR system for drug delivery applications.[227, 228]

4.4 Conclusions

The aim of this chapter was to demonstrate the biocompatibility of the QRs as well as their internalisation process. The QRs non-cytotoxic effect is crucial before looking at their PTT potential as the QRs need to selectively

kill cancer cells, but only in a controlled manner once they are triggered by NIR light. The first part of the chapter demonstrated that the QRs, employed at a high concentration,[146] are well tolerated by cells over the few days of a typical therapeutic intervention *in vivo*.[113, 146, 225]

The second part of the chapter focused on the internalisation process of the QRs to investigate both the intracellular fate of the QRs as well as their potential for fluorescent live imaging. The QRs internalisation was verified by three complementary techniques that suggested QR trafficking *via* endocytotic pathways to the perinuclear region. The internalised QRs can be imaged in the NIR through both their native fluorescence and conjugated fluorescent dyes, proving their use for cancer detection. Moreover, the simple functionalisation procedure demonstrated in this study, shows great possibilities for designing a more advanced QR system with improved or added properties.

Chapter 5

Quantum Rattles Mediate Hyperthermia *In Vitro*

5.1 Introduction

Despite years of research and drug development for cancer treatment, cancer still remains one of the leading cause of death worldwide.[22] Traditionally, chemotherapy, radiotherapy and surgical ablation of tumours have been used, in combination, to treat many cancers,[7, 144, 168, 169] however all these methods have limitations.[25,170] Anticancer drug treatments may exhibit limited efficacy while causing high morbidity due to unwanted side effects.[23, 25, 170] At the same time, radiotherapy can be very demanding on a patient's body, causing significant collateral damage to healthy tissue and resulting in additional morbidity.[231, 232] Likewise, surgery is highly invasive, requires long convalescence periods and cannot be undertaken for the treatment of metastatic cancers or tumours that are not easily accessible.[170]

Over the past years, new technologies have attempted to address the limitations of conventional cancer treatments by:

- Identifying specific early biomarkers with a view to developing reliable tools for early cancer detection and to monitor cancer recurrence;

- Developing cost-effective, fast and non-invasive screening techniques for clinical implementation;
- Developing diagnostic tools capable of imaging tumours throughout the entire body;
- Engineering hybrid materials with powerful therapeutic activity, highly specific and selective tumour targeting and significantly lower associated side effects.

In particular, nanotechnology has played a crucial role in the development of new cancer therapeutics.[7, 23–28] Recently, cancer nanomedicine research has focused on systems that can improve diagnostic and therapeutic capabilities, by enhancing efficacy, reducing side effects, targeting and translocating across biological barriers, improving biodistribution and combining therapies.[23, 28, 81, 91, 198] Among the advanced nanomaterials that hold the greatest promise for new cancer treatments, silica and gold nanostructures are of particular interest and stand at the core of simple, yet efficient nanotechnologies.[190, 233] For example, mesoporous silica nanomaterials are effective drug carriers due to their large specific surface area and pore volume, favourable biocompatibility and ease of functionalisation through silane chemistry.[175–177] Likewise, gold nanostructures are promising candidates for cancer treatments, in particular as photothermal therapy (PTT) agents due to their optical absorbance in the visible and near-infrared (NIR).[23, 25, 28, 50, 92, 148]

While Chapter 6 focuses on the drug delivery application of the QRs, this chapter investigates the potential of QR-mediated PTT. Like chemotherapy, PTT is a cancer treatment that relies on selective targeting and the increased sensitivity of cancer cells to cytotoxic damage.[6] However, instead of using drugs to kill cancerous cells, PTT generates heat to destroy the tumour. The direct delivery of localised photoenergy to the tumour, makes PTT a less invasive alternative to conventional cancer therapies.[92] Depending on the temperature increase achieved *in vivo* by PTT, either hyperthermia or thermal ablation occurs.[92] Hyperthermia is defined as the heating of tissues to temperatures between 42 °C and 46 °C,[150] while

thermal ablation is defined as irreversible PTT-induced necrosis.[234] Previous studies demonstrated that, by comparison with healthy tissue, tumours are selectively destroyed when subjected to temperature increases in the range of 42 °C to 46 °C.[6, 148, 149] Such selective destruction of tumour tissue is caused by reduced heat tolerance which, in turn, is mainly due to inferior vascularisation.[6, 148, 149] The rate of heat dissipation by blood flow in tumours is slower than that in normal tissues, and thus the higher temperature in the tumour is sustained longer compared to normal tissue.[235, 236] Furthermore, upon heating, the intratumorous environment becomes even more acidic, hypoxic, and nutritionally deprived.[236] Such a suboptimal environment in the heated tumours potentiates the response of tumour cells to hyperthermia and inhibits the repair of thermal damage.[149, 235, 236]

The strong plasmonic properties of gold nanoparticles (NPs) make them attractive candidates for PTT.[23, 54, 92] In 2003, Hirsch and co-workers were the first to demonstrate the use of gold NPs as a photothermal agent.[29] Compared to traditional photothermal agents, such as light-absorbing dyes, gold NPs exhibit enhanced optical cross-sections (up to 5 orders of magnitude stronger) and higher photostability.[129, 148, 151] In addition, gold NPs have a strong surface plasmon resonance that can easily be tailored by varying the composition, size or shape of the NPs. The gold NP plasmon resonance can either radiate (Mie scattering) or can be converted to heat (absorption).[129] Although spherical gold NPs have been investigated as photothermal agents,[158, 159] they mainly absorb light in the visible region (around 530 nm),[28] which has a shallow penetration depth in tissue compared to the NIR 'bio-window' (650 nm and 900 nm), where blood and soft tissue are relatively transparent.[6, 23, 28, 115, 129] In order to circumvent this major drawback, NPs can be aggregated or clustered to shift the absorbance away from the visible spectrum and towards the NIR.[55, 237]

Other strategies have been developed in order to attain a shift in the gold NP plasmon resonance towards the NIR (Table 5.1). NP systems, consisting of gold nanoshells formed around a dielectric silica core, were shown to

have a resonance span from the visible to the NIR, depending on the silica core dimension and gold shell thickness.[152,153] Likewise, by tailoring the dimensions of hollow gold nanoshells[109, 154, 161, 162] and gold nanocages,[155, 156, 163] absorbance in the NIR can be obtained. Furthermore, gold nanorods can easily be tuned to absorb light in the NIR.[139, 157] Their elongated shape offer a stronger absorption cross-section and they heat faster than gold (-silica) nanoshells or nanocages.[10, 164–167] The gold NP systems, pointed out above and in Table 5.1, with absorbance in the NIR bio-window, are highly promising for PTT. Also, the hollow core of the nanoshells and nanocages can additionally be used as a vector for delivering therapeutic agents.[238] Finally, the advance to clinical trials of some gold-based systems (*e.g.* Nanospectra Bioscience and CytImmune) for PTT and drug/gene delivery further indicates the great potential of gold NPs to improve cancer treatment.[29, 50]

The aim of this chapter is to examine the potential of QR-mediated PTT. By demonstrating the QRs photothermal ability, in addition to the their native photoluminescence (Chapter 3) and use for *in vitro* NIR live imaging (Chapter 3), the QRs would prove to be an advanced, natively multimodal system compared to existing NPs for PTT (the QRs potential for drug delivery will be examined in Chapter 6). To date, the optical properties of AuQDs have never been used for PTT applications (Table 5.1). It is hypothesised that the AuQDs in the silica shells of the QRs, having an extinction peak in the NIR at 672 nm (Chapter 3), will generate heat upon laser irradiation, thereby causing cell death in cancerous tissue. First, the NIR photothermal conversion ability of the QR system is explored on dry surfaces and in solution by measuring temperature changes upon laser irradiation. Next, QR-incubated HeLa cells are subjected to NIR irradiation to investigate the potential of the QR system to induce cell death *in vitro*. Lastly, *ex vivo* characterisation of the PTT potential of the QRs is investigated as a final step towards a future study using an animal model.

Table 5.1: Detailed overview of gold-based platforms for cancer treatment and diagnosis, summarising the advantages and disadvantages of each system compared to the Quantum Rattles.

	Spherical Gold Nanoparticles	Gold Nanoshells (SiO_2 core)	Gold Nanorods	Gold Nanocages	Quantum Rattles
Hyperthermia	✓ Absorb light by SPR, works *in vitro* x Does not work *in vivo*, not in NIR	✓ Light absorption by SPR in the NIR ✓ Tuneable absorption peak	✓ Light absorption by LSPR in the NIR ✓ Tuneable absorption peak x Unstable LSPR peak position & Intensity	✓ Light absorption by SPR in the NIR ✓ Tuneable absorption peak	✓ Light absorption by molecular transition in the NIR from AuQDs x Peak position fixed at 672 nm (c.f. Chapter 7)
Imaging	x No native imaging x Quenching of fluorophores	x No native imaging x Quenching of fluorophores ✓ Incorporation of iron oxide Particles	x No native imaging x Quenching of fluorophores	x No native imaging x Quenching of fluorophores ✓ Incorporation of iron oxide Particles	✓ Native, stable NIR fluorescence ✓ Does not quench fluorophores ✓ Natively paramagnetic (Appendices) ✓ Can incorporate MRI and CT contrast agents (NPs and molecules)
Drug Delivery	x Limited to surface functionalisation x No sustained release	x Limited to surface functionalisation x No sustained release	x Limited to surface functionalisation x No sustained release	✓ Yes but relatively low payloads	✓ High loading of hydrophobic drugs due to hydrophobic core (AuNPs) ✓ Control over sustained release through pore size, length, and silica degradation
Targeting	✓ Passive by EPR if in the right size range ✓ Active by functionalisation of targeting ligand to gold surface	✓ Passive by EPR ✓ Active by functionalisation of targeting ligand to gold surface	✓ Passive by EPR if in the right size range ✓ Active by functionalisation of targeting ligand to gold surface	✓ Passive by EPR ✓ Active by functionalisation of targeting ligand to gold surface	✓ Passive by EPR ✓ Active by functionalisation of targeting ligand to silica surface (c.f. Chapter 7)
Biocompatibility	x Au ligand directly exposed to bioenvironment x Non-biodegradable	x Au ligand directly exposed to bioenvironment x Non-biodegradable x Size does not allow renal clearance	x Au ligand directly exposed to bioenvironment x Non-biodegradable x Size does not allow renal clearance	x Au ligand directly exposed to bioenvironment x Non-biodegradable x Size does not allow renal clearance	✓ Biocompatible silica shields Au ligand from bioenvironment ✓ Silica component is biodegradable ✓ AuQD component is within renal clearance range
Synthesis	✓ Most documented ✓ Simple ✓ Scalable	✓ Simple ✓ Scalable	✓ Scalable x Complex synthesis x Difficult purification x Harsh chemistry (retains cytotoxic molecules)	✓ Scalable x Complex Synthesis x Low reproducibility	+/- Simple but two-steps ✓ Scalable ✓ Simple purification
Other	✓ In clinical trials for drug/gene delivery (Aurimmune)	✓ In clinical trials for PTT (AuroLase)	+/- Anisotropic shape		✓ Orthogonal system: two independent chemistries to exploit, silica and gold
Main references	El-Sayed *et al.* Cancer Lett. (2006) Li *et al. Cancer Lett.* (2009)	Hirsch *et al.* PNAS. (2003) Loo *et al.* Nano Lett. (2005)	Huang *et al.* JACS. (2006) and Adv Mater. (2009)	Melancon *et al.* Mol Cancer Ther. (2008) Chen *et al.* Nano Lett. (2007)	

5.2 Materials and Methods

Mr. Ji Qi from Dr. Daniel Elson's group at Imperial College London helped with the set up and use of the thermal camera employed in the assessment of the QRs photothermal potential experiment and provided us with the 57 mW, 671 nm diode laser (DreamLaser, China). The 300 mW, 671 nm diode laser (DreamLaser, China) was provided by Prof. Søren Hassing at the University of Southern Denmark, Denmark. The high resolution transmission electron microscopy images were acquired with the help of Dr. Sergio Bertazzo.

Materials: Solvents, such as absolute ethanol, were purchased from VWR, UK. LIVE/DEAD® Viability/Cytotoxicity Kit (L-3224), Dulbecco's modified eagle medium (DMEM), trypsin-EDTA, foetal bovine serum (FBS), Antibiotic-Antimycotic (A/A), phosphate buffer (PBS, pH 7.4), were purchased from Invitrogen, UK. The chicken thighs for the *ex vivo* study were purchased from Waitrose, UK.

5.2.1 Photothermal Properties of the Quantum Rattles

Temperature Measurement of Dry Quantum Rattles: To assess the NIR photothermal properties of the QRs on dried surfaces, QR and HS suspensions (2 $mg.mL^{-1}$) were first prepared in ethanol. A drop of the suspensions was then deposited on borosilicate coverslips and left to dry. The process was repeated 3 times. The dry coverslips were mounted in the path of 300 mW and 57 mW, 671 nm diode lasers (38 $W.cm^{-2}$, and 7 $W.cm^{-2}$, respectively) and the temperature data was recorded through a thermal camera. Data were logged for more than 10 min, with 10 sec interval collected prior to the laser being turned on and 1 min interval between 5 min and 4 min acquisition times with the laser turned on. The maximum temperature in a 1.5 mm diameter disk area centred on the laser spot was recorded for each sample. The experiments were repeated three times.

Temperature Measurement of Quantum Rattles in Solution: To assess the NIR photothermal properties of QRs and HSs in solutions, QR and HS suspensions (2 mg.mL^{-1}) were prepared in MilliQ H_2O. A quartz cuvette containing 1 mL of suspension was placed in the path of a 300 mW, 671 nm diode laser (38 W.cm^{-2}), while the temperature profile of the solution was recorded using a mini-hypodermic probe, type T thermocouple (Omega, UK) and a RTD thermometer (Omega, UK). The mini-hypodermic probe was placed at the top of the quartz cuvette with its active extremity in the QR dispersion, whereas the laser was shone upon the QR dispersion at the bottom of the cuvette. This ensured that any heating recorded was not due to the laser/probe interaction. Data was logged until no further increase in temperature was recorded. The experiments were repeated three times.

Laser Irradiation Effect on QRs Morphology: High resolution transmission electron microscopy (HRTEM) was used to determine the morphology of the QRs after NIR irradiation. HRTEM images of the particles were acquired using a FEI TITAN 80/300 STEM/TEM operating at an accelerating voltage of 200 kV. Samples were dissolved in EtOH (1 mg.ml^{-1}) and drop-deposited on TEM grids. The TEM grids were placed under the path of a 30 mW, 671 nm laser (38 W.cm^{-2}) for 15 min prior to analysis.

5.2.2 *In Vitro* Assessment of the Quantum Rattles Photothermal Properties

LIVE/DEAD Assay

The QRs potential to mediate controlled cell death upon NIR light activation was investigated *in vitro* by assaying cell viability against HeLa cells using a LIVE/DEAD assay after NIR irradiation. Cells incubated with either media with no particles or containing HS were used as controls. This two-colour assay determines viability in a cell population based on plasma membrane integrity and esterase activity. Membrane-permeant calcein AM (LIVE stain) is cleaved by esterases in live cells to yield cytoplasmic green fluorescence, and membrane-impermeant ethidium homodimer-1

labels nucleic acids of membrane-compromised cells with red fluorescence. HeLa cells were cultured as previously described (*c.f.* section 4.2.1) in 6-well plates at a density of 2.10^4 cells.cm^{-2} and cultured in 5% CO_2 at 37 °C for 1 day. The QRs and HSs sterilisation was performed identically to the *in vitro* studies performed in chapter 4 (*c.f.* section 4.2.1). Cell culture media was replaced with media containing particles at a concentration of 10^{11} particle.mL^{-1}. The cells were then incubated under the same conditions for another period of 1 day. At the end of the incubation period, samples were irradiated with a 300 mW, 671 nm laser (38 W.cm^{-2}) for 0 min, 2 min, 5 min, 8 min, 10 min and 15 min. The total amount of time outside the incubator for any sample was 15 min. Afterwards, the media containing the particles was removed, and 1 mL of LIVE/DEAD solution (2 µM calcein AM, 2 µM ethidium homodimer-1 in PBS) was added. The samples were incubated for another 45 min at 37 °C before being imaged using a Leica epifluorescent inverted microscope. The 'LIVE' green and 'DEAD' red images were merged using Photoshop CS5 (Adobe) to obtain the LIVE/DEAD images used to quantify cell death. The experiment was performed four times.

LIVE/DEAD Assay Quantification

Image processing and segmentation algorithms were used to quantify the QR-mediated cell death. Masks were applied to the fluorescent microscopy images in Photoshop CS5 (Adobe) to obtain the exact areas of the irradiated cell population (Figure 5.1a) and of the cell population adjacent to the irradiated surface (Figure 5.1b). The masks were the inverse of a 1 mm disk centred on the laser spot (Figure 5.1a) for the irradiated cell population and the inverse of a 0.3 mm thick ring around the laser spot (Figure 5.1b) for the adjacent cell population.

The images of both LIVE and DEAD channels were then segmented using MatLab R2012a (MathWorks) to obtain binary images representing the surface of live and dead cells, respectively (Figure 5.2). The MatLab script used to obtain the binary images is described in the Appendices

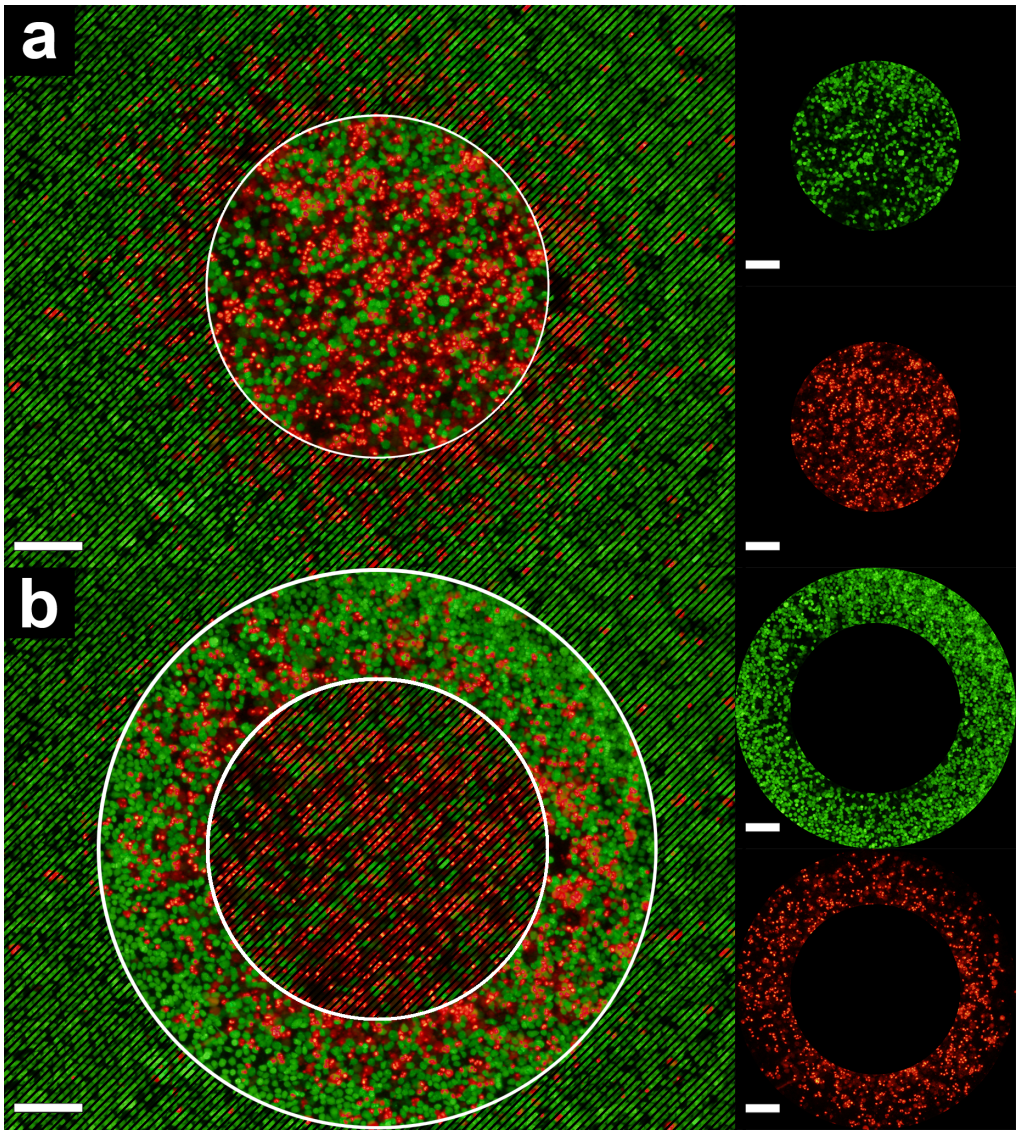


Figure 5.1: LIVE/DEAD assays quantification - irradiated cell population (a-b) Representative merged fluorescent microscopy image series of LIVE/DEAD assays performed on HeLa cells (live cells in green, dead cells in red) incubated with Quantum Rattles for 1 day and irradiated for 8 min with 671 nm laser light (38 $W.cm^{-2}$). The dashed surface represents the mask applied to obtain the cropped image of the LIVE and DEAD channels of (a) the irradiated cell population and (b) the cells adjacent to the laser spot. Scale bars: 200 µm

(script A.9). The percentage cell death was obtained by calculating the sum of the binary image matrices and normalising the DEAD channel value over the total of both LIVE and DEAD channel values.

LIVE/DEAD Assay - Time-Lapse Confocal Microscopy

Time-lapse confocal microscopy was used to follow the real-time cell viability of HeLa cells incubated with QRs. HeLa cells were cultured as previously described (*c.f.* section 5.2.2) in 8-well glass chamber slides (Lab-Tek®). Briefly, the cells were seeded at a density of 2.10^4 cells.cm^{-2} and cultured for 1 day before they were incubated with QRs at a concentration of 10^{11} particle.mL^{-1}. After the medium was removed, the cells were washed 3 times with PBS and 1 mL of LIVE/DEAD solution (2 µM calcein AM, 2 µM ethidium homodimer-1 in PBS) was added. The QR-incubated cells were observed under a confocal microscope (Leica SP5 MP/Flim inverted) equipped with an environmental chamber. The QR-incubated cells were irradiated using a multiphoton NIR laser at 710 nm.[1] LIVE and DEAD channels were defined as the emission window of calcein (494 nm - 517 nm) and DNA-bound ethidium homodimer-1 (528 nm - 617 nm), respectively. Bright-field and LIVE channels were recorded during laser treatments of 2 or 5 min after which the laser treatment was stopped and the DEAD channel was recorded in addition to the LIVE channel for a further 40 min.[2] The movie clips were created using Fiji (National Institutes of Health) and assembled in iMovie (Apple).

[1] Although the NIR multiphoton laser range is from 690 nm to 1100 nm, 710 nm was chosen because the power attenuation below this wavelength was too strong. At 710 nm the effective power of the multiphoton laser was 500 mW compared to $<$ 200 mW at 690 nm.

[2] The DEAD channel could not be recorded at the same time because the laser treatment as the wavelength used to treat the cells (710 nm) and the emission wavelength window of DNA-bound ethidium homodimer-1 were too close, resulting in saturation of the DEAD channel while treating the cells with NIR light.

Figure 5.2: LIVE/DEAD assays quantification - image segmentation. Representative fluorescent microscopy image series of LIVE/DEAD assays performed on HeLa cells (live cells in green, dead cells in red) incubated with either cell media only, hollow silica shells (HS) or Quantum Rattles (QRs) for 1 day and irradiated for either 0, 2, 5, 8, 10 or 15 min with 671 nm laser light (38 $W.cm^{-2}$) showing their corresponding binary image series obtained after applying a segmentation algorithm. The percentage cell death is calculated by calculating the sum of the binary image matrices and normalising the DEAD channel value over the total of both LIVE and DEAD channel values.

5.2.3 *Ex Vivo* Assessment of the Quantum Rattles Photothermal Properties

The QRs photothermal potential in tissue upon NIR irradiation was investigated *ex vivo* using chicken muscles from the thigh (Figure 5.3). QR suspension (2 $mg.mL^{-1}$) was prepared in PBS and approximately 500 µL was subcutaneously injected in the chicken thighs. Chicken tissue injected with PBS (without any QRs) and untreated chicken tissue served as controls. The chicken thighs were placed under the path of a 300 mW, 671 nm diode laser (38 $W.cm^{-2}$) and the tissue temperature profiles were recorded using a mini-hypodermic probe, type T thermocouple (Omega, UK) and a RTD thermometer (Omega, UK). The mini-hypodermic probe was inserted 1 to 3 mm under the skin of the chicken thigh and the temperature profile was recorded before and after NIR irradiation. The experiments were repeated 3 times.

5.3 Results and Discussion

5.3.1 Photothermal Properties of the Quantum Rattles

Dried Quantum Rattles

The NIR extinction peak of the QRs at 672 nm (*c.f.* Chapter 3) could be used for QR-mediated PTT, if the photothermal conversion of the QRs is high enough to induce hyperthermia. The QRs photothermal conversion efficiency of NIR light to heat was investigated using a thermal camera, while using a 671 nm laser (38 $W.cm^{-2}$) to irradiate QRs deposited on a borosilicate glass surface (Figure 5.4). During the first minute of laser irradiation, the QRs induce a rapid temperature increase of approximately 6 °C, whereas the HS control did not record any heat increase. The temperature stabilises after the first minute of laser irradiation and rapidly drops

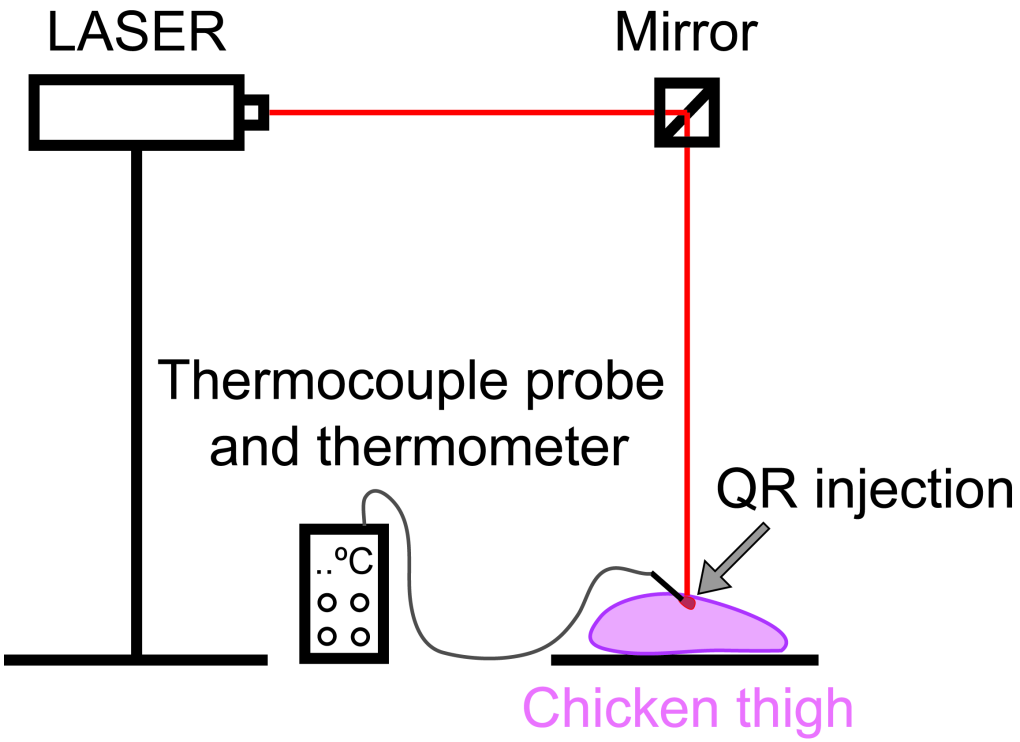


Figure 5.3: Schematic of the experimental set-up used for the *ex vivo* study of Quantum Rattles (QRs) NIR light absorption potential. QRs were subcutaneously injected in chicken thighs, which were subsequently treated with NIR light at 671 nm (38 W.cm^{-2}). Temperature profiles were monitored using a thermocouple probe inserted under the skin of the chicken thigh and recorded with a RTD thermometer.

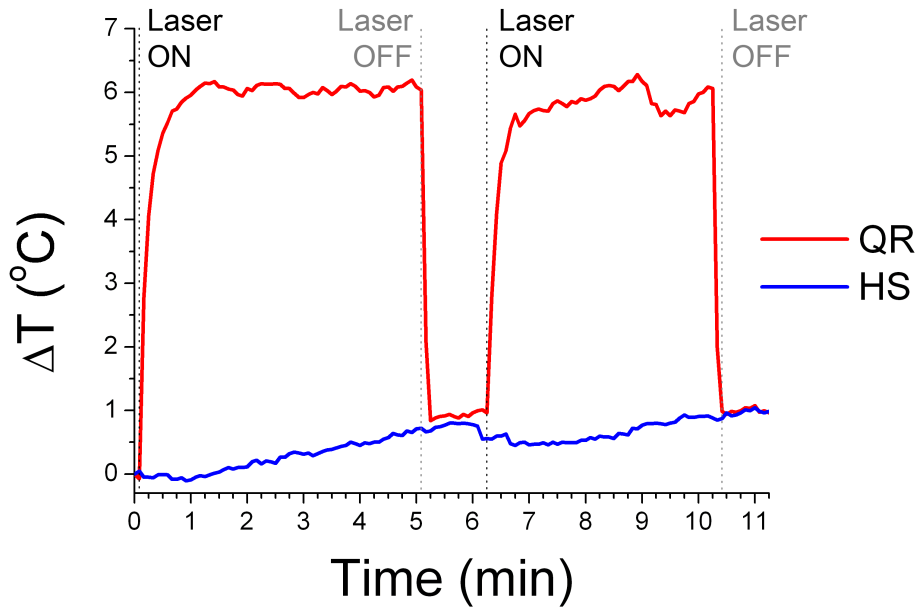


Figure 5.4: Photothermal properties of Quantum Rattles. Temperature profiles monitored with a thermal camera of hollow mesoporous silica shells (HS, blue) and Quantum Rattles (QR, red) dried on a glass slide showing a temperature increase in the QR samples upon irradiation with a 671 nm laser (38 W.cm^{-2}) compared to the HS control.

to the initial value after closing the laser shutter. The reproducibility of the QR-induced heating phenomenon was tested by reopening the laser shutter after one minute. Subjecting the QRs to the laser light again induces the same temperature profile as in the first experiment, indicating that the heating of the QRs does not alter their photothermal ability.

The same photothermal efficiency experiment was performed on the QRs and HSs at a lower power density (7 W.cm^{-2}) using a less powerful 57 mW, 671 nm diode laser (Figure 5.5). Movies of the temperature acquisition by the thermal camera and real-time heating of the QRs are viewable in the Appendices (Movies A.1 and A.2). Although the lower power density laser irradiation (7 W.cm^{-2}) causes heating of the QRs, the measured increase in temperature is just 1.5 °C compared to 6 °C for QRs irradiated at a

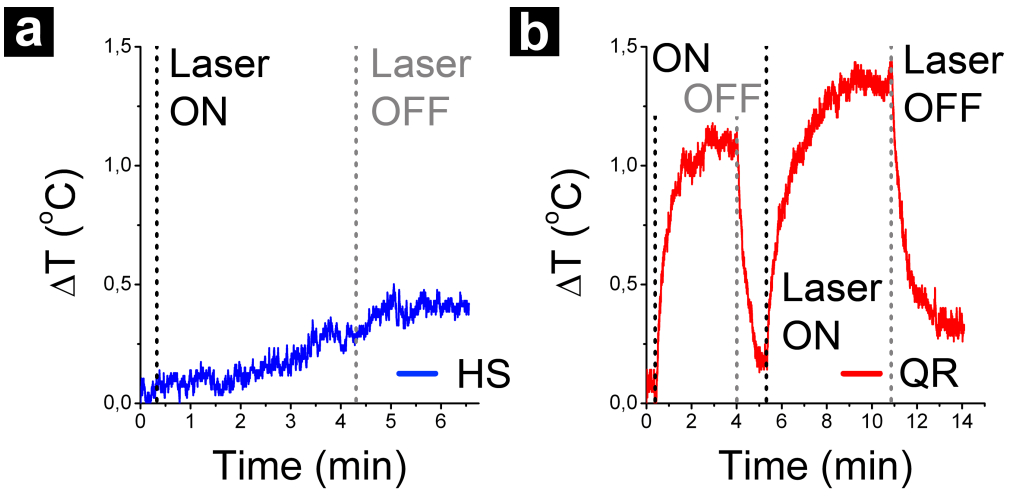


Figure 5.5: Photothermal properties of Quantum Rattles. Temperature profiles monitored through a thermal camera of (a) hollow mesoporous silica shells (HS, blue) and (b) Quantum Rattles (QR, red) dried on a glass slide showing a temperature increase in the QR samples upon irradiation with a 671 nm laser (7 W.cm^{-2}) compared to the HS control. The temperature increase is lower than when the QR are irradiated at a power density of 38 W.cm^{-2}(Figure 5.4), demonstrating the photothermal conversion is dependent on the incident laser irradiation power.

higher power density of NIR laser light (38 W.cm^{-2}). Hence, the observed temperature increase is dependent on the power of the incident irradiation. This NIR light dose dependency needs to be taken into account in order to modulate the QRs efficiency when mediating hyperthermia in tumours.

Quantum Rattles in Solution

After assessing the photothermal conversion efficiency of QRs in a dry state on a surface, QRs were dispersed in water to investigate their ability to heat a bulk volume of solvent (Figure 5.6). Upon irradiation with a 671 nm laser (38 W.cm^{-2}), the QRs induce an increase of 3 °C in temperature of the surrounding water (1 mL) within a time period of 5 - 10 min, whereas the HS control do not generate any heat. Compared to the QRs irradiated in a dry environment, the QRs in solution cause a slower and lower temperature

increase. However, this lower heat increase is to be expected as the temperature probe was placed outside the laser spot to demonstrate that an entire volume of water can be heated by a localised application of NIR light and, at the same time, ensure that any temperature increase is not due to probe/laser interaction. This bulk heating of a macroscopic volume of water shows great promise for *in vivo* QR-mediated PTT application, where the whole tumour needs to be heated homogeneously over the treatment period.

Compared to other NP systems that possess very high absorbance cross-sections, such as gold nanorods, the QRs quantum plasmon peak at 672 nm is different in nature to the local surface plasmon peak.[6, 28] In the case of AuQDs incorporated in the QR shell, quantum confinement effects govern the optical absorption, whereas the local surface plasmon exhibited by gold nanorods arises from coherent, collective dipolar oscillations of conduction band electrons. This difference in physical phenomena causing the extinction peak of the QRs compared to other NP systems might lead to different approaches and uses of the QRs for PTT. It is important to note that the NIR extinction peak (at 672 nm) of the QRs is utilised for exploiting both the imaging and therapeutic properties of the QR system. Therefore, an unavoidable trade-off exists between the amount of absorbed incident NIR light converted to photoluminescent emission (used to image the QR) and the amount of absorbed light converted to heat (used to mediate hyperthermia). Nevertheless, combining tumour imaging and hyperthermia within one sole agent guarantees distinct therapeutic targeting on the imaged area only.

Effect of Laser Irradiation on Quantum Rattle Morphology

In order to assess the effect of laser irradiation on the QRs morphology and structure, QRs that underwent laser irradiation (671 nm, 38 $W.cm^{-2}$) for 15 min were analysed by HRTEM (Figure 5.7). When compared to the HRTEM images of the non-irradiated QRs (c.f. Figure 3.9), the HRTEM images of the irradiated QRs show that the laser does not influence the

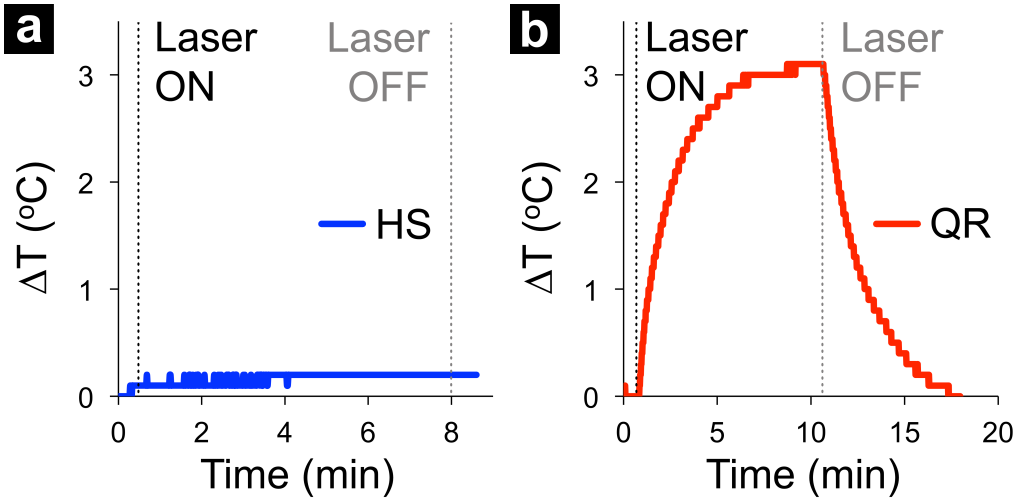


Figure 5.6: Photothermal properties of Quantum Rattles. Temperature profiles monitored through a thermocouple probe of (a) hollow mesoporous silica shells (HS, blue) and (b) Quantum Rattles (QR, red) in solution showing a bulk increase in the solvent temperature upon irradiation with a 671 nm laser (38 $W.cm^{-2}$) for the QRs compared to the HS control.

morphology of the silica shell. Furthermore, the AuQDs are still present in the QR silica shell after laser irradiation. The mesopores in the silica shell, encapsulating the AuQDs, appear to stabilise the structure of the AuQDs and preserve them from alterations caused by the heating process. This is an important feature of the QRs, as laser irradiation of gold NPs have been reported to lead to fragmentation of the NPs.[239, 240] The slow heat release of the deposited laser energy into the surrounding environment by the gold NPs, can result in the melting and even vaporisation of the gold atoms.[89] As the gold NPs cannot cool down as fast as they are heated, they fragment into smaller nanodots.[89] In addition, gold nanostructures for PTT that have high photothermal conversion efficiency, such as gold nanorods, have also been reported to change shape under the influence of laser light.[89, 164, 241] However, previous studies have also demonstrated that the addition of a silica layer around gold nanorods can prevent the morphological change of the gold due to the laser light,[241] which can be an explanation for the preserved AuQDs in the QR silica shell. This

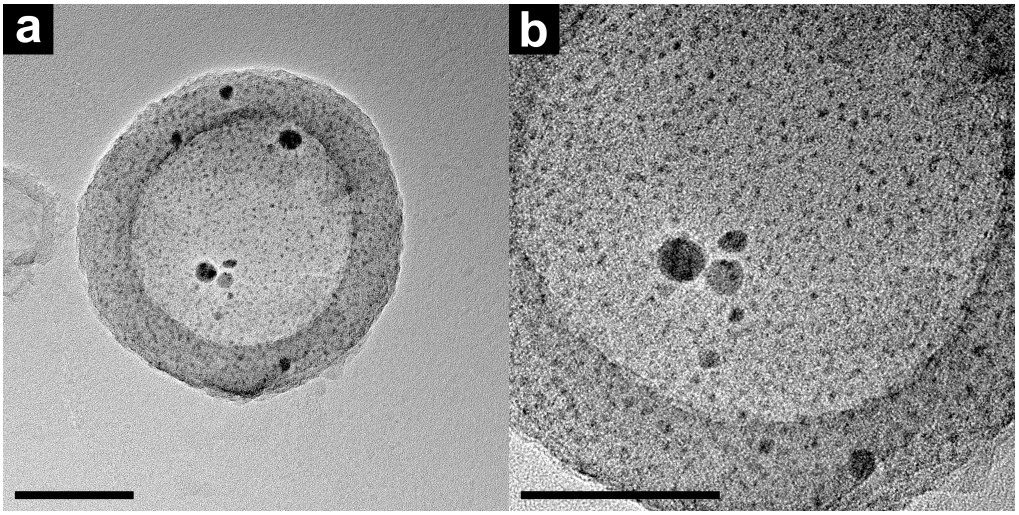


Figure 5.7: Effect of irradiation on the Quantum Rattles. Bright Field high resolution transmission electron microscopy (HRTEM) images of (a) overview and (b) close-up of a Quantum Rattle after irradiation by a 671 nm laser (38 W.cm^{-2}) for 15 min. Scale bars: 50 nm.

non-destructive character of the QR upon laser irradiation shows again the great potential of the QR system for PTT purposes.

5.3.2 *In Vitro* Assessment of the Quantum Rattles Photothermal Properties

The QRs temperature profiles monitored on a surface or in solution upon laser irradiation, show the potential of the QRs for inducing hyperthermia in cells by means of AuQD-mediated heat generation. The next step in this study, was to try and induce localised cell death *in vitro* using the novel QR system. HeLa cells were incubated with QRs for 1 day and irradiated with a 671 nm laser (38 W.cm^{-2}) to establish the QRs efficiency at inducing cell death (Figure 5.8). LIVE/DEAD assays were used to determine the performance of the QRs at inducing localised cell death. Cells incubated with either no particles or HSs were used as controls. All QR-incubated cells remain viable below 2 min of irradiation (Figure 5.8a-b). After this threshold of 2 min of laser light, circular regions of cell death are seen in the

LIVE/DEAD fluorescence microscopy images (Figure 5.8c-f). The amount of cell death in and around the area of the laser spot is irradiation-time dependent. On the other hand, laser irradiation on cells incubated with no particles or HSs do not induce any cell death, demonstrating the need of QRs for NIR laser-triggered cell death and, therefore, the QRs potential for PTT (Figure 5.8g-h). Although cell death clearly occurs in the centre of the laser treatment area, cells also die in close proximity of the laser spot. This result can be explained by heat diffusing from the irradiated QRs inside the laser spot to the cells outside the beam area.

Image processing and segmentation algorithms of the LIVE/DEAD assays provided quantification of QR-mediated cell death by computing the percentage of cell death. Cell death within the laser spot is proportional to irradiation times between 2 and 10 min and then saturates reaching 97% cell death (Figures 5.9). Cells outside the laser beam are indirectly affected by the laser irradiation. Quantifications of the cell death in the cell population adjacent to the laser beam show that the percentage of cell death in this region is linearly proportional to the irradiation time, with a squared correlation coefficient R^2 value of 0.97 (Figures 5.10). After 15 min of laser irradiation, the percentage of cell death reaches 84% in close proximity to the laser beam.

Previous *in vitro* studies of gold nanosystems-mediated cell death do not report on the evolution of cell death depending on irradiation time and, therefore, the question of the fate of the cells adjacent to the laser beam remains unclear.[29, 136, 153] The *in vitro* QR-mediated PTT experiments demonstrate the importance of a trade-off between the time or dose of a treatment, the amount of cell death in the laser treatment area and the amount of collateral damage outside the treatment area. However, *in vitro* studies do not allow the differentiation of NP-induced photothermal effects between cancerous cells and healthy cells. Nevertheless, for *in vivo* NP-mediated PTT applications, other parameters besides the NIR irradiation area prevent damage to healthy cells, such as targeting (passive or active) and the lower sensitivity of healthy cells to heat damage compared to cancer

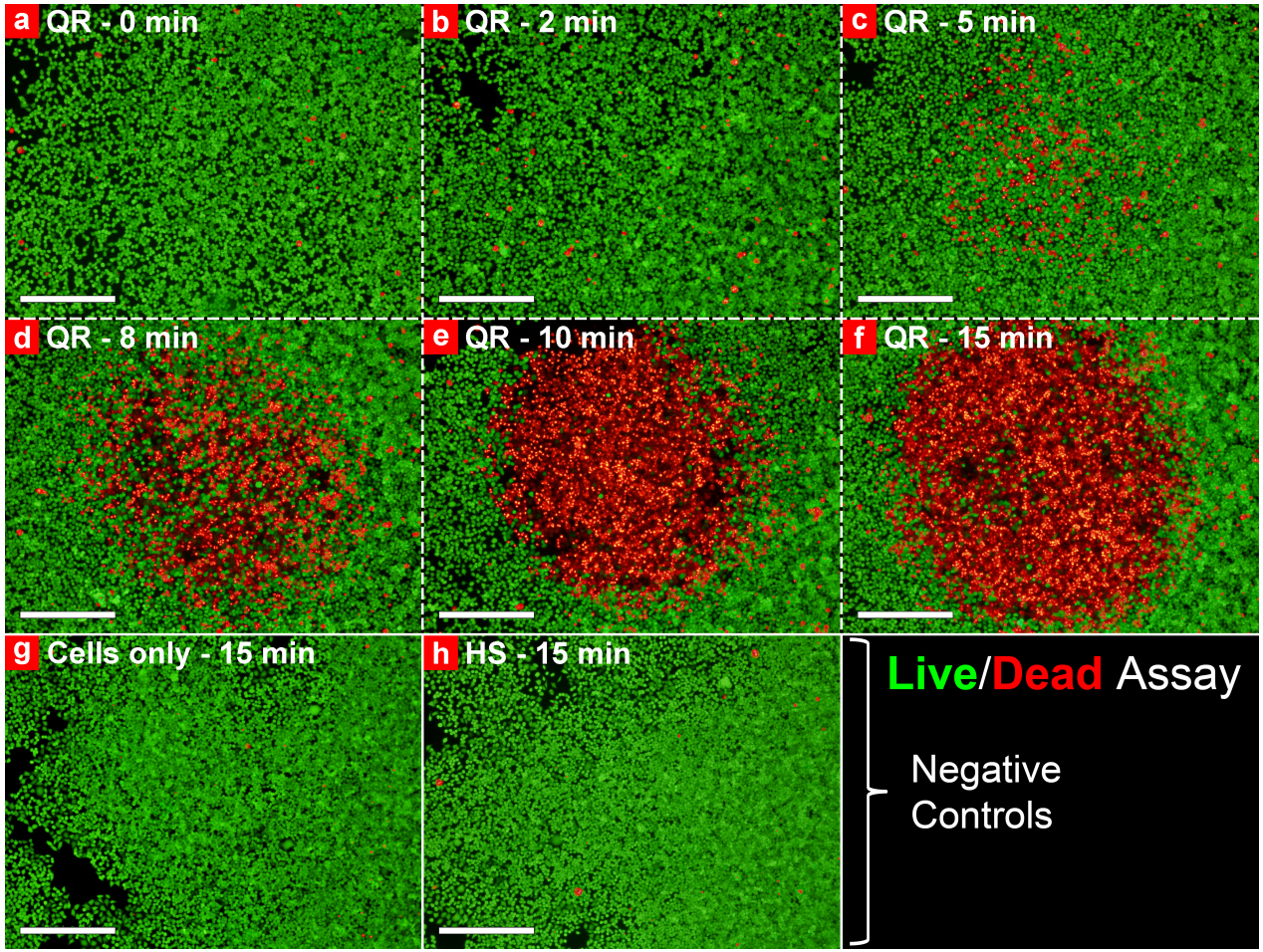


Figure 5.8: Quantum Rattles mediate hyperthermia *in vitro*. LIVE/DEAD assays on HeLa cells (live cells in green, dead cells in red) treated with 671 nm laser light (38 W.cm^{-2}, spot size ~ 1mm). Representative fluorescent microscopy images of (a-f) cells incubated for 1 day with Quantum Rattles (QRs) and irradiated for 0, 2, 5, 8, 10 and 15 min; (g) cells irradiated for 15 min; (h) cells incubated with hollow mesoporous silica shells (HS) for 1 day and irradiated for 15 min. Scale bars: 500 µm.

cells.

Cell death was followed by time-lapse confocal microscopy on HeLa cells incubated with QRs, in order to gain a further understanding of the underlying process involved in QR-mediated cell death (Movie 5.1). In the time-lapse sequence the LIVE stain (calcein) rapidly disappeared (within 2 min) from most cells under NIR laser irradiation, indicating compromised cell viability by the quick loss of intracellular esterase activity (Movie 5.1a). The DEAD stain (DNA-bound ethidium homodimer-1) appears afterwards proving the loss of plasma membrane integrity and, ultimately, cell death (Movie 5.1c-d). Finally, cell death only occurs within the limits of the irradiated area, indicating an efficient localisation for QR-mediated hyperthermia for a short treatment time (Figure 5.8, Movie 5.1d). Previous studies on hyperthermic effects at the cellular level show changes to the cytoskeletal structure, cell membrane rupture, protein denaturation, impairment of DNA and RNA synthesis and programmed apoptosis occur as a result of the heat increase in living tissue.[28] Movie 5.1 shows changes in cell structure and cell membrane rupturing take place upon laser irradiation. However, as no temperature profile of the cells was recorded during laser treatment, it cannot be stated yet if these effects are induced by hyperthermia.

The first published results[29] on gold nanoshell-mediated PTT led to the commercialisation of the AuroLase system (NanoSpectra), which is currently undergoing clinical trials. In this study, gold nanoshell-mediated cell death was investigated *in vitro* on human breast epithelial carcinoma SK-BR-3 cells. The QR performance on HeLa cells is comparable to that of the gold nanoshells, where cell death occurred upon laser treatment of 7 min at 820 nm (35 $W.cm^{-2}$).[29] This result provides encouraging support for the use of QR-mediated cancer therapy through PTT. Moreover, in contrast to the gold nanoshells, the QRs native properties offer potential for not only PTT but also NIR live imaging (*c.f.* Chapter 4) and combined therapy through targeted drug delivery (*c.f.* Chapter 6).

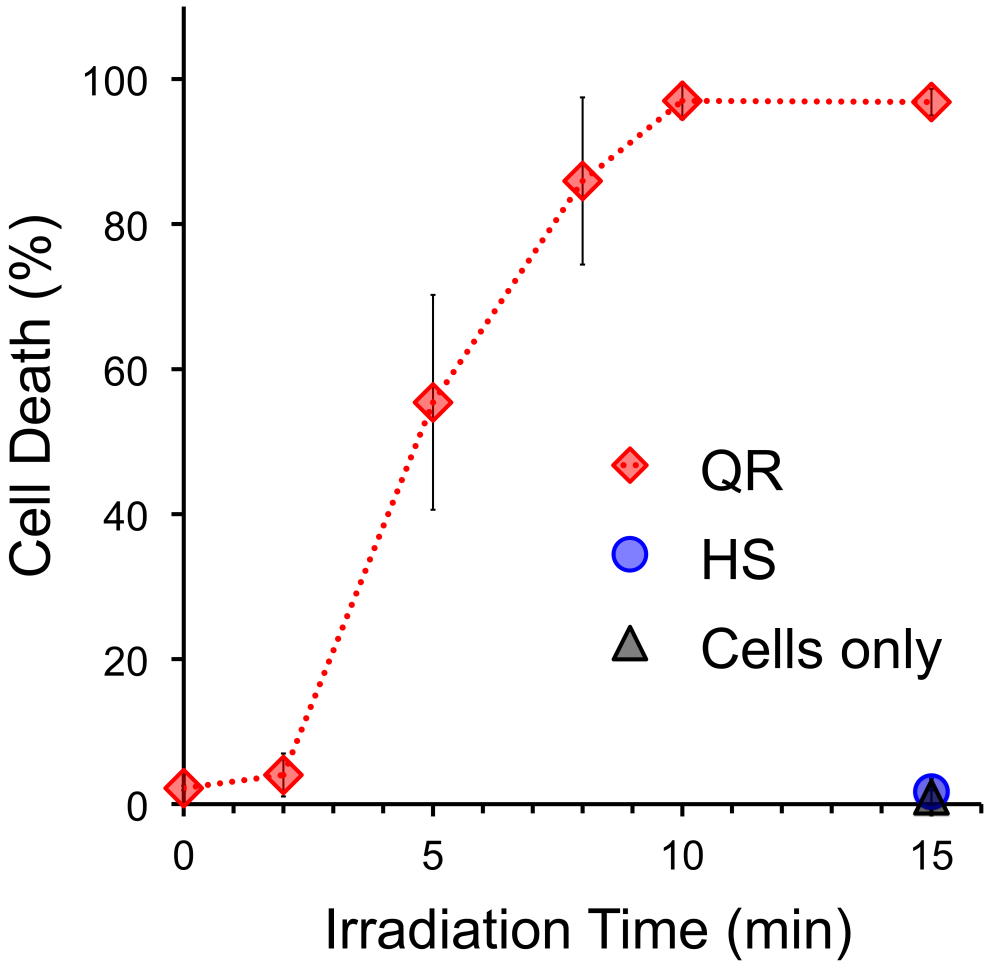


Figure 5.9: Quantum Rattles mediate hyperthermia *in vitro*. LIVE/DEAD assay quantification. Percentage of cell death inside the laser spot saturates after 10 min of laser irradiation. The hyperthermia and cell death caused by the QRs/laser light combination is dose dependent (*i.e.* dependent on the energy provided by the laser irradiation). Error bars represent the standard deviations of quadruplicate experiments.

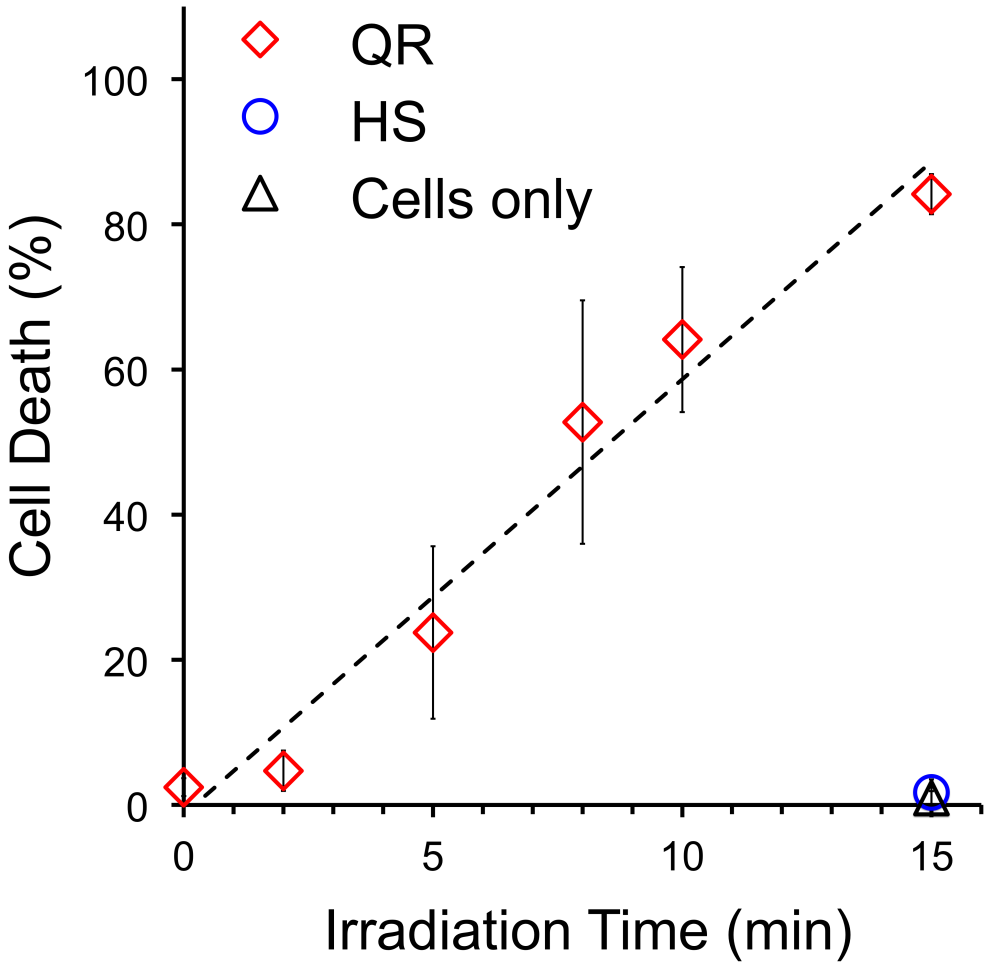
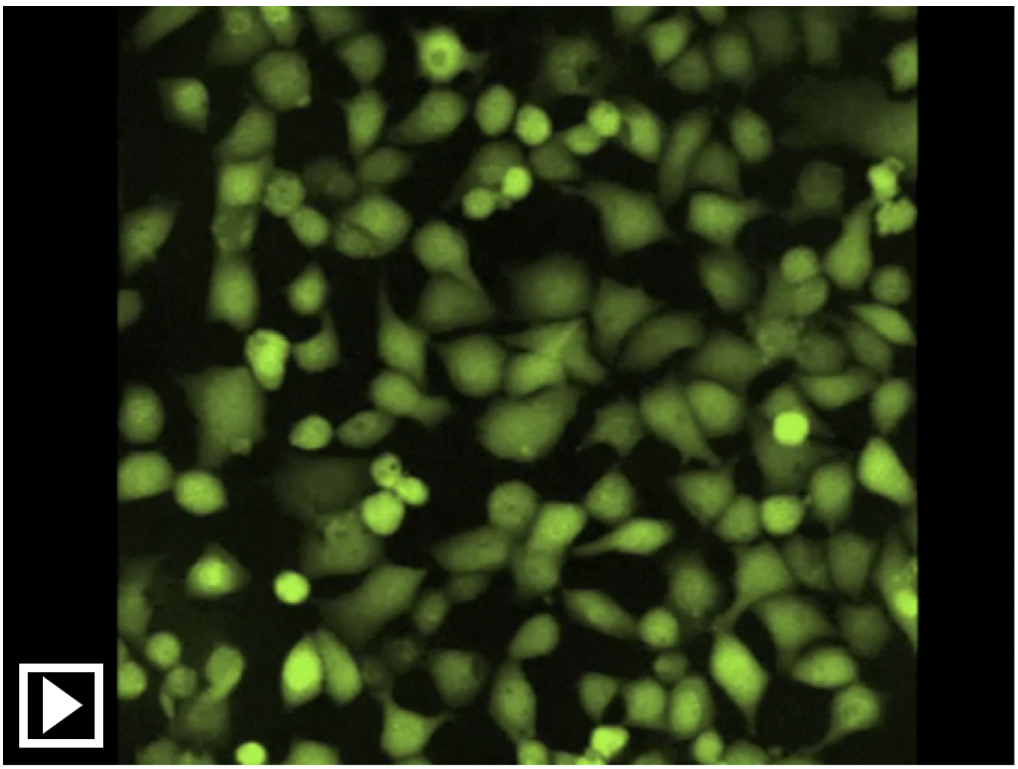


Figure 5.10: Quantum Rattles mediate hyperthermia *in vitro*. LIVE/DEAD assay quantification. Percentage of cell death outside the laser spot showing a linear trend ($R^2 = 0.97$) between cell death and irradiation time in the close proximity of the laser spot. Error bars represent the standard deviations of quadruplicate experiments.



Movie 5.1: Confocal time-lapse series of HeLa cells incubated with Quantum Rattles for 1 day. (a-b) LIVE channel during laser irradiation showing calcein (LIVE stain, green) disappearing due to the loss of intracellular esterase activity with cell death. (b) Zoomed-in view with bright field (inset) showing cells bursting during death with cytoplasm leaking and, organelles and nuclei appearing. (c-d) LIVE and DEAD channels after laser irradiation of 2 and 5 min, showing DNA-bound ethidium bromide homodimer-1 (DEAD stain, red) appearing indicating the loss of plasma membrane integrity (d) Zoomed-out view after laser irradiation showing laser spot. *(Click to play. Requires Adobe Reader 8.× or higher)*

5.3.3 *Ex Vivo* Assessment of the Quantum Rattles Photothermal Properties

In order to obtain a better understanding of the PTT performance and behaviour of QRs in tissue, *ex vivo* experiments were performed on chicken muscles from the thigh used as tissue phantoms (Figure 5.11). Although the QRs show great promise at mediating localised cell death *in vitro*, the therapeutic NIR extinction peak of the QRs at 672 nm is close to the limit of the NIR bio-window. Therefore, scattering of the incident light could impede the QR efficiency at inducing hyperthermia. The aim of this study is to assess QRs efficiency at inducing hyperthermia in tissue before future *in vivo* studies. The temperature increase induced by subcutaneously injected QRs upon NIR irradiation was recorded using a mini-hypodermic probe and compared to PBS and no injection controls (Figure 5.11a-c). It should be noted that this *ex vivo* study primarily aims at looking at the feasibility of an *in vivo* study by testing if enough NIR light can be absorbed and subsequently converted to heat in a medium (as close as possible) comparable to living tissue. The chicken thighs are a test system for NIR light absorption by the QRs in animal tissue. Results gathered from the generated heat in the chicken thighs only give an indication of adequate light absorption by the QRs, and do not prove that the QRs can mediate hyperthermia in living tissues. In order to fully investigate QR-mediated cell death an extensive *in vivo* study involving a tumour model should be undertaken.

Upon irradiation with a 671 nm laser (38 $W.cm^{-2}$), the QRs induce a temperature increase of approximately 38 °C to the surrounding chicken tissue in less than 1 min (Figure 5.11d). The PBS and no injection controls generate an increase in tissue temperature of approximately 10 °C and 11 °C, respectively (Figure 5.11d). The heat increase observed in both controls can be attributed to the laser power directly heating the tissue. This explanation is in good qualitative agreement with theoretical and experimental data published previously on light interaction with tissue.[242, 243]

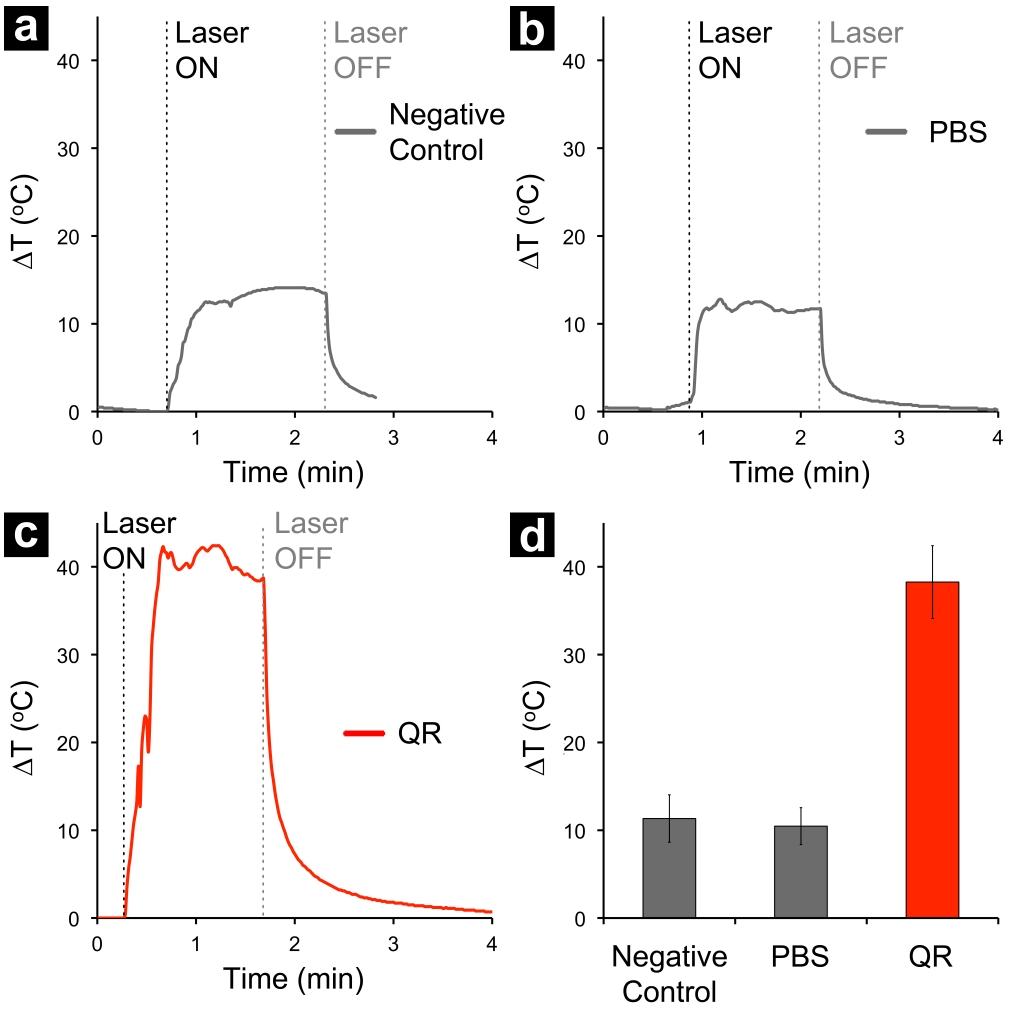


Figure 5.11: The photothermal potential of Quantum Rattles *ex vivo*. Temperature profiles monitored through a thermocouple probe inserted under the skin of a chicken thigh after (a) no injection (Negative Control, grey), (b) phosphate buffer injection (PBS, grey) and (c) Quantum Rattles in PBS injection (QR, red). (d) Maximum temperature increase recorded for QRs in PBS injections (QR, red) compared to no injections (Negative Control, grey) and PBS alone injections (PBS, grey). A higher temperature increase is observed upon irradiation with a 671 nm laser (38 $W.cm^{-2}$) for the QR injection compared to the two controls, which show identical temperature profiles. Error bars represent the standard deviations of triplicate experiments.

QR-mediated therapy raises temperatures well above the damage threshold needed to induce irreversible tissue damage.[244] At the same time, the heating levels caused by both controls show average tissue heating levels that are insufficient to induce irreversible tissue damage.[244] Furthermore, the average tissue heating observed in the QR-treated chicken is comparable to the average tumour heating previously reported *in vivo*, where mice were treated with nanoshells intratumourly.[29] In the same mouse study, saline controls showed equivalent heating to the temperature increase observed for PBS and no injection controls in the chicken thigh *ex vivo* study presented here. This *ex vivo* study demonstrates the great potential of the QR system for *in vivo* PTT cancer treatment.

5.4 Conclusions

This chapter demonstrated the photothermal properties of the QR system and showed their potential for cancer therapy and, more specifically, as a PTT agent. The photothermal properties of the QR system were first confirmed from a physical standpoint before being tested from a more biological point of view by means of *in vitro* studies on a cancer cell line followed by an *ex vivo* assessment using a chicken model.

The QRs converted incident NIR light into vibrational energy or heat, when deposited on dry surfaces or in solution. The temperature profiles showed that the degree of heating of the QR surroundings depends on the power density of the incident NIR laser irradiation. Furthermore, the silica shell of the QRs protects the encapsulated AuQDs from changes in morphology, and, therefore any associated changes in optical properties. *In vitro* studies showed the QR system induced localised cell death, where the killing efficiency is dependent on the NIR irradiation dose. Only after 10 minutes of NIR laser treatment, 97% of all cells in a treated area were killed. Furthermore, the cancer cell membranes rupture upon irradiation, suggesting that the QRs initiate hyperthermia.[28] Finally, the subcutaneous injection of QRs in chicken thighs, in combination with NIR light activation, induced

a rise of approximately 38 °C in tissue temperature. This tissue heating is well above the damage threshold required to induce irreversible damage in tissue.[244]

To conclude, both *in vitro* and *ex vivo* biological assessments of the QR potential for PTT showed results and performance that are similar to previously published NP-based PTT system and in particular gold nanoshells, which are currently the most researched nanosystem for PTT.[29, 136, 153] However, by comparison with other systems such as gold nanoshells, the QRs offer the advantage of being natively multifunctional and ideally suited for both diagnostic (NIR live imaging, *c.f.* Chapter 4) as well as combined therapy (photo- and chemotherapy, *c.f.* Chapter 6). To date, this is the first study demonstrating the efficient use of AuQDs for cancer treatment *via* NIR phototherapy.

Chapter 6

Quantum Rattles for Drug Delivery

6.1 Introduction

From its earliest beginnings, medical practice has strived to heal injuries and cure diseases by introducing drugs and other therapies into the body. Over the years, drug delivery methods have progressed from the primitive chewing of leaves and roots of medicinal plants to, more recently, injections, tablets and capsules.[245] These systemic drug delivery approaches that distribute the medications throughout the body, are most commonly used due to their ease of administration. However, systemic delivery may result in suboptimal drug concentration in the target organ and, next to that, may affect healthy tissue in the body. In order to efficiently achieve therapeutic drug levels, targeted local drug delivery methods can be applied.[104, 105] Such controlled drug delivery systems (DDS) are engineered to release drugs in the target area over a period of time in a controlled manner.[246]

Controlled drug delivery technology is amongst the most promising applications for human health care and represents one of the most rapidly advancing fields for biomedical materials sciences.[173, 246, 247] Controlled DDSs offer various advantages compared to more traditional dosage forms.[104, 246, 248, 249] These advantages include:

- Increased performance compared to current commercial drugs;
- Potential applications of new drug molecules that are currently not used in the clinic due to problems, such as low drug solubility and systemic toxicity;
- Reduced undesirable side effects;
- More precise and lower drug dosages and concomitant costs.

Chemotherapy, the treatment of cancer with drugs, is often accompanied by severe side effects due to the cytotoxicity of the chemotherapy drug combined with its non-specific distribution in the body.[105, 146] An obstacle towards the development of more advanced chemotherapies with reduced side effects concerns the limited availability of efficient biocompatible DDSs for most hydrophobic anticancer drugs.[249] For example, the low solubility of most anticancer drugs in aqueous media hampers their effective use *via* intravenous injections.[249] In order to overcome the poor water solubility of these anticancer molecules, the development of novel DDSs to carry the hydrophobic agents without the use of toxic organic solvents has received significant interest.[184, 249] In particular, nanotechnology offers great potential in designing DDSs for targeted delivery of therapeutic agents into organs or cells.[105,250,251] Nanoengineered DDSs could overcome the lack of specificity of conventional chemotherapeutic agents and reduce overall cytotoxicity by using both passive and active targeting strategies and by enhancing the local dosages of drugs into the tumours.[105, 146, 248]

Various organic and inorganic NPs that can circulate through the bloodstream and target tumours, while carrying small payloads of anticancer drugs, have been examined.[9, 102, 104, 252] For example, the high loading capacity of liposomes allows the delivery of drugs to target sites *in vivo*, minimising side effects and toxicity of the drug payloads.[173, 174] However, such organic systems suffer from poor thermal and chemical stability as well as rapid elimination by the immune system. In contrast, inorganic silica particles offer an biocompatible and stable alternative as a carrier for therapeutic cancer drugs.[180, 184, 245]

In this context, mesoporous silica nanomaterials are showing great promise for delivering anticancer and other water-insoluble drugs into human cancer cells.[82, 104, 185, 253] The high surface area, tuneable pore diameter, and uniform porous structure of mesoporous silica nanomaterials offer a unique advantage for loading and releasing large quantities of biomedical agents.[175–179] Furthermore, the favourable biocompatibility and ease of functionalisation through silane chemistry of silica nanomaterials are beneficial for designing tumour-targeting vectors.[105, 175–177] Mesoporous silica nanosystems with a hollow structure are of particular interest as they show particularly high drug loading efficiency, due to their the interstitial hollow space, which can selectively and efficiently accommodate drug molecules.[104, 213, 254] Recently, hollow rattle-type nanosystems with a mesoporous silica shell have shown promising results as drug delivery vectors.[3, 98, 145, 189, 255–257] Not only can the inner material be chosen to confer new functionalities to the system, such as diagnosis *via* MRI (in the case of Fe_3O_4 NPs)[255] but their added available surface further enhances their drug loading efficiency.[98] Such multifunctional nanostructured materials, which are able to combine targeted diagnosis and therapy in one system can simultaneously image early tumour site, deliver polyvalent payloads and kill cancer cells in a controlled manner.[30, 91, 190]

The first parts of this thesis (*c.f.* Chapter 4 and Chapter 5) reported on the QRs capabilities and potential for NIR imaging and photothermal applications. This chapter moves on to investigate the potential use of the QR systems for drug delivery in cancer treatment. By combining controlled drug delivery with NIR imaging and photothermal capabilities, the QRs can be demonstrated as highly multifunctional agents and thus extremely suitable for combined cancer diagnosis and therapy. As a starting point, it is hypothesised that the presence of multiple hydrophobic gold NPs inside the cavity of the silica shell will enhance the drug loading capacity because of the increase in reactive surface area and the favourable interaction of gold with hydrophobic anticancer drugs. Moreover, it is hypothesised that the mesoporous silica shell will act as a diffusion membrane that allows

a sustained drug release. In this study, both the drug loading capacity and drug release kinetics of the QRs were examined by using the small hydrophobic anticancer drug doxorubicin (DOX) as a model drug. DOX has been widely used as a model for small hydrophobic drugs because of its potent therapeutic effect and its photonic properties, which can be used to quantify the amount of DOX present.[248, 252, 258]

6.2 Materials and Methods

Materials: Doxorubicin (DOX) was purchased from Sigma-Aldrich, UK. Solvents such as absolute ethanol were purchased from VWR, UK. Phosphate buffer (PBS, pH 7.4) was purchased from Invitrogen, UK.

6.2.1 Drug Loading

In order to investigate the drug loading efficiency of the QR system, DOX was used as an anticancer drug model. The DOX drug loading efficiency of the QRs was compared to hollow mesoporous silica particles (HSs) and non-hollow Quantum Rattles (NQRs) as controls. The red fluorescence of DOX was used to quantify the amount of DOX loaded in the three types of particles. Stock solutions of QRs, HSs or NQRs were prepared by dispersing them in MilliQ H_2O at a concentration of 5 mg.mL^{-1}. Six different stock solutions of DOX were prepared in MilliQ H_2O ranging from 1 mg.mL^{-1}to 31.3×10^{-3} mg.mL^{-1} in concentration. Samples for the drug loading experiments were obtained by adding 10 µL of stock particle dispersions to 50 µL of stock DOX solutions and 40 µL of MilliQ H_2O resulting in a final particle concentration of 0.5 mg.mL^{-1} and a DOX concentration range of 0.5 mg.mL^{-1} to 15.6×10^{-3} mg.mL^{-1}. The samples were left to rotate overnight in the dark at room temperature. Afterwards, the samples were washed three times in MilliQ H_2O at 14000 rpm.min^{-1}and resuspended in MilliQ H_2O. The fluorescence emission of the loaded QR, HS or NQR particles was monitored at 590 nm with an excitation wavelength set at

470 nm using a microplate reader (SpectraMax M5). From the fluorescence results, the amount of DOX was calculated using a DOX standard curve constructed from a DOX dilution series ranging from 3.91×10^{-3} mg.mL^{-1}to 2.56×10^{-6} mg.mL^{-1} in concentration.[1] The loading efficiency was expressed as the ratio of DOX loaded in the particles to the mass of particles. The experiment was run in triplicate and the results are presented as averages ± standard deviation.

6.2.2 Drug Release

The anticancer drug model DOX, in addition to being used for testing drug loading efficiency, also served as a model for investigating the release profile of the QR system. The release profile of the QRs was compared to HSs and NQRs as controls. The red fluorescence of DOX was used to quantify the amount of DOX released by the three types of particles. Stock solutions of QRs, HSs or NQRs were prepared by dispersing them in MilliQ H_2O at a concentration of 5 mg.mL^{-1}. A stock solution of 1 mg.mL^{-1} of DOX was prepared in MilliQ H_2O. Samples for the drug loading experiments were obtained by adding 10 µL of stock particle dispersions to 50 µL of stock DOX solutions and 40 µL of MilliQ H_2O resulting in a final particle concentration of 0.5 mg.mL^{-1} and DOX concentration of 0.5 mg.mL^{-1}. The samples were left to rotate overnight in the dark at room temperature. Afterwards, the samples were washed three times in MilliQ H_2O at 14000 rpm.min^{-1}, resuspended in PBS and left to rotate in the dark at room temperature. At 0.5, 1, 2, 4, 8, 12 and 24 h, the supernatants of the samples were collected by centrifuging the samples at 14000 rpm.min^{-1}for 5 min. The particles were resuspended in PBS and the fluorescence emission of the collected supernatant was monitored at 590 nm with an excitation wavelength set at 470 nm using a microplate reader (SpectraMax M5). From the fluorescence

[1]No point higher than 10 µM (5.44×10^{-3} mg.mL^{-1}) was used to construct the standard curve as above 10 µM of DOX, DOX molecules have been shown to self-associate resulting in quenching.[258] Therefore, the linear behaviour of the fluorescence emission of DOX with regards to concentration can only be assumed for concentrations lower than 10 µM.

results, DOX release from the DOX-loaded particles was calculated using a DOX standard curve constructed from a DOX dilution series ranging from 3.91×10^{-3} mg.mL^{-1}to 2.56×10^{-6} mg.mL^{-1} in concentration.[1] The DOX release profile shows the accumulated value of the mass of DOX released by the particles over time. The experiment was run in triplicate and the results are presented as averages ± standard deviation.

6.3 Results and Discussion

6.3.1 Drug Loading

The small molecule drug doxorubicin (DOX) was used to evaluate the QRs potential as a drug carrier. The QRs show a significant increase in DOX loading efficiency compared to the HS and NQRs, from DOX loading concentrations as low as 31.3×10^{-3} mg.mL^{-1} (Figure 6.1). At the highest loading concentration of DOX (0.5 mg.mL^{-1}), the QRs load up to 9 and 5 times more DOX than the HS and NQRs, respectively, with a loading efficiency of 87 mg.g^{-1}.

In previous studies, the reported drug loading efficiencies for mesoporous silica based nanosystems have varied widely.[91, 146, 213, 253, 255] For example, Huang *et al.*[253] showed a DOX loading efficiency of 30.8 mg.g^{-1} for multi-shelled mesoporous silica rattle-type NPs, whereas Zhu *et al.*[255] and Chen *et al.*[213] reported DOX loading efficiencies of 302 mg.g^{-1} and 1222 mg.g^{-1}, respectively, for Fe_3O_4@SiO_2 rattle-type NPs and hollow rattle-type mesoporous silica NPs. This wide variation might be due to the different methods used to obtain the loading efficiency. Most studies use the absorption peak of DOX at 480 nm to quantify the loading efficiencies of their systems.[91, 98, 213, 255, 259] These absorption-based methods tend to obtain higher loading efficiency values compared to quantification approaches that use the fluorescence emission of DOX at 585 nm.[253] However, none of the reported absorbance- and fluorescence-based methods directly quantify the loading efficiency from the DOX-loaded NPs, using

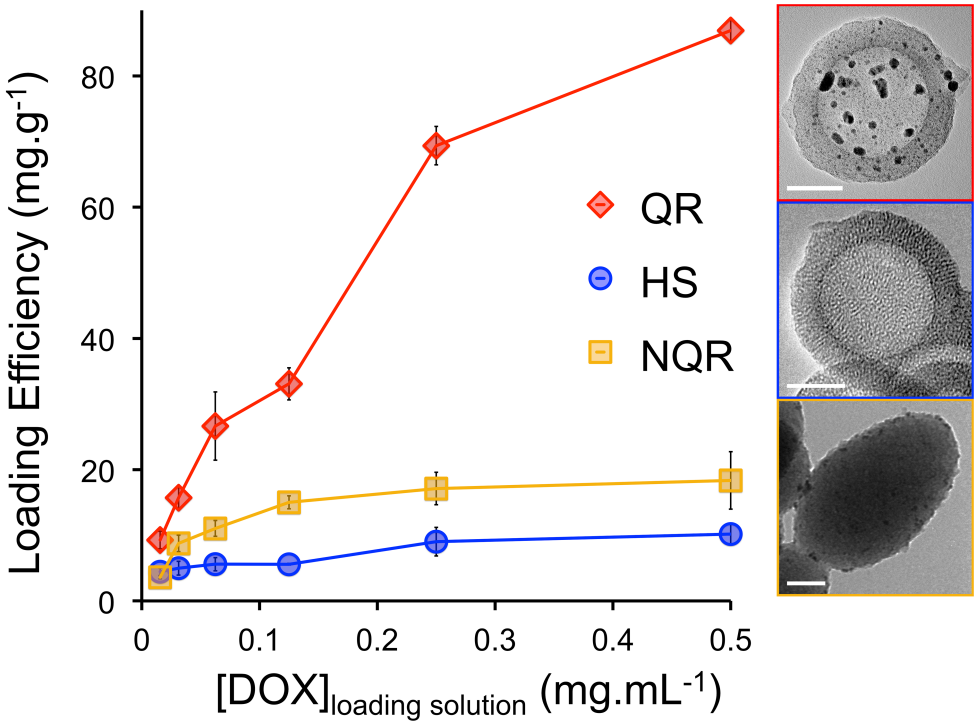


Figure 6.1: Quantum Rattles loading efficiency of doxorubicin (DOX). DOX loading efficiency of Quantum Rattles (QR, red) compared to hollow mesoporous silica shells without gold (HS, blue) and non-hollow Quantum Rattles (NQR, orange) showing up to 9 and 5 fold increased loading efficiency for the QRs compared to the HSs and NQRs, respectively. The higher surface area and hydrophobic environment provided by the gold nanoparticles inside the cavity of the silica shell drastically enhance the DOX loading efficiency of the system, starting from concentrations as low of 31.3 µg.mL^{-1}. Error bars represent the standard deviation of triplicate experiments. Inset: Transmission electron micrographs of QR, NQRs and HS. Scale bars: 50 nm.

only that obtained from the residual supernatant. This indirect approach is very sensitive to methodological factors, such as the purification process, which can explain the many differences observed in loading efficiency values for similar systems.

In the results reported here, however, the drug loading efficiency is calculated directly from the fluorescent response of DOX loaded inside the QRs. By using this direct quantification approach, effects due to experimental factors are limited when compared to indirect methods that calculate loading efficiency through the non-loaded DOX remaining in the loading solution. However, luminescence self-quenching of the loaded DOX molecules might occur within the QRs due to higher-order packing interactions, as previously reported with DOX-loaded carbon nanotubes and graphene oxide.[259,260] More specifically, the denser packing of DOX molecules inside the QR cavity compared to DOX molecules in solutions result in a lower fluorescence emission obtained from the DOX inside the QRs than from the supernatant. This might be an explanation for the relatively low quantified drug loading efficiency of the QRs.

It is difficult to directly compare the absolute value observed for the loading efficiency of the QRs with drug delivery results of other mesoporous silica-based nanosystems. However, it seems likely that the presence of the hydrophobic AuNPs inside the hollow core of the QRs greatly enhances the loading efficiency of the QR system compared to both hollow mesoporous silica and non-hollow mesoporous silica particles filled with gold nanostructures. Due to the hydrophobic AuNPs hosted in the QRs central cavity, the QRs offer a large hydrophobic surface in an isolated chamber. The hydrophobic surfaces created by the AuNPs within the QRs cavity have two distinct effects. Firstly, the hydrophobic cavity environment increases the diffusivity of anticancer drugs from the hydrophilic exterior environment through the mesoporous silica shell. Secondly, the gold surfaces functionalised with the hydrophobic thiol-ligand enhance the interaction with the hydrophobic anticancer drugs, thus leading to greater loading and a reduction in the release rate of the drug. Finally, compared to existing Au@SiO_2

rattle-type systems, such as the one developed by Wang *et al.*,[91] the QR system offers the advantage of a higher surface area of gold inside the cavity.

6.3.2 Drug Release

The QRs ability to control drug release was evaluated using the small anticancer drug molecule DOX (Figure 6.2). The QRs release 10 and 4 times more DOX than the HSs and NQRs, respectively, which is in good qualitative agreement with the differences in the amount of loaded DOX between each type of particle observed in the previous loading study (*c.f.* section 6.3.1). More than 75% of the total DOX release occurs in the first 4 h for all particle types. However, for the HSs, the DOX release plateaus already after 4 h, whereas the QRs and NQRs modulate DOX release up to 12 h.

When comparing the drug release profile from the three types of particles, two observations can be drawn:

- Addition of gold quantum dots (AuQDs) inside the mesopores seems to modulate sustained release compared to empty mesopores and;
- A hollow cavity does not affect the release kinetics, but does affect the loading.

The later observation seems counter-intuitive, as the thin silica shell of the QRs is expected to be less of a diffusion barrier compared to the NQRs solid mesoporous silica. However, the presence of AuQDs randomly distributed inside the mesostructure might make the length of the mesopores less significant in the drug release kinetics. The modulated 12 h release observed for both QRs and NQRs suggest that the mesopores are being occupied by AuQDs. Similar to studies described by Torney *et al.* and Vivero-Escoto *et al.*,[186,187] where AuNPs were used as hard caps for the pores of mesoporous silica vectors, the AuQDs inside the QRs and NQRs mesoporous structure seem to limit the outwards diffusion of the loaded

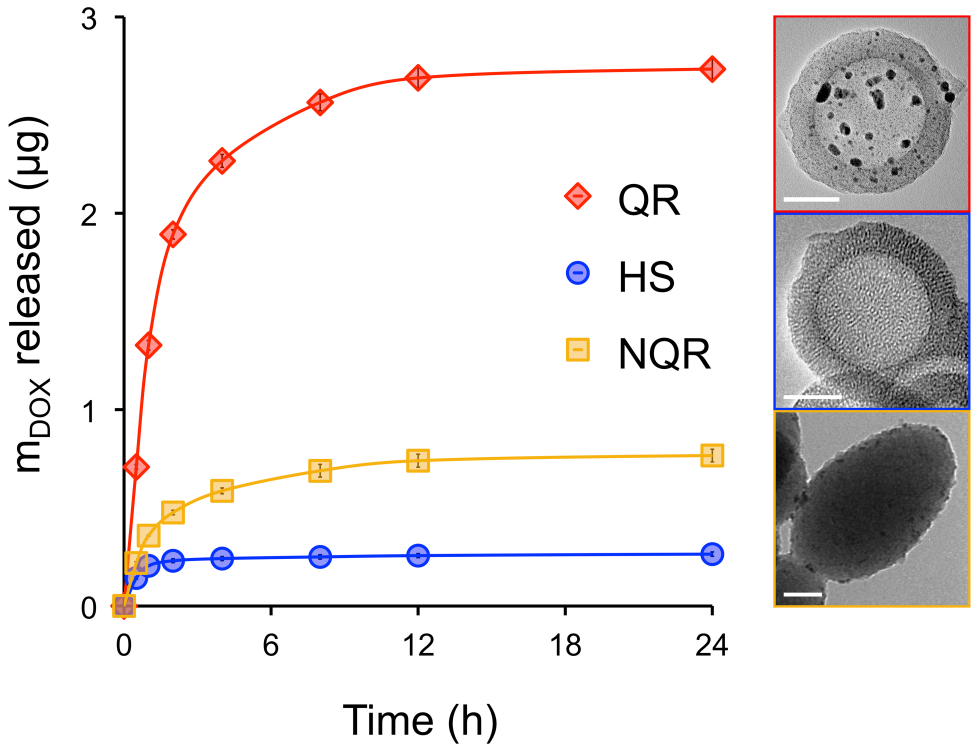


Figure 6.2: Release of doxorubicin (DOX) from Quantum Rattles. Drug release profile of Quantum Rattles (QR, red) compared to hollow mesoporous silica shells without gold (HS, blue) and non-hollow Quantum Rattles (NQR, orange) showing a 10 and 4 fold increase in the total DOX released compared to the HSs and NQRs, respectively. The QRs appear to modulate the release kinetics providing prolonged release for up to 12 h compared to HSs where the DOX release plateaus after 4 h. Error bars represent the standard deviation of triplicate experiments. Inset: Transmission electron micrographs of QR, NQRs and HS. Scale bars: 50 nm.

drugs. Therefore, the drug molecules have fewer pores available through which they can evade the particle.

The QRs seem to modulate a more sustained release than HSs. Future work on stimuli-responsive release should be undertaken to further improve on the potential use of the QRs as controlled drug delivery agents. The addition of a polymer coating with stimuli-responsive properties (*e.g.* pH or temperature responsive) can greatly improve the drug release kinetics of the QRs. For example, as tumour tissues are more acidic than healthy tissues,[183] an option to achieve a more site-selective controlled drug release is to design a pH-responsive QR.[261] Furthermore, by coating the QRs with a temperature-responsive coating, a NIR light-triggered anticancer drug release could be added during photothermal treatment of a tumour, thereby, efficiently combining chemo- and photothermal therapy.

6.4 Conclusions

The purpose of this chapter was to demonstrate the QRs potential for drug delivery applications in cancer treatment. Compared to gold-silica rattle-type particles obtained through other methods,[3, 91] the QRs possess the advantage of not only encapsulating multiple AuNPs, thereby obtaining a higher surface-to-volume ratio, but also of having the AuNPs surface functionalised with hydrophobic ligands, which enhances the potential for interactions with hydrophobic drug molecules. The results of this study showed that the presence of the hydrophobic AuNPs inside the cavity of the QR enhanced the QRs drug loading capacity. Furthermore, particles incorporating AuQDs inside their silica shell showed a more sustained release profile compared to plain hollow silica particles, which suggests that the AuQDs trapped inside the silica partly blocked off some of the drug diffusion pathways. To conclude, the QRs display the potential to favourably modulate the handling of a large drug payload for small hydrophobic anticancer drugs compared to mesoporous silica carriers. Hence, this study indicates new possibilities for enabling the design of stimuli-responsive QR

systems for localised cancer treatment by combining photothermal therapy with triggered drug release.

Chapter 7

Conclusions and Future Work

Optimising nanosystems for cancer treatment is a non trivial undertaking subject to many and varied considerations, which may sometimes require the adoption of design compromises.[3, 21, 23, 82] In this thesis, a novel gold-silica rattle-type system, the Quantum Rattle (QR) has been designed and presented. The QRs possess emergent properties that arise from a simple synergistic design in which the overall performance exceeds that of the individual constituents. Furthermore, the QR performance efficacy is accompanied by versatility, multifunctionality and scalability.

Making gold quantum dots (AuQDs) available for biomedicine has been a longstanding research goal that promises to open opportunities for multifunctional treatment and imaging options.[52] The QR synthetic approach, as presented in this thesis, provides stable, water soluble, biocompatible AuQDs that are effective in biological conditions by trapping them within mesopores. The AuQDs endow the QRs with simultaneous heat generation and NIR light emission capabilities when excited in the NIR bio-window. Consequently, the therapeutic and imaging agents are linked in the QRs, which provides an optimal combination for imaging of therapeutic efficacy. In addition, this combination avoids the various problems related to differential biodistribution that are associated with multiple agents.

Following the introduction of AuQDs, their therapeutic and imaging potential has been compromised by their lack of stability in aqueous solvent

and the lack of bioavailability and toxicology necessary for their safe and effective use.[75] Free AuQDs tend to merge rapidly into inactive gold nanoparticles (AuNPs) with faster kinetics at higher temperatures, which hampers their use for PTT. Furthermore, AuQDs with photonic properties in the NIR bio-window,[71, 79] tend to aggregate in biological buffers and interact disruptively with biological structures both at the cellular and biomolecular level. To circumvent such problems, AuQDs require a protecting, stabilising template that enables proficient biological interactions while still retaining photonic properties.[75] The QRs address these issues by entrapping AuQDs in the mesopores of a hydrophilic NP that is dispersible in biological buffers and mediates interaction with biological systems. At the same time, the QRs size range prolongs circulation half-life and is suitable to passively target disease-associated vasculature.

Inclusion of AuQDs within hollow silica shells is sufficient to create a unified platform for combining treatments involving chemotherapy, PTT and imaging. The possibility of carrying the drug payload within the same particle inducing the thermal ablation is a formidable additional advantage, as it would insure their combined delivery in known and optimised proportions and guarantee overlapping effects on the same target. Many other gold-based PTT systems are attempting to achieve an adjuvant effect between chemotherapy and PTT, but positive results are elusive due to imposition of various necessary design constraints. In the case of the QRs, however, the AuNPs within the silica shells act in unison to control the loading and release of the drug payload, allowing increased payload concentration and favourable release kinetics that can extend over a wider range than that of the silica shells.

By integrating diverse elements of chemistry, material science, photonics and biology, the system reported in this thesis has been developed into a multifunctional hybrid system showing clear evidence of intrinsic and efficient therapeutic and diagnostic potential *in vitro*. These promising results should be followed by a thorough assessment of the QR performance for cancer treatment *in vivo*. In this context, a study assessing the QR poten-

tial for combined photothermal therapy and NIR live imaging in a mouse model, has recently been funded by the Rosetrees Trust. QRs will be intratumourly injected in live mice to examine their ability to act as contrast agents for NIR imaging in parallel to their ability for inducing controlled cell death (*c.f.* preliminary results in Appendix A.2). In addition, the QR distribution upon systemic injection in the bloodstream will be examined in a mice model to fully demonstrate and characterise the QR capacities for passive targeting of tumours. In the same study, active targeting can also be investigated. The QRs silica shell functionalisation by means of silane chemistry (*c.f.* Chapter 4) opens the door to active targeting of tumours with QRs. Thus, QR accumulation in tumours by active and passive targeting can be compared with the objective of assessing and formulating the best strategies for targeting tumours.

In parallel, further work on the use of QRs as drug delivery agents should be undertaken with particular emphasis on examining the possibility of using the QR platform for trigger-responsive, drug delivery vectors. Novel studies focusing on the coating of QRs with temperature- and pH-responsive polymers have already commenced. The added temperature-responsiveness could be combined with the QR intrinsic photothermal properties to control drug delivery with a NIR light-trigger. Additionally, given that tumour tissues are more acidic than healthy tissues,[183] pH-responsive QRs could possibly achieve a more site-selective controlled drug release.

Recently, a preliminary study using SQUID magnetometry demonstrated the paramagnetic attributes of the QR system (*c.f.* preliminary results in Appendix A.3). These very promising results pave the way towards the incorporation of yet another native functionality into the QR platform. Possessing magnetic properties, the QR system could offer the advantages of both MRI and NIR imaging, combining high spatial and temporal resolution (MRI) and high sensitivity (NIR imaging).[7] The QRs ability to be used as MRI contrast agent should be investigated to assess the QR potential for multimodal imaging. Compared with existing multimodal imaging systems that rely almost exclusively on Fe_3O_4NP-based nanosystems, the

QRs would not require the addition of reliable coatings to promote favourable interactions with the host biological system.[7]

In summary, the QR system offers a relatively simple yet powerful platform for developing a new and vast range of multimodal, multifunctional systems to be used in the treatment and imaging of disease. However, the range and scope of QR applications need not be confined solely to the biological systems outlined in this thesis. Other potential uses of the QR system should be investigated. For example, the highly catalytic nature of AuQDs, which are trapped inside the QR silica shell, make QRs of special interest for catalytic applications.[11, 99, 262, 263] The QRs can act as a high performance nanoreactor with AuNPs and AuQDs readily available in aqueous solvent for catalysis.

To conclude, the simple synthesis pathway developed during this PhD study generated an efficient rattle-like particle system with a variety of highly attractive, intrinsic properties for cancer treatment. However, the QRs potential is not confined solely to applications in oncology. Overall, the QR platform represents an emerging technology that seems destined for a golden future.

Appendix A

Appendices

A.1 Photonic Properties of 'Thick' Quantum Rattles

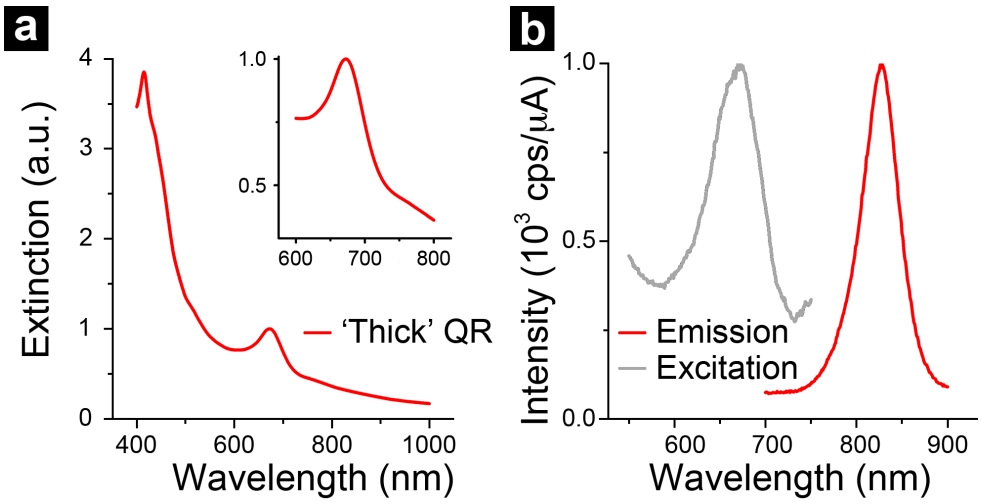


Figure A.1: Photonic properties of thick Quantum Rattles (silica shell thickness of $\sim$ 50 nm for a total diameter of $\sim$ 200 nm). (a) Extinction spectra of thick Quantum Rattles (thick QR, red) showing the same characteristic features as the thin QRs extinction spectra. Inset: zoomed in on the near infrared region of interest showing an extinction peak centred around 672 nm. (b) Photoluminescence spectra of thick QR showing an excitation peak centred at 672 nm and an emission peak centred at 827 nm. Both emission spectrum (λ_{ex} = 672 nm, red) and excitation spectrum (λ_{em} = 827 nm, grey) are identical to the thin QRs photoluminescent spectra.

A.2 NIR Imaging Potential of the Quantum Rattles

NIR imaging of the Quantum Rattles (QRs) was carried out by Dr. Daniel Stuckey and Dr. Josef Habib in Prof. Michael Schneider's group at the National Heart and Lung Institute at Imperial College London, UK. The tumour inoculation and QR injections were performed by Dr. Adam Gormley of Prof. Hamid Ghandehari's group at the Utah Center for Nanomedicine at the University of Utah, USA.

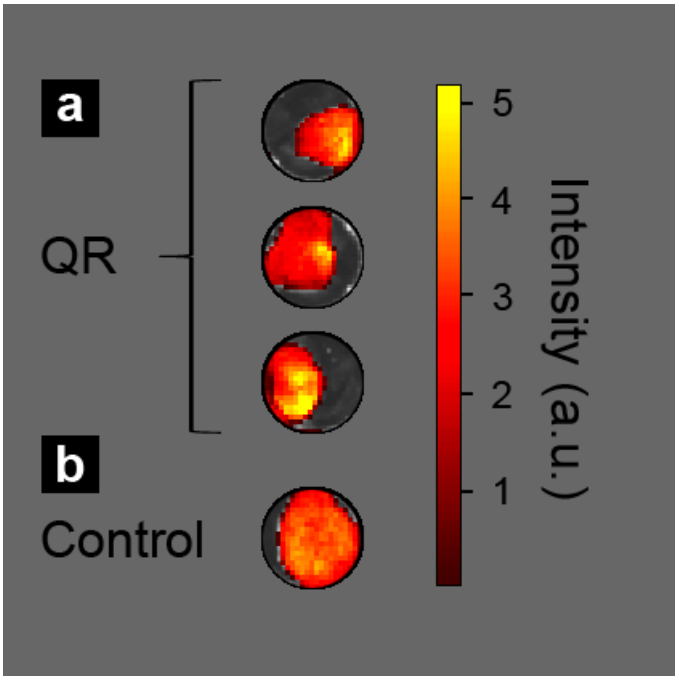


Figure A.2: NIR imaging of Quantum Rattles. DU145 bilateral prostate tumours in NU/NU mice were injected with 500 µL of (a) Quantum Rattles (QR, 20 mg.mL^{-1} in PBS) or (b) saline solution. The mice were sacrificed 1 day after the intratumoural injections and the excised tumours were fixed in 4% paraformaldehyde (PFA). QRs are localised by their own photoluminescence within the tumours, accumulating in intense epifluorescent spots, which are not observed in tumorous tissue injected with saline solution. These results show the great potential of the strong NIR absorption of the QRs for selective photothermal tumour ablation. NIR imaging set-up: λ_{ex} = 675 nm and λ_{em} = 840 nm.

A.3 Magnetic Properties of the Quantum Rattles

The SQUID measurements were performed by Dr. Sai Katla in Prof. Challa Kumar's group at the Center for Advanced Microstructures and Devices at the Louisiana State University, USA.

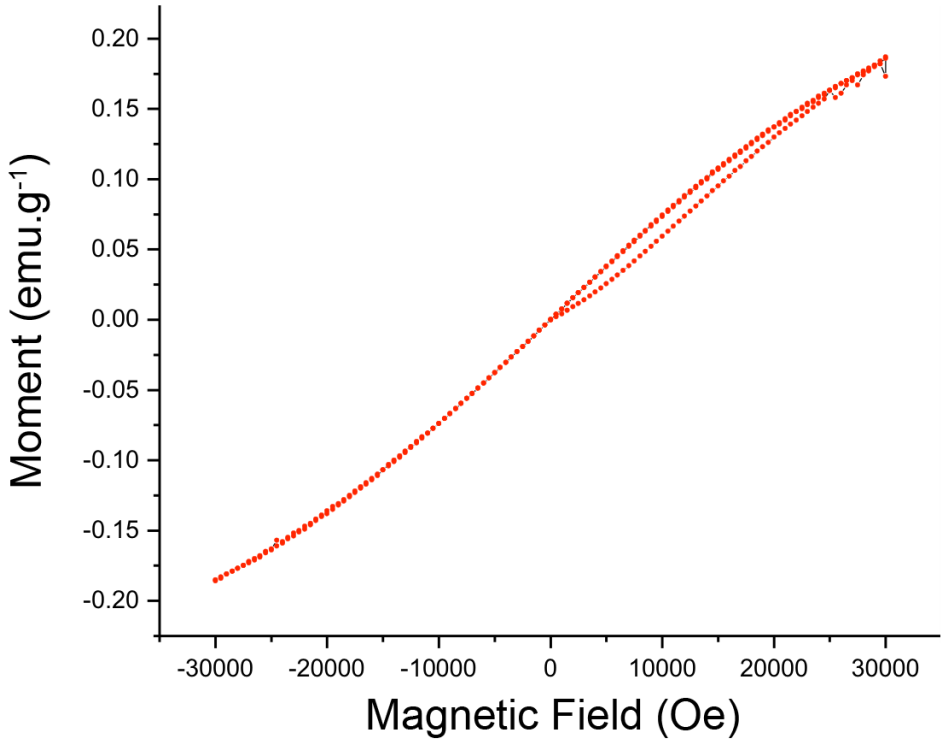


Figure A.3: Magnetic properties of the Quantum Rattle. Magnetisation curve of Quantum Rattles (QR, red dotted line) at 2 K showing paramagnetic properties. These intrinsic QR paramagnetic characteristics could enable efficient MRI imaging, thereby providing another imaging modality to the QR system.

A.4 Statistical Analyses

The statistical analyses were performed using MatLab R2012a (MathWorks).

A.4.1 *In Vitro* Cytotoxicity

MTT Assays

Fluorescein-functionalised Quantum Rattles:

Statistical analysis was performed on the MTT assay of cells cultured in the presence of fluorescein-functionalised QRs (*c.f.* Figure 4.1). A one-way ANOVA combined with a post-hoc Tukey-Kramer Multiple comparisons test was used to statistically assess differences in cell viability at various concentrations ('100%', '10%', '1%' and '0.1%') between thick and thin fluorescein-functionalised QRs ('thick_fQR' and 'thin_fQR', respectively), thick and thin fluorescein-functionalised hollow mesoporous silica particles (HSs) ('thick_fHS' and 'thin_fHS', respectively), medical grade PVC negative control ('Ctrl-') and organo-tin PVC positive control ('Ctrl+'). These differences were then deemed significant if the probability of the results occurring by random chance was less than 5% ($p < 0.05$).

Listing A.1: Statistical significance calculation MatLab script for the MTT assay of cells cultured in the presence of fluorescein-functionalised Quantum Rattles.

```
close all;
clear all;

p1 = 0.05;

load MTT_fQR;
res = Res';
groups={'Ctrl- 100%' 'Ctrl- 10%' 'Ctrl- 1%' 'Ctrl- 0.1%'
   'Ctrl+ 100%' 'Ctrl+ 10%' 'Ctrl+ 1%' 'Ctrl+ 0.1%' '
   thick HS 100%' 'thick HS 10%' 'thick HS 1%' 'thick HS
   0.1%' 'thick QR 100%' 'thick QR 10%' 'thick QR 1%' '
   thick QR 0.1%' 'thin HS 100%' 'thin HS 10%' 'thin HS
   1%' 'thin HS 0.1%' 'thin QR 100%' 'thin QR 10%' 'thin
   QR 1%' 'thin QR 0.1%'};
```

```
[p2,t,st] = anova1(res,groups);

figure;
[c,m,h,nms] = multcompare(st, 'alpha', p1, 'ctype', 'hsd'
    );
[nms num2cell(m)]
```

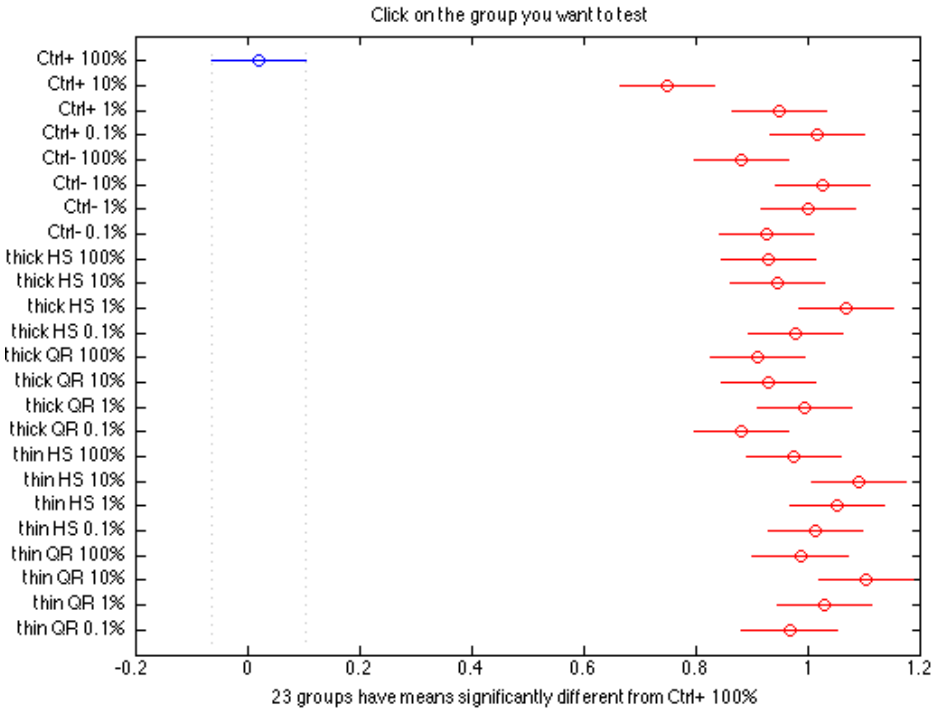


Figure A.4: Multicomparison test for the MTT assay of cells cultured in the presence of fluorescein-functionalised Quantum Rattles.

Native Quantum Rattles:

Statistical analysis was performed on the MTT assay of cells cultured in the presence of QRs (*c.f.* Figure 4.2). A one-way ANOVA combined with a post-hoc Tukey-Kramer Multiple comparisons test was used to statistically assess differences in cell viability at two time points ('1day' and '3days') between thick and thin QRs ('thick_QR' and 'thin_QR', respectively),

thick and thin HSs ('thick_HS' and 'thin_HS', respectively), medical grade PVC negative control (group 'Ctrl-') and organo-tin PVC positive control ('Ctrl+'). These differences were then deemed significant if the probability of the results occurring by random chance was less than 5% ($p < 0.05$).

Listing A.2: Statistical significance calculation MatLab script for the MTT assay of cells cultured in the presence of Quantum Rattles.

```
1  close all;
2  clear all;
3
4  p1 = 0.05;
5
6  load MTT_QR;
7  res = Res';
8  groups={'Ctrl+ 1day' 'Ctrl- 1day' 'thick HS 1day' 'thick
       QR 1day' 'thin HS 1day' 'thin QR 1day' 'Ctrl+ 3days' '
       Ctrl- 3days' 'thick HS 3days' 'thick QR 3days' 'thin
       HS 3days' 'thin QR 3days'};
9  [p2,t,st] = anova1(res,groups);
10
11 figure;
12 [c,m,h,nms] = multcompare(st, 'alpha', p1, 'ctype', 'hsd'
       );
13 [nms num2cell(m)]
```

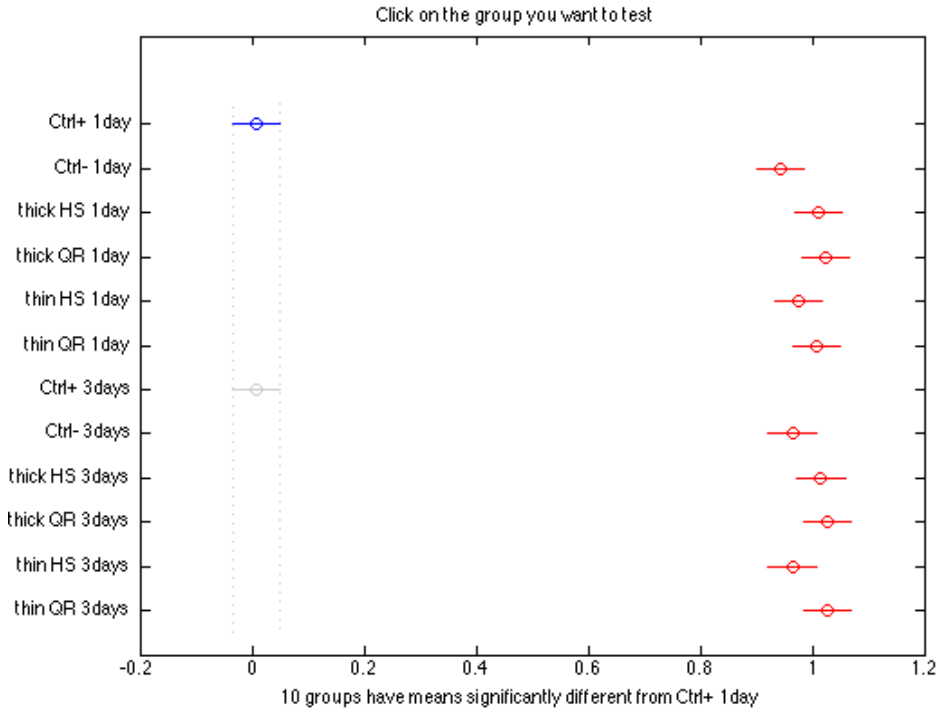


Figure A.5: Multicomparison test for the MTT assay of cells cultured in the presence of Quantum Rattles.

Total DNA Assays

Statistical analysis was performed on the tDNA assay of cells cultured in the presence of QRs (*c.f.* Figure 4.3). A one-way ANOVA combined with a post-hoc Tukey-Kramer Multiple comparisons test was used to statistically assess differences in cell proliferation at two time points ('1day' and '3days') between thick and thin QRs ('thick_QR' and 'thin_QR', respectively), thick and thin HSs ('thick_HS' and 'thin_HS', respectively), medical grade PVC negative control ('Ctrl-') and organo-tin PVC positive control ('Ctrl+'). These differences were then deemed significant if the probability of the results occurring by random chance was less than 5% ($p < 0.05$).

Listing A.3: Statistical significance calculation MatLab script for the tDNA assay of cells cultured in the presence of Quantum Rattles.

```
close all;
clear all;

p1 = 0.05;

load tDNA;
res = Res';
groups={'Ctrl+ 1day' 'Ctrl- 1day' 'thick HS 1day' 'thick
   QR 1day' 'thin HS 1day' 'thin QR 1day' 'Ctrl+ 3days' '
   Ctrl- 3days' 'thick HS 3days' 'thick QR 3days' 'thin
   HS 3days' 'thin QR 3days'};
[p2,t,st] = anova1(res,groups);

figure;
[c,m,h,nms] = multcompare(st, 'alpha', p1, 'ctype', 'hsd'
   );
[nms num2cell(m)]
```

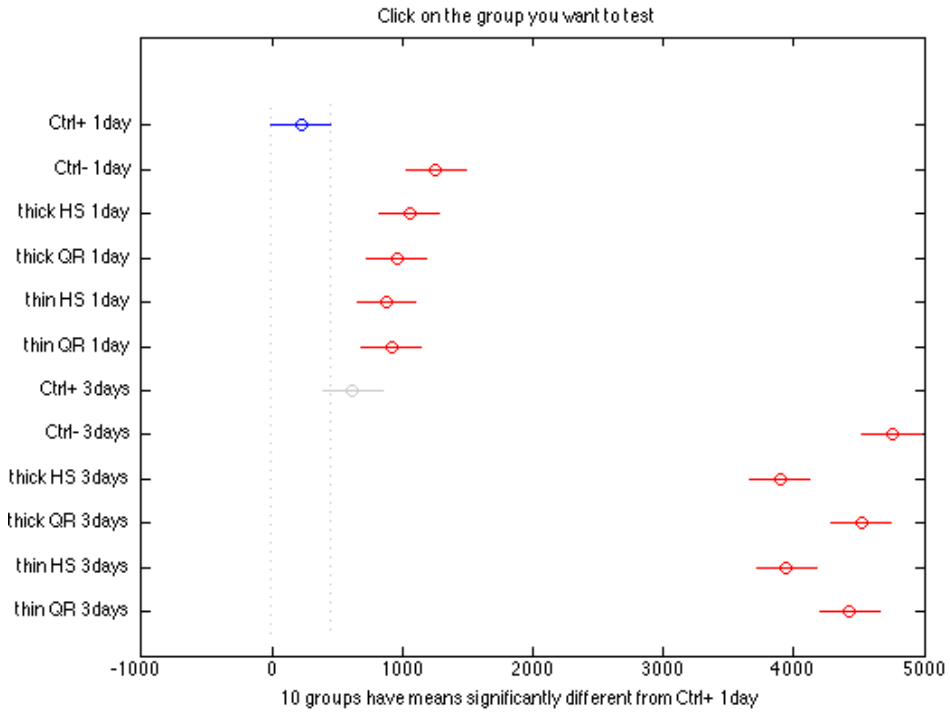


Figure A.6: Multicomparison test for the tDNA assay of cells cultured in the presence of Quantum Rattles.

A.4.2 LIVE/DEAD Quantification Study

LIVE/DEAD quantification study for the HeLa cell population inside the NIR laser spot:

Statistical analysis was performed on the LIVE/DEAD assay quantification results of the cell population inside the laser spot (*c.f.* Figure 5.9). A one-way ANOVA combined with a post-hoc Tukey-Kramer Multiple comparisons test was used to statistically assess differences in cell death at different NIR irradiation time treatment between the QRs ('0min' '2min' '5min' '8min' '10min' '15min', depending on the NIR irradiation time), HS control ('HS') and no particle control ('blank'). These differences were then deemed significant if the probability of the results occurring by random chance was less than 1% ($p < 0.01$).

Listing A.4: Statistical significance calculation MatLab script for the LIVE/DEAD study of the cell population inside the laser spot, which has been incubated with Quantum Rattles and treated with NIR light.

```
close all;
clear all;

p1 = 0.01;

load Keff;
res = Res';
groups={'blank' 'HS' '0min' '2min' '5min' '8min' '10min'
   '15min'};
[p2,t,st] = anova1(res,groups);

figure;
[c,m,h,nms] = multcompare(st, 'alpha', p1, 'ctype', 'hsd'
   );
[nms num2cell(m)]
```

LIVE/DEAD quantification study for the HeLa cell population outside the

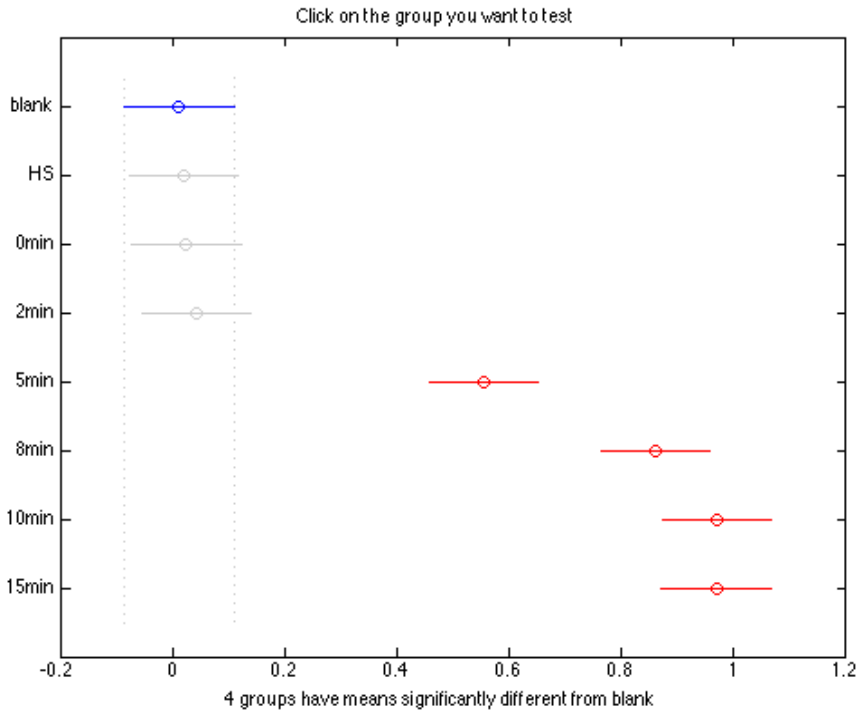


Figure A.7: Multicomparison test for the LIVE/DEAD study of the cell population inside the laser spot, which has been incubated with Quantum Rattles and treated with NIR light.

NIR laser spot:

Statistical analysis was performed on the LIVE/DEAD assay results of the cell population adjacent to the laser spot (*c.f.* Figure 5.10). A one-way ANOVA combined with a post-hoc Tukey-Kramer Multiple comparisons test was used to statistically assess differences in cell death at different NIR irradiation time treatment between the QRs ('0min' '2min' '5min' '8min' '10min' '15min', depending on the NIR irradiation time), HS control ('HS') and no particle control ('blank'). These differences were then deemed significant if the probability of the results occurring by random chance was less than 1% ($p < 0.01$).

Listing A.5: Statistical significance calculation MatLab script for the LIVE/DEAD study of the cell population adjacent to the laser spot, which has been incubated with Quantum Rattles and treated with NIR light.

```
close all;
clear all;

p1 = 0.01;

load Keff_OUT;
res = Res';
groups={'blank' 'HS' '0min' '2min' '5min' '8min' '10min'
   '15min'};
[p2,t,st] = anova1(res,groups);

figure;
[c,m,h,nms] = multcompare(st, 'alpha', p1, 'ctype', 'hsd'
   );
[nms num2cell(m)]
```

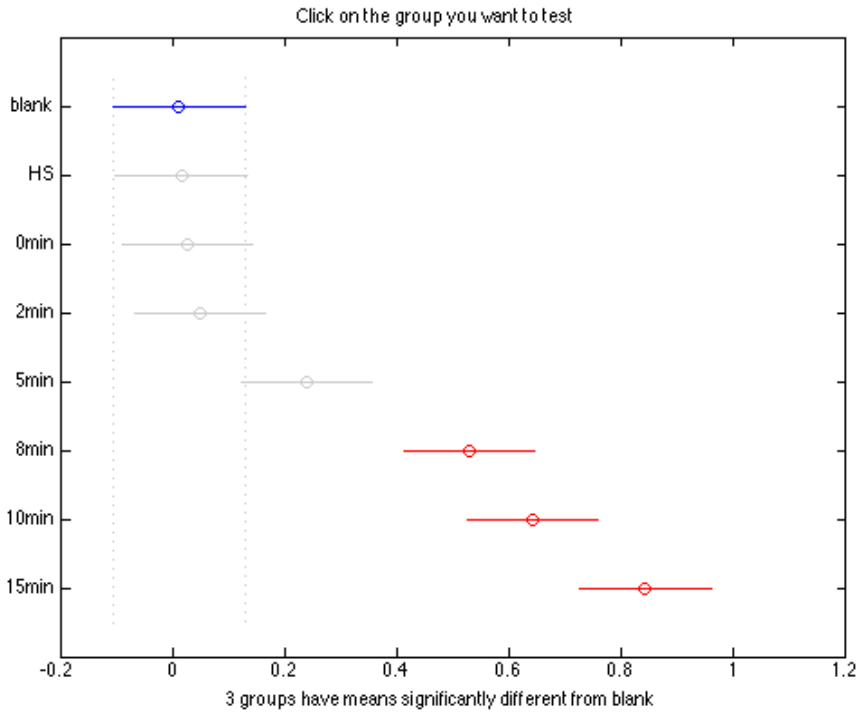


Figure A.8: Multicomparison test for the LIVE/DEAD study of the cell population adjacent to the laser spot, which has been incubated with Quantum Rattles and treated with NIR light.

A.4.3 *Ex Vivo* Assessment of the Quantum Rattles Photothermal Properties Study

Statistical analysis was performed on the *ex vivo* assessment of the Quantum Rattles photothermal properties study (*c.f.* Figure 5.11). A one-way ANOVA combined with a post-hoc Tukey-Kramer Multiple comparisons test was used to statistically assess differences in the maximum temperature increase between the QRs ('QR'), PBS control ('PBS) and no injection control ('Ctrl-'). These differences were then deemed significant if the probability of the results occurring by random chance was less than 1% ($p < 0.01$).

Listing A.6: Statistical significance calculation MatLab script for the *ex vivo* assessment of the Quantum Rattles photothermal properties study.

```
close all;
clear all;

p1 = 0.01;

load ExVivo;
res = Res';
groups={'Ctrl-' 'PBS' 'QR'};
[p2,t,st] = anova1(res,groups);

figure;
[c,m,h,nms] = multcompare(st, 'alpha', p1, 'ctype', 'hsd'
   );
[nms num2cell(m)]
```

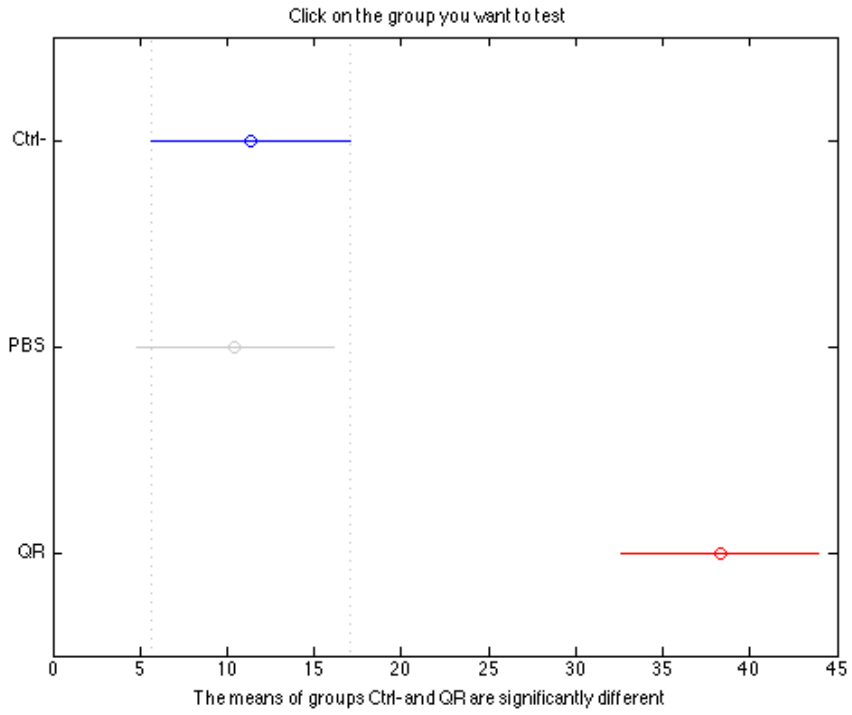


Figure A.9: Multicomparison test for the *ex vivo* assessment of the Quantum Rattles photothermal properties study.

A.4.4 Drug Delivery Study

Doxorubicin loading efficiency study:

Statistical analysis was performed on the doxorubicin (DOX) loading efficiency study (*c.f.* Figure 6.1). A one-way ANOVA combined with a post-hoc Tukey-Kramer Multiple comparisons test was used to statistically assess differences in DOX loading efficiency between the QRs ('QR'), HSs ('HS') and non-hollow Quantum Rattles (NQRs) ('NQR'). These differences were then deemed significant if the probability of the results occurring by random chance was less than 5% ($p < 0.05$).

Listing A.7: Statistical significance calculation MatLab script for the Quantum Rattles doxorubicin loading efficiency study.

```
close all;
clear all;

p1 = 0.05;

load DOXload;
res = Res';
groups={'HS 0.5 mg/mL' 'HS 0.25 mg/mL' 'HS 0.125 mg/mL' '
   HS 0.0625 mg/mL' 'HS 0.03125 mg/mL' 'HS 0.015625 mg/mL
   ' 'NQR 0.5 mg/mL' 'NQR 0.25 mg/mL' 'NQR 0.125 mg/mL' '
   NQR 0.0625 mg/mL' 'NQR 0.03125 mg/mL' 'NQR 0.015625 mg
   /mL' 'QR 0.5 mg/mL' 'QR 0.25 mg/mL' 'QR 0.125 mg/mL' '
   QR 0.0625 mg/mL' 'QR 0.03125 mg/mL' 'QR 0.015625 mg/mL
   '};
[p2,t,st] = anova1(res,groups);

figure;
[c,m,h,nms] = multcompare(st, 'alpha', p1, 'ctype', 'hsd'
   );
[nms num2cell(m)]
```

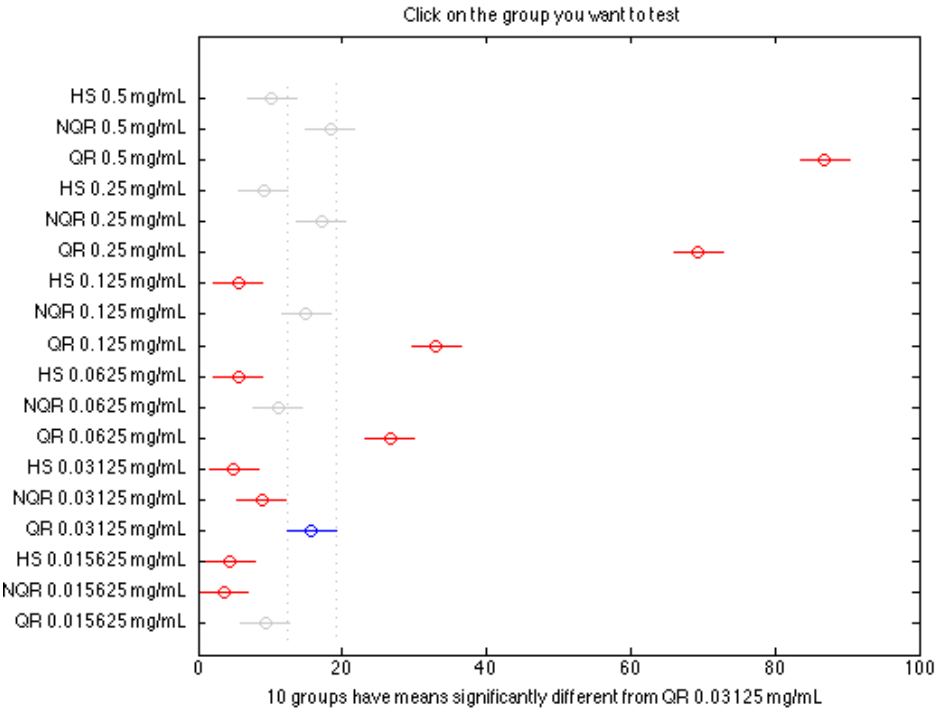


Figure A.10: Multicomparison test for the Quantum Rattles doxorubicin loading efficiency study.

Doxorubicin release study:

Statistical analysis was performed on the DOX release study (*c.f.* Figure 6.2). A one-way ANOVA combined with a post-hoc Tukey-Kramer Multiple comparisons test was used to statistically assess differences in DOX release kinetics between the QRs ('QR') HSs ('HS') and NQRs ('NQR'). These differences were then deemed significant if the probability of the results occurring by random chance was less than 5% ($p < 0.05$).

Listing A.8: Statistical significance calculation MatLab script for the Quantum Rattles doxorubicin release study.

```
1 close all;
2 clear all;
3
4 p1 = 0.05;
```

```
5
6  load DOXrelease;
7  res = Res';
8  groups={'HS 0.5h' 'NQR 0.5h' 'QR 0.5h' 'HS 1h' 'NQR 1h' '
       QR 1h' 'HS 2h'  'NQR 2h' 'QR 2h' 'HS 4h' 'NQR 4h' 'QR
       4h' 'HS 8h' 'NQR 8h' 'QR 8h' 'HS 12h' 'NQR 12h' 'QR 12
       h' 'HS 24h' 'NQR 24h' 'QR 24h'};
9  [p2,t,st] = anova1(res,groups);
10
11 figure;
12 [c,m,h,nms] = multcompare(st, 'alpha', p1, 'ctype', 'hsd'
       );
13 [nms num2cell(m)]
```

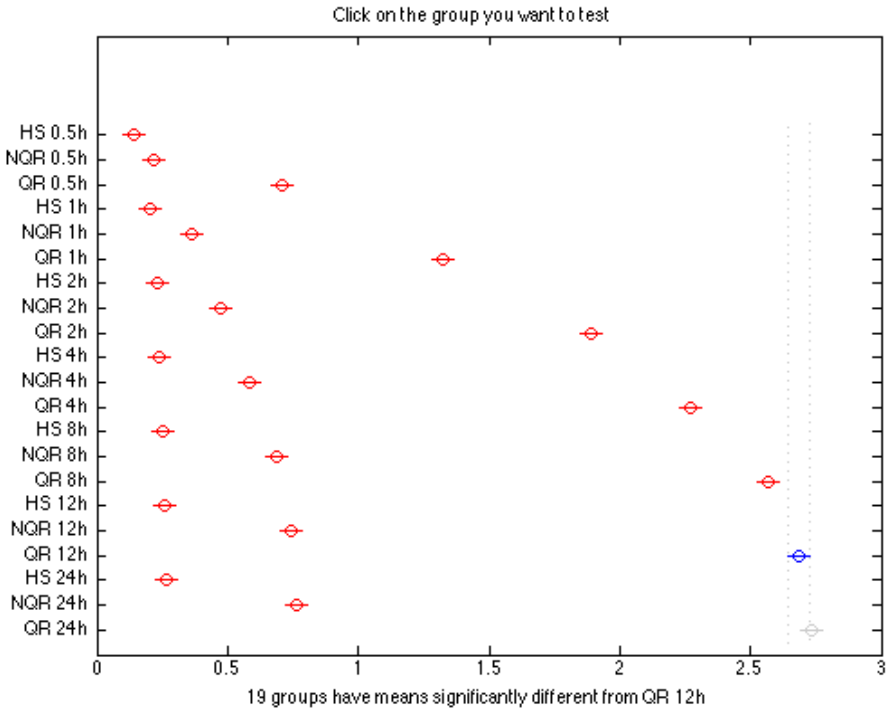
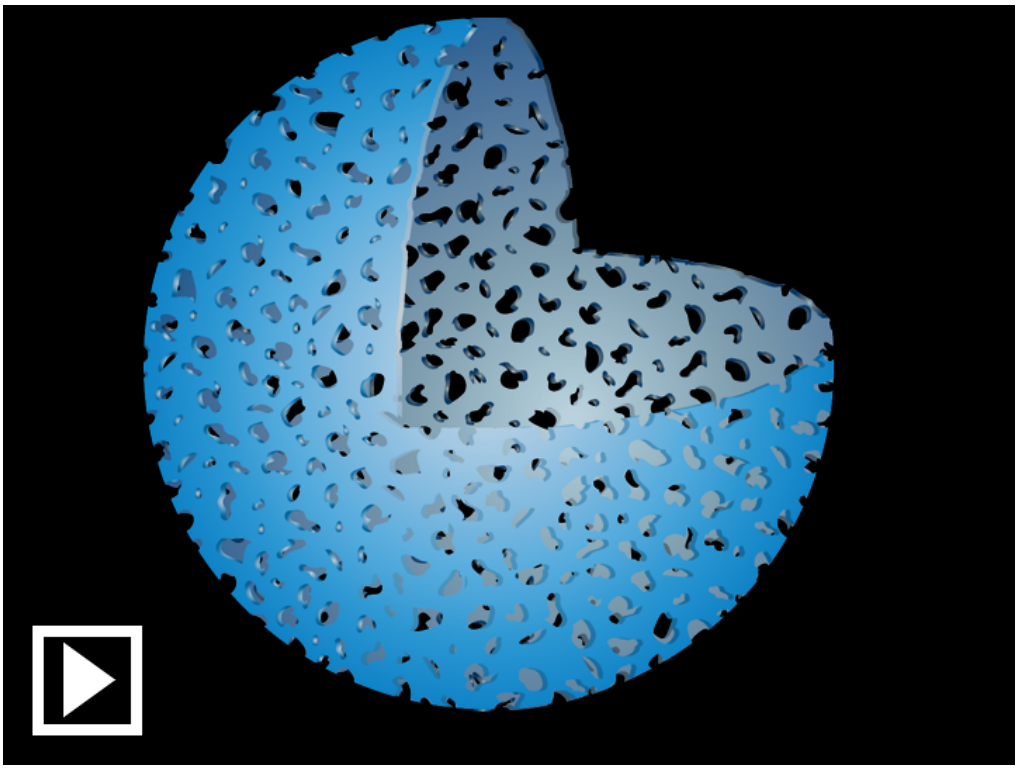
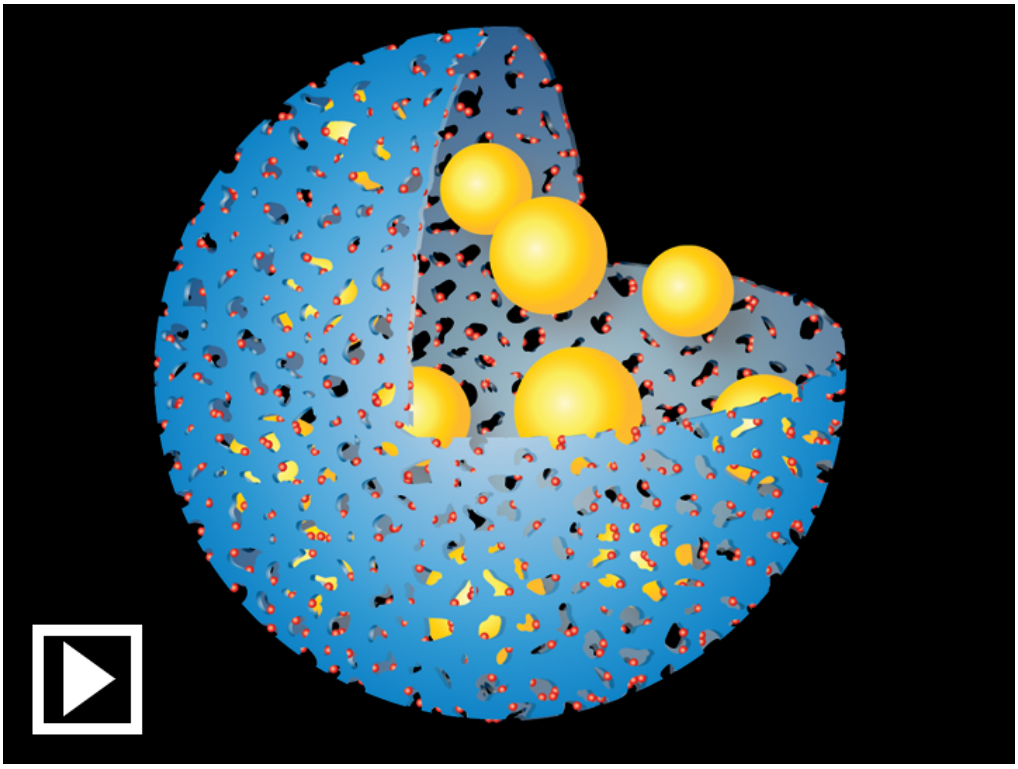


Figure A.11: Multicomparison test for the Quantum Rattles doxorubicin release study.

A.5 Thermal Camera Movies - Real-Time Temperature Acquisition



Movie A.1: Hollow mesoporous silica particles photothermal properties. Movie showing the real-time acquisition by a thermal camera of the temperature profile of a coverslip with hollow mesoporous silica particles (HSs) drop-deposited on its surface. No heat increase is observed when a 671 nm laser is irradiated on the HS. *(Click to play. Requires Adobe Reader 8.× or higher)*



Movie A.2: Quantum Rattles photothermal properties. Movie showing the real-time acquisition by a thermal camera of the temperature profile of a coverslip with Quantum Rattles (QRs) drop-deposited on its surface. A temperature increase of $\sim$ 1.5 °C is observed upon irradiation by a 671 nm laser of the QR sample. *(Click to play. Requires Adobe Reader 8.× or higher)*

A.6 LIVE/DEAD Assay Quantification - Killing Efficiency

After the raw fluorescent images of the LIVE/DEAD assays (*c.f.* section 5.2.2) were cropped to the laser spot (1 mm disk) or the adjacent area to the laser spot (0.3 mm thick ring around laser spot) they were segmented using MatLab R2012a (MathWorks) to obtain binary images representing the surface of live and dead cells, respectively. Images were loaded as IMxy, where $x = g$ or r refers to either the LIVE (green, g) or DEAD (red, r) images and $y = 1$ - 8 refers to the different conditions (1: Cell only control, 2: HS control, 3 - 8: QRs with 0, 2, 5, 8, 10 or 15 min laser irradiation). Both thresholds for the red (Tr) and green (Tg) images series are set manually by examining the histograms figure (1) and (2) in the script.

Listing A.9: LIVE/DEAD assay quantification. Segmentation script for the fluorescent images obtained from the LIVE/DEAD study and percentage cell death computation.

```
%% Segmentation

close all,

% Thresholds values defined iteratively
Tg = 80;
Tr = 10;

% Convert rgb images to grayscale
Gg1 = rgb2gray(IMg1);
Gg2 = rgb2gray(IMg2);
Gg3 = rgb2gray(IMg3);
Gg4 = rgb2gray(IMg4);
Gg5 = rgb2gray(IMg5);
Gg6 = rgb2gray(IMg6);
```

```
16 Gg7 = rgb2gray(IMg7);
17 Gg8 = rgb2gray(IMg8);
18
19 Gr1 = rgb2gray(IMr1);
20 Gr2 = rgb2gray(IMr2);
21 Gr3 = rgb2gray(IMr3);
22 Gr4 = rgb2gray(IMr4);
23 Gr5 = rgb2gray(IMr5);
24 Gr6 = rgb2gray(IMr6);
25 Gr7 = rgb2gray(IMr7);
26 Gr8 = rgb2gray(IMr8);
27
28
29
30 % Definition of red, green and blue colourmaps for image
      display
31 % column_ramp = [0:1/255:1]';
32 % redmap = [column_ramp,zeros(256,1),zeros(256,1)];
33 % greenmap = [zeros(256,1),column_ramp,zeros(256,1)];
34 % bluemap = [zeros(256,1),zeros(256,1),column_ramp];
35 % figure;
36 % subplot(1,2,1);colormap(greenmap);imagesc(Gg5);
37 % subplot(1,2,2);colormap(redmap);imagesc(Gr5);
38
39 % Matrices conversion for histograms display. Histograms
      were used to set Tr and Tg.
40 Gg1 = double(Gg1);
41 gg1 = Gg1(:);
42 Gg2 = double(Gg2);
43 gg2 = Gg2(:);
44 Gg3 = double(Gg3);
45 gg3 = Gg3(:);
46 Gg4 = double(Gg4);
47 gg4 = Gg4(:);
48 Gg5 = double(Gg5);
```

```
gg5 = Gg5(:);
Gg6 = double(Gg6);
gg6 = Gg6(:);
Gg7 = double(Gg7);
gg7 = Gg7(:);
Gg8 = double(Gg8);
gg8 = Gg8(:);

Gr1 = double(Gr1);
gr1 = Gr1(:);
Gr2 = double(Gr2);
gr2 = Gr2(:);
Gr3 = double(Gr3);
gr3 = Gr3(:);
Gr4 = double(Gr4);
gr4 = Gr4(:);
Gr5 = double(Gr5);
gr5 = Gr5(:);
Gr6 = double(Gr6);
gr6 = Gr6(:);
Gr7 = double(Gr7);
gr7 = Gr7(:);
Gr8 = double(Gr8);
gr8 = Gr8(:);

% figure(1);
% subplot(2,8,1); image(IMg1);title('1');
% subplot(2,8,2); image(IMg2);title('2');
% subplot(2,8,3); image(IMg3);title('3');
% subplot(2,8,4); image(IMg4);title('4');
% subplot(2,8,5); image(IMg5);title('5');
% subplot(2,8,6); image(IMg6);title('6');
% subplot(2,8,7); image(IMg7);title('7');
% subplot(2,8,8); image(IMg8);title('8');
% subplot(2,8,9); hist(gg1,100);title('9');
```

```
% subplot(2,8,10); hist(gg2,100);title('10');
% subplot(2,8,11); hist(gg3,100);title('11');
% subplot(2,8,12); hist(gg4,100);title('12');
% subplot(2,8,13); hist(gg5,100);title('13');
% subplot(2,8,14); hist(gg6,100);title('14');
% subplot(2,8,15); hist(gg7,100);title('15');
% subplot(2,8,16); hist(gg8,100);title('16');
%
% figure(2);
% subplot(2,8,1); image(IMr1);title('1');
% subplot(2,8,2); image(IMr2);title('2');
% subplot(2,8,3); image(IMr3);title('3');
% subplot(2,8,4); image(IMr4);title('4');
% subplot(2,8,5); image(IMr5);title('5');
% subplot(2,8,6); image(IMr6);title('6');
% subplot(2,8,7); image(IMr7);title('7');
% subplot(2,8,8); image(IMr8);title('8');
% subplot(2,8,9); hist(gr1,100);title('9');
% subplot(2,8,10); hist(gr2,100);title('10');
% subplot(2,8,11); hist(gr3,100);title('11');
% subplot(2,8,12); hist(gr4,100);title('12');
% subplot(2,8,13); hist(gr5,100);title('13');
% subplot(2,8,14); hist(gr6,100);title('14');
% subplot(2,8,15); hist(gr7,100);title('15');
% subplot(2,8,16); hist(gr8,100);title('16');

% Thresholding
gg1bin = (Gg1 > Tg);
gg2bin = (Gg2 > Tg);
gg3bin = (Gg3 > Tg);
gg4bin = (Gg4 > Tg);
gg5bin = (Gg5 > Tg);
gg6bin = (Gg6 > Tg);
gg7bin = (Gg7 > Tg);
gg8bin = (Gg8 > Tg);
```

```
119
120 gr1bin = (Gr1 > Tr);
121 gr2bin = (Gr2 > Tr);
122 gr3bin = (Gr3 > Tr);
123 gr4bin = (Gr4 > Tr);
124 gr5bin = (Gr5 > Tr);
125 gr6bin = (Gr6 > Tr);
126 gr7bin = (Gr7 > Tr);
127 gr8bin = (Gr8 > Tr);
128
129 % Quantification of the LIVE and DEAD coefficient
130 LIVE1 = sum(gg1bin(:));
131 LIVE2 = sum(gg2bin(:));
132 LIVE3 = sum(gg3bin(:));
133 LIVE4 = sum(gg4bin(:));
134 LIVE5 = sum(gg5bin(:));
135 LIVE6 = sum(gg6bin(:));
136 LIVE7 = sum(gg7bin(:));
137 LIVE8 = sum(gg8bin(:));
138
139 DEAD1 = sum(gr1bin(:));
140 DEAD2 = sum(gr2bin(:));
141 DEAD3 = sum(gr3bin(:));
142 DEAD4 = sum(gr4bin(:));
143 DEAD5 = sum(gr5bin(:));
144 DEAD6 = sum(gr6bin(:));
145 DEAD7 = sum(gr7bin(:));
146 DEAD8 = sum(gr8bin(:));
147
148 % Figure of the segementation results
149 figure('Color',[0 0 0]); colormap(gray(256));
150 subplot(4,8,1); imagesc(IMg1);title('Blank','fontsize'
      ,12,'Color',[1 1 1]);axis ('image','off');
151 subplot(4,8,2); imagesc(IMg2);title('HS','fontsize',12,'
      Color',[1 1 1]);axis ('image','off');
```

```
152 subplot(4,8,3); imagesc(IMg3);title('0m','fontsize',12,'
    Color',[1 1 1]);axis ('image','off');
153 subplot(4,8,4); imagesc(IMg4);title('2m','fontsize',12,'
    Color',[1 1 1]);axis ('image','off');
154 subplot(4,8,5); imagesc(IMg5);title('5m','fontsize',12,'
    Color',[1 1 1]);axis ('image','off');
155 subplot(4,8,6); imagesc(IMg6);title('8m','fontsize',12,'
    Color',[1 1 1]);axis ('image','off');
156 subplot(4,8,7); imagesc(IMg7);title('10m','fontsize',12,'
    Color',[1 1 1]);axis ('image','off');
157 subplot(4,8,8); imagesc(IMg8);title('15m','fontsize',12,'
    Color',[1 1 1]);axis ('image','off');
158 subplot(4,8,9); imagesc(gg1bin);axis ('image','off');
159 subplot(4,8,10); imagesc(gg2bin);axis ('image','off');
160 subplot(4,8,11); imagesc(gg3bin);axis ('image','off');
161 subplot(4,8,12); imagesc(gg4bin);axis ('image','off');
162 subplot(4,8,13); imagesc(gg5bin);axis ('image','off');
163 subplot(4,8,14); imagesc(gg6bin);axis ('image','off');
164 subplot(4,8,15); imagesc(gg7bin);axis ('image','off');
165 subplot(4,8,16); imagesc(gg8bin);axis ('image','off');
166 subplot(4,8,17); imagesc(IMr1);axis ('image','off');
167 subplot(4,8,18); imagesc(IMr2);axis ('image','off');
168 subplot(4,8,19); imagesc(IMr3);axis ('image','off');
169 subplot(4,8,20); imagesc(IMr4);axis ('image','off');
170 subplot(4,8,21); imagesc(IMr5);axis ('image','off');
171 subplot(4,8,22); imagesc(IMr6);axis ('image','off');
172 subplot(4,8,23); imagesc(IMr7);axis ('image','off');
173 subplot(4,8,24); imagesc(IMr8);axis ('image','off');
174 subplot(4,8,25); imagesc(gr1bin);axis ('image','off');
175 subplot(4,8,26); imagesc(gr2bin);axis ('image','off');
176 subplot(4,8,27); imagesc(gr3bin);axis ('image','off');
177 subplot(4,8,28); imagesc(gr4bin);axis ('image','off');
178 subplot(4,8,29); imagesc(gr5bin);axis ('image','off');
179 subplot(4,8,30); imagesc(gr6bin);axis ('image','off');
180 subplot(4,8,31); imagesc(gr7bin);axis ('image','off');
```

```
181 subplot(4,8,32); imagesc(gr8bin);axis ('image','off');
182
183 IM1 = IMg1 + IMr1;
184 IM2 = IMg2 + IMr2;
185 IM3 = IMg3 + IMr3;
186 IM4 = IMg4 + IMr4;
187 IM5 = IMg5 + IMr5;
188 IM6 = IMg6 + IMr6;
189 IM7 = IMg7 + IMr7;
190 IM8 = IMg8 + IMr8;
191
192 % Figure of the cropped and merged image
193 figure('Color',[0 0 0]); colormap(gray(256));
194 subplot(3,3,7); imagesc(IM1);title('Blank','fontsize',12,
       'Color',[1 1 1]);axis ('image','off');
195 subplot(3,3,8); imagesc(IM2);title('HS','fontsize',12,'
       Color',[1 1 1]);axis ('image','off');
196 subplot(3,3,1); imagesc(IM3);title('0m','fontsize',12,'
       Color',[1 1 1]);axis ('image','off');
197 subplot(3,3,2); imagesc(IM4);title('2m','fontsize',12,'
       Color',[1 1 1]);axis ('image','off');
198 subplot(3,3,3); imagesc(IM5);title('5m','fontsize',12,'
       Color',[1 1 1]);axis ('image','off');
199 subplot(3,3,4); imagesc(IM6);title('8m','fontsize',12,'
       Color',[1 1 1]);axis ('image','off');
200 subplot(3,3,5); imagesc(IM7);title('10m','fontsize',12,'
       Color',[1 1 1]);axis ('image','off');
201 subplot(3,3,6); imagesc(IM8);title('15m','fontsize',12,'
       Color',[1 1 1]);axis ('image','off');
202
203 S = [[1 LIVE1 DEAD1];[2 LIVE2 DEAD2];[3 LIVE3 DEAD3];[4
       LIVE4 DEAD4];[5 LIVE5 DEAD5];[6 LIVE6 DEAD6];[7 LIVE7
       DEAD7];[8 LIVE8 DEAD8]];
204
205 LIVE = [LIVE1 LIVE2 LIVE3 LIVE4 LIVE5 LIVE6 LIVE7 LIVE8];
```

```
206 DEAD = [DEAD1 DEAD2 DEAD3 DEAD4 DEAD5 DEAD6 DEAD7 DEAD8];
207
208 %Killing efficiency calculation
209 Keff = [DEAD1/(DEAD1+LIVE1) DEAD2/(DEAD2+LIVE2) DEAD3/(
       DEAD3+LIVE3) DEAD4/(DEAD4+LIVE4) DEAD5/(DEAD5+LIVE5)
       DEAD6/(DEAD6+LIVE6) DEAD7/(DEAD7+LIVE7) DEAD8/(DEAD8+
       LIVE8)];
210
211 %Displays results in the command window of MatLab
212 Tg,Tr,
213 S,
214 Keff = Keff(:)
```

Bibliography

[1] Kelly, K. L, Coronado, E, Zhao, L. L, & Schatz, G. C. (2003) The Optical Properties of Metal Nanoparticles: The Influence of Size, Shape, and Dielectric Environment. *Journal of Physical Chemistry B* **107**, 668–677.

[2] Zhu, M, Aikens, C, Hollander, F, Schatz, G, & Jin, R. (2008) Correlating the crystal structure of a thiol-protected Au25 cluster and optical properties. *Journal of the American Chemical Society* **130**, 5883–5885.

[3] Liu, J, Qiao, S. Z, Chen, J. S, Lou, X. W. D, Xing, X, & Lu, G. Q. M. (2011) Yolk/shell nanoparticles: new platforms for nanoreactors, drug delivery and lithium-ion batteries. *Chemical communications (Cambridge, England)* **47**, 12578–12591.

[4] Lee, J, Park, J. C, & Song, H. (2008) A Nanoreactor Framework of a Au@SiO2 Yolk/Shell Structure for Catalytic Reduction of p-Nitrophenol. *Advanced Materials* **20**, 1523–1528.

[5] Wu, S.-H, Tseng, C.-T, Lin, Y.-S, Lin, C.-H, Hung, Y, & Mou, C.-Y. (2010) Catalytic nano-rattle of Au@hollow silica: towards a poison-resistant nanocatalyst. *Journal of Materials Chemistry* **21**, 789–794.

[6] Dreaden, E. C, Mackey, M. A, Huang, X, Kang, B, & El-Sayed, M. A. (2011) Beating cancer in multiple ways using nanogold. *Chemical Society Reviews* **40**, 3391–3404.

[7] Huang, Y, He, S, Cao, W, Cai, K, & Liang, X.-J. (2012) Biomedical nanomaterials for imaging-guided cancer therapy. *Nanoscale* **4**, 6135–6149.

[8] Weissleder, R. (2001) A clearer vision for in vivo imaging. *Nature Biotechnology* **19**, 316–317.

[9] Faraji, A. H & Wipf, P. (2009) Nanoparticles in cellular drug delivery. *Bioorganic & Medicinal Chemistry* **17**, 2950–2962.

[10] Alivisatos, A. P. (1996) Semiconductor Clusters, Nanocrystals, and Quantum Dots. *Science (New York, NY)* **271**, 933–937.

[11] Daniel, M & Astruc, D. (2004) Gold nanoparticles: Assembly, supramolecular chemistry, quantum-size-related properties, and applications toward biology, catalysis, and nanotechnology. *Chemical Reviews* **104**, 293–346.

[12] Nealon, G. L, Donnio, B, Greget, R, Kappler, J.-P, Terazzi, E, & Gallani, J.-L. (2012) Magnetism in gold nanoparticles. *Nanoscale* **4**, 5244–5258.

[13] Yu, M, Files, B, Arepalli, S, & Ruoff, R. (2000) Tensile loading of ropes of single wall carbon nanotubes and their mechanical properties. *Physical Review Letters* **84**, 5552–5555.

[14] Baron, R, Willner, B, & Willner, I. (2007) Biomolecule-nanoparticle hybrids as functional units for nanobiotechnology. *Chemical Communications* pp. 323–332.

[15] Ghadiali, J. E & Stevens, M. M. (2008) Enzyme-responsive nanoparticle systems. *Advanced materials (Deerfield Beach, Fla.)* **20**, 4359–4363.

[16] Ghadiali, J. E, Cohen, B. E, & Stevens, M. M. (2010) Protein kinase-actuated resonance energy transfer in quantum dot-peptide conjugates. *ACS Nano* **4**, 4915–4919.

[17] Lowe, S. B, Dick, J. A. G, Cohen, B. E, & Stevens, M. M. (2011) Multiplex Sensing of Protease and Kinase Enzyme Activity via Orthogonal Coupling of Quantum Dot-Peptide Conjugates. *ACS Nano* **6**, 851–857.

[18] Gupta, S, Andresen, H, Ghadiali, J. E, & Stevens, M. M. (2010) Kinase-Actuated Immunoaggregation of Peptide-Conjugated Gold Nanoparticles. *Small* **6**, 1509–1513.

[19] Ghadiali, J. E, Lowe, S. B, & Stevens, M. M. (2011) Quantum-Dot-Based FRET Detection of Histone Acetyltransferase Activity. *Angewandte Chemie* **123**, 3479–3482.

[20] Aili, D, Mager, M, Roche, D, & Stevens, M. M. (2011) Hybrid nanoparticle-liposome detection of phospholipase activity. *Nano Letters* **11**, 1401–1405.

[21] Sailor, M. J & Park, J.-H. (2012) Hybrid nanoparticles for detection and treatment of cancer. *Advanced materials (Deerfield Beach, Fla.)* **24**, 3779–3802.

[22] Jemal, A, Siegel, R, Xu, J, & Ward, E. (2010) Cancer statistics, 2010. *CA: a cancer journal for clinicians* **60**, 277–300.

[23] Llevot, A & Astruc, D. (2012) Applications of vectorized gold nanoparticles to the diagnosis and therapy of cancer. *Chemical Society Reviews* **41**, 242–257.

[24] Ferrari, M. (2005) Cancer nanotechnology: opportunities and challenges. *Nature Reviews Cancer* **5**, 161–171.

[25] Minelli, C, Lowe, S. B, & Stevens, M. M. (2010) Engineering Nanocomposite Materials for Cancer Therapy. *Small* **6**, 2336–2357.

[26] Cai, W, Gao, T, Hong, H, & Sun, J. (2008) Applications of gold nanoparticles in cancer nanotechnology. *Nanotechnology Science and Applications* **1**, 17–32.

[27] Pissuwan, D, Valenzuela, S. M, & Cortie, M. B. (2006) Therapeutic possibilities of plasmonically heated gold nanoparticles. *Trends in Biotechnology* **24**, 62–67.

[28] Kennedy, L. C, Bickford, L. R, Lewinski, N. A, Coughlin, A. J, Hu, Y, Day, E. S, West, J. L, & Drezek, R. A. (2011) A new era for cancer

treatment: gold-nanoparticle-mediated thermal therapies. *Small* **7**, 169–183.

[29] Hirsch, L. R, Stafford, R. J, Bankson, J. A, Sershen, S. R, Rivera, B, Price, R. E, Hazle, J. D, Halas, N. J, & West, J. L. (2003) Nanoshell-mediated near-infrared thermal therapy of tumors under magnetic resonance guidance. *Proceedings of the National Academy of Sciences of the United States of America* **100**, 13549–13554.

[30] Park, J.-H, von Maltzahn, G, Xu, M. J, Fogal, V, Kotamraju, V. R, Ruoslahti, E, Bhatia, S. N, & Sailor, M. J. (2010) Cooperative nanomaterial system to sensitize, target, and treat tumors. *Proceedings of the National Academy of Sciences of the United States of America* **107**, 981–986.

[31] Park, J.-H, von Maltzahn, G, Ruoslahti, E, Bhatia, S. N, & Sailor, M. J. (2008) Micellar hybrid nanoparticles for simultaneous magnetofluorescent imaging and drug delivery. *Angewandte Chemie-International Edition* **47**, 7284–7288.

[32] Tkachenko, A, Xie, H, Coleman, D, Glomm, W, Ryan, J, Anderson, M, Franzen, S, & Feldheim, D. (2003) Multifunctional gold nanoparticle-peptide complexes for nuclear targeting. *Journal of the American Chemical Society* **125**, 4700–4701.

[33] Boisselier, E & Astruc, D. (2009) Gold nanoparticles in nanomedicine: preparations, imaging, diagnostics, therapies and toxicity. *Chemical Society Reviews* **38**, 1759–1782.

[34] Laromaine, A, Koh, L, Murugesan, M, Ulijn, R. V, & Stevens, M. M. (2007) Protease-triggered dispersion of nanoparticle assemblies. *Journal of the American Chemical Society* **129**, 4156–4157.

[35] Love, J, Estroff, L, Kriebel, J, Nuzzo, R, & Whitesides, G. (2005) Self-assembled monolayers of thiolates on metals as a form of nanotechnology. *Chemical Reviews* **105**, 1103–1169.

[36] Piner, R, Zhu, J, Xu, F, Hong, S, & Mirkin, C. (1999) "Dip-pen" nanolithography. *Science (New York, NY)* **283**, 661–663.

[37] Templeton, A, Wuelfing, M, & Murray, R. (2000) Monolayer protected cluster molecules. *Accounts Of Chemical Research* **33**, 27–36.

[38] Brust, M, Walker, M, Bethell, D, Schiffrin, D, & Whyman, R. (1994) Synthesis of Thiol-Derivatized Gold Nanoparticles in a 2-Phase Liquid-Liquid System. *Journal of the Chemical Society-Chemical Communications* pp. 801–802.

[39] Niemeyer, C. (2001) Nanoparticles, proteins, and nucleic acids: Biotechnology meets materials science. *Angewandte Chemie-International Edition* **40**, 4128–4158.

[40] Empedocles, S, Neuhauser, R, Shimizu, K, & Bawendi, M. (1999) Photoluminescence from single semiconductor nanostructures. *Advanced Materials* **11**, 1243–1256.

[41] Link, S & El-Sayed, M. (2000) Shape and size dependence of radiative, non-radiative and photothermal properties of gold nanocrystals. *International Reviews in Physical Chemistry* **19**, 409–453.

[42] Faraday, M. (1857) The Bakerian lecture: experimental relations of gold (and other metals) to light. *Philosophical Transactions of the Royal Society of London* **147**, 145–181.

[43] Turkevich, J, Stevenson, P.C., & Hillier, J. (1951) A study of the nucleation and growth processes in the synthesis of colloidal gold. *Discuss. Faraday Soc.* **11**, 55–75.

[44] Frens, G. (1973) Controlled nucleation for the regulation of the particle size in monodisperse gold suspensions. *Nature* **241**, 20–22.

[45] Brust, M, Fink, J, Bethell, D, Schiffrin, D. J, & Kiely, C. (1995) Synthesis and reactions of functionalised gold nanoparticles. *Journal of the Chemical Society-Chemical Communications* pp. 1655–1656.

[46] Jana, N. R & Peng, X. (2003) Single-phase and gram-scale routes toward nearly monodisperse Au and other noble metal nanocrystals. *Journal of the American Chemical Society* **125**, 14280–14281.

[47] Rowe, M. P, Plass, K. E, Kim, K, Kurdak, C, Zellers, E. T, & Matzger, A. J. (2004) Single-phase synthesis of functionalized gold nanoparticles. *Chemistry of Materials* **16**, 3513–3517.

[48] Zheng, N, Fan, J, & Stucky, G. D. (2006) One-Step One-Phase Synthesis of Monodisperse Noble-Metallic Nanoparticles and Their Colloidal Crystals. *Journal of the American Chemical Society* **128**, 6550–6551.

[49] Scholl, J. A, Koh, A. L, & Dionne, J. A. (2012) Quantum plasmon resonances of individual metallic nanoparticles. *Nature* **483**, 421–427.

[50] Hu, M, Chen, J, Li, Z.-Y, Au, L, Hartland, G. V, Li, X, Marquez, M, & Xia, Y. (2006) Gold nanostructures: engineering their plasmonic properties for biomedical applications. *Chemical Society Reviews* **35**, 1084–1094.

[51] Mie, G. (1908) Beiträge zur optik trüber medien, speziell kolloidaler metallösungen. *Annalen der Physik* **25**, 377–445.

[52] Qian, H, Zhu, M, Wu, Z, & Jin, R. (2012) Quantum sized gold nanoclusters with atomic precision. *Accounts Of Chemical Research* **45**, 1470–1479.

[53] Hutter, E & Fendler, J. H. (2004) Exploitation of localized surface plasmon resonance. *Advanced materials (Deerfield Beach, Fla.)* **16**, 1685–1706.

[54] Link, S & El-Sayed, M. A. (1999) Size and Temperature Dependence of the Plasmon Absorption of Colloidal Gold Nanoparticles. *Journal of Physical Chemistry B* **103**, 4212–4217.

[55] Khlebtsov, B, Zharov, V, Melnikov, A, Tuchin, V, & Khlebtsov, N. (2006) Optical amplification of photothermal therapy with gold nanoparticles and nanoclusters. *Nanotechnology* **17**, 5167–5179.

[56] Perner, M, Bost, P, Lemmer, U, vonPlessen, G, Feldmann, J, Becker, U, Mennig, M, Schmitt, M, & Schmidt, H. (1997) Optically induced damping of the surface plasmon resonance in gold colloids. *Physical Review Letters* **78**, 2192–2195.

[57] Goettmann, F, Moores, A, Boissière, C, Le Floch, P, & Sanchez, C. (2005) A Selective Chemical Sensor Based on the Plasmonic Response of Phosphinine-Stabilized Gold Nanoparticles Hosted on Periodically Organized Mesoporous Silica Thin Layers. *Small* **1**, 636–639.

[58] Liu, X, Atwater, M, Wang, J, & Huo, Q. (2007) Extinction coefficient of gold nanoparticles with different sizes and different capping ligands. *Colloids and Surfaces, B: Biointerfaces* **58**, 3–7.

[59] Hostetler, M, Wingate, J, Zhong, C, Harris, J, Vachet, R, Clark, M, Londono, J, Green, S, Stokes, J, Wignall, G, Glish, G, Porter, M, Evans, N, & Murray, R. (1998) Alkanethiolate gold cluster molecules with core diameters from 1.5 to 5.2 nm: Core and monolayer properties as a function of core size. *Langmuir* **14**, 17–30.

[60] Genzel, L, Martin, T. P, & Kreibig, U. (1975) Dielectric function and plasma resonances of small metal particles. *Zeitschrift für Physik B Condensed Matter and Quanta* **21**, 339–346.

[61] Peng, S, McMahon, J. M, Schatz, G. C, Gray, S. K, & Sun, Y. (2010) Reversing the size-dependence of surface plasmon resonances. *Proceedings of the National Academy of Sciences of the United States of America* **107**, 14530–14534.

[62] Bakr, O. M, Amendola, V, Aikens, C. M, Wenseleers, W, Li, R, Dal Negro, L, Schatz, G. C, & Stellacci, F. (2009) Silver nanoparticles with broad multiband linear optical absorption. *Angewandte Chemie-International Edition* **48**, 5921–5926.

[63] Schaaff, T. G, Knight, G, Shafigullin, M. N, Borkman, R. F, & Whetten, R. L. (1998) Isolation and selected properties of a 10.4 kDa gold: glutathione cluster compound. *Journal of Physical Chemistry B* **102**, 10643–10646.

[64] Kubo, R, Kawabata, A, & Kobayashi, S. (1984) Electronic properties of small particles. *Annual Review of Materials Science* **14**, 49–66.

[65] Schaaff, T. G, Shafigullin, M. N, Khoury, J. T, Vezmar, I, Whetten, R. L, Cullen, W. G, First, P. N, GutierrezWing, C, Ascensio, J,

& JoseYacaman, M. J. (1997) Isolation of smaller nanocrystal au molecules: Robust quantum effects in optical spectra. *Journal of Physical Chemistry B* **101**, 7885–7891.

[66] Whetten, R. L, Khoury, J. T, Alvarez, M. M, Murthy, S, Vezmar, I, Wang, Z. L, Stephens, P. W, Cleveland, C. L, Luedtke, W. D, & Landman, U. (1996) Nanocrystal gold molecules. *Advanced materials (Deerfield Beach, Fla.)* **8**, 428–433.

[67] Link, S, Beeby, A, FitzGerald, S, El-Sayed, M. A, Schaaff, T. G, & Whetten, R. L. (2002) Visible to Infrared Luminescence from a 28-Atom Gold Cluster. *Journal of Physical Chemistry B* **106**, 3410–3415.

[68] Zhu, M, Lanni, E, Garg, N, Bier, M. E, & Jin, R. (2008) Kinetically controlled, high-yield synthesis of Au25 clusters. *Journal of the American Chemical Society* **130**, 1138–1139.

[69] Wu, Z, Suhan, J, & Jin, R. (2009) One-pot synthesis of atomically monodisperse, thiol-functionalized Au25 nanoclusters. *Journal of Materials Chemistry* **19**, 622–626.

[70] Jin, R, Qian, H, Wu, Z, Zhu, Y, Zhu, M, Mohanty, A, & Garg, N. (2010) Size Focusing: A Methodology for Synthesizing Atomically Precise Gold Nanoclusters. *Journal of Physical Chemistry Letters* **1**, 2903–2910.

[71] Park, S & Lee, D. (2012) Synthesis and Electrochemical and Spectroscopic Characterization of Biicosahedral Au 25Clusters. *Langmuir* **28**, 7049–7054.

[72] Shichibu, Y, Negishi, Y, Tsukuda, T, & Teranishi, T. (2005) Large-scale synthesis of thiolated Au25 clusters via ligand exchange reactions of phosphine-stabilized Au11 clusters. *Journal of the American Chemical Society* **127**, 13464–13465.

[73] Shibu, E. S, Muhammed, M. A. H, Tsukuda, T, & Pradeep, T. (2008) Ligand Exchange of Au25SG18 Leading to Functionalized

Gold Clusters: Spectroscopy, Kinetics, and Luminescence. *Journal of Physical Chemistry C* **112**, 12168–12176.

[74] Jin, R. (2010) Quantum sized, thiolate-protected gold nanoclusters. *Nanoscale* **2**, 343–362.

[75] Wu, X, He, X, Wang, K, Xie, C, Zhou, B, & Qing, Z. (2010) Ultrasmall near-infrared gold nanoclusters for tumor fluorescence imaging in vivo. *Nanoscale* **2**, 2244–2249.

[76] Zheng, J, Petty, J. T, & Dickson, R. M. (2003) High Quantum Yield Blue Emission from Water-Soluble Au 8Nanodots. *Journal of the American Chemical Society* **125**, 7780–7781.

[77] Wu, Z & Jin, R. (2010) On the ligand's role in the fluorescence of gold nanoclusters. *Nano Letters* **10**, 2568–2573.

[78] Bigioni, T. P, Whetten, R. L, & Dag, Ö. (2000) Near-infrared luminescence from small gold nanocrystals. *Journal of Physical Chemistry B* **104**, 6983–6986.

[79] Yang, Y & Chen, S. (2003) Surface Manipulation of the Electronic Energy of Subnanometer-Sized Gold Clusters: An Electrochemical and Spectroscopic Investigation. *Nano Letters* **3**, 75–79.

[80] Donnio, B, Derory, A, Terazzi, E, Drillon, M, Guillon, D, & Gallani, J.-L. (2010) Very slow high-temperature relaxation of the remnant magnetic moment in 2 nm mesomorphic gold nanoparticles. *Soft Matter* **6**, 965–970.

[81] Davis, M. E, Chen, Z. G, & Shin, D. M. (2008) Nanoparticle therapeutics: an emerging treatment modality for cancer. *Nature Reviews Drug Discovery* **7**, 771–782.

[82] Lee, J. E, Lee, N, Kim, T, Kim, J, & Hyeon, T. (2011) Multifunctional mesoporous silica nanocomposite nanoparticles for theranostic applications. *Accounts Of Chemical Research* **44**, 893–902.

[83] Wang, S, Zhang, M, & Zhang, W. (2011) Yolk-Shell Catalyst of Single

Au Nanoparticle Encapsulated within Hollow Mesoporous Silica Microspheres. *ACS Catalysis* **1**, 207–211.

[84] Zhang, W. M, Hu, J. S, Guo, Y. G, Zheng, S. F, Zhong, L. S, Song, W. G, & Wan, L. J. (2008) Tin-Nanoparticles Encapsulated in Elastic Hollow Carbon Spheres for High-Performance Anode Material in Lithium-Ion Batteries. *Advanced Materials* **20**, 1160–1165.

[85] Qian, J, Liu, P, Xiao, Y, Jiang, Y, Cao, Y, Ai, X, & Yang, H. (2009) TiO2-Coated Multilayered SnO2 Hollow Microspheres for Dye-Sensitized Solar Cells. *Advanced Materials* **21**, 3663–3667.

[86] Li, L, Tang, F, Liu, H, Liu, T, Hao, N, Chen, D, Teng, X, & He, J. (2010) In Vivo Delivery of Silica Nanorattle Encapsulated Docetaxel for Liver Cancer Therapy with Low Toxicity and High Efficacy. *ACS Nano* **4**, 6874–6882.

[87] Geng, B, Liu, J, Zhao, Y, & Wang, C. (2010) A Room-Temperature Chemical Route to Homogeneous Core-Shell Cu2O Structures and Their Application in Biosensors. *CrystEngComm* **13**, 697–701.

[88] Roca, M & Haes, A. J. (2008) Silica-Void-Gold Nanoparticles: Temporally Stable Surface-Enhanced Raman Scattering Substrates. *Journal of the American Chemical Society* **130**, 14273–14279.

[89] Link, S & El-Sayed, M. A. (2003) Optical properties and ultrafast dynamics of metallic nanocrystals. *Annual review of physical chemistry* **54**, 331–366.

[90] Zhan, Q, Qian, J, Li, X, & He, S. (2010) A Study of Mesoporous Silica-Encapsulated Gold Nanorods as Enhanced Light Scattering Probes for Cancer Cell Imaging. *Nanotechnology* **21**, 055704–055716.

[91] Wang, T.-T, Chai, F, Wang, C.-G, Li, L, Liu, H.-Y, Zhang, L.-Y, Su, Z.-M, & Liao, Y. (2011) Fluorescent hollow/rattle-type mesoporous Au@SiO2 nanocapsules for drug delivery and fluorescence imaging of cancer cells. *Journal of Colloid and Interface Science* **358**, 109–115.

[92] Melancon, M. P, Zhou, M, & Li, C. (2011) Cancer theranostics with

near-infrared light-activatable multimodal nanoparticles. *Accounts Of Chemical Research* **44**, 947–956.

[93] Kamata, K, Lu, Y, & Xia, Y. (2003) Synthesis and Characterization of Monodispersed Core-Shell Spherical Colloids with Movable Cores. *Journal of the American Chemical Society* **125**, 2384–2385.

[94] Zhao, Y & Jiang, L. (2009) Hollow Micro/Nanomaterials with Multilevel Interior Structures. *Advanced Materials* **21**, 3621–3638.

[95] Lou, X. W. D, Archer, L. A, & Yang, Z. (2008) Hollow Micro-/Nanostructures: Synthesis and Applications. *Advanced Materials* **20**, 3987–4019.

[96] Wu, X. J & Xu, D. (2010) Soft Template Synthesis of Yolk/Silica Shell particles. *Advanced Materials* **22**, 1516–1520.

[97] Liu, J, Qiao, S. Z, Budi Hartono, S, & Lu, G. Q. M. (2010) Monodisperse Yolk-Shell Nanoparticles with a Hierarchical Porous Structure for Delivery Vehicles and Nanoreactors. *Angewandte Chemie-International Edition* **49**, 4981–4985.

[98] Chen, Y, Chen, H, Zeng, D, Tian, Y, Chen, F, Feng, J, & Shi, J. (2010) Core/shell structured hollow mesoporous nanocapsules: a potential platform for simultaneous cell imaging and anticancer drug delivery. *ACS Nano* **4**, 6001–6013.

[99] Park, J. C & Song, H. (2010) Metal@Silica Yolk-Shell Nanostructures as Versatile Bifunctional Nanocatalysts. *Nano Research* **4**, 33–49.

[100] Liu, J, Fan, F, Feng, Z, Zhang, L, Bai, S, Yang, Q, & Li, C. (2008) From Hollow Nanosphere to Hollow Microsphere: Mild Buffer Provides Easy Access to Tunable Silica Structure. *Journal of Physical Chemistry C* **112**, 16445–16451.

[101] Liu, J, Bai, S, Zhong, H, Li, C, & Yang, Q. (2010) Tunable Assembly of Organosilica Hollow Nanospheres. *Journal of Physical Chemistry C* **114**, 953–961.

[102] Duncan, R. (2003) The dawning era of polymer therapeutics. *Nature Reviews Drug Discovery* **2**, 347–360.

[103] Langer, R. (1998) Drug delivery and targeting. *Nature* **392**, 5–10.

[104] Vallet-Regi, M, Balas, F, & Arcos, D. (2007) Mesoporous materials for drug delivery. *Angewandte Chemie-International Edition* **46**, 7548–7558.

[105] Cho, K, Wang, X, Nie, S, Chen, Z. G, & Shin, D. M. (2008) Therapeutic nanoparticles for drug delivery in cancer. *Clinical cancer research : an official journal of the American Association for Cancer Research* **14**, 1310–1316.

[106] Allen, T. M. (2002) Ligand-targeted therapeutics in anticancer therapy. *Nature Reviews Cancer* **2**, 750–763.

[107] Jain, R. K. (1998) The next frontier of molecular medicine: delivery of therapeutics. *Nature Medicine* **4**, 655–657.

[108] Serda, R. E, Mack, A, Pulikkathara, M, Zaske, A. M, Chiappini, C, Fakhoury, J. R, Webb, D, Godin, B, Conyers, J. L, Liu, X. W, Bankson, J. A, & Ferrari, M. (2010) Cellular Association and Assembly of a Multistage Delivery System. *Small* **6**, 1329–1340.

[109] Melancon, M. P, Lu, W, Yang, Z, Zhang, R, Cheng, Z, Elliot, A. M, Stafford, J, Olson, T, Zhang, J. Z, & Li, C. (2008) In vitro and in vivo targeting of hollow gold nanoshells directed at epidermal growth factor receptor for photothermal ablation therapy. *Molecular Cancer Therapeutics* **7**, 1730–1739.

[110] Lu, W, Xiong, C, Zhang, G, Huang, Q, Zhang, R, Zhang, J. Z, & Li, C. (2009) Targeted Photothermal Ablation of Murine Melanomas with Melanocyte-Stimulating Hormone Analog-Conjugated Hollow Gold Nanospheres. *Clinical Cancer Research* **15**, 876–886.

[111] Choi, C. H. J, Alabi, C. A, Webster, P, & Davis, M. E. (2010) Mechanism of active targeting in solid tumors with transferrin-containing gold nanoparticles. *Proceedings of the National Academy of Sciences of the United States of America* **107**, 1235–1240.

[112] Pirollo, K. F & Chang, E. H. (2008) Does a targeting ligand influence nanoparticle tumor localization or uptake? *Trends in Biotechnology* **26**, 552–558.

[113] O'Neal, D. P, Hirsch, L. R, Halas, N. J, Payne, J. D, & West, J. L. (2004) Photo-thermal tumor ablation in mice using near infrared-absorbing nanoparticles. *Cancer Letters* **209**, 171–176.

[114] Matsumura, Y & Maeda, H. (1986) A new concept for macromolecular therapeutics in cancer chemotherapy: mechanism of tumoritropic accumulation of proteins and the antitumor agent smancs. *Cancer Research* **46**, 6387–6392.

[115] He, X, Wang, K, & Cheng, Z. (2010) In vivo near-infrared fluorescence imaging of cancer with nanoparticle-based probes. *Wiley Interdisciplinary Reviews: Nanomedicine and Nanobiotechnology* **2**, 349–366.

[116] Luo, S, Zhang, E, Su, Y, Cheng, T, & Shi, C. (2011) A review of NIR dyes in cancer targeting and imaging. *Biomaterials* **32**, 7127–7138.

[117] Mahmoudi, M, Serpooshan, V, & Laurent, S. (2011) Engineered nanoparticles for biomolecular imaging. *Nanoscale* **3**, 3007–3026.

[118] Willmann, J. K, van Bruggen, N, Dinkelborg, L. M, & Gambhir, S. S. (2008) Molecular imaging in drug development. *Nature Reviews Drug Discovery* **7**, 591–607.

[119] Aswathy, R. G, Yoshida, Y, Maekawa, T, & Kumar, D. S. (2010) Near-infrared quantum dots for deep tissue imaging. *Analytical and Bioanalytical Chemistry* **397**, 1417–1435.

[120] Hilderbrand, S. A & Weissleder, R. (2010) Near-infrared fluorescence: application to in vivo molecular imaging. *Current Opinion In Chemical Biology* **14**, 71–79.

[121] Sipkins, D. A, Cheresh, D. A, Kazemi, M. R, Nevin, L. M, Bednarski, M. D, & Li, K. C. P. (1998) Detection of tumor angiogenesis in vivo by avß3-targeted magnetic resonance imaging. *Nature Medicine* **4**, 623–626.

[122] Paulus, M. J, Gleason, S. S, Kennel, S. J, Hunsicker, P. R, & Johnson, D. K. (2000) High resolution X-ray computed tomography: an emerging tool for small animal cancer research. *Neoplasia* **2**, 62–70.

[123] de Wit, M, Bumann, D, Beyer, W, Herbst, K, Clausen, M, & Hossfeld, D. K. (1997) Whole-body positron emission tomography (PET) for diagnosis of residual mass in patients with lymphoma. *Annals of oncology* **8 Suppl 1**, 57–60.

[124] Warner, E, Plewes, D. B, Shumak, R. S, Catzavelos, G. C, Di Prospero, L. S, Yaffe, M. J, Goel, V, Ramsay, E, Chart, P. L, Cole, D. E, Taylor, G. A, Cutrara, M, Samuels, T. H, Murphy, J. P, Murphy, J. M, & Narod, S. A. (2001) Comparison of breast magnetic resonance imaging, mammography, and ultrasound for surveillance of women at high risk for hereditary breast cancer. *Journal of Clinical Oncology* **19**, 3524–3531.

[125] Badr, C. E & Tannous, B. A. (2011) Bioluminescence imaging: progress and applications. *Trends in Biotechnology* **29**, 624–633.

[126] Sadikot, R. T & Blackwell, T. S. (2005) Bioluminescence Imaging. *Proceedings of the American Thoracic Society* **2**, 537–540.

[127] Hoffman, R. M. (2005) The multiple uses of fluorescent proteins to visualize cancer in vivo. *Nature Reviews Cancer* **5**, 796–806.

[128] Condeelis, J & Segall, J. E. (2003) Intravital imaging of cell movement in tumours. *Nature Reviews Cancer* **3**, 921–930.

[129] Jain, P. K, Huang, X, El-Sayed, I. H, & El-Sayed, M. A. (2008) Noble metals on the nanoscale: optical and photothermal properties and some applications in imaging, sensing, biology, and medicine. *Accounts Of Chemical Research* **41**, 1578–1586.

[130] Smith, A. M, Mancini, M. C, & Nie, S. (2009) Bioimaging: Second window for in vivo imaging. *Nature Nanotechnology* **4**, 710–711.

[131] Mahmood, U & Weissleder, R. (2003) Near-infrared optical imaging of proteases in cancer. *Molecular Cancer Therapeutics* **2**, 489–496.

[132] Sevick-Muraca, E. M. (2012) Translation of Near-Infrared Fluorescence Imaging Technologies: Emerging Clinical Applications. *Annual Review of Medicine* **63**, 217–231.

[133] Frangioni, J. (2003) In vivo near-infrared fluorescence imaging. *Current Opinion In Chemical Biology* **7**, 626–634.

[134] Xing, Y & Rao, J. (2008) Quantum dot bioconjugates for in vitro diagnostics and in vivo imaging. *Cancer Biomarkers* **4**, 307–319.

[135] Gao, X, Cui, Y, Levenson, R. M, Chung, L. W. K, & Nie, S. (2004) In vivo cancer targeting and imaging with semiconductor quantum dots. *Nature Biotechnology* **22**, 969–976.

[136] Bardhan, R, Chen, W, Perez-Torres, C, Bartels, M, Huschka, R. M, Zhao, L. L, Morosan, E, Pautler, R. G, Joshi, A, & Halas, N. J. (2009) Nanoshells with Targeted Simultaneous Enhancement of Magnetic and Optical Imaging and Photothermal Therapeutic Response. *Advanced Functional Materials* **19**, 3901–3909.

[137] Smith, A. M, Gao, X, & Nie, S. (2004) Quantum dot nanocrystals for in vivo molecular and cellular imaging. *Photochemistry and Photobiology* **80**, 377–385.

[138] Zheng, Y, Gao, S, & Ying, J. Y. (2007) Synthesis and Cell-Imaging Applications of Glutathione-Capped CdTe Quantum Dots. *Advanced Materials* **19**, 376–380.

[139] Huang, X, El-Sayed, I. H, Qian, W, & El-Sayed, M. A. (2006) Cancer cell imaging and photothermal therapy in the near-infrared region by using gold nanorods. *Journal of the American Chemical Society* **128**, 2115–2120.

[140] Lin, C.-A. J, Yang, T.-Y, Lee, C.-H, Huang, S. H, Sperling, R. A, Zanella, M, Li, J. K, Shen, J.-L, Wang, H.-H, Yeh, H.-I, Parak, W. J, & Chang, W. H. (2009) Synthesis, Characterization, and Bioconjugation of Fluorescent Gold Nanoclusters toward Biological Labeling Applications. *ACS Nano* **3**, 395–401.

[141] Yu, J, Choi, S, Richards, C. I, Antoku, Y, & Dickson, R. M. (2008) Live Cell Surface Labeling with Fluorescent Ag Nanocluster Conjugates . *Photochemistry and Photobiology* **84**, 1435–1439.

[142] Chevrier, D. M, Chatt, A, & Zhang, P. (2012) Properties and applications of protein-stabilized fluorescent gold nanoclusters: short review. *Journal of Nanophotonics* **6**, 064504–1–064504–16.

[143] Kircher, M. F, Mahmood, U, King, R. S, Weissleder, R, & Josephson, L. (2003) A multimodal nanoparticle for preoperative magnetic resonance imaging and intraoperative optical brain tumor delineation. *Cancer Research* **63**, 8122–8125.

[144] Bardhan, R, Lal, S, Joshi, A, & Halas, N. J. (2011) Theranostic nanoshells: from probe design to imaging and treatment of cancer. *Accounts Of Chemical Research* **44**, 936–946.

[145] Zhang, L, Wang, T, Yang, L, Liu, C, Wang, C, Liu, H, Wang, Y. A, & Su, Z. (2012) General Route to Multifunctional Uniform Yolk/Mesoporous Silica Shell Nanocapsules: A Platform for Simultaneous Cancer-Targeted Imaging and Magnetically Guided Drug Delivery. *Chemistry-A European Journal* **18**, 12512–12521.

[146] Zhang, F, Braun, G. B, Pallaoro, A, Zhang, Y, Shi, Y, Cui, D, Moskovits, M, Zhao, D, & Stucky, G. D. (2012) Mesoporous Multifunctional Upconversion Luminescent and Magnetic "Nanorattle" Materials for Targeted Chemotherapy. *Nano Letters* **12**, 61–67.

[147] Ma, M, Chen, H, Chen, Y, Wang, X, Chen, F, Cui, X, & Shi, J. (2012) Au capped magnetic core/mesoporous silica shell nanoparticles for combined photothermo-/chemo-therapy and multimodal imaging. *Biomaterials* **33**, 989–998.

[148] Huang, X, Jain, P. K, El-Sayed, I. H, & El-Sayed, M. A. (2007) Plasmonic photothermal therapy (PPTT) using gold nanoparticles. *Lasers in Medical Science* **23**, 217–228.

[149] Cavaliere, R, Ciocatto, E. C, Giovanella, B. C, Heidelberger, C, Johnson, R. O, Margottini, M, Mondovi, B, Moricca, G, & Rossi Fanelli,

A. (1967) Selective heat sensitivity of cancer cells. Biochemical and clinical studies. *Cancer* **20**, 1351–1381.

[150] Overgaard, J, Gonzalez, D. G, Hulshof, M, Arcangeli, G, Dahl, O, Mella, O, & Bentzen, S. M. (1996) Hyperthermia as an adjuvant to radiation therapy of recurrent or metastatic malignant melanoma. A multicentre randomized trial by the European Society for Hyperthermic Oncology. *International Journal of Hyperthermia* **12**, 3–20.

[151] Cobley, C. M, Chen, J, Cho, E. C, Wang, L. V, & Xia, Y. (2010) Gold nanostructures: a class of multifunctional materials for biomedical applications. *Chemical Society Reviews* **40**, 44–56.

[152] Averitt, R, Sarkar, D, & Halas, N. (1997) Plasmon Resonance Shifts of Au-Coated Au2S Nanoshells: Insight into Multicomponent Nanoparticle Growth. *Physical Review Letters* **78**, 4217–4220.

[153] Loo, C, Lowery, A, Halas, N, West, J, & Drezek, R. (2005) Immunotargeted Nanoshells for Integrated Cancer Imaging and Therapy. *Nano Letters* **5**, 709–711.

[154] Na, H. B, Song, I. C, & Hyeon, T. (2009) Inorganic Nanoparticles for MRI Contrast Agents. *Advanced Materials* **21**, 2133–2148.

[155] Xu, S.-L & Cui, H. (2007) Luminol chemiluminescence catalysed by colloidal platinum nanoparticles. *Luminescence* **22**, 77–87.

[156] Chen, J, Wang, D, Xi, J, Au, L, Siekkinen, A, Warsen, A, Li, Z.-Y, Zhang, H, Xia, Y, & Li, X. (2007) Immuno Gold Nanocages with Tailored Optical Properties for Targeted Photothermal Destruction of Cancer Cells. *Nano Letters* **7**, 1318–1322.

[157] Huang, X, Neretina, S, & El-Sayed, M. A. (2009) Gold Nanorods: From Synthesis and Properties to Biological and Biomedical Applications. *Advanced Materials* **21**, 4880–4910.

[158] El-Sayed, I, Huang, X, & El-Sayed, M. (2006) Selective Laser Photo-Thermal Therapy of Epithelial Carcinoma Using Anti-Egfr Antibody Conjugated Gold Nanoparticles. *Cancer Letters* **239**, 129–135.

[159] Li, J.-L, Wang, L, Liu, X.-Y, Zhang, Z.-P, Guo, H.-C, Liu, W.-M, & Tang, S.-H. (2009) In vitro cancer cell imaging and therapy using transferrin-conjugated gold nanoparticles. *Cancer Letters* **274**, 319–326.

[160] Hirsch, F. R, Franklin, W. A, Gazdar, A. F, & Bunn, P. A. (2001) Early detection of lung cancer: clinical perspectives of recent advances in biology and radiology. *Clinical cancer research : an official journal of the American Association for Cancer Research* **7**, 5–22.

[161] Sosnovik, D. E, Nahrendorf, M, & Weissleder, R. (2008) Magnetic nanoparticles for MR imaging: agents, techniques and cardiovascular applications. *Basic Research in Cardiology* **103**, 122–130.

[162] Wunderbaldinger, P, Josephson, L, & Weissleder, R. (2002) Crosslinked Iron Oxides (Clio): a New Platform for the Development of Targeted Mr Contrast Agents. *Academic Radiology* **9**, S304–S306.

[163] Sun, Y. (2002) Shape-Controlled Synthesis of Gold and Silver Nanoparticles. *Science (New York, NY)* **298**, 2176–2179.

[164] Cole, J. R, Mirin, N. A, Knight, M. W, Goodrich, G. P, & Halas, N. J. (2009) Photothermal Efficiencies of Nanoshells and Nanorods for Clinical Therapeutic Applications. *Journal of Physical Chemistry C* **113**, 12090–12094.

[165] Parak, W, Gerion, D, Pellegrino, T, Zanchet, D, Micheel, C, Williams, S, Boudreau, R, Le Gros, M, Larabell, C, & Alivisatos, A. (2003) Biological applications of colloidal nanocrystals. *Nanotechnology* **14**, R15–R27.

[166] Jain, P. K, Lee, K. S, El-Sayed, I. H, & El-Sayed, M. A. (2006) Calculated Absorption and Scattering Properties of Gold Nanoparticles of Different Size, Shape, and Composition: Applications in Biological Imaging and Biomedicine. *Journal of Physical Chemistry B* **110**, 7238–7248.

[167] von Maltzahn, G, Park, J. H, Agrawal, A, Bandaru, N. K, Das, S. K, Sailor, M. J, & Bhatia, S. N. (2009) Computationally Guided Photo-

thermal Tumor Therapy Using Long-Circulating Gold Nanorod Antennas. *Cancer Research* **69**, 3892–3900.

[168] Schwartz, J. A, Shetty, A. M, Price, R. E, Stafford, R. J, Wang, J. C, Uthamanthil, R. K, Pham, K, McNichols, R. J, Coleman, C. L, & Payne, J. D. (2009) Feasibility study of particle-assisted laser ablation of brain tumors in orthotopic canine model. *Cancer Research* **69**, 1659–1667.

[169] Eichler, A. F & Loeffler, J. S. (2007) Multidisciplinary management of brain metastases. *Oncologist* **12**, 884–898.

[170] Lasa-Saracibar, B, Estella-Hermoso de Mendoza, A, Guada, M, Dios-Vieitez, C, & Blanco-Prieto, M. J. (2012) Lipid nanoparticles for cancer therapy: state of the art and future prospects. *Expert opinion on drug delivery* **9**, 1245–1261.

[171] Li, K. C. P, Pandit, S. D, Guccione, S, & Bednarski, M. D. (2004) Molecular imaging applications in nanomedicine. *Biomedical microdevices* **6**, 113–116.

[172] Minelli, C, Kikuta, A, Tsud, N, Ball, M, & Yamamoto, A. (2008) A micro-fluidic study of whole blood behaviour on PMMA topographical nanostructures. *Journal of Nanobiotechnology* **6**, 3–13.

[173] Torchilin, V. P. (2005) Recent advances with liposomes as pharmaceutical carriers. *Nature Reviews Drug Discovery* **4**, 145–160.

[174] Torchilin, V. P. (1996) Liposomes as delivery agents for medical imaging. *Molecular medicine today* **2**, 242–249.

[175] Li, J, Liu, J, Wang, D, Guo, R, Li, X, & Qi, W. (2010) Interfacially controlled synthesis of hollow mesoporous silica spheres with radially oriented pore structures. *Langmuir* **26**, 12267–12272.

[176] An, K & Hyeon, T. (2009) Synthesis and biomedical applications of hollow nanostructures. *Nano Today* **4**, 359–373.

[177] Zhao, Y, Sun, X, Zhang, G, Trewyn, B. G, Slowing, I. I, & Lin, V. S.-Y. (2011) Interaction of mesoporous silica nanoparticles with human

red blood cell membranes: size and surface effects. *ACS Nano* **5**, 1366–1375.

[178] Song, S.-W, Hidajat, K, & Kawi, S. (2005) Functionalized SBA-15 materials as carriers for controlled drug delivery: influence of surface properties on matrix-drug interactions. *Langmuir* **21**, 9568–9575.

[179] Muñoz, B, Ramila, A, Perez-Pariente, J, Díaz, I, & Vallet-Regi, M. (2003) MCM-41 Organic Modification as Drug Delivery Rate Regulator. *Chemistry of Materials* **15**, 500–503.

[180] Trewyn, B. G, Slowing, I. I, Giri, S, Chen, H.-T, & Lin, V. S.-Y. (2007) Synthesis and Functionalization of a Mesoporous Silica Nanoparticle Based on the Sol–Gel Process and Applications in Controlled Release. *Accounts Of Chemical Research* **40**, 846–853.

[181] Beck, J. S, Vartuli, J. C, Roth, W. J, Leonowicz, M. E, Kresge, C. T, Schmitt, K. D, Chu, C. T, Olson, D. H, Sheppard, E. W, McCullen, S. B, Higgins, J. B, & L, S. J. (1992) A New Family of Mesoporous Molecular Sieves Prepared with Liquid Crystal Templates. *Journal of the American Chemical Society* **114**, 10834–10843.

[182] Yu, T, Malugin, A, & Ghandehari, H. (2011) Impact of Silica Nanoparticle Design on Cellular Toxicity and Hemolytic Activity. *ACS Nano* **5**, 5717–5728.

[183] He, Q & Shi, J. (2011) Mesoporous silica nanoparticle based nano drug delivery systems: synthesis, controlled drug release and delivery, pharmacokinetics and biocompatibility. *Journal of Materials Chemistry* **21**, 5845–5855.

[184] Slowing, I. I, Trewyn, B. G, Giri, S, & Lin, V. S. Y. (2007) Mesoporous Silica Nanoparticles for Drug Delivery and Biosensing Applications. *Advanced Functional Materials* **17**, 1225–1236.

[185] Vallet-Regi, M, Ramila, A, del Real, R, & Perez-Pariente, J. (2001) A New Property of MCM-41: Drug Delivery System. *Chemistry of Materials* **13**, 308–311.

[186] Torney, F, Trewyn, B. G, Lin, V. S.-Y, & Wang, K. (2007) Mesoporous silica nanoparticles deliver DNA and chemicals into plants. *Nature Nanotechnology* **2**, 295–300.

[187] Vivero-Escoto, J. L, Slowing, I. I, Wu, C.-W, & Lin, V. S.-Y. (2009) Photoinduced Intracellular Controlled Release Drug Delivery in Human Cells by Gold-Capped Mesoporous Silica Nanosphere. *Journal of the American Chemical Society* **131**, 3462–3463.

[188] Slowing, I. I, Vivero-Escoto, J. L, Wu, C. W, & Lin, V. S. Y. (2008) Mesoporous silica nanoparticles as controlled release drug delivery and gene transfection carriers. *Advanced drug delivery reviews* **60**, 1278–1288.

[189] Liu, H, Chen, D, Li, L, Liu, T, Tan, L, Wu, X, & Tang, F. (2011) Multifunctional Gold Nanoshells on Silica Nanorattles: A Platform for the Combination of Photothermal Therapy and Chemotherapy with Low Systemic Toxicity. *Angewandte Chemie-International Edition* **50**, 891–895.

[190] Liu, H, Liu, T, Wu, X, Li, L, Tan, L, Chen, D, & Tang, F. (2012) Targeting gold nanoshells on silica nanorattles: a drug cocktail to fight breast tumors via a single irradiation with near-infrared laser light. *Advanced materials (Deerfield Beach, Fla.)* **24**, 755–761.

[191] Williams, D. B & Carter, C. B. (2009) *Transmission Electron Microscopy: A Textbook for Materials Science*. (Springer).

[192] Prasad, V, Semwogerere, D, & Weeks, E. R. (2007) Confocal microscopy of colloids. *Journal of Physics: Condensed Matter* **19**, 113102–113127.

[193] Lohela, M & Werb, Z. (2010) Intravital imaging of stromal cell dynamics in tumors. *Current Opinion in Genetics & Development* **20**, 72–78.

[194] Boassa, D, Solan, J. L, Papas, A, Thornton, P, Lampe, P. D, & Sosinsky, G. E. (2010) Trafficking and Recycling of the Connexin43 Gap Junction Protein during Mitosis. *Traffic* **11**, 1471–1486.

[195] Li, Z, Wen, L, Shao, L, & Chen, J. (2004) Fabrication of porous hollow silica nanoparticles and their applications in drug release control. *Journal of Controlled Release* **98**, 245–254.

[196] Chen, Z, Cui, Z.-M, Niu, F, Jiang, L, & Song, W. G. (2010) Pd Nanoparticles in Silica Hollow Spheres with Mesoporous Walls: a Nanoreactor with Extremely High Activity. *Chemical communications (Cambridge, England)* **46**, 6524–6526.

[197] Ding, S, Chen, J. S, Qi, G, Duan, X, Wang, Z, Giannelis, E. P, Archer, L. A, & Lou, X. W. (2011) Formation of SnO2 Hollow Nanospheres Inside Mesoporous Silica Nanoreactors. *Journal of the American Chemical Society* **133**, 21–23.

[198] De, M, Ghosh, P. S, & Rotello, V. M. (2008) Applications of Nanoparticles in Biology. *Advanced Materials* **20**, 4225–4241.

[199] Blas, H, Save, M, Pasetto, P, Boissière, C, Sanchez, C, & Charleux, B. (2008) Elaboration of Monodisperse Spherical Hollow Particles with Ordered Mesoporous Silica Shells via Dual Latex/Surfactant Templating: Radial Orientation of Mesopore Channels. *Langmuir* **24**, 13132–13137.

[200] Feng, Z, Li, Y, Niu, D, Li, L, Zhao, W, Chen, H, Li, L, Gao, J, Ruan, M, & Shi, J. (2008) A facile route to hollow nanospheres of mesoporous silica with tunable size. *Chemical communications (Cambridge, England)* pp. 2629–2631.

[201] Sun, Q, Kooyman, P. J, Grossmann, J. G, Bomans, P. H. H, Frederik, P. M, Magusin, P. C. M. M, Beelen, T. P. M, van Santen, R. A, & Sommerdijk, N. A. J. M. (2003) The Formation of Well-Defined Hollow Silica Spheres with Multilamellar Shell Structure. *Advanced Materials* **15**, 1097–1100.

[202] Zhu, Y, Shi, J, Shen, W, Chen, H, Dong, X, & Ruan, M. (2005) Preparation of novel hollow mesoporous silica spheres and their sustained-release property. *Nanotechnology* **16**, 2633–2638.

[203] Tan, B & Rankin, S. E. (2005) Dual latex/surfactant templating of hollow spherical silica particles with ordered mesoporous shells. *Langmuir* **21**, 8180–8187.

[204] Wu, X, Tian, Y, Cui, Y, Wei, L, Wang, Q, & Chen, Y. (2007) Raspberry-like silica hollow spheres: hierarchical structures by dual latex-surfactant templating route. *Journal of Physical Chemistry C* **111**, 9704–9708.

[205] Fowler, C. E, Khushalani, D, Lebeau, B, & Mann, S. (2001) Nanoscale materials with mesostructured interiors. *Advanced materials (Deerfield Beach, Fla.)* **13**, 649–652.

[206] Li, Z. Z, Xu, S. A, Wen, L. X, Liu, F, Liu, A. Q, Wang, Q, Sun, H. Y, Yu, W, & Chen, J. F. (2006) Controlled release of avermectin from porous hollow silica nanoparticles: influence of shell thickness on loading efficiency, UV-shielding property and release. *Journal of Controlled Release* **111**, 81–88.

[207] Park, S. J, Kim, Y. J, & Park, S. J. (2008) Size-dependent shape evolution of silica nanoparticles into hollow structures. *Langmuir* **24**, 12134–12137.

[208] Woehrle, G. H, Warner, M. G, & Hutchison, J. E. (2002) Ligand Exchange Reactions Yield Subnanometer, Thiol-Stabilized Gold Particles with Defined Optical Transitions. *Journal of Physical Chemistry B* **106**, 9979–9981.

[209] Weare, W. W, Reed, S. M, Warner, M. G, & Hutchison, J. E. (2000) Improved synthesis of small (d core= 1.5 nm) phosphine-stabilized gold nanoparticles. *Journal of the American Chemical Society* **122**, 12890–12891.

[210] Woehrle, G. H, Brown, L. O, & Hutchison, J. E. (2005) Thiol-functionalized, 1.5-nm gold nanoparticles through ligand exchange reactions: scope and mechanism of ligand exchange. *Journal of the American Chemical Society* **127**, 2172–2183.

[211] Donkers, R. L, Lee, D, & Murray, R. (2004) Synthesis and isolation of the molecule-like cluster Au38 (PhCH2CH2S) 24. *Langmuir* **20**, 1945–1952.

[212] Blas, H, Save, M, Boissière, C, Sanchez, C, & Charleux, B. (2011) Surface-Initiated Nitroxide-Mediated Polymerization from Ordered Mesoporous Silica. *Macromolecules* **44**, 2577–2588.

[213] Chen, Y, Chen, H, Guo, L, He, Q, Chen, F, Zhou, J, Feng, J, & Shi, J. (2010) Hollow/rattle-type mesoporous nanostructures by a structural difference-based selective etching strategy. *ACS Nano* **4**, 529–539.

[214] Yang, S, Zhou, C, Liu, J, Yu, M, & Zheng, J. (2012) One-Step Interfacial Synthesis and Assembly of Ultrathin Luminescent AuNPs/Silica Membranes. *Advanced Materials* **24**, 3218–3222.

[215] Aikens, C. M. (2011) Electronic Structure of Ligand-Passivated Gold and Silver Nanoclusters. *Journal of Physical Chemistry Letters* **2**, 99–104.

[216] Yang, P, Quan, Z, Hou, Z, Li, C, Kang, X, Cheng, Z, & Lin, J. (2009) A magnetic, luminescent and mesoporous core–shell structured composite material as drug carrier. *Biomaterials* **30**, 4786–4795.

[217] Bass, J. D, Grosso, D, Boissière, C, Belamie, E, Coradin, T, & Sanchez, C. (2007) Stability of mesoporous oxide and mixed metal oxide materials under biologically relevant conditions. *Chemistry of Materials* **19**, 4349–4356.

[218] Soo Choi, H, Liu, W, Misra, P, Tanaka, E, Zimmer, J. P, Itty Ipe, B, Bawendi, M. G, & Frangioni, J. V. (2007) Renal clearance of quantum dots. *Nature Biotechnology* **25**, 1165–1170.

[219] Cai, W & Chen, X. (2008) Preparation of peptide-conjugated quantum dots for tumor vasculature-targeted imaging. *Nature Protocols* **3**, 89–96.

[220] Michalet, X. (2005) Quantum Dots for Live Cells, in Vivo Imaging, and Diagnostics. *Science (New York, NY)* **307**, 538–544.

[221] Rahbari, R, Sheahan, T, Modes, V, Collier, P, Macfarlane, C, & Badge, R. M. (2009) A novel L1 retrotransposon marker for HeLa cell line identification. *BioTechniques* **46**, 277–284.

[222] Sieuwerts, A. M, Klijn, J. G. M, Peters, H. A, & Foekens, J. A. (1995) The MTT Tetrazolium Salt Assay Scrutinized: How to Use this Assay Reliably to Measure Metabolic Activity of Cell Cultures in vitro for the Assessment of Growth Characteristics, IC 5 0-Values and Cell Survival. *European Journal of Clinical Chemistry and Clinical Biochemistry* **33**, 813–824.

[223] Wallin, R. F & Arscott, E. F. (1998) A practical guide to ISO 10993-5: Cytotoxicity. *Medical device & diagnostic industry* **20**, 96.

[224] Hedegaard, M, Matthäus, C, Hassing, S, Krafft, C, Diem, M, & Popp, J. (2011) Spectral unmixing and clustering algorithms for assessment of single cells by Raman microscopic imaging. *Theoretical Chemistry Accounts* **130**, 1249–1260.

[225] Kircher, M. F, de la Zerda, A, Jokerst, J. V, Zavaleta, C. L, Kempen, P. J, Mittra, E, Pitter, K, Huang, R, Campos, C, Habte, F, Sinclair, R, Brennan, C. W, Mellinghoff, I. K, Holland, E. C, & Gambhir, S. S. (2012) A brain tumor molecular imaging strategy using a new triple-modality MRI-photoacoustic-Raman nanoparticle. *Nature Medicine* **18**, 829–834.

[226] Conner, S. D & Schmid, S. L. (2003) Regulated portals of entry into the cell. *Nature* **422**, 37–44.

[227] Wang, J, Byrne, J. D, Napier, M. E, & DeSimone, J. M. (2011) More effective nanomedicines through particle design. *Small* **7**, 1919–1931.

[228] Petros, R. A & DeSimone, J. M. (2010) Strategies in the design of nanoparticles for therapeutic applications. *Nature Reviews Drug Discovery* **9**, 615–627.

[229] Rejman, J, Oberle, V, Zuhorn, I. S, & Hoekstra, D. (2004) Size-dependent internalization of particles via the pathways of clathrin-

and caveolae-mediated endocytosis. *Biochemical Journal* **377**, 159–169.

[230] Bathori, G, Cervenak, L, & Karadi, I. (2004) Caveolae - An Alternative Endocytotic Pathway for Targeted Drug Delivery. *Critical Reviews in Therapeutic Drug Carrier Systems* **21**, 67–96.

[231] Hall, E. J. (2006) Intensity-modulated radiation therapy, protons, and the risk of second cancers. *International Journal of Radiation Oncology, Biology, Physics* **65**, 1–7.

[232] Zietman, A. L, DeSilvio, M. L, Slater, J. D, Rossi, C. J, Miller, D. W, Adams, J. A, & Shipley, W. U. (2005) Comparison of conventional-dose vs high-dose conformal radiation therapy in clinically localized adenocarcinoma of the prostate: a randomized controlled trial. *Journal of the American Medical Association* **294**, 1233–1239.

[233] Li, L, Guan, Y, Liu, H, Hao, N, Liu, T, Meng, X, Fu, C, Li, Y, Qu, Q, Zhang, Y, Ji, S, Chen, L, Chen, D, & Tang, F. (2011) Silica nanorattle-doxorubicin-anchored mesenchymal stem cells for tumor-tropic therapy. *ACS Nano* **5**, 7462–7470.

[234] Sapareto, S. A & Dewey, W. C. (1984) Thermal dose determination in cancer therapy. *International Journal of Radiation Oncology, Biology, Physics* **10**, 787–800.

[235] Song, C. W. (1984) Effect of local hyperthermia on blood flow and microenvironment: a review. *Cancer Research* **44**, 4721s–4730s.

[236] Halperin, E. C, Perez, C. A, Brady, L. W, & Wazer, D. E. (2007) *Perez and Brady's Principles and Practice of Radiation Oncology.* (Wolters Kluwer Health/Lippincott Williams & Wilkins.).

[237] Zharov, V. P, Letfullin, R. R, & Galitovskaya, E. N. (2005) Microbubbles-overlapping mode for laser killing of cancer cells with absorbing nanoparticle clusters. *Journal of Physics D: Applied Physics* **38**, 2571–2581.

[238] Yavuz, M. S, Cheng, Y, Chen, J, Cobley, C. M, Zhang, Q, Rycenga, M, Xie, J, Kim, C, Song, K. H, Schwartz, A. G, Wang, L. V, & Xia,

Y. (2009) Gold nanocages covered by smart polymers for controlled release with near-infrared light. *Nature Materials* **8**, 935–939.

[239] Kurita, H, Takami, A, & Koda, S. (1998) Size reduction of gold particles in aqueous solution by pulsed laser irradiation. *Applied Physics Letters* **72**, 789–791.

[240] Takami, A, Kurita, H, & Koda, S. (1999) Laser-induced size reduction of noble metal particles. *Journal of Physical Chemistry B* **103**, 1226–1232.

[241] Chen, Y.-S, Frey, W, Kim, S, Homan, K, Kruizinga, P, Sokolov, K, & Emelianov, S. (2010) Enhanced thermal stability of silica-coated gold nanorods for photoacoustic imaging and image-guided therapy. *Optics Express* **18**, 8867–8878.

[242] Van Gemert, M. J. C, Jacques, S. L, Sterenborg, H. J. C. M, & Star, W. M. (1989) Skin optics. *IEEE Transactions on Biomedical Engineering* **36**, 1146–1154.

[243] Flock, S. T, Patterson, M. S, Wilson, B. C, & Wyman, D. R. (1989) Monte Carlo modeling of light propagation in highly scattering tissues. I. Model predictions and comparison with diffusion theory. *IEEE Transactions on Biomedical Engineering* **36**, 1162–1168.

[244] Welch, A. J & van Gemert, M. J. C. (2011) *Optical-Thermal Response of Laser-Irradiated Tissue.* (Springer).

[245] Barbé, C, Bartlett, J, Kong, L, Finnie, K, Lin, H. Q, Larkin, M, Calleja, S, Bush, A, & Calleja, G. (2004) Silica Particles: A Novel Drug-Delivery System. *Advanced materials (Deerfield Beach, Fla.)* **16**, 1959–1966.

[246] Vallet-Regi, M. (2006) Ordered mesoporous materials in the context of drug delivery systems and bone tissue engineering. *Chemistry-A European Journal* **12**, 5934–5943.

[247] Lee, K. Y, Peters, M. C, & Mooney, D. J. (2001) Controlled drug delivery from polymers by mechanical signals. *Advanced materials (Deerfield Beach, Fla.)* **13**, 837–839.

[248] Gao, F, Li, L, Liu, T, Hao, N, Liu, H, Tan, L, Li, H, Huang, X, Peng, B, Yan, C, Yang, L, Wu, X, Chen, D, & Tang, F. (2012) Doxorubicin loaded silica nanorattles actively seek tumors with improved anti-tumor effects. *Nanoscale* **4**, 3365–3372.

[249] Lu, J, Liong, M, Zink, J. I, & Tamanoi, F. (2007) Mesoporous Silica Nanoparticles as a Delivery System for Hydrophobic Anticancer Drugs. *Small* **3**, 1341–1346.

[250] Farokhzad, O. C, Karp, J. M, & Langer, R. (2006) Nanoparticle–aptamer bioconjugates for cancer targeting. *Expert opinion on drug delivery* **3**, 311–324.

[251] Cuenca, A. G, Jiang, H, Hochwald, S. N, Delano, M, Cance, W. G, & Grobmyer, S. R. (2006) Emerging implications of nanotechnology on cancer diagnostics and therapeutics. *Cancer* **107**, 459–466.

[252] Markman, M. (2006) Pegylated liposomal doxorubicin in the treatment of cancers of the breast and ovary. *Expert opinion on pharmacotherapy* **7**, 1469–1474.

[253] Huang, C.-C, Huang, W, & Yeh, C.-S. (2011) Shell-by-shell synthesis of multi-shelled mesoporous silica nanospheres for optical imaging and drug delivery. *Biomaterials* **32**, 556–564.

[254] Zhu, Y, Shi, J, Shen, W, Dong, X, Feng, J, Ruan, M, & Li, Y. (2005) Stimuli-Responsive Controlled Drug Release from a Hollow Mesoporous Silica Sphere/Polyelectrolyte Multilayer Core-Shell Structure. *Angewandte Chemie* **117**, 5213–5217.

[255] Zhu, Y, Ikoma, T, Hanagata, N, & Kaskel, S. (2010) Rattle-type Fe(3)O(4)@SiO(2) hollow mesoporous spheres as carriers for drug delivery. *Small* **6**, 471–478.

[256] Liu, J, Qiao, S. Z, Hu, Q. H, & Lu, G. Q. (2011) Magnetic nanocomposites with mesoporous structures: synthesis and applications. *Small* **7**, 425–443.

[257] Wu, H, Liu, G, Zhang, S, Shi, J, Zhang, L, Chen, Y, Chen, F, & Chen, H. (2011) Biocompatibility, MR imaging and targeted drug

delivery of a rattle-type magnetic mesoporous silica nanosphere system conjugated with PEG and cancer-cell-specific ligands. *Journal of Materials Chemistry* **21**, 3037–3045.

[258] Karukstis, K. K, Thompson, E. H, Whiles, J. A, & Rosenfeld, R. J. (1998) Deciphering the fluorescence signature of daunomycin and doxorubicin. *Biophysical chemistry* **73**, 249–263.

[259] Liu, Z, Sun, X, Nakayama-Ratchford, N, & Dai, H. (2007) Supramolecular chemistry on water-soluble carbon nanotubes for drug loading and delivery. *ACS Nano* **1**, 50–56.

[260] Liu, Z, Robinson, J. T, Sun, X, & Dai, H. (2008) PEGylated nanographene oxide for delivery of water-insoluble cancer drugs. *Journal of the American Chemical Society* **130**, 10876–10877.

[261] Xing, L, Zheng, H, Cao, Y, & Che, S. (2012) Coordination polymer coated mesoporous silica nanoparticles for pH-responsive drug release. *Advanced materials (Deerfield Beach, Fla.)* **24**, 6433–6437.

[262] Gorin, D. J, Sherry, B. D, & Toste, F. D. (2008) Ligand effects in homogeneous Au catalysis. *Chemical Reviews* **108**, 3351–3378.

[263] Gorin, D. J & Toste, F. D. (2007) Relativistic effects in homogeneous gold catalysis. *Nature* **446**, 395–403.